Dynamic Materials: Exploring Covalent Adaptable Networks in Bioinspired Composites

Dissertation

Zur Erlangung des Grades

„Doktor der Naturwissenschaften“

Im Promotionsfach Chemie

Am Fachbereich

Chemie, Pharmazie, Geographie und Geowissenschaften

der Johannes Gutenberg-Universität Mainz

Sjoerd Engels

geboren in Maasbree

Mainz, Januar 2025



JOHANNES GUTENBERG UNIVERSITÄT MAINZ

Referee 1: REDACTED

Referee 2: REDACTED

Date of oral examination:

‘’παντα ρει” (*Panta Rhei;* everything flows)

– Heraclitus

Author Contributions

The work done in the context of this thesis was performed under supervision of Prof. Dr. Andreas Walther at the Life-Like Materials and Systems laboratory in the Department of Chemistry at the Johannes Gutenberg University Mainz in Germany.

The work described in **Chapter 2** has been published:

''**Sjoerd Engels**[1], Andreas Walther[1]*, Tunable Waterborne Aspartic Acid-Based Covalent Adaptable Networks with Internal Catalysis and Incorporation in Bioinspired Nanocomposites, *Macromolecules* **2024**, 57, 16, 7701-7712. DOI: https://doi.org/10.1021/acs.macromol.4c00666''

[1]Life-Like Materials and Systems, Department of Chemistry, University of Mainz, Duesbergweg 10-14, 55128 Mainz, Germany.

*Corresponding author

The work described in **Chapter 3** will be submitted for publication:

''**Sjoerd Engels**[1], Sophie Marie Koch[2], Ingo Burgert[2]*, Andreas Walther[1]*, Three-Dimensional Shaping and Shape-Memory in Transparent Covalent Adaptable Network-Infused Wood Composites''

[1]Life-Like Materials and Systems, Department of Chemistry, University of Mainz, Duesbergweg 10-14, 55128 Mainz, Germany.

[2]Wood Materials Science, Institute for Building Materials, ETH Zürich, 8093 Zürich, Switzerland.

*Corresponding author

The work described in **Chapter 4** is based on unpublished results

The contributions of each author are described in detail at the start of each chapter.

Abstract

Covalent adaptable networks (CANs) are crosslinked polymer materials that possess advanced dynamic properties based on their ability to undergo covalent bond exchanges. These dynamic properties allow for various applications, including improvements in terms of recycling. While intriguing on their own, they can also be integrated into other polymer-based materials that rely on other phases as well. Such composites are widely used, benefiting from their reinforcing phases and hierarchical architectures to achieve properties beyond those of pure polymers. Bioinspired composites are particularly unique: They utilize design elements based on natural or biological materials to achieve advanced properties or features. However, most composites, and certainly bioinspired composites, suffer greatly from complex preparation methods and an inability to be recycled.

We show that incorporating CANs as the polymeric phase in bioinspired composites can significantly enhance recyclability. This includes the ability to mill used composites and perform compression molding, enabling the formation of new samples, as well as the potential for healing, allowing for the reuse of materials that would otherwise be discarded. Moreover, we show that the benefits of dynamic properties can extend beyond recyclability alone. The dynamic chemistries of CANs can facilitate enhanced interphase interactions and synergies, leading to improvements in mechanical performance. Additionally, we demonstrate that unique functions of polymer phases, such as shape memory behavior, can be extended to the overall composite through stress transfer between the compatible phases. Lastly, we show that (re)shaping of bioinspired composites can be a remarkably impactful feature of dynamic properties. The ability to fabricate complex geometries significantly expands the functional range of composite materials and can enable them to replace metals or polymers in applications where they were previously not viable on account of limited options for sample shapes.

In this thesis I demonstrate these concepts by showing three self-contained bioinspired (nano)composite designs:

1. **Chapter 2** introduces waterborne CANs that feature internal catalysis, dissociative bond exchange and customizable properties through selection of different crosslinkers. Random copolymers based on aspartic acid can catalyze the exchange of dynamic covalent ester bonds when combined with nucleophilic crosslinkers. We also prepare advanced weldable and shapeable nacre-mimetic nanocomposites by combining the CAN with sodium fluorohectorite nanoplatelets.

2. **Chapter 3** demonstrates the incorporation of epoxy-based CANs in wood-based composites. These components demonstrate their compatibility via impregnation of the CAN into the lumens and intercellular spaces of delignified wood, yielding a flexible reinforced composite

material. The transparent composites can be shaped to high curvatures and in three dimensions based on partial cellulose dissolution induced by the transesterification catalyst utilized in the CAN phase.

3. **Chapter 4** introduces a variety of dynamic polyurethanes that are first dispersed in aqueous media, which allows further combination with cellulose nanofibrils in aqueous conditions to prepare bioinspired nanocomposites. Using both siloxane and disulfide chemistries imbues crosslinked polyurethanes with dynamic properties that we use to allow for shaping and laminate formation in the context of the composites. Because of the nature of the aqueous polyurethane dispersions, they exhibit unique synergy with the cellulose nanofibrils, leading to mechanical properties that surpass those of pure cellulose nanofibrils.

This thesis explores a range of approaches to incorporate dynamic polymer systems into bioinspired composite materials, based on different types of CAN polymers as well as variations of the reinforcing phase.

Kurzzusammenfassung

Covalent adaptable networks (CANs) sind vernetzte Polymermaterialien, die fortschrittliche dynamische Eigenschaften besitzen, die auf ihrer Fähigkeit zum kovalenten Bindungsaustausch beruhen. Diese dynamischen Eigenschaften ermöglichen verschiedene Anwendungen, einschließlich verbesserte Recyclingeigenschaften. Obwohl sie für sich genommen schon interessant sind, können sie auch in andere polymerbasierte Materialien integriert werden, die auf anderen Phasen beruhen. Solche Komposite werden weit verbreitet eingesetzt und profitieren von ihren verstärkenden Phasen und hierarchischen Architekturen, um Eigenschaften zu erreichen, die über die von reinen Polymeren hinausgehen. Besonders einzigartig sind bioinspirierte Komposite: Sie nutzen Designelemente, die auf natürlichen oder biologischen Materialien basieren, um fortschrittliche Eigenschaften oder Merkmale zu erzielen. Die meisten Komposite und insbesondere bioinspirierte Komposite leiden jedoch stark unter komplexen Herstellungsverfahren und ihrer fehlenden Recyclingfähigkeit.

Wir zeigen, dass die Integration von CANs als Polymerphase in bioinspirierten Komposite die Rezyklierbarkeit erheblich verbessern kann. Dies umfasst die Fähigkeit, gebrauchte Komposite zu mahlen und eine Kompressionsformung durchzuführen, um neue Proben zu bilden, sowie das Potenzial für Heilbarkeit, was die Wiederverwendung von Materialien ermöglicht, die sonst entsorgt würden. Darüber hinaus zeigen wir, dass die Vorteile dynamischer Eigenschaften über das Recycling hinausgehen können. Die dynamischen Chemien der CANs können verbesserte Interphaseninteraktionen und Synergien ermöglichen, was zu Verbesserungen der mechanischen Eigenschaften führt. Zusätzlich demonstrieren wir, dass einzigartige Funktionen der Polymerphasen, wie z. B. Formgedächtnisverhalten, auf den gesamten Komposit übertragen werden können, indem Stressübertragung zwischen den kompatiblen Phasen erfolgt. Abschließend zeigen wir, dass das (Um-)Formen bioinspirierter Komposite eine bemerkenswert wirkungsvolle Eigenschaft dynamischer Materialien sein kann. Die Fähigkeit, komplexe Geometrien herzustellen, erweitert das Funktionsspektrum von Komposite erheblich und kann es ihnen ermöglichen, Metalle oder Polymere in Anwendungen zu ersetzen, in denen sie aufgrund begrenzter Formoptionen für Proben zuvor nicht geeignet waren.

In dieser Dissertation demonstriere ich diese Konzepte anhand von drei eigenständigen bioinspirierten (Nano)verbundwerkstoff-Designs:

1. **Kapitel 2** führt wasserbasierte CANs ein, die durch interne Katalyse, dissoziativen Bindungsaustausch und die Wahl unterschiedlicher Vernetzer anpassbare Eigenschaften aufweisen. Zufällige Copolymere auf Basis von Asparaginsäure können den Austausch dynamischer kovalenter Esterbindungen katalysieren, wenn sie mit nukleophilen Vernetzern kombiniert werden. In Kombination mit Natriumfluorohektorit-Nanoplättchen stellen wir fortschrittliche, schweißbare und formbare Perlmutt-mimetische Nanokomposite her.

2. **Kapitel 3** zeigt die Integration von epoxidbasierten CANs in holzbasierte Komposite. Diese Komponenten demonstrieren ihre Kompatibilität durch die Impregnation des CAN in die Lumen und Interzellularräume entlignifizierten Holzes, was ein flexibles verstärktes Verbundmaterial ergibt. Die transparenten Kompositen können in stark verkrümmt und in drei Dimensionen geformt werden, basierend auf einer teilweisen Zellulosedissolution, die durch den Transesterifikationskatalysator in der CAN-Phase induziert wird.

3. **Kapitel 4** führt eine Reihe dynamischer Polyurethane ein, die zunächst in wässrigen Medien dispergiert werden, was eine weitere Kombination mit Zellulosenanofibrillen unter wässrigen Bedingungen ermöglicht, um bioinspirierte Nanokomposite herzustellen. Durch die Verwendung sowohl von Siloxan- als auch Disulfid-Chemie wird vernetztem Polyurethan dynamische Eigenschaften verliehen, die die Bildung von Formteilen und Schicht im Kontext der Komposite ermöglichen. Aufgrund der Natur der wässrigen Polyurethan-Dispersionen wird eine einzigartige Synergie mit den Zellulosenanofibrillen beobachtet, die zu mechanischen Eigenschaften führt, die die der reinen Zellulosenanofibrillen übertreffen.

Diese Dissertation untersucht eine Reihe von Ansätzen, um dynamische Polymersysteme in bioinspirierte Komposite zu integrieren, basierend auf verschiedenen Arten von CAN-Polymeren sowie Variationen der verstärkenden Phase.

Table of Contents

Author Contributions ..... **IV**
Abstract ..... **V**
Kurzzusammenfassung ..... **VII**
Table of Contents ..... **IX**
List of Abbreviations ..... **XII**
1. Introduction **1**
1.1. Polymer Materials 2
1.1.1. Thermoplastics 3
1.1.2. Thermosets 4
1.1.3. Stimuli-Responsive Polymers 5
1.2. Covalent Adaptable Networks (CANs) 6
1.2.1. Overview of Materials and Chemistries 6
1.2.2. Catalyzing Bond Exchange 11
1.2.3. Viscoelasticity and Dynamic Thermal Response 13
1.2.4. Associative and Dissociative Bond Exchange 15
1.3. Polymer Composites 18
1.3.1. (Bioinspired) Nanocomposites 19
1.3.2. Continuous Filament Wood Composites 22
1.3.3. Dynamic CAN Composites 23
1.4. Motivation and Outline 26
1.5. References 29
2. Tunable Waterborne Aspartic Acid-Based Covalent Adaptable Networks with Internal Catalysis and Incorporation in Bioinspired Nanocomposites **41**
2.1. Abstract 42
2.2. Introduction 43
2.3. Results and Discussion 45
2.3.1. General System Design for Tunable Waterborne CANs based on Aqueous Prepolymers 45
2.3.2. Pre-CAN Synthesis and Network Formation 47
2.3.3. Tensile Mechanical Properties 49
2.3.4. Dynamic Exchange and Dissociation 51
2.3.5. Recycling 56
2.3.6. Waterborne Nanocomposites 57
2.4. Conclusion 59
2.5. Supporting Information 61
2.5.1. Instrumentation 62
2.5.2. Materials 63
2.5.3. Synthesis Procedures 64
2.5.4. Covalent Adaptable Network (CAN) Preparation 65
2.5.5. Bioinspired Nanocomposite Preparation 66
2.5.6. Swelling Tests 66
2.5.7. Water Content Determination 66

2.5.8. Fitting Stress Relaxation Data....70
2.6. References....76
3. Three-Dimensional Shaping and Shape-Memory in Transparent Covalent Adaptable Network-Infused Wood Composites....81
3.1. Abstract....82
3.2. Introduction....83
3.3. Results and Discussion....86
3.3.1. General CAN Design and Variation Based on Monomer Components....86
3.3.2. CAN Formulation Viscosities and Curing Behaviors....87
3.3.3. Comparative CAN Characterization: Thermal, Chemical, and Mechanical Properties....91
3.3.4. A100-4S Thermomechanical Properties and Dynamic Behavior....95
3.3.5. Impregnation of Delignified Wood with CANs to form Transparent Wood-based Composites....99
3.3.6. CAN-Induced Cellulose Modification and Mechanical Implications....102
3.3.7. Thermal Shaping and Shape-Memory Behavior through Dynamic Bond Exchange....106
3.3.8. End-of-Life Recycling to form 2nd Life Composites....109
3.4. Conclusion....111
3.5. Supporting Information....113
3.5.1. Instrumentation....114
3.5.2. Materials....116
3.5.3. Synthesis of CAN Networks: A100-3S, A100-4S, A90N10-4S, A50N50-4S, N100-4S, A50M50-4S, and A100-4S(No Catalyst)....116
3.5.4. Delignification of Wood Scaffolds....117
3.5.5. Delignified Wood Solvent Exchange....117
3.5.6. Preparation of Bioinspired A100-4S/Wood Composites....117
3.5.7. Preparation of 2nd Life Composites....118
3.5.8. Swelling Tests (Insoluble Fraction Determination)....118
3.5.9. Composite Weight Content Determination....118
3.5.10. Composite Shaping....118
3.5.11. Shape-Memory Tests....118
3.6. References....121
4. Polyurethane Covalent Adaptable Networks: Unlocking Superior Mechanical Properties in Cellulose Nanofiber-Based Bioinspired Nanocomposites....127
4.1. Abstract....128
4.2. Introduction....129
4.3. Results and Discussion....131
4.3.1. PU and PHU Synthesis and Dispersion in Water by Phase Inversion....131
4.3.2. Characterization of PU and PHU Dispersions and their Mechanical Properties....134
4.3.3. Thermal Behavior and Recycling of Dynamic Networks and Polymers....137
4.3.4. Preparation of Bioinspired NCs by Combining PU and PHU Dispersions and CNFs....140
4.3.5. Dynamic Properties of Bioinspired NCs Enabled by Covalent Bond Exchange....141
4.3.6. Tensile Properties of NCs: Variability and Influencing Factors....143
4.4. Conclusion....150
4.5. Supporting Information....153

4.5.1. Instrumentation....154
4.5.2. Materials....155
4.5.3. Synthesis of PUs and Preparation of Aqueous Dispersions via the Acetone Process (PU-PPG1000, PU-PPG$_{1000}$-SiO, PU-PPG$_{1000}$-SiO-SS, PU-PCl$_{2000}$, PU-PCl$_{2000}$-SiO, PU-PCl$_{2000}$-SiO-SS)....155
4.5.4. Synthesis of PHU and Preparation of Aqueous Dispersion via the Acetone Process....157
4.5.5. Preparation of Bioinspired CNF NCs....157
4.5.6. Swelling Tests (Insoluble Fraction Determination)....157
4.5.7. Dispersion Weight Content Determination....157
4.5.8. Bioinspired CNF NC Reshaping....158
4.5.9. NC Laminate Preparation....158
4.6. References....159
5. Synopsis....165
5.1. Introduction....166
5.2. Discussion and Future Research Directions....166
5.3. References....170
Back Matter....173
Acknowledgements....174
Funding Acknowledgements....176
Statement on AI Use....177
Curriculum Vitae....178

List of Abbreviations

3S	trimethylolpropane tris(3-mercaptopropionate)
4S	pentaerythritol tetrakis(3-mercaptopropionate)
A	bisphenol A diglycidyl ether (Chapter 3)
A	Pre-exponential factor Arrhenius equation (Chapter 1)
A3	L-aspartic acid appended acrylamide
APTES	3-aminopropyl triethoxysilane
a_T	Shift factor (relaxation time)
BD	1,4-butanediol
b_T	Shift factor (plateau modulus)
C1	*N*-methyldiethanolamine
C2	1,6-hexanediol
C3	triethanolamine
CAN	Covalent Adaptable Network
CNF	Cellulose nanofibril
Đ	Dispersity
DBTDL	dibutyltin dilaurate
DLS	Dynamic Light Scattering
DMA	Dynamic Mechanical Analysis
DMPA	dimethylolpropionic acid
DMSO	dimethyl sulfoxide
DNA	DeoxyriboNucleic Acid
DP_v	Degree of polymerization (determined by viscosimetry)
DSC	Differential Scanning Calorimetry
E	Young's modulus
E(t)	Relaxation modulus (tensile)
E'	Storage modulus (tensile)
E''	Loss modulus (tensile)

E_0	Plateau modulus (tensile)
E_a	Activation energy
$E_{a,G0}$	Activation energy of bond dissociation
$E_{a,\tau}$	Activation energy of stress relaxation process
EG	methoxy triethylene glycol acrylamide
f	Frequency
FTIR	Fourier Transform Infrared Spectroscopy
$G(t)$	Relaxation modulus (shear)
G^*	Complex modulus (shear)
G'	Storage Modulus (shear)
G''	Loss Modulus (shear)
G_0	Plateau modulus (shear)
G_∞	Equilibrium modulus
GPC	Gel Permeation Chromatography
IPDI	isophorone diisocyanate
k	Rate constant
K_{eq}	Equilibrium constant
M	glycidyl 2-methylphenyl ether
M_n	Number-average molecular weights
N	neopentyl glycol diglycidyl ether
NC	Nanocomposite
NHT	Sodium fluorohectorite
NMR	Nuclear Magnetic Resonance
PCl_{2000}	polycaprolactone diol (M_n = 2000 g/mol)
PHU	polyhydroxyurethane
PPG_{1000}	polypropylene glycol (M_n = 1000 g/mol)
PU	polyurethane
R	Universal gas constant
RH	Relative humidity

RNA	RiboNucleic Acid
S	2-acrylamido-2-methylpropane sulfonic acid
SEM	Scanning Electron Microscopy
Sn(II)Oct	(tin(II) 2-ethylhexanoate)
SS	4,4'-dihydroxy diphenyl disulfide
T	Temperature
t	Time
TBA	tetrabutylammonium
T_g	Glass transition temperature
$t_{G'=G''}$	Gelation crossover point
TMS	tetramethylsilane
TTS	Time-temperature superposition
U_t	Toughness
WLF	Williams-Landel-Ferry
wt%	Weight percentage
XRD	X-ray diffraction
β	Stretching factor
$\Delta_r H°$	Standard enthalpy change
$\Delta_r S°$	Standard entropy change
ε_b	Strain at break
ε_y	Yield strain
η^*	Complex Viscosity
σ_b	Stress at break
σ_y	Yield stress
τ	Relaxation time
τ^*	Characteristic relaxation time
ω	Angular Frequency

Chapter 1. Introduction

Sjoerd Engels

Affiliation

Life-Like Materials and Systems, Department of Chemistry, University of Mainz, Duesbergweg 10-14, 55128 Mainz, Germany.

1.1 Polymer Materials

Polymers are abundant, incorporated in almost every aspect of our lives, from everyday consumer goods (*e.g.* packaging and textiles) to industry (*e.g.* adhesives, paints and coatings, transportation or infrastructure materials) and technology (*e.g.* electronics and medical devices).[1–5] Beyond human-made applications, polymers are also present in nature, serving as structural elements and fulfilling various other biological functions. For instance, cellulose, chitin, and keratin provide structural support in plants, fungi, and animals, while DNA and RNA encode genetic information and proteins performs a wide range of specialized functions.[6]

Fundamentally, polymers are large molecules composed of repeating structural units, typically bonded together in long chains or networks (**Figure 1**).[1,3] These complex assemblies are the foundation for an incredibly diverse library of materials, with unique properties and applications that have revolutionized the world of materials since their inception. For example, some polymers are flexible and elastic, like those used in rubber bands, while others are tough and durable, like the Kevlar used in protective equipment. This versatility stems from the fact that polymers can be tailored on a molecular level, allowing for the design of materials with specific characteristics for a vast array of applications. As such, we can group polymers into a variety of classes, focusing on different characteristics of their origin, preparation, properties or application. One might distinguish natural and synthetic polymers, which have great differences in properties and uses. Nucleic acids and proteins are classes of polymers that are integral to life and biological function, but also have some relevance in terms of human-made structural materials.[6–8] Cellulose is the most prominent structural polymer of natural origin and is highly complex and tailored towards its function by numerous generations of the evolutionary process. In the form of wood-based materials (*e.g.* timber and paper) cellulose fills a distinct and important structural role.[9] Beyond this direct approach, it can be challenging to modify and process cellulose for alternate materials, but great efforts are made in the realms of, for example, composite materials.[10–15] Alternatively, synthetic polymers are often distinguished by the method of their synthesis.[3,16] Such an approach is highly relevant in production design and tailoring the process of polymer synthesis itself, but can lack direct correlation to the final material properties.

This thesis makes use of both synthetic and natural polymers and involves various synthetic procedures in the preparation of bioinspired composites. However, in the context of functional structural materials, as discussed in this thesis, classifying polymers based on their properties is the most practical approach. These properties in turn help to identify the applications. Common examples of such a classification include hydrogel-forming polymers, elastomers, glassy polymers, semicrystalline polymers, etc., which give direct information on the properties and (potential) applications of the materials. Along these lines, bulk polymeric materials (macroscale materials consisting entirely of the polymer phase) are often classified as being either thermosets or

thermoplastics.[1–3,16] Thermoplastics are often characterized by their ability to show a first-order phase transition (melting) on account of their non-crosslinked architecture (*e.g.* linear or branched chains). This contrasts with thermosets which can move between glassy and rubbery states but cannot melt due to their covalently crosslinked nature.

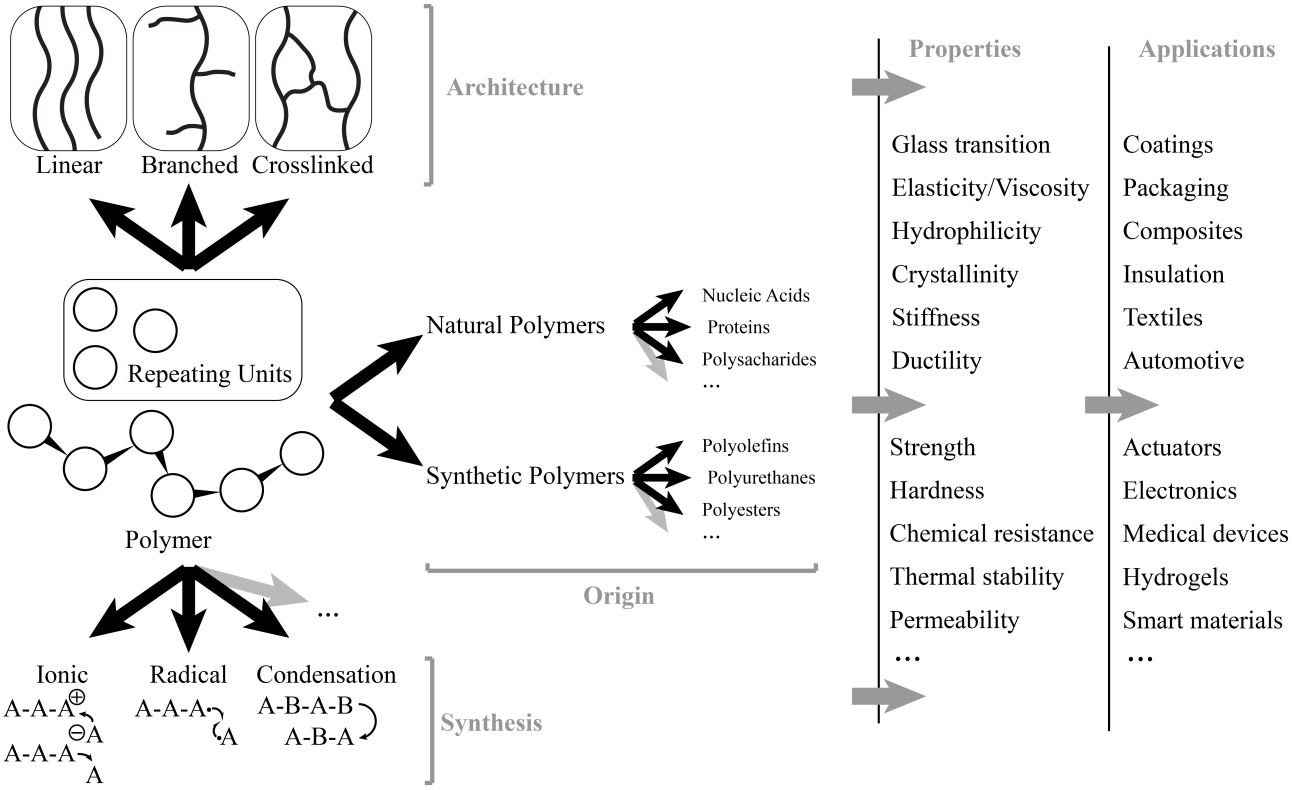

Figure 1. Schematic representation of polymers and their various classifications (left). Depiction of key properties of polymers and a range of applications (right).

1.1.1 Thermoplastics

Thermoplastics possess the capability to thermally melt (a first-order phase transition), which is why they are widely chosen for their excellent processability and adaptability. On a mechanical level, the critical behavior involved with such processability is flow. Flow, often regarded as the key difference between solids and liquids, allows for reorientation on a molecular level (although, as is discussed in later sections, flow in polymers is not limited to the melt state).[17] As such, thermoplastics can be rapidly prepared and are often available for continuous processing through melt-processing (*e.g.* extrusion, injection molding, and 3D printing). In addition, even after initial preparation, they can be further processed through subsequent heating and molding/shaping/remodeling without requiring chemical change.[18] These characteristics allow not only for fast and economical production, but also for easy preparation of complex shapes and for quick adaptation to required applications.

Moreover, in the framework of sustainability, an ever important topic with concerns ranging from environmental pollution to climate change, as well as natural resource exhaustion, the capability to recycle materials we use in everyday life is of vital importance.[19] While even for thermoplastics the details of large scale societal recycling are exceedingly complex, thermoplastics are perhaps the number one candidate for materials that can be recycled fully.[20]

1.1.2 Thermosets

In contrast, thermosets are polymeric materials that lack the advantages associated with (re)processing on account of their crosslinked nature. This means that once chemically prepared, the material consists of an interconnected network that is unable to melt and whose segments possess only limited mobility.[1–3,16] As such, these materials cannot be readily shaped, reprocessed, or recycled. In other words: thermosets cannot exhibit flow as they are composed of a single bonded molecular structure. However, while less ubiquitous than thermoplastics, thermosets are equally important in everyday life with their own set of unique advantages relating to their crosslinked nature. These advantages include structural improvements provided by the crosslinks (*e.g.* stiffness and strength) and water- and solvent-resistance (important in food packaging, outdoor applications, industrial applications, etc.).[2,3] Additionally, the crosslinks enable superior resistance to unwanted changes induced by heat, such as flow. Flow, while beneficial in terms of (re)processability, can impede function when materials are subjected to stresses over prolonged periods of time or in varying or demanding thermal conditions. An important concept in this context is creep (**Sidebar 1**): the time-dependent deformation of materials under constant or repeated loads (distinct from failure, where the material deforms because the load exceeds its strength).[2,21–23] Many applications do not allow for creep as it impacts longevity, safety or function. Thermoplastics are often unable to fill such roles,

Sidebar 1: Creep

Creep is a time-dependent strain, induced by a constant stress.[2,21–23] It can also be described as a gradual, slow deformation that solid-like materials, including many polymers, can undergo when subjected to stresses. Polymer creep is distinct from the continuous flow of traditional liquids and gases because it occurs in viscoelastic materials that exhibit both elastic (solid-like) and viscous (liquid-like) components. It is dependent on stress alongside time and temperature. As such, creep can occur well below the melting point of thermoplastics, while crosslinked thermosets are typically much more resilient against creep. Beyond viscoelastic materials, creep can alternatively also be used to describe forms of time-dependent plastic deformation under a fixed stress, in for example heated metals, ceramics or composites, where viscosity plays little to no role.[22,23] Examples of polymer creep in everyday life include polymeric pipes changing diameter, epoxy adhesives losing integrity, polymer springs or clips losing tension, sealants losing function, plastic bottles deforming, etc.[21]

especially when service temperatures approach the melting point.[21] Thermosets, on the other hand, are much more resistant against creep.

1.1.3 Stimuli-Responsive Polymers

To bridge the gap between thermoplastics and thermosets and their properties, there has been increasing activity in the design of stimuli-responsive materials. Specifically, there is interest in materials that can exhibit resistance to flow, creep, and solvation during operation but that can also switch to a more processable state upon exposure to a stimulus, such as heat. Noncovalent polymer strategies to achieve this involve supramolecular interactions, such as hydrogen bonds, or π-π and ionic interactions, to develop materials that are highly dynamic.[24–27] While possessing benefits of their own, these materials tend to be more thermally and structurally labile compared to covalent networks on account of their much lower bond energies, which is less desirable for creep- or solvent-resistance.[28–32] This thesis focuses on covalent adaptable networks (CANs) that exhibit such dynamic behavior by utilizing exchangeable covalent bonds, which allows them to maintain a higher degree of cohesion. CANs are discussed in more detail in the next section. However, first I briefly mention some alternative responsive materials.

Beyond bulk materials, the broadly developed field of responsive functional materials comprises a multitude of strategies and potential applications, not limited to structural or large-scale systems.[33–35] For instance, responsive nanomaterials are sought after for life-like systems or probing, encapsulation and delivery in a medical context as well as sensing or agricultural and environmental applications.[36–39] Hydrogels are broadly investigated in a multitude of applications, ranging from the biomedical field (*e.g.* wound dressing and drug delivery, tissue engineering, food science, cell cultures, etc.) to soft robotics and actuators.[40–44] Beyond these, there are also important responsive materials in the fields of liquid crystals (*e.g.* displays, optical devices, sensors) and photo responsive systems (*e.g.* photomechanical devices).[45–47] What all these systems have in common is a design element that enables targeted responses to specific stimuli in order to access unique properties. While these systems are beyond the primary scope of this thesis, they highlight approaches and applications that have been applied and can be transferrable to CAN materials.

1.2 Covalent Adaptable Networks (CANs)

1.2.1 Overview of Materials and Chemistries

CANs are an important cornerstone of responsive polymer materials that have gained a lot of attention in the past decade. The defining design elements of CANs are their dynamic covalent bonds, which can undergo bond exchange, specifically under certain triggers (*e.g.* chemical trigger, light, heating).[29,31,48] As such, topology rearrangement and consequently macroscopic remodeling or reshaping is possible. This enables bridging of the benefits normally limited to thermoplastic and thermosets, respectively. CANs are highly (re)processable compared to thermosets considering elevated temperatures enable crosslink exchange but are more cohesive than thermoplastics in terms of chemical or melting resistance on account of their network structures (**Figure 2**). The term CAN covers all covalently crosslinked networks with adaptable covalent bonds, thus it is broader in scope than another commonly used term, 'vitrimers'. This includes networks with properties that are not always associated with vitrimers, such as non-Arrhenius behavior (more detailed discussion in section 1.2.3.), dissociative crosslinks (more detailed discussion in section 1.2.4.) or alternative function of bond exchanges (*e.g.* shape memory or topological programming).[29,49–52] In the context of this thesis, I describe all such materials as ''CANs'' for the sake of consistency and accuracy with further subclassifications going into their different properties or chemistries.

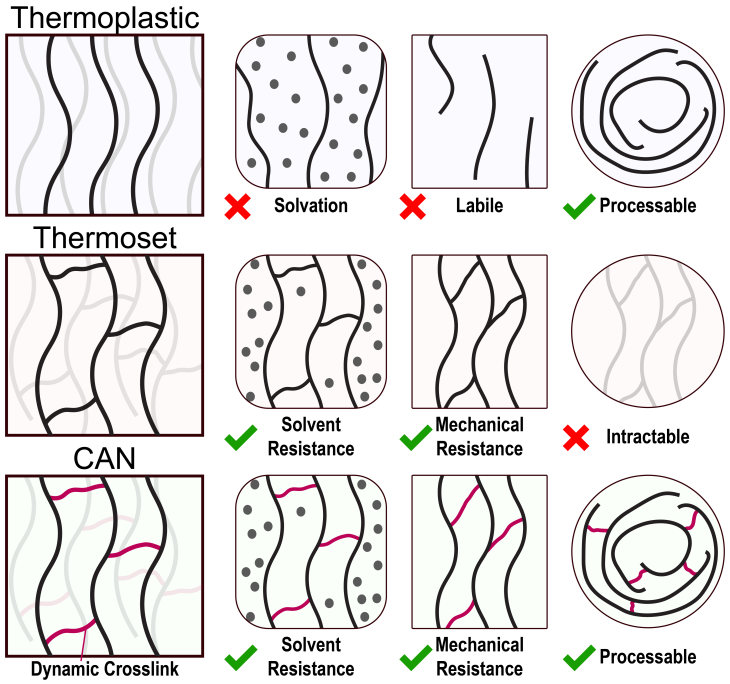

Figure 2. Schematic depiction of the architecture, advantages, and disadvantages of thermoplastics and thermosets in comparison to CANs

While more recent advances sparked the large-scale interest in CANs and breathed life into the field, it would be remiss to not briefly mention the long history of covalent dynamic crosslinks. For instance, in 1954 it was demonstrated how polydimethylsiloxane elastomers could undergo stress relaxation

after being crosslinked (**Figure 3**a).[53] The authors investigated the role of base or acid as catalysts for the stress relaxation and posited how their findings indicated reversible chemical bond (siloxane) exchange rather than irreversible chain rupture and termination. Interestingly, they also demonstrated catalytic effects of gaseous nitrogen, water, and carbon dioxide on the stress relaxation rates, which is only sparsely discussed in modern CAN research. In addition, studies from 1964 demonstrate rapid stress relaxation in crosslinked polyethylene and polyurethane networks through polysulfide exchanges, even in the absence of catalyst (**Figure 3**b).[54–56] It has long been known how the S–S bond is a reactive bond that can form the basis of dynamic structural functions, whether in natural materials such as polypeptides (*e.g.* keratin and collagen) or in synthetic materials such as vulcanized rubber.[57–60] Interestingly, it has been shown both in these older publications as well as more recently how not just disulfides, but polysulfides in general can undergo bond exchange.[54–56,61] This is another example of a key insight that is yet to be explored in detail in the modern CAN field, which focusses on disulfides over other polysulfides.

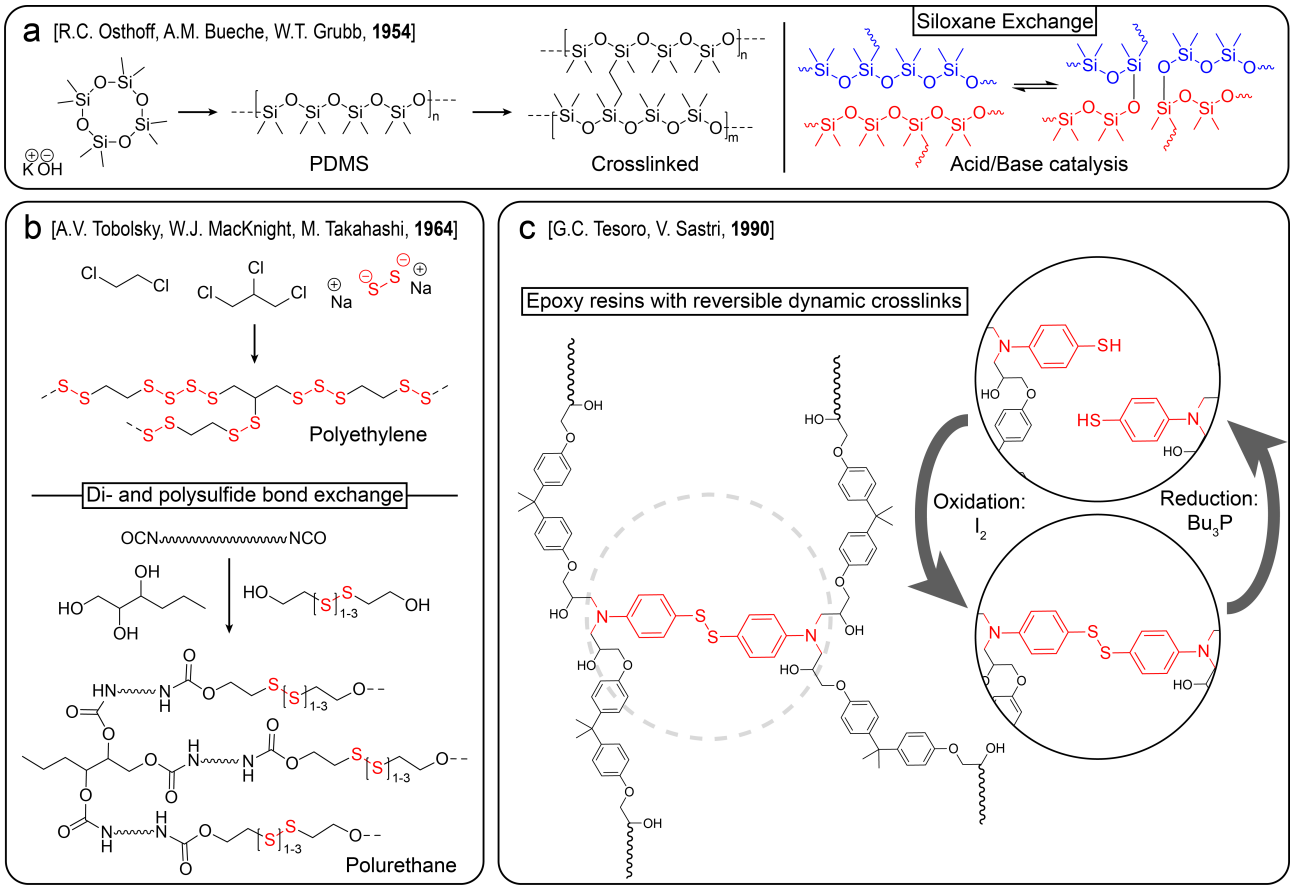

Figure 3. Historical overview of CANs. (a) CAN based on crosslinked polydimethylsiloxane with siloxane exchange facilitated via acid or base catalysis.[53] (b) Polyethylene and polyurethane CANs utilizing di- and polysulfide bond exchange.[54–56] (c) Epoxy resin featuring reversible disulfide crosslinks through reduction and oxidation reactions.[62]

Another interesting study from the last century is on materials reminiscent of many recent disulfide-based CANs where rather than focusing on dynamic disulfide exchange at elevated temperatures, the authors considered the possibility to reversibly break and form the disulfide crosslinks via

reduction and oxidation, respectively (**Figure 3**c).[62,63] Such a strategy is not always considered under the umbrella of CANs. However, all these examples demonstrate well the extensive toolbox for designing new functionalities by intelligent application and incorporation of well-established chemistries.

After the previous examples that superseded the official establishment of CANs as a material class to bridge the gap between thermoplastics and thermosets, I shift to a few prominent examples that initiated the field as it is known today. In a groundbreaking study from 2011 the authors prepared a classical epoxy network based on common components (bisphenol A diglycidyl ether and fatty di- and tricarboxylic acids), thereby forming a network containing both ester groups and hydroxyl groups as is required for the transesterification reaction (**Figure 4**a).[28] However, they additionally enriched the network with a transesterification catalyst in zinc acetate. The resulting crosslinked material behaved like an elastomer at room temperature but was able to relax stresses at elevated temperatures based on the covalent bond exchange.

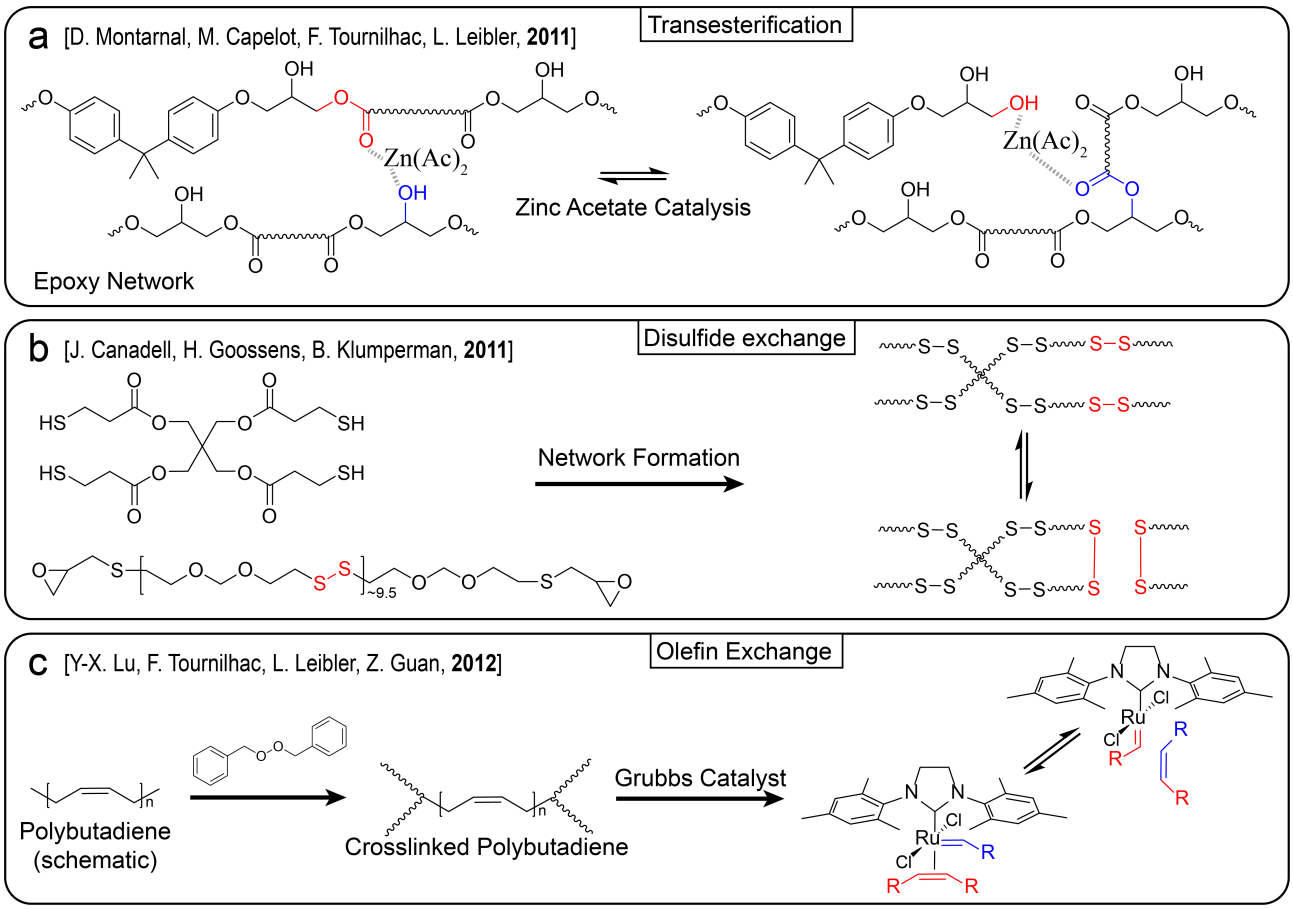

Figure 4. Overview of CAN development. (a) CAN based on epoxy resin with transesterification catalyzed by zinc acetate.[28] (b) Thioester CAN resin featuring disulfide bond exchange.[64] (c) Polybutadiene crosslinked by reaction with benzyl peroxide, employing olefin bond exchange through use of Grubbs catalyst.[65,66]

A key insight they gained is how the viscosity response to temperature changes follows a gradual Arrhenius-like behavior (**Sidebar 2**), comparable to that of vitreous silica, hence the name "vitrimer". Crucially, this behavior is distinct from organic compounds and polymers whose viscosity change

abruptly around phase- or glass transition temperatures. The covalent bond exchange translates macroscopically to a unique form of flow whereby crosslink density is maintained but the shuffling of the crosslinks allows for a dynamic topology that changes over time when subjected to external stresses. This flow is guided by the chemical reactivity of the bond exchange rather than physical phase transition, which results in the aforementioned Arrhenius behavior.[67–71] Another publication from 2011 presented a CAN based on disulfide bonds that does not require any catalysts for effective bond exchange (**Figure 4**b).[64] Especially considering how disulfide bond exchange can be triggered by light irradiation as well as temperature changes, this example further emphasizes the suitability of disulfides as dynamic bonds.[72] The final example to discuss is a CAN based on olefin exchange reactions in polybutadiene networks by use of a Grubbs catalyst (**Figure 4**c).[65,66] Remarkably, implementation of this catalyst is effectively done without modification or complex procedures, demonstrating impressive dynamic function without specialized design. These methods highlight how the field of CANs originated by bringing dynamic network properties to thermoset-like materials. To achieve this, previously known covalent chemistries can be adapted and employed to achieve dynamic bonds rather than designing novel chemistries from the ground up. This approach is beneficial because it makes application and integration of the CAN field to (industrially) established polymer materials science more achievable. Furthermore, an extensive toolbox for tailoring CANs is available by considering known chemistries from other fields. Several examples include transesterification[28,73,74], transcarbamoylation[75,76], carbonate exchange[77,78], silyl ether trans alkoxylation[53,79–82], dioxaborolane exchange[83–86], vinylogous urethane transamination[87–89], urea exchange[90–92], imine exchange[93–95], olefin exchange[65,66], disulfide exchange[64,96–98], 1,2,3-triazolium salts exchange[99,100] (**Figure 5**).

Sidebar 2: Arrhenius behavior

Arrhenius behavior describes the exponential dependence of reaction rates on temperature. This follows the equation:[67–71]

$$k = Ae^{-\frac{E_a}{RT}} \quad (1)$$

where k is the rate constant, A is a pre-exponential factor, E_a is the activation energy, R is the gas constant, and T is the absolute temperature. This behavior is typically plotted as ln(k) against 1/T which leads to a linear plot.

In the framework of CANs, the reaction rate of bond exchange reactions is linked to the stress relaxation times (τ) and thus ln(τ) is plotted against 1/T (or often 1000/T).[70,101] A linear relationship indicates how the temperature response relies predominantly on the reaction rate of the bond exchange (specifically a singular mechanism of bond exchange). It is important to note that this is usually only true within a certain temperature range, above or below which factors such as glass transition or side reactions (*e.g.* degradation or alternative crosslinking) can play a more important role.

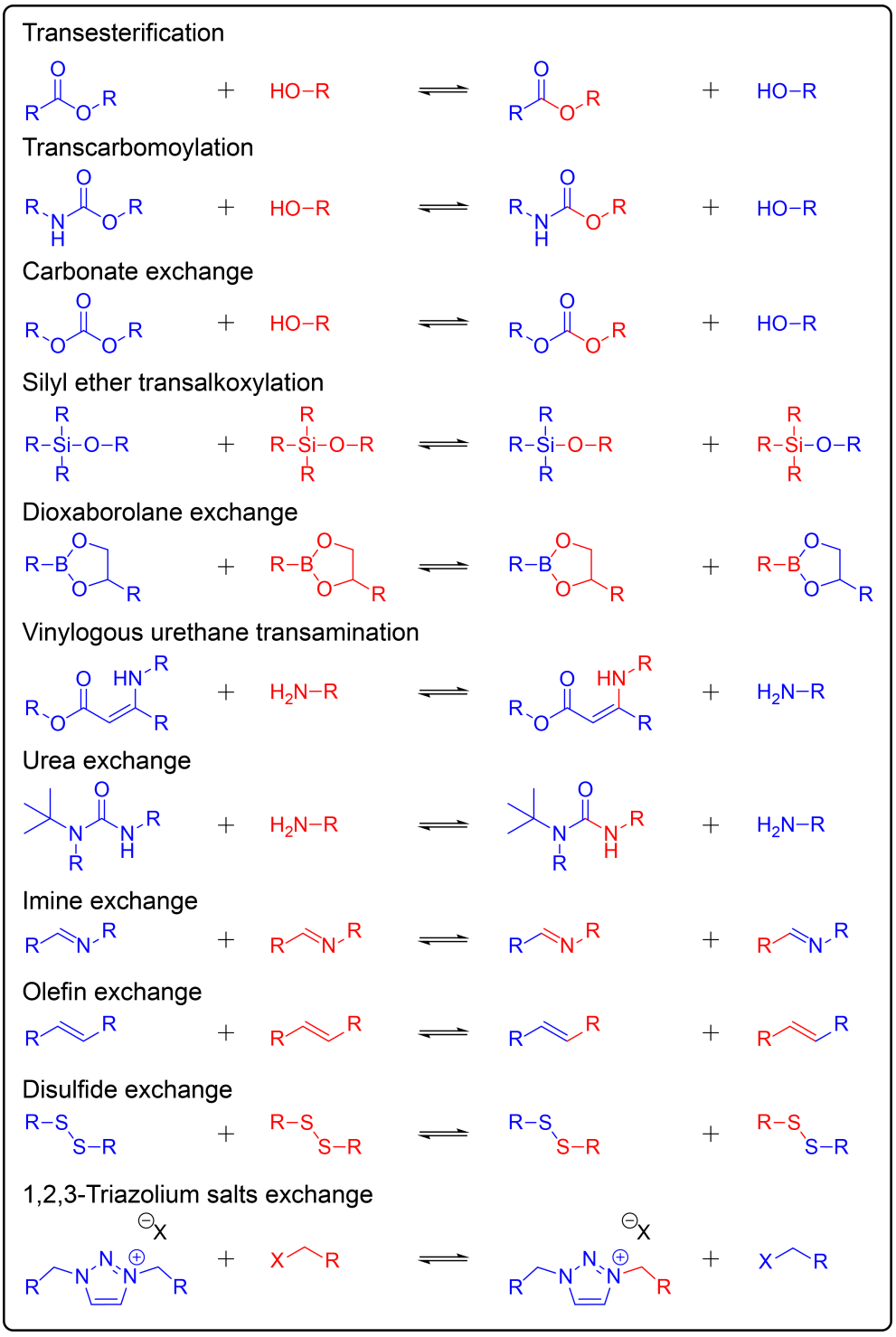

Figure 5. Overview of bond exchange chemistries commonly employed in CANs. The net reactions are depicted without inclusion of reaction conditions or catalysts used.

1.2.2 Catalyzing Bond Exchange

Catalysis is important to discuss in the context of CANs. Generally, CAN bond exchange relies on either of two options: (i) incorporation of thermodynamically unstable or labile bonds that form crosslinks but are relatively easy to break and reform (*i.e.* low activation energy).[102] This enables the bond exchange to occur at faster rates and at temperatures at which most types of bonds would remain static. (ii) The addition of a catalyst (externally or internally) that aids significantly in the bond exchange via coordination, acid/base stabilization or nucleophilic attack. The most common example of the former approach is the previously described disulfide bond. However, generally most CANs fall in the latter category. Catalysts function by lowering the energy barrier for a reaction to occur and thus accelerate the reaction kinetics.[71]

External catalysts, such as triazabicyclodecene, *p*-toluenesulfonic acid, and zinc acetate, are small molecules or compounds that are mixed into material networks to facilitate bond exchange without being covalently tethered to the polymer matrix.[28,30,103–105] This approach is intuitive as it relies on established catalysts used in organic or polymer synthesis. Consequently, advantages include ease of use (*e.g.* simple mixing with the monomer formulation prior to network formation or swelling of the network in catalyst solution), commercial purchase of the catalyst, wide availability of different candidates, and tried-and-tested catalytic activity. However, such catalysts can suffer from relatively poor network integration and chemical stability, catalyst leaching, and phase-separation or aggregation.[30,102,106]

In contrast, a second approach that has gained traction more recently involves the usage of internal catalysts, which are functional groups that are covalently tethered to the polymer matrix (**Figure 6**). Many of the disadvantages for external catalysts are avoided when using internal catalysts.[30,102,106] Moreover, with the right design, internal catalysis can enable some of the fastest bond exchange rates that have been demonstrated in CANs.[107,108] The catalysts function by being tethered near the reaction site, making the effective concentration higher than the actual bulk concentration. In many cases, their orientation with regards to the reaction site is optimized as well, in a fashion analogous to intramolecular catalysis or neighboring group participation in classical organic chemistry, or the proximity effect in enzymes.[71]

For instance, a series of studies in 2019 and 2020 investigated phthalate-based polyester networks with a variety of catalysts to understand the rates of bond exchange (**Figure 6**a).[107–109] Phthalate-based polyester networks are industrially relevant materials and can be given dynamic behavior by catalyzing transesterification. Zinc acetylacetonate was used as a common external catalyst and resulted in a material with reasonable stress relaxation. However, the use of a carboxylic acid moiety in the phthalate structure as an internal catalyst instead yielded comparatively faster stress relaxation rates. The free carboxylic acid can speed up the transesterification by forming the intermediate

anhydride via elimination, which is then a more reactive target for nucleophilic attack by another hydroxy group. Subsequently, the studies investigated a similar form of internal catalysis based on sulfonic acid, addition of an external tertiary amine as a second catalyst, and addition of an internal tertiary amine as a second catalyst, all of which demonstrated improved stress relaxation compared to the previous result. These results demonstrate well how catalysts generally impact the dynamic properties but also how internal catalysts can show superior bond exchange enhancement compared to external catalysts. Another example is based on a number of acrylate-based CANs used for 3D printing dynamic materials, whereby incorporation of a phosphonic acid monomer yielded superior stress relaxation for the network compared to conventional external catalysts tested (**Figure 6**b).[110,111] Interestingly, a phosphonic acid positioned within a crosslink rather than at the backbone had better performance as a catalyst, although the reason is not fully understood. It is important to mention that the internal catalysis approach can be less accessible, as it tends to rely on modification or functionalization of the monomer components and can require careful network design to make the catalyst compatible with the material.

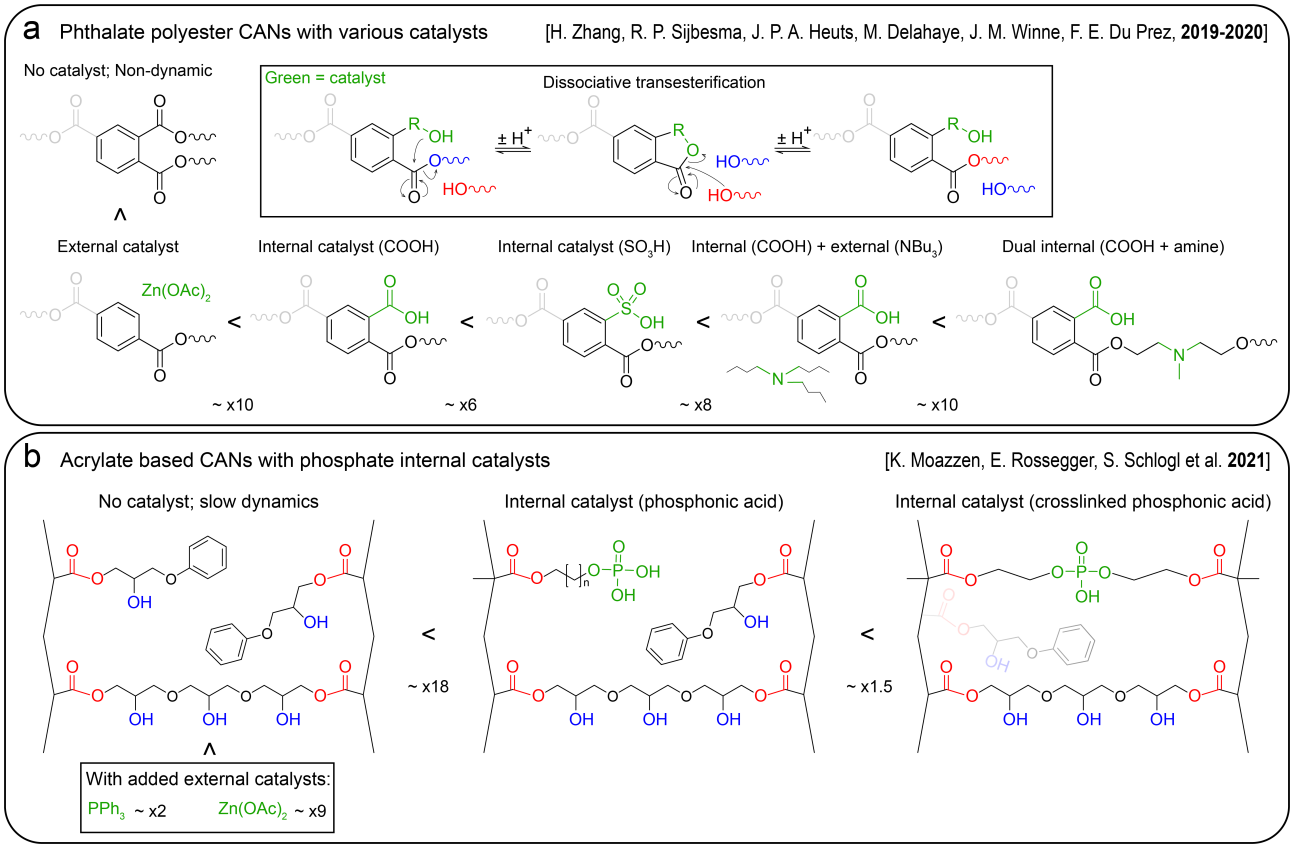

Figure 6. Internal catalysis in CANs. (a) Comparison of various types of catalysis phthalate polyester CANs.[107–109] (b) Phosphonic acid as internal catalyst in comparison to external catalysts in polyacrylate-based CANs.[110,111]

1.2.3 Viscoelasticity and Dynamic Thermal Response

As previously mentioned, the bond exchanges of CANs enable distinct thermomechanical properties compared to other materials (**Figure 7a**). The bond exchange reactions of CANs usually exhibit an Arrhenius-like temperature dependence, which is characteristic for chemical reactions.[67–71] Consequently, this behavior related to the chemistry of bond exchange results in Arrhenius dependences of the thermomechanical properties of CANs (*e.g.* stress relaxation or viscosity) as well. This indicates how the dynamic behavior of CANs is directly related to the rate of chemical reactions rather than a physical transition (**Figure 7**b). As such, relaxation behavior is the most analyzed property of CAN materials and gives information about the dynamic chemistry involved on a molecular level, especially considering how most other methods to analyze on a molecular level are unsuitable for insoluble crosslinked networks (*e.g.* NMR and chromatography). It is important to note however, that this straight-forward Arrhenius behavior can fail when there are multiple or multistep reactions or different reaction mechanisms going on in parallel, something that is often the case in CANs.[48,49,89,112,113] In addition, deviation from Arrhenius behavior has also been reported in relation to effects such as the glass transition (below which relaxation is highly limited; see **Sidebar 3**), segmental dynamics slowing down even above the T_g (sometimes observed up to $T = T_g + 100$ K), or other types of relaxation effects (*e.g.* monomer friction or network strand relaxation).[29,31,101,114–116] As such, factors like hydrophilicity, backbone mobility, crosslink density, etc. all have complex interplay with regard to determining the exact thermomechanical properties. Despite these complications, the relaxation of CANs within a relevant thermal and temporal range is often well described by an Arrhenius curve. This is the case because relevant relaxation measurements typically occur at temperatures that are far above the T_g, while keeping temperatures low enough to avoid significant side-reactions. Furthermore, most CANs rely on one mechanism of bond exchange that dominates the mechanical response and thus precludes significant deviation from Arrhenius behavior during analysis.

Sidebar 3: Glass transition in CANs

As the glass transition temperature indicates the transition of glassy behavior to rubbery behavior of polymers, it marks a change in segmental motion and mobility of polymer segments. This mobility is crucial to relax stress in all polymers, but in the context of CANs it is specifically required to bring reactive moieties together and to relax stress through the bond exchange processes. This essentially means CANs only demonstrate significant dynamic behavior above the T_g even when the bond exchange reaction is already rapid below.[29,31,48,101] Interestingly, while the glass transition is sometimes simplified as a sharp phase transition, it has been extensively shown in CANs how stress relaxation deviates from Arrhenius behavior for temperatures above the T_g (sometimes up to $T = T_g + 100$ K), instead following William-Landel-Ferry behavior. This indicates how the reduced segmental motion in this temperature range majorly impact the relaxation process.[31,48,101,114–116]

Generally, the discussed relaxation times at various temperatures are measured via one of three measurement types: (i) small-amplitude oscillatory sweep experiments, (ii) stress relaxation experiments, and (iii) creep and recovery experiments. All these measurements attempt to measure the same intrinsic properties of the material (relaxation times) but have their own advantages and disadvantages in terms of experimental considerations. For a more detailed overview of these methods, I recommend the excellent tutorial review by Ricarte and Shanbhag on linear rheology for CANs.[101] In the context of this thesis, I rely predominantly on stress relaxation experiments to investigate the dynamic CAN properties.

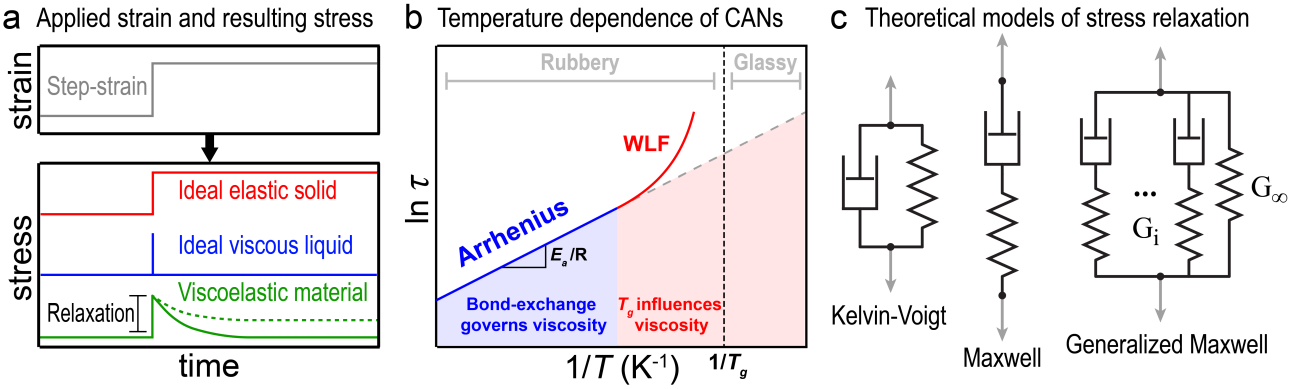

Figure 7. Stress relaxation in CANs. (a) Schematic representation of the stress response to a step-strain input for ideal elastic solids, ideal viscous liquids, and viscoelastic materials (such as CANs). (b) Temperature dependence of relaxation times for common CANs, illustrating the transition from Arrhenius behavior to Williams-Landel-Ferry (WLF) behavior near the glass transition temperature (T_g). (c) Theoretical models of stress relaxation based on Hookean spring and dashpot elements.

Stress relaxation can be modeled via several related equations, based on a combination of elastic behavior, modeled by a Hookean spring, and viscous behavior, modeled by a dashpot element (**Figure 7**c). In the simplest, but still highly relevant models, this constitutes a single spring and dashpot either in series or in parallel, known respectively as the Maxwell model and the Kelvin-Voigt model.[101] Upon an external stress, the spring instantly responds and stores the stress as potential energy. Then as time goes on the dashpot slowly relaxes stress (dissipated as heat) at a rate based on the viscosity of the dashpot. I focus on the Maxwell variant, where the stress relaxation modulus is described as:

$$G(t) = G_0 e^{-(t/\tau)} \tag{2}$$

where $G(t)$ is the relaxation modulus, G_0 is the plateau modulus, t is the time, and τ is the relaxation time. An important variation on this model is the generalized Maxwell model (also possible for the Kelvin-Voigt model), whereby the spring and dashpots can be extended in parallel to capture subsequent contributors to the overall relaxation (**Figure 7**c).[101] An example of this could be chemical side reactions or different mechanisms, but also something such as chain relaxation that occurs in all polymers irrespective of bond exchange reactions, or relaxing supramolecular interactions.[116,117] The general description of this is:

$$G(t) = G_\infty + \sum_{i=1}^{n} G_i e^{-(t/\tau_i)} \quad (3)$$

where G_∞ is the equilibrium modulus, n is the number of discrete relaxation modes, and G_i and τ_i are the modulus and relaxation time associated with relaxation mode i, respectively. The more elements used the more accurate the model will be but also the more intensive to compute and difficult to interpret.[114,116] A method to mimic the contribution of secondary effects while maintaining simplicity of the original models is the stretched exponential model whereby an empirical stretch on the exponential decay tries to cover all relaxation modes:

$$G(t) = G_0 e^{-(t/\tau^*)^\beta} \quad (4)$$

where β is the stretching factor of the function. This method is often sufficient to fit experimental curves but the characteristic relaxation time (τ^*) does not directly correlate to individual processes occurring during the stress relaxation.[101]

In this thesis, I fit stress relaxation data using the stretched exponential function. This approach prioritizes a general analysis of relaxation rates over the precise attribution of distinct relaxation processes, which is often not feasible without further extensive analysis. This methodology is particularly good for understanding the bond exchange processes when comparing similar CAN materials, such as in Chapter 2, where other factors influencing relaxation are likely to be similar. However, it is important to note that stretched exponential fitting (and fitting in general) can underestimate terminal relaxation.[101] Therefore, it is essential to complement the stress relaxation experiments with practical (re)processing data, such as recycling experiments, to demonstrate the effectiveness of the bond exchange process.

This segment discussed the thermomechanical properties of CANs and how they are impacted in various polymer networks with a focus on what is necessary for understanding the work done in the context of this thesis. For more in-depth discussions on the topic, the reader is referred to various reviews written on CANs that go into more detail on bond exchange mechanisms, internal catalysis, comparison of various chemistries, dynamic mechanical analysis (DMA), etc.[29–31,48,49,101,102,106]

1.2.4 Associative and Dissociative bond exchange

Lastly, I will briefly describe the notion of associative and dissociative bond exchange mechanisms as this is relevant for most CANs and impacts the thermomechanical properties and how to interpret them. CANs are often subdivided into two categories based on the mechanism of their bond exchange: associative reactions (*e.g.* standard transesterification and vinylogous urethane

transamination) and dissociative reactions (*e.g.* 1,2,3-triazolium salt exchange and Furan-maleimide Diels-Alder exchange) (**Figure 8**a,b).[29,31,48,49]

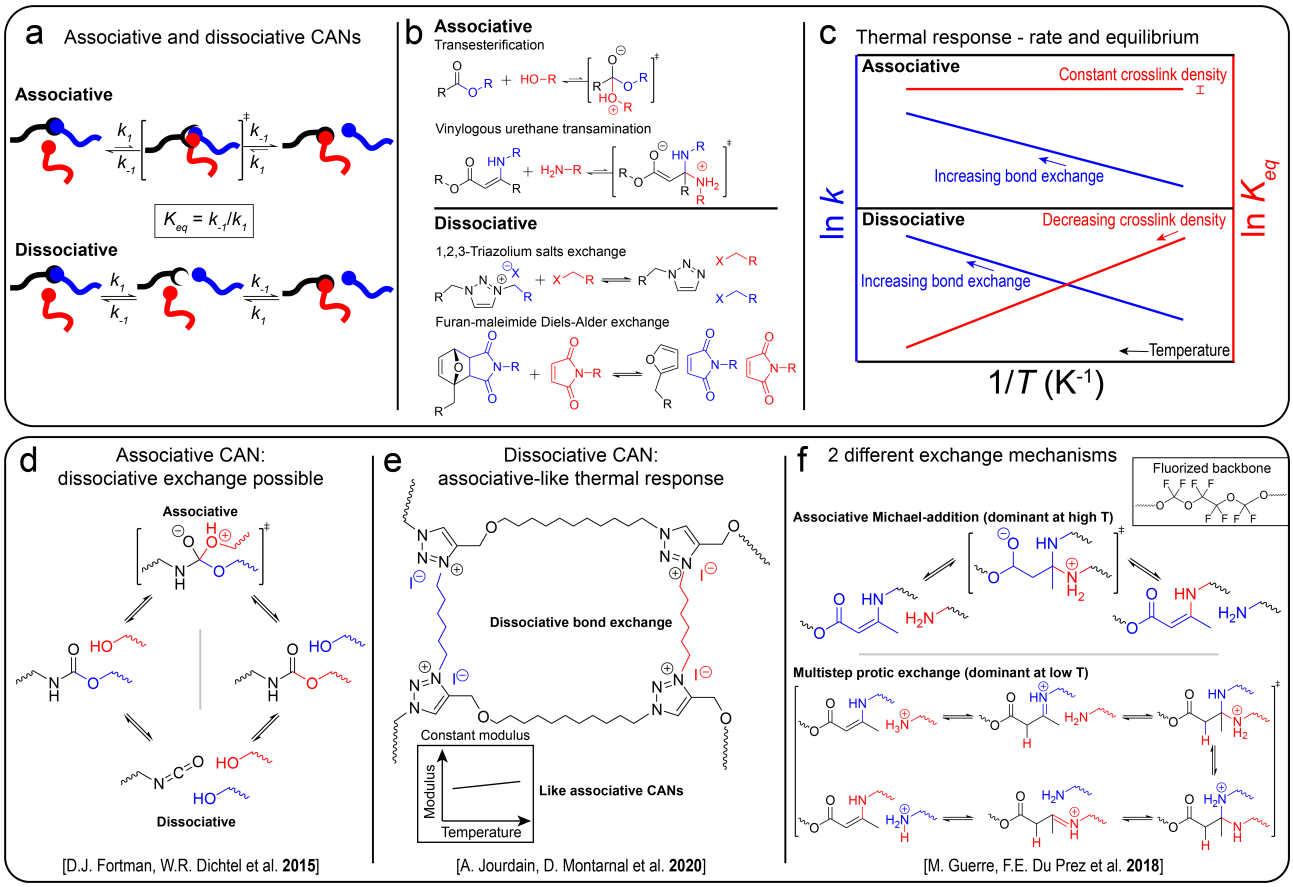

Figure 8. Associative and dissociative bond exchange mechanisms. (a) Schematic representation of associative and dissociative bond exchange. (b) Common examples of bond exchange chemistries typically considered associative and dissociative, respectively. (c) Theoretical thermal response for the bond exchange mechanisms. (d) Associative and dissociative mechanisms in polyhydroxyurethanes CAN.[118] (e) Dissociative CAN based on 1,2,3-triazolium salts exhibiting a thermal response commonly associated with associative CANs.[50] (f) Vinylogous urethane CAN with a fluorinated backbone demonstrating two distinct mechanisms for bond exchange based on temperature.[48,112]

Associative CANs are typically regarded as networks with a constant crosslink density, which remains unchanged with temperature. In these systems, covalent bond exchange occurs via an associative transition state or intermediate. However, since the lifetime of these tend to be negligible, it does not significantly affect the overall crosslink density. Consequently, associative CANs are recognized on a material level by an almost constant plateau modulus, irrespective of temperature. In contrast, dissociative CANs involve equilibrium reactions between associated and dissociated states, with both being relatively stable. These dissociation and reassociation reactions involve both enthalpic and entropic factors, whereby the former favors bonding, and the latter favors debonding. At higher temperatures the entropic factor becomes more dominant following the van 't Hoff equation,[70,119]

$$R\ln K_{eq} = \frac{-\Delta_r H^\circ}{T} + \Delta_r S^\circ \qquad (5)$$

where K_{eq} is the equilibrium constant of the reaction, R is the universal gas constant, T is the temperature, $\Delta_r H°$ is the standard enthalpy change, and $\Delta_r S°$ is the standard entropy change for reaction equilibriums.

As a result, dissociative CANs do not maintain a constant crosslink density over a wide temperature range. Instead, they exhibit a crosslink density that depends on the equilibrium of the reaction (**Figure 8**c). This distinction is crucial because the state of the equilibrium is temperature dependent: it shifts more towards the entropically favorable dissociated state as temperature increases.[29,31,48,49] This means that the thermal response of dissociative CANs exhibits a decrease in the crosslink density, which can correspond to a decrease in the plateau modulus.

The distinction between dissociative and associative CANs can be impactful on a material level. Associative CANs are more likely to maintain similar mechanical properties, resistance to solvation, and Arrhenius behavior over a wide temperature range.[29,31,48,49] Their increasing bond exchange kinetics are the major temperature-response they exhibit. In contrast, dissociative CANs can sometimes access a higher level of softening or flow at higher temperatures (deviation from Arrhenius).[29,31,48,49] In addition, crosslink dissociation can further enhance the mobility of reactive groups in the network. These factors can enhance the (re)processability of dissociative CANs. Dissociative reactions can also be beneficial if changes in stiffness or ductility based on the temperature are desirable traits. However, it is important to be aware of the limitations of this classification. In practice, many CANs operate on the complex interface between idealized conceptualizations of ‘associative’ and ‘dissociative’.[48,49] For instance, many examples of dissociative CANs behave much like associative CANs because the equilibrium of their bond exchange reaction is strongly favoring the associated state (**Figure 8**e).[48–50] The temperatures at which the equilibrium shifts to a significant dissociated state might be out of reach in any realistic temperature range. On the other hand, there are associative CANs (*i.e.* CANs operating primarily via an associative reaction mechanism) which can display new dissociative mechanisms of bond exchange once temperatures reach certain levels (**Figure 8**d).[48,49,118,120] Beyond this, many bond exchange reactions proceed via more complex multistep processes and even the architecture of the network (*e.g.* crosslink distribution, chain length, backbone, etc.) impacts bond exchange entropy and thus affects the thermal response of CANs (**Figure 8**f).[48,49,112] As such, prediction of the thermomechanical properties based solely on the type of exchange chemistry is not possible. It is vital to analyze the thermomechanical properties through relaxation experiments for each specific material to understand the bond exchange mechanisms and dynamic properties of the CAN material.

1.3 Polymer Composites

Composite materials are abundant in nature, whereby a hierarchical structure consists of a continuous and, usually, discontinuous phase to achieve their enhanced properties.[2,3,121,122] Bone and nacre are examples based on combination of an organic and inorganic phase, while wood represents a composite where cellulose, an organic component, performs a similar reinforcing role within the wood matrix.[123,124] In the context of synthetic materials, composites usually consist of a synthetic polymer phase as the matrix and a reinforcing phase, such as carbon, metals, silica, aromatic polyamides (*e.g.* Kevlar), but also natural reinforcements such as cellulosics (**Figure 9**).[2,3] Composites have been produced from almost any synthetic polymer and almost any conceivable filler, which demonstrates the broad appeal of such materials.

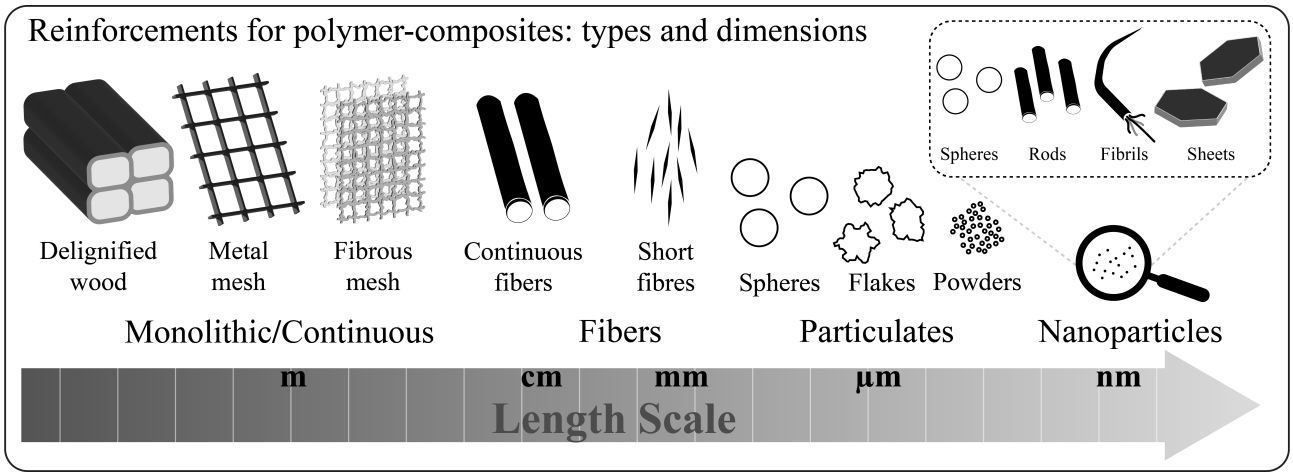

Figure 9. Schematic overview of the length scales and types of reinforcements commonly used in polymer composite materials.

The design principle of composites is based on the combination of two phases, each with unique properties, to yield a material characterized by enhancements compared to either of the separate components. Common property enhancements achieved in such a way include elevated mechanical properties (*e.g.* strength, stiffness, toughness, hardness, etc.) and creep resistance (superior even to thermosets).[2,3,21,125] For instance, combination of polymeric resin and reinforcing filaments like glass or carbon fibers is a widespread method to construct stronger and stiffer materials than the individual resin. These mechanical properties are often particularly impressive because of the relatively light weight of composites, for instance compared to metals. The reinforcing effects rely on strong interfacial interactions, such as van der Waals or polar interactions or even covalent bonds, which facilitate transfer and distribution of stresses from the matrix to the reinforcement. Many of the applications of composites rely heavily on these benefits, such as in the marine, aerospace, and automotive sectors, where it is crucial for load-bearing materials to be strong, creep resistant, as well as light. Other than these sectors, composites are used in biomaterials (*e.g.* prosthetics), industry (*e.g.* reaction and storage vessels and pipes), renewable energy (*e.g.* windmill blades, solar panels, batteries and fuel cells), electronics, sports products, construction, packaging, etc.[2,3] But the

introduction of reinforcing phases to polymers is also linked to a host of other benefits, such as: flame resistance, corrosion resistance, antibacterial properties, weathering or abrasion resistance, electrical or thermal conductivity or insulation, fluid barrier properties, vibration damping, tailored optical properties, electromagnetic shielding, chemical resistance, water resistance, environmental sustainability, and economical benefits.[2,3,126–129] Many of these benefits include some form of resistance to the various conditions (*e.g.* chemical, water, heat, etc.) composites are exposed to in the aforementioned applications, which aptly demonstrates the utility of composite materials. Lastly, an important consideration for composites is that they are often anisotropic in nature as the orientation of the reinforcing phase within the composite affects the properties per spatial direction. This can be a limitation in some circumstances, but it is generally an advantage for implementation of directional properties, such as load-bearing performance or conductivity.[2,3]

1.3.1 (Bioinspired) Nanocomposites

Nanocomposites comprise a specific subset of composites where the reinforcing phase is composed of individual particles on the nanoscale (typically less than 100 nm in at least one dimension) (**Figure 9**).[2,3,121,122] Common examples here include nanoclays (layered silicates), graphene and graphene oxide nanosheets, carbon nanotubes, inorganics such as titanium oxide, metallic nanoparticles, cellulose nanocrystals and nanofibers, and silica nanoparticles. What makes nanocomposites unique is how the scale of the individual particles is much closer to the dimensions of polymer chains or segments, which allows for interfacial interactions on the molecular level (*e.g.* supramolecular interactions like ionic or hydrogen bonding, physical interactions like entanglements, or even chemical reactions).[2,3,121,122] Crucially, the mechanical properties associated with nanoparticles tend to be superior compared to their larger counterparts. Nanofillers also have a high surface area per weight fraction which allows for more homogenous mixing of the polymer and reinforcing phases compared to macroscopic composites. For the purposes of nanocomposites this means that larger degrees of reinforcement are possible as well as unique properties, such as transparency, gas-barrier properties, homogeneous conductivity, and various optical properties (*e.g.* nonlinear optical behavior, luminescence, iridescence, chirality).[3,130–132] Although the nanocomposites explored in this thesis typically possess high reinforcement content, it is important to note that even at low nanoparticle concentrations, they can significantly enhance the properties of materials.[133–135]

Bioinspired nanocomposites with high degrees of reinforcement are of particular interest as they can reach excellent mechanical properties on account of their hierarchical architectures.[123,124,136–139] For instance, natural nacre is a hierarchical assembly composed of organic biopolymer and inorganic nanoplatelets (**Figure 10**a). Nacre-mimetic nanocomposite designs make use of a synergistic brick-and-mortar architecture whereby nanosheet particles with high stiffness are layered within a softer polymer matrix (**Figure 10**c).[123,124,140–144] This architecture enhances the mechanical properties (*e.g.*

both toughness and stiffness) of the materials through stress distribution and energy dissipation. Such structures rely on the homogeneous dispersion of nanoparticles in the polymer matrix and on careful hierarchical assembly. This is illustrated by the detrimental impact that defects, misalignment or phase separation and aggregation have on the nanocomposite properties. Synthetic nacre-mimetics are prepared from a wide array of different nanoplatelets (*e.g.* nanoclay, graphene and graphene oxide, MXene, etc.) and have even managed to exceed the properties of natural nacre by making intelligent use of nature's design principles, demonstrating the potential of such materials.[140,142,144,145] Most preparation methods of synthetic bioinspired nanocomposites rely on internal architectures formed predominantly through self-assembly driven by the design of the building blocks. However, techniques such as specialized additive manufacturing or wet-spinning have also enabled the preparation of bioinspired materials by directly imprinting hierarchical designs, showcasing the diverse approaches to nanocomposite development.[146,147]

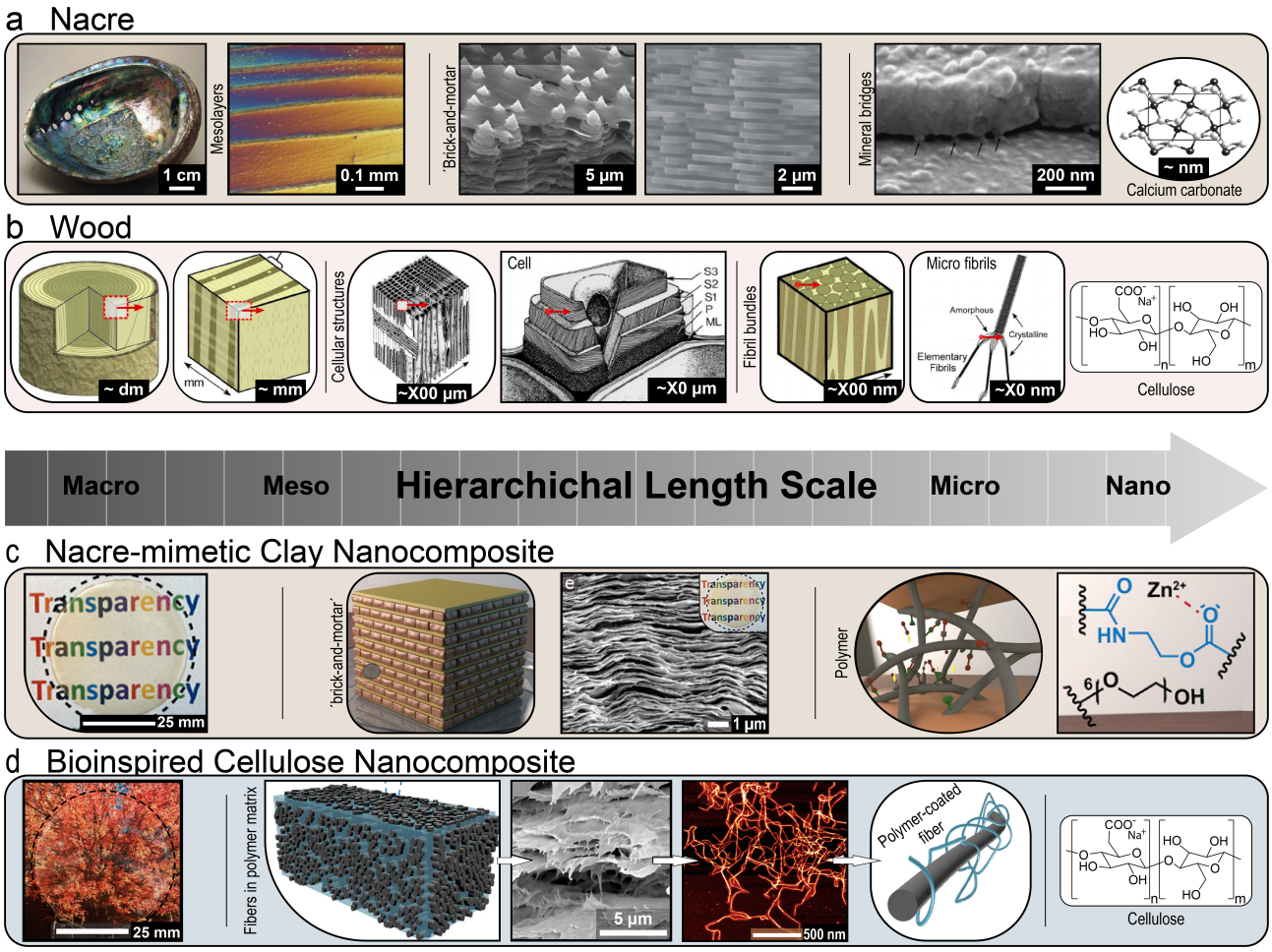

Figure 10. Schematic overview of hierarchical architectures. (a) Nacre from abalone shell: structures at various length scales. (b) Hierarchical (simplified) architecture of wood down to the cellulose level. (c) Nacre-mimetic clay nanocomposite with the characteristic 'brick-and-mortar' architecture. (d) Bioinspired cellulose nanocomposite self-assembled from polymer-coated cellulose fibers. Reproduced with permission from reference.[148–153]

In the context of this thesis, I highlight one particular method for preparing nacre-mimetic nanocomposites in more detail. In this method, polymer-coated core/shell platelets are prepared by

aqueous mixing of a clay nanoplatelet (~ 1 nm thickness) dispersion with a polymer solution.[140,154,155] The adsorption of polymer onto the nanoplatelets is facilitated by both supramolecular and entropic interactions. The resulting core/shell particles have a ~ 1 nm layer of polymer surrounding the nanoparticle, as determined via atomic force microscopy. Subsequently, slow ambient evaporation of water enables self-assembly of the core/shell particles into the brick-and-mortar architecture, yielding lamellar nanocomposites with high stiffness and strength. Analogous methodologies via formation of polymer-coated nanoparticles as building blocks are suited for other types of nanocomposites as well. For instance, cellulose nanofibers in conjunction with polymers yield a variety of remarkable nanocomposites (**Figure 10**d). Polyurethanes are relatively polar synthetic polymers whereby urethane, ester, and urea functionalities are excellent in facilitating strong hydrogen bonding with the cellulose fibers. This principle is demonstrated by preparation of nanocellulose films from polymer-coated (~ 2 nm layer) cellulose nanofibrils (~ 4 nm diameter), with strength, stiffness, and toughness exceeding far beyond the individual components.[152] As with the nacre-mimetics, cellulosic composites rely on careful design of the architecture. For instance, alignment of the fibrils is vital to achieve optimal results as well as to guide the porosity, which is similarly achieved by making use of core/shell building block design and careful self-assembly.[139,156] This type of synergy between the phases is the hallmark of effective nanocomposite design. The aqueous self-assembly routes described here constitute an economical and green pathway towards the production of relatively large-area composites. I explore this method of preparing composite films further for clay nanoplatelets and cellulose nanofibrils in combination with CANs in Chapter 2 and Chapter 4, respectively.

The composition of nanocomposites allows for various ways to tailor these materials for specific applications. First, the polymer and reinforcement types are selected, whereby it is crucial to consider their compatibility in terms of interaction and dispersibility (*e.g.* avoiding unwanted aggregation).[138,156] Additionally, simple variation of the compositional ratios of nanoparticle and polymer enables tuning of the nanoscale periodicities and thus movement between stronger and stiffer or more ductile and tougher composites. Naturally, to obtain the hierarchical architecture, there are some limitations on what compositional ratios are possible. Further tunability can be achieved by varying the sizes or aspect ratios of the nanoparticles, resulting in notable changes in mechanical properties.[138,155] For example, as the aspect ratio of nanoparticles increases, the failure mechanism may transition from nanoparticle pullout (linked to energy dissipation and toughness) to nanoparticle fracture (linked to high stiffness and strength).[138] Alternatively, addressing the polymer properties such as the T_g or architecture (*e.g.* linear versus brushed) is another method to achieve such property refinements.[138,157] Moving away from reinforcements and polymers themselves, counterions often play a key role in the interactions within the nanocomposite architectures. Variations in counterions have been shown to greatly affect the mechanical properties in both nacre-mimetic clay-based structures and cellulose nanofiber films.[138,158]

Beyond the mechanical property space, bioinspired nanocomposites can also incorporate several alternate features. While the possibilities are too extensive to go over in detail and beyond the scope of this thesis, I will briefly describe some to demonstrate the utility of these types of materials. Intrinsically, many bioinspired nanocomposites are fully or partially transparent as the homogeneous dispersion of nanoparticles avoids significant light scattering.[121,155] In addition, excellent gas barrier properties and fire shielding capabilities have been shown for nacre-mimetic clay nanocomposites.[159–161] Conductivity, both thermal and electrical, is another feature that is key for a wide range of applications. Interestingly, multiple avenues to achieve this have been demonstrated: use of a conductive polymer phase and use of a conductive reinforcing phase (*e.g.* carbon nanotubes or graphene), respectively.[162–164] Furthermore, many unique optical properties are within reach because of the nanoscale of the reinforcements. For instance, switchable lasers were self-assembled by using plant-based cellulose nanocrystals and fluorescent polymers, relying on a cholesteric architecture to yield photonic bandgap materials.[165] As a final example, MXene particles have been used to prepare photosensitive ion channels transducing a light stimulus into a photothermal gradient that in turn induces a net ionic current.[166] Use of nanocomposite materials thus enables combined benefits of excellent structural function and advanced functionalities, broadening their applicability across diverse fields.

1.3.2 Continuous Filament Wood Composites

Wood-based polymer composites are a unique type of bioinspired composite that is difficult to categorize among others.[167,168] Considering the ubiquity of wood, there are numerous different subcategories of such materials. However, here I focus briefly on composites whereby wood is first delignified and subsequently infiltrated with a polymer phase.[167] Lignin has a variety of functions, but structurally it acts as a cohesive component to keep cellulosic micro- and macrostructures together, especially perpendicular to the cellulose fiber alignment.[167] Delignification removes mostly lignin and part of the hemicelluloses from the complex hierarchical architecture of natural wood, leaving a porous cellulosic skeleton that maintains the hierarchical structures of native wood. This process enables various strategies for property enhancement, such as introduction of new components, treatment of the cellulose, and materials with higher cellulose fractions. To prepare composites, one option is to impregnate the pores, such as the inner lumen areas and potentially the intercellular spaces, with a (synthetic) polymer phase.[167] Usually, this polymer phase will enable a new property that native wood does not possess (*e.g.* transparency, mechanical property improvements, thermal insulation and fire retardancy, heat-storage, antimicrobial performance, corrosion resistance, etc.).[169–177] In turn, the advantage of cellulosic fibers in a polymeric matrix lies in the hierarchical structure they provide, which primarily benefits mechanical function, as well as their environmentally green nature.[167,169] The hierarchical length scales of the wood reinforcement are unique, ranging

from the macroscopic growth rings to the wood cellular microstructures, to the fibril-matrix microstructures, all the way down to the nanoscale cellulose fibers (**Figure 10**b).[167,170] As such, (delignified) wood scaffolds are macroscale objects that interact with the polymer phases on the microscale and nanoscale as well. This feature provides potential for similar synergies and properties described in the nanocomposite section, such as effective stress transfer between the polymeric and reinforcing phases or anisotropy-induced optical or thermal effects.[169,171,178] Impregnation of a CAN as the polymer phase into a continuous delignified wood scaffold is explored in Chapter 3 of this thesis.

1.3.3 Dynamic CAN Composites

While there is a remarkable variety among composite architectures and compositions, they generally exhibit limited possibilities for (re)processing.[2,121,179] Naturally, the intricate hierarchical architectures that contribute to many remarkable properties also complicate the processes of preparation and shaping. Preparation often involves irreversible processes (*e.g.* polymer curing, impregnation, interphase adhesion), which afterwards restrict the ability to manipulate the composite phases separately.[21] In the case of bioinspired nanocomposites, relatively complex preparations are typically required to ensure good dispersion and alignment of the nanoparticles in the matrix.[121,122] This process usually includes mixing in the liquid phase, followed by some form of casting, potentially evaporation, and curing. As a result, these composites are generally limited to relatively thin and flat dimensions, and they exhibit resilience to strain due to reduced polymer chain mobility and the inherently stiff and brittle nature of most reinforcements. This (anisotropic) dimensional stability thus hampers their capacity for shaping. As such, preparing complex nanocomposite shapes is a major challenge, and reshaping or recycling after preparation is often impossible. Wood and some wood-based composites can be shaped to a degree through complex methods (*e.g.* shaping in the wet state) but are largely limited by the hierarchical internal structure.[180–182] Additionally, many polymer wood composites are unsuitable even for such shaping methods because the impregnated polymer hinders water absorption and leaves little to no porosity in the final material.

To address this limitation, it is possible to integrate CANs into the design of composite materials. The thermal responsiveness and network reorganization of CANs, as discussed in prior sections, allow for enhanced composite shapeability when exposed to heat. Such a strategy is key for better recyclability or repairability but could also enable the production of more complex shapes. This approach has been demonstrated in composites with macroscopic reinforcements, such as glass fiber and carbon fiber reinforced dynamic epoxy resins, to allow for thermoforming into new shapes.[183,184]

On a bioinspired nanocomposite level, nacre-mimetics with CANs as the soft phase have shown remarkable possibilities, both in terms of shaping as well as full scale recycling (**Figure 11**a).

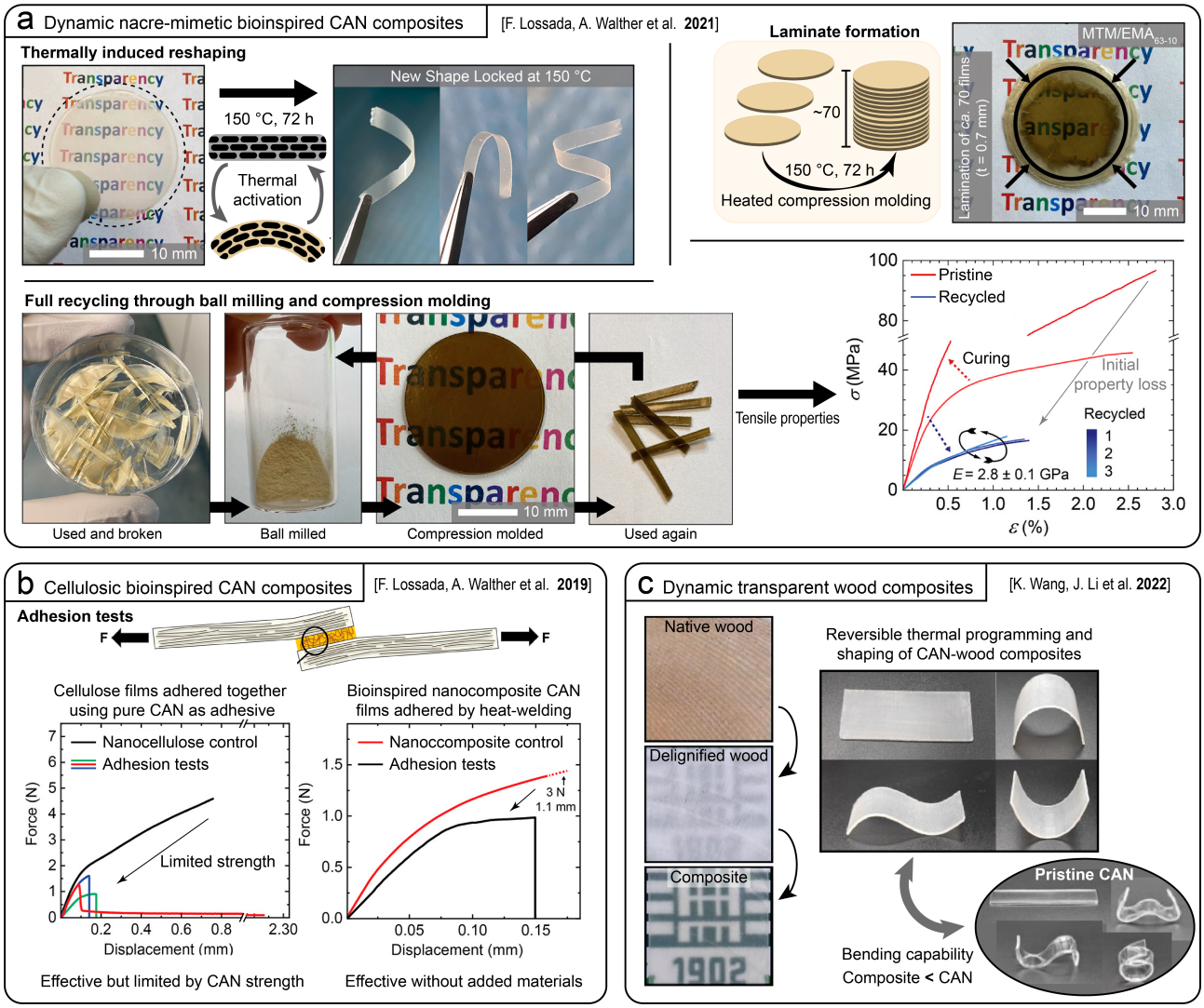

Figure 11. Dynamic properties of CAN-based bioinspired composites. (a) Reshaping, annealing, and full recycling of dynamic nacre-mimetic bioinspired CAN-clay nanocomposites, including tensile tests of pristine and recycled samples. (b) Adhesion tests of cellulose nanofiber films adhered by a layer of CAN and of CAN-based bioinspired nanocomposites welded without additional chemicals, including tensile tests of each case and of control samples. (c) Shapeability of pristine CAN and of CAN-based transparent wood composites, including images of native wood, delignified wood, and composite. Graphics adapted with permission from references.[151,185,186]

For instance, shape-locking of previously flat films into three dimensional shapes was possible by application of heat.[151] Furthermore, complete recycling was achieved by ball milling nanocomposite samples into a fine powder, followed by compression molding to produce new cohesive nanocomposite films or disks for second-life applications.[151] This principle has also been applied to develop faster preparation methods that do not depend on ambient evaporation of the aqueous phase, but instead utilize freeze-drying techniques to expedite the process.[187] Another possibility that has not yet been discussed is based on the adhesive properties of CANs (**Figure 11**b). Welding and annealing of nanocomposites have been demonstrated by employing the bond exchange process,

which enables both repair of broken parts as well as more complex constructions based on multiple annealed parts.[151,185] To reach the full potential of CAN (nano)composites, it is essential to utilize CANs with effective and fast dynamic properties. However, this can sometimes lead to a trade-off resulting in less compatibility and synergy of the CAN with the reinforcing phase. For instance, cellulosic bioinspired nanocomposites incorporating CANs have not yet been able to reach the incredible synergy with the cellulose nanofibers that has been demonstrated in other cases.[152,185] In the case of nacre-mimetic composites, a similar trade-off in the mechanical properties was observed.[140,151]

Concerning wood composites, some studies have demonstrated samples that can be reversibly shaped to moderate degrees, although not in the fiber direction, using straightforward heating techniques (**Figure 11**c).[186,188,189] However, their limitation is that they utilize very lightweight softwood (balsa), resulting in a remarkably low cellulose-reinforcement content in the final material. This strategy enables the dynamic properties of the CAN at the cost of the desired reinforcement effect. Wood-CAN composites with a higher cellulose content are essential to effectively maintain the exceptional structural characteristics inherent to wood. Based on these challenges, there is significant potential for property improvement by designing CANs tailored to have synergy with specific types of reinforcement, considering both the bond exchange chemistries and the overall network or backbone structure.

1.4 Motivation and Outline

Combination of CANs and reinforcements, especially nanostructures, forms an excellent opportunity to create complex hierarchical structures with unique properties only available through this synergy of the phases (**Figure 12**). The overarching goal of this thesis is to utilize the dynamic properties of CANs for unique structural and thermoresponsive properties in bioinspired (nano)composites. On a surface level, there exist two strategies: (i) Development of a novel CAN system that is particularly specialized for combination with an established type of composite. (ii) Utilization of an established CAN and subsequently modifying the preparation conditions or reinforcements in such a way to be able to assemble the composite. While the more nuanced approach relies on some adjustments on both sides, the main strategies presented throughout this thesis will predominantly fit one of the two options.

I integrate CANs in (nano)composites to add dynamic properties to materials that traditionally already have a broad range of possibilities and advantages but often suffer greatly from (re)processing limitations. In this thesis I demonstrate that this concept is compatible with a range of composite types, polymer types, and preparation methods by showing three self-contained bioinspired (nano)composite designs:

1. Waterborne CANs are rare in the field despite unique advantages relating to various applications. Specifically, hierarchical assembly of bioinspired nanocomposites based on clay nanoplatelets relies greatly on an aqueous medium.[140,154,155] **Chapter 2** introduces waterborne CANs that feature dual internal catalysis, dissociative bond exchange and highly customizable properties through specific selection of different crosslinkers (**Figure 12a**). Random copolymers derived from aspartic acid can catalyze formation and exchange of dynamic covalent ester bonds when combined with nucleophilic crosslinkers, to yield CAN networks. Combining the system with sodium fluorohectorite nanoplatelets allows to prepare advanced weldable and shapeable nacre-mimetic nanocomposites.

2. While incorporating a polymer phase in wood is a challenge due to the structural complexity of wood, wood-based composites demonstrate unique properties derived from exactly this structural complexity.[172,190,191] **Chapter 3** demonstrates incorporation of CANs in wood-based composites, which constitutes a comparatively novel material (**Figure 12b**). The transparent composites are shaped to high curvatures and in three dimensions via the utilization of (i) delignified wood in the wet state as a porous cellulose scaffold with all the hierarchical architecture of wood, (ii) an epoxy-based CAN that combines high crosslink density and adhesion with hydrophilic hydroxy and ester functionalities, and (iii) tin 2-ethylhexanoate as a transesterification catalyst, which additionally modifies the cellulose structures via partial dissolution. These components demonstrate their compatibility via impregnation of the CAN

into the lumens and intercellular spaces of delignified wood, yielding a flexible reinforced composite material that even possesses shape-memory properties.

3. Polyurethanes are a ubiquitous class of polymer materials named after the urethane bond, but further defined by their relatively high hydrophilicity and tailorability.[192] The urethane and urea bonds present in these polymers are known to undergo strong hydrogen bonding interactions, which can be used in conjunction with cellulose nanoparticles to yield homogeneous and strong and tough nanocomposites.[152,157] **Chapter 4** introduces a variety of dynamic polyurethanes that are used to prepare such nanocomposites in conjunction with cellulose nanofibrils (**Figure 12c**). Using both siloxane and disulfide chemistries imbues crosslinked polyurethanes with dynamic properties. These polymers are functionalized with ionic moieties to allow for dispersion in water via a solvent exchange process and thus combination with cellulose nanofibrils via aqueous assembly.

This thesis explores a range of approaches to incorporate dynamic polymer systems into composite materials, based on different types of CAN polymers as well as variations on the reinforcing phase. The synopsis chapter (**Chapter 5**) provides a more detailed discussion of the significance of each approach within bioinspired composite science, along with future strategies for applying dynamic CAN properties to the wider field of composite materials.

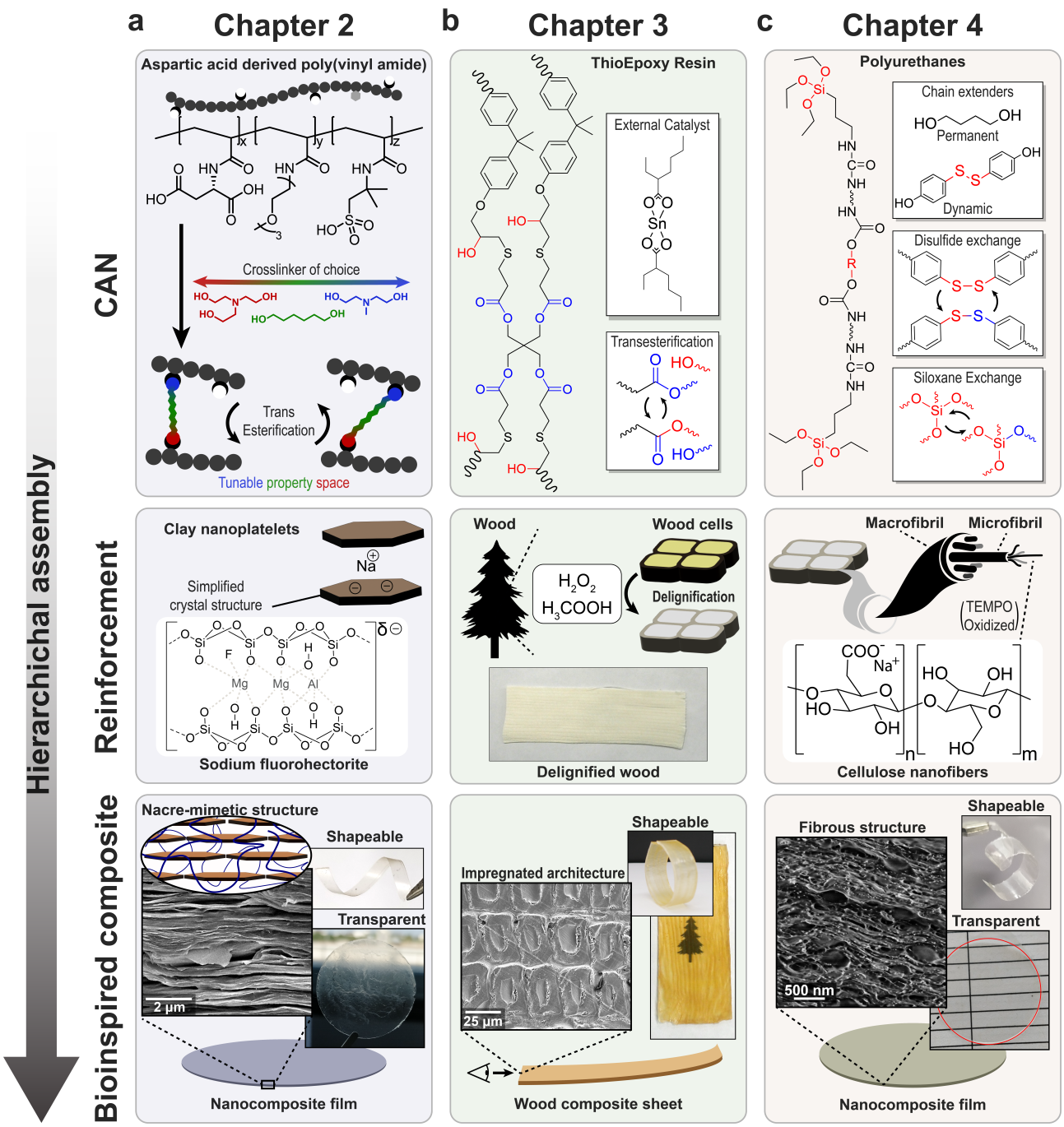

Figure 12. Depiction of CANs, reinforcements, and the bioinspired (nano)composites prepared from their combination. (a) Tunable waterborne aspartic acid-based CANs combined with clay nanoplatelets to form stiff nacre-mimetic nanocomposites. (b) Thioepoxy CAN resin with dynamic transesterification catalyzed by tin ethylhexanoate impregnated into delignified wood scaffold to yield transparent shapeable wood composites. (c) Library of polyurethane thermoplastics and CANs based on siloxanes and disulfides used in tough cellulose nanofibril composite films.

1.5 References

(1) Walton, D.; Lorimer, P. *Polymers*; Oxford University Press: Oxford, 2000.

(2) Biron, M. *Thermosets and Composites*; Elsevier, 2003.

(3) Carraher, C. E. Jr.; Carraher, C. E.; Seymour, R. B. *Seymour/Carraher's Polymer Chemistry*, 7th ed.; CRC Press: Boca Raton, 2007. https://doi.org/10.1201/9781420051032.

(4) *Applications of Polymers*; Seymour, R. B., Mark, H. F., Eds.; Springer US: Boston, MA, 1988. https://doi.org/10.1007/978-1-4684-5448-2.

(5) Freitag, W.; Stoye, D. *Paints, Coatings and Solvents*; John Wiley & Sons, 2008.

(6) Nelson, D. L.; Cox, M. M. *Lehninger Principles of Biochemistry*, 6th ed.; Lehninger, A. L., Ed.; Macmillan Learning, 2012.

(7) Akintayo, C. O.; Creusen, G.; Straub, P.; Walther, A. Tunable and Large-Scale Model Network StarPEG-DNA Hydrogels. *Macromolecules* **2021**, *54* (15), 7125–7133. https://doi.org/10.1021/acs.macromol.1c00600.

(8) Wang, Z.; Chen, R.; Yang, S.; Li, S.; Gao, Z. Design and Application of Stimuli-Responsive DNA Hydrogels: A Review. *Mater. Today Bio* **2022**, *16*, 100430. https://doi.org/10.1016/j.mtbio.2022.100430.

(9) Ross, R. *Wood Handbook: Wood as an Engineering Material*; General Technical Report FPL-GTR-282; U.S. Department of Agriculture, Forest Service, Forest Products Laboratory: Madison, WI, 2021; pp 1–543. https://research.fs.usda.gov/treesearch/62200 (accessed 2025-02-04).

(10) Gardner, D. J.; Bousfield, D.; Bilodeau, M. Challenges and Opportunities in the Scale-up of Cellulose Nanofibril (CNF) Production. In *Technical Proceedings of the 2013 NSTI Nanotechnology Conference and Expo, NSTI-Nanotech 2013*; 2013; Vol. 1, pp 495–497.

(11) Sun, Z.; Fridrich, B.; de Santi, A.; Elangovan, S.; Barta, K. Bright Side of Lignin Depolymerization: Toward New Platform Chemicals. *Chem. Rev.* **2018**, *118* (2), 614–678. https://doi.org/10.1021/acs.chemrev.7b00588.

(12) Wang, J.; Wang, L.; Gardner, D. J.; Shaler, S. M.; Cai, Z. Towards a Cellulose-Based Society: Opportunities and Challenges. *Cellulose* **2021**, *28* (8), 4511–4543. https://doi.org/10.1007/s10570-021-03771-4.

(13) Qiao, H.; Li, M.; Wang, C.; Zhang, Y.; Zhou, H. Progress, Challenge, and Perspective of Fabricating Cellulose. *Macromol. Rapid Commun.* **2022**, *43* (18), 2200208. https://doi.org/10.1002/marc.202200208.

(14) Masek, A.; Kosmalska, A. Technological Limitations in Obtaining and Using Cellulose Biocomposites. *Front. Bioeng. Biotechnol.* **2022**, *10*, 912052. https://doi.org/10.3389/fbioe.2022.912052.

(15) Aziz, T.; Haq, F.; Farid, A.; Kiran, M.; Faisal, S.; Ullah, A.; Ullah, N.; Bokhari, A.; Mubashir, M.; Chuah, L. F.; Show, P. L. Challenges Associated with Cellulose Composite Material: Facet Engineering and Prospective. *Environ. Res.* **2023**, *223*, 115429. https://doi.org/10.1016/j.envres.2023.115429.

(16) Flory, P. J. *Principles of Polymer Chemistry*; Cornell University Press, 1953.

(17) Serway, R. A.; Jewett, J. W. *Physics for Scientists and Engineers with Modern, Chapters 1-46*; Cengage Learning, 2009.

(18) Fink, J. K.; Thomas, S.; M, V. P. *Handbook of Engineering and Specialty Thermoplastics, 4 Volume Set*, 1st ed.; Wiley-Scrivener: Salem, Mass, 2011.

(19) Yang, M.; Chen, L.; Wang, J.; Msigwa, G.; Osman, A. I.; Fawzy, S.; Rooney, D. W.; Yap, P.-S. Circular Economy Strategies for Combating Climate Change and Other Environmental Issues. *Environ. Chem. Lett.* **2023**, *21* (1), 55–80. https://doi.org/10.1007/s10311-022-01499-6.

(20) Geyer, R.; Jambeck, J. R.; Law, K. L. Production, Use, and Fate of All Plastics Ever Made. *Sci. Adv.* **2017**, *3* (7), e1700782. https://doi.org/10.1126/sciadv.1700782.

(21) Aboudi, J.; Al Azzawi, W.; Alampalli, S.; Aniskevich, A.; Barbero, E. J.; Beyle, A.; Bhuiyan, F. H.; Epaarachchi, J.; Fertig, R. S.; Glaskova-Kuzmina, T.; Guedes, R. M.; Herath, M.; Jayaraman, R.; Kim, H. S.; Kontou, E.; Koyanagi, J.; Lin, C.; Muliana, A.; Nakada, M.; Papanicolaou, G. C.; Pupure, L.; Sato, M.; Sevenois, R. D. B.; Van Paepegem, W.; Varna, J.; Zaoutsos, S. P. *Creep and Fatigue in Polymer Matrix Composites*, 2nd ed.; Guedes, R. M., Ed.; Woodhead Publishing Series in Composites Science and Engineering; Woodhead Publishing, 2019. https://doi.org/10.1016/B978-0-08-102601-4.09991-4.

(22) Turner, S. Creep in Glassy Polymers. In *The Physics of Glassy Polymers*; Haward, R. N., Ed.; Springer Netherlands: Dordrecht, 1973; pp 223–278. https://doi.org/10.1007/978-94-010-2355-9_5.

(23) Kassner, M. E. Chapter 1 - Fundamentals of Creep in Materials. In *Fundamentals of Creep in Metals and Alloys*; Kassner, M. E., Ed.; Butterworth-Heinemann: Boston, 2015; pp 1–6. https://doi.org/10.1016/B978-0-08-099427-7.00001-3.
(24) Cordier, P.; Tournilhac, F.; Soulié-Ziakovic, C.; Leibler, L. Self-Healing and Thermoreversible Rubber from Supramolecular Assembly. *Nature* **2008**, *451* (7181), 977–980. https://doi.org/10.1038/nature06669.
(25) Burattini, S.; Greenland, B. W.; Merino, D. H.; Weng, W.; Seppala, J.; Colquhoun, H. M.; Hayes, W.; Mackay, M. E.; Hamley, I. W.; Rowan, S. J. A Healable Supramolecular Polymer Blend Based on Aromatic Π−π Stacking and Hydrogen-Bonding Interactions. *J. Am. Chem. Soc.* **2010**, *132* (34), 12051–12058. https://doi.org/10.1021/ja104446r.
(26) Wojtecki, R. J.; Meador, M. A.; Rowan, S. J. Using the Dynamic Bond to Access Macroscopically Responsive Structurally Dynamic Polymers. *Nat. Mater.* **2011**, *10* (1), 14–27. https://doi.org/10.1038/nmat2891.
(27) Seiffert, S.; Sprakel, J. Physical Chemistry of Supramolecular Polymer Networks. *Chem. Soc. Rev.* **2012**, *41* (2), 909–930. https://doi.org/10.1039/C1CS15191F.
(28) Montarnal, D.; Capelot, M.; Tournilhac, F.; Leibler, L. Silica-Like Malleable Materials from Permanent Organic Networks. *Science* **2011**, *334* (6058), 965–968. https://doi.org/10.1126/science.1212648.
(29) Denissen, W.; Winne, J. M.; Du Prez, F. E. Vitrimers: Permanent Organic Networks with Glass-like Fluidity. *Chem. Sci.* **2016**, *7* (1), 30–38. https://doi.org/10.1039/C5SC02223A.
(30) Guerre, M.; Taplan, C.; Winne, J. M.; Du Prez, F. E. Vitrimers: Directing Chemical Reactivity to Control Material Properties. *Chem. Sci.* **2020**, *11* (19), 4855–4870. https://doi.org/10.1039/D0SC01069C.
(31) Van Zee, N. J.; Nicolaÿ, R. Vitrimers: Permanently Crosslinked Polymers with Dynamic Network Topology. *Prog. Polym. Sci.* **2020**, *104*, 101233. https://doi.org/10.1016/j.progpolymsci.2020.101233.
(32) Steed, J. W.; Turner, D. R.; Wallace, K. J. *Core Concepts in Supramolecular Chemistry and Nanochemistry*; John Wiley & Sons, 2007.
(33) Che, H.; Hest, J. C. M. van. Stimuli-Responsive Polymersomes and Nanoreactors. *J. Mater. Chem. B* **2016**, *4* (27), 4632–4647. https://doi.org/10.1039/C6TB01163B.
(34) Wei, M.; Gao, Y.; Li, X.; Serpe, M. J. Stimuli-Responsive Polymers and Their Applications. *Polym. Chem.* **2016**, *8* (1), 127–143. https://doi.org/10.1039/C6PY01585A.
(35) Xia, X.; Spadaccini, C. M.; Greer, J. R. Responsive Materials Architected in Space and Time. *Nat. Rev. Mater.* **2022**, *7* (9), 683–701. https://doi.org/10.1038/s41578-022-00450-z.
(36) Löwik, D. W. P. M.; Leunissen, E. H. P.; Heuvel, M. van den; Hansen, M. B.; Hest, J. C. M. van. Stimulus Responsive Peptide Based Materials. *Chem. Soc. Rev.* **2010**, *39* (9), 3394–3412. https://doi.org/10.1039/B914342B.
(37) Lu, C.; Urban, M. W. Stimuli-Responsive Polymer Nano-Science: Shape Anisotropy, Responsiveness, Applications. *Prog. Polym. Sci.* **2018**, *78*, 24–46. https://doi.org/10.1016/j.progpolymsci.2017.07.005.
(38) Zhao, C.; Kang, J.; Li, Y.; Wang, Y.; Tang, X.; Jiang, Z. Carbon-Based Stimuli-Responsive Nanomaterials: Classification and Application. *Cyborg Bionic Syst.* **2023**, *4*, 0022. https://doi.org/10.34133/cbsystems.0022.
(39) Son, J.; Parveen, S.; MacPherson, D.; Marciano, Y.; Huang, R. H.; Ulijn, R. V. MMP-Responsive Nanomaterials. *Biomater. Sci.* **2023**, *11* (19), 6457–6479. https://doi.org/10.1039/D3BM00840A.
(40) Koetting, M. C.; Peters, J. T.; Steichen, S. D.; Peppas, N. A. Stimulus-Responsive Hydrogels: Theory, Modern Advances, and Applications. *Mater. Sci. Eng. R Rep.* **2015**, *93*, 1–49. https://doi.org/10.1016/j.mser.2015.04.001.
(41) Moulin, E.; Faour, L.; Carmona-Vargas, C. C.; Giuseppone, N. From Molecular Machines to Stimuli-Responsive Materials. *Adv. Mater.* **2020**, *32* (20), 1906036. https://doi.org/10.1002/adma.201906036.
(42) Tanaka, M.; Nakahata, M.; Linke, P.; Kaufmann, S. Stimuli-Responsive Hydrogels as a Model of the Dynamic Cellular Microenvironment. *Polym. J.* **2020**, *52* (8), 861–870. https://doi.org/10.1038/s41428-020-0353-6.
(43) Yang, Z.; Chen, L.; McClements, D. J.; Qiu, C.; Li, C.; Zhang, Z.; Miao, M.; Tian, Y.; Zhu, K.; Jin, Z. Stimulus-Responsive Hydrogels in Food Science: A Review. *Food Hydrocoll.* **2022**, *124*, 107218. https://doi.org/10.1016/j.foodhyd.2021.107218.

(44) Chen, M.; Ren, X.; Dong, L.; Li, X.; Cheng, H. Preparation of Dynamic Covalently Crosslinking Keratin Hydrogels Based on Thiol/Disulfide Bonds Exchange Strategy. *Int. J. Biol. Macromol.* **2021**, *182*, 1259–1267. https://doi.org/10.1016/j.ijbiomac.2021.05.057.

(45) White, T. J.; McConney, M. E.; Bunning, T. J. Dynamic Color in Stimuli-Responsive Cholesteric Liquid Crystals. *J. Mater. Chem.* **2010**, *20* (44), 9832–9847. https://doi.org/10.1039/C0JM00843E.

(46) Bukusoglu, E.; Pantoja, M. B.; Mushenheim, P. C.; Wang, X.; Abbott, N. L. Design of Responsive and Active (Soft) Materials Using Liquid Crystals. *Annu. Rev. Chem. Biomol. Eng.* **2016**, *7*, 163–196. https://doi.org/10.1146/annurev-chembioeng-061114-123323.

(47) Mehta, K.; Peeketi, A. R.; Liu, L.; Broer, D.; Onck, P.; Annabattula, R. K. Design and Applications of Light Responsive Liquid Crystal Polymer Thin Films. *Appl. Phys. Rev.* **2020**, *7* (4), 041306. https://doi.org/10.1063/5.0014619.

(48) Scheutz, G. M.; Lessard, J. J.; Sims, M. B.; Sumerlin, B. S. Adaptable Crosslinks in Polymeric Materials: Resolving the Intersection of Thermoplastics and Thermosets. *J. Am. Chem. Soc.* **2019**, *141* (41), 16181–16196. https://doi.org/10.1021/jacs.9b07922.

(49) Winne, J. M.; Leibler, L.; Du Prez, F. E. Dynamic Covalent Chemistry in Polymer Networks: A Mechanistic Perspective. *Polym. Chem.* **2019**, *10* (45), 6091–6108. https://doi.org/10.1039/c9py01260e.

(50) Jourdain, A.; Asbai, R.; Anaya, O.; Chehimi, M. M.; Drockenmuller, E.; Montarnal, D. Rheological Properties of Covalent Adaptable Networks with 1,2,3-Triazolium Cross-Links: The Missing Link between Vitrimers and Dissociative Networks. *Macromolecules* **2020**, *53* (6), 1884–1900. https://doi.org/10.1021/acs.macromol.9b02204.

(51) Miao, W.; Zou, W.; Jin, B.; Ni, C.; Zheng, N.; Zhao, Q.; Xie, T. On Demand Shape Memory Polymer via Light Regulated Topological Defects in a Dynamic Covalent Network. *Nat. Commun.* **2020**, *11* (1), 4257. https://doi.org/10.1038/s41467-020-18116-1.

(52) Zou, W.; Jin, B.; Wu, Y.; Song, H.; Luo, Y.; Huang, F.; Qian, J.; Zhao, Q.; Xie, T. Light-Triggered Topological Programmability in a Dynamic Covalent Polymer Network. *Sci. Adv.* **2020**, *6* (13), eaaz2362. https://doi.org/10.1126/sciadv.aaz2362.

(53) Osthoff, R. C.; Bueche, A. M.; Grubb, W. T. Chemical Stress-Relaxation of Polydimethylsiloxane Elastomers1. *J. Am. Chem. Soc.* **1954**, *76* (18), 4659–4663. https://doi.org/10.1021/ja01647a052.

(54) Tobolsky, A. V.; Beevers, R. B.; Owen, G. D. T. The Viscoelastic Properties of Crosslinked Poly(Ethylene Tetrasulfide) Polymers. II. *J. Colloid Sci.* **1963**, *18* (4), 359–369. https://doi.org/10.1016/0095-8522(63)90027-8.

(55) Owen, G. D. T.; MacKnight, W. J.; Tobolsky, A. V. Urethane Elastomers Containing Disulfide and Tetrasulfide Linkages. *J. Phys. Chem.* **1964**, *68* (4), 784–786. https://doi.org/10.1021/j100786a012.

(56) Tobolsky, A. V.; MacKnight, W. J.; Takahashi, M. Relaxation of Disulfide and Tetrasulfide Polymers. *J. Phys. Chem.* **1964**, *68* (4), 787–790. https://doi.org/10.1021/j100786a013.

(57) Ward, W. H.; Lundgren, H. P. The Formation, Composition, and Properties of the Keratins. In *Advances in Protein Chemistry*; Anson, M. L., Bailey, K., Edsall, J. T., Eds.; Academic Press, 1954; Vol. 9, pp 243–297. https://doi.org/10.1016/S0065-3233(08)60208-9.

(58) Ziegler, K. Crosslinking and Self-Crosslinking in Keratin Fibers. In *Chemistry of Natural Protein Fibers*; Asquith, R. S., Ed.; Springer US: Boston, MA, 1977; pp 267–300. https://doi.org/10.1007/978-1-4613-4109-3_6.

(59) Feige, M. J.; Braakman, I.; Hendershot, L. M. Disulfide Bonds in Protein Folding and Stability. In *Oxidative Folding of Proteins: Basic Principles, Cellular Regulation and Engineering*; Feige, M. J., Ed.; The Royal Society of Chemistry, 2018; p 0. https://doi.org/10.1039/9781788013253-00001.

(60) Goodyear, Charles. Improvement in India-Rubber Fabrics. US3633A, June 15, 1844. https://patents.google.com/patent/US3633A/en (accessed 2024-10-17).

(61) Hernández, M.; Grande, A. M.; Dierkes, W.; Bijleveld, J.; van der Zwaag, S.; García, S. J. Turning Vulcanized Natural Rubber into a Self-Healing Polymer: Effect of the Disulfide/Polysulfide Ratio. *ACS Sustain. Chem. Eng.* **2016**, *4* (10), 5776–5784. https://doi.org/10.1021/acssuschemeng.6b01760.

(62) Tesoro, G. C.; Sastri, V. Reversible Crosslinking in Epoxy Resins. I. Feasibility Studies. *J. Appl. Polym. Sci.* **1990**, *39* (7), 1425–1437. https://doi.org/10.1002/app.1990.070390702.

(63) Hayashi, M.; Katayama, A. Preparation of Colorless, Highly Transparent, Epoxy-Based Vitrimers by the Thiol-Epoxy Click Reaction and Evaluation of Their Shape-Memory Properties. *ACS Appl. Polym. Mater.* **2020**, *2* (6), 2452–2457. https://doi.org/10.1021/acsapm.0c00397.
(64) Canadell, J.; Goossens, H.; Klumperman, B. Self-Healing Materials Based on Disulfide Links. *Macromolecules* **2011**, *44* (8), 2536–2541. https://doi.org/10.1021/ma2001492.
(65) Lu, Y.-X.; Tournilhac, F.; Leibler, L.; Guan, Z. Making Insoluble Polymer Networks Malleable via Olefin Metathesis. *J. Am. Chem. Soc.* **2012**, *134* (20), 8424–8427. https://doi.org/10.1021/ja303356z.
(66) Lu, Y.-X.; Guan, Z. Olefin Metathesis for Effective Polymer Healing via Dynamic Exchange of Strong Carbon–Carbon Double Bonds. *J. Am. Chem. Soc.* **2012**, *134* (34), 14226–14231. https://doi.org/10.1021/ja306287s.
(67) Arrhenius, S. Über die Reaktionsgeschwindigkeit bei der Inversion von Rohrzucker durch Säuren. *Z. Für Phys. Chem.* **1889**, *4U* (1), 226–248. https://doi.org/10.1515/zpch-1889-0416.
(68) Arrhenius, S. Über die Dissociationswärme und den Einfluss der Temperatur auf den Dissociationsgrad der Elektrolyte. *Z. Für Phys. Chem.* **1889**, *4U* (1), 96–116. https://doi.org/10.1515/zpch-1889-0408.
(69) Laidler, K. J. *Chemical Kinetics*; Harper & Row, 1987.
(70) Atkins, P. W.; Paula, J. D.; Keeler, J. *Atkins' Physical Chemistry*; Oxford University Press, 2018.
(71) Bruice, P. Y. *Organic Chemistry*; Pearson Education, 2013.
(72) Yan, S.; Hu, K.; Chen, S.; Li, T.; Zhang, W.; Yin, J.; Jiang, X. Photo-Induced Stress Relaxation in Reconfigurable Disulfide-Crosslinked Supramolecular Films Visualized by Dynamic Wrinkling. *Nat. Commun.* **2022**, *13* (1), 7434. https://doi.org/10.1038/s41467-022-35271-9.
(73) Zhou, Y.; Goossens, J. G. P.; Sijbesma, R. P.; Heuts, J. P. A. Poly(Butylene Terephthalate)/Glycerol-Based Vitrimers via Solid-State Polymerization. *Macromolecules* **2017**, *50* (17), 6742–6751. https://doi.org/10.1021/acs.macromol.7b01142.
(74) Han, J.; Liu, T.; Hao, C.; Zhang, S.; Guo, B.; Zhang, J. A Catalyst-Free Epoxy Vitrimer System Based on Multifunctional Hyperbranched Polymer. *Macromolecules* **2018**, *51* (17), 6789–6799. https://doi.org/10.1021/acs.macromol.8b01424.
(75) Bakkali-Hassani, C.; Berne, D.; Ladmiral, V.; Caillol, S. Transcarbamoylation in Polyurethanes: Underestimated Exchange Reactions? *Macromolecules* **2022**, *55* (18), 7974–7991. https://doi.org/10.1021/acs.macromol.2c01184.
(76) Chen, X.; Li, L.; Jin, K.; Torkelson, J. M. Reprocessable Polyhydroxyurethane Networks Exhibiting Full Property Recovery and Concurrent Associative and Dissociative Dynamic Chemistry via Transcarbamoylation and Reversible Cyclic Carbonate Aminolysis. *Polym. Chem.* **2017**, *8* (41), 6349–6355. https://doi.org/10.1039/C7PY01160A.
(77) Snyder, R. L.; Fortman, D. J.; De Hoe, G. X.; Hillmyer, M. A.; Dichtel, W. R. Reprocessable Acid-Degradable Polycarbonate Vitrimers. *Macromolecules* **2018**, *51* (2), 389–397. https://doi.org/10.1021/acs.macromol.7b02299.
(78) Baek, S.; Lee, J.; Kim, H.; Cha, I.; Song, C. Self-Healable and Recyclable Biomass-Derived Polyurethane Networks through Carbon Dioxide Immobilization. *Polymers* **2021**, *13* (24), 4381. https://doi.org/10.3390/polym13244381.
(79) Zheng, P.; McCarthy, T. J. A Surprise from 1954: Siloxane Equilibration Is a Simple, Robust, and Obvious Polymer Self-Healing Mechanism. *J. Am. Chem. Soc.* **2012**, *134* (4), 2024–2027. https://doi.org/10.1021/ja2113257.
(80) Zych, A.; Pinalli, R.; Soliman, M.; Vachon, J.; Dalcanale, E. Polyethylene Vitrimers via Silyl Ether Exchange Reaction. *Polymer* **2020**, *199*, 122567. https://doi.org/10.1016/j.polymer.2020.122567.
(81) Nishimura, Y.; Chung, J.; Muradyan, H.; Guan, Z. Silyl Ether as a Robust and Thermally Stable Dynamic Covalent Motif for Malleable Polymer Design. *J. Am. Chem. Soc.* **2017**, *139* (42), 14881–14884. https://doi.org/10.1021/jacs.7b08826.
(82) Tretbar, C. A.; Neal, J. A.; Guan, Z. Direct Silyl Ether Metathesis for Vitrimers with Exceptional Thermal Stability. *J. Am. Chem. Soc.* **2019**, *141* (42), 16595–16599. https://doi.org/10.1021/jacs.9b08876.
(83) Breuillac, A.; Kassalias, A.; Nicolaÿ, R. Polybutadiene Vitrimers Based on Dioxaborolane Chemistry and Dual Networks with Static and Dynamic Cross-Links. *Macromolecules* **2019**, *52* (18), 7102–7113. https://doi.org/10.1021/acs.macromol.9b01288.

(84) Cash, J. J.; Kubo, T.; Dobbins, D. J.; Sumerlin, B. S. Maximizing the Symbiosis of Static and Dynamic Bonds in Self-Healing Boronic Ester Networks. *Polym. Chem.* **2018**, *9* (15), 2011–2020. https://doi.org/10.1039/C8PY00123E.

(85) Cromwell, O. R.; Chung, J.; Guan, Z. Malleable and Self-Healing Covalent Polymer Networks through Tunable Dynamic Boronic Ester Bonds. *J. Am. Chem. Soc.* **2015**, *137* (20), 6492–6495. https://doi.org/10.1021/jacs.5b03551.

(86) Röttger, M.; Domenech, T.; van der Weegen, R.; Breuillac, A.; Nicolaÿ, R.; Leibler, L. High-Performance Vitrimers from Commodity Thermoplastics through Dioxaborolane Metathesis. *Science* **2017**, *356* (6333), 62–65. https://doi.org/10.1126/science.aah5281.

(87) Denissen, W.; Rivero, G.; Nicolaÿ, R.; Leibler, L.; Winne, J. M.; Du Prez, F. E. Vinylogous Urethane Vitrimers. *Adv. Funct. Mater.* **2015**, *25* (16), 2451–2457. https://doi.org/10.1002/adfm.201404553.

(88) Stukenbroeker, T.; Wang, W.; Winne, J. M.; Du Prez, F. E.; Nicolaÿ, R.; Leibler, L. Polydimethylsiloxane Quenchable Vitrimers. *Polym. Chem.* **2017**, *8* (43), 6590–6593. https://doi.org/10.1039/C7PY01488K.

(89) Denissen, W.; Droesbeke, M.; Nicolaÿ, R.; Leibler, L.; Winne, J. M.; Du Prez, F. E. Chemical Control of the Viscoelastic Properties of Vinylogous Urethane Vitrimers. *Nat. Commun.* **2017**, *8* (1), 14857. https://doi.org/10.1038/ncomms14857.

(90) Erice, A.; Ruiz de Luzuriaga, A.; Matxain, J. M.; Ruipérez, F.; Asua, J. M.; Grande, H.-J.; Rekondo, A. Reprocessable and Recyclable Crosslinked Poly(Urea-Urethane)s Based on Dynamic Amine/Urea Exchange. *Polymer* **2018**, *145*, 127–136. https://doi.org/10.1016/j.polymer.2018.04.076.

(91) Zhang, L.; Rowan, S. J. Effect of Sterics and Degree of Cross-Linking on the Mechanical Properties of Dynamic Poly(Alkylurea–Urethane) Networks. *Macromolecules* **2017**, *50* (13), 5051–5060. https://doi.org/10.1021/acs.macromol.7b01016.

(92) Ying, H.; Zhang, Y.; Cheng, J. Dynamic Urea Bond for the Design of Reversible and Self-Healing Polymers. *Nat. Commun.* **2014**, *5* (1), 3218. https://doi.org/10.1038/ncomms4218.

(93) Zhao, S.; Abu-Omar, M. M. Recyclable and Malleable Epoxy Thermoset Bearing Aromatic Imine Bonds. *Macromolecules* **2018**, *51* (23), 9816–9824. https://doi.org/10.1021/acs.macromol.8b01976.

(94) Taynton, P.; Yu, K.; Shoemaker, R. K.; Jin, Y.; Qi, H. J.; Zhang, W. Heat- or Water-Driven Malleability in a Highly Recyclable Covalent Network Polymer. *Adv. Mater.* **2014**, *26* (23), 3938–3942. https://doi.org/10.1002/adma.201400317.

(95) Zheng, H.; Liu, Q.; Lei, X.; Chen, Y.; Zhang, B.; Zhang, Q. A Conjugation Polyimine Vitrimer: Fabrication and Performance. *J Polym Sci Part APolym Chem* **2018**, *56* (22), 2531–2538. https://doi.org/10.1002/pola.29232.

(96) Lafont, U.; van Zeijl, H.; van der Zwaag, S. Influence of Cross-Linkers on the Cohesive and Adhesive Self-Healing Ability of Polysulfide-Based Thermosets. *ACS Appl. Mater. Interfaces* **2012**, *4* (11), 6280–6288. https://doi.org/10.1021/am301879z.

(97) Amamoto, Y.; Otsuka, H.; Takahara, A.; Matyjaszewski, K. Self-Healing of Covalently Cross-Linked Polymers by Reshuffling Thiuram Disulfide Moieties in Air under Visible Light. *Adv. Mater.* **2012**, *24* (29), 3975–3980. https://doi.org/10.1002/adma.201201928.

(98) Rekondo, A.; Martin, R.; Luzuriaga, A. R. de; Cabañero, G.; Grande, H. J.; Odriozola, I. Catalyst-Free Room-Temperature Self-Healing Elastomers Based on Aromatic Disulfide Metathesis. *Mater. Horiz.* **2014**, *1* (2), 237–240. https://doi.org/10.1039/C3MH00061C.

(99) Obadia, M. M.; Jourdain, A.; Cassagnau, P.; Montarnal, D.; Drockenmuller, E. Tuning the Viscosity Profile of Ionic Vitrimers Incorporating 1,2,3-Triazolium Cross-Links. *Adv. Funct. Mater.* **2017**, *27* (45), 1703258. https://doi.org/10.1002/adfm.201703258.

(100) Obadia, M. M.; Mudraboyina, B. P.; Serghei, A.; Montarnal, D.; Drockenmuller, E. Reprocessing and Recycling of Highly Cross-Linked Ion-Conducting Networks through Transalkylation Exchanges of C–N Bonds. *J. Am. Chem. Soc.* **2015**, *137* (18), 6078–6083. https://doi.org/10.1021/jacs.5b02653.

(101) Ricarte, R. G.; Shanbhag, S. A Tutorial Review of Linear Rheology for Polymer Chemists: Basics and Best Practices for Covalent Adaptable Networks. *Polym. Chem.* **2024**, *15*, 815–846. https://doi.org/10.1039/D3PY01367G.

(102) Lijsebetten, F. V.; Holloway, J. O.; Winne, J. M.; Du Prez, F. E. Internal Catalysis for Dynamic Covalent Chemistry Applications and Polymer Science. *Chem. Soc. Rev.* **2020**, *49* (23), 8425–8438. https://doi.org/10.1039/D0CS00452A.

(103) Moradi, S.; Fernández-Francos, X.; Konuray, O.; Ramis, X. Recyclable Dual-Curing Thiol-Isocyanate-Epoxy Vitrimers with Sequential Relaxation Profiles. *Eur. Polym. J.* **2023**, *196*, 112290. https://doi.org/10.1016/j.eurpolymj.2023.112290.
(104) Kim, J. G.; Lee, G. S.; Lee, A. Triazabicyclodecene: A Versatile Catalyst for Polymer Synthesis. *J. Polym. Sci.* **2024**, *62* (1), 42–91. https://doi.org/10.1002/pol.20230643.
(105) Haida, P.; Abetz, V. Acid-Mediated Autocatalysis in Vinylogous Urethane Vitrimers. *Macromol. Rapid Commun.* **2020**, *41* (16), 2000273. https://doi.org/10.1002/marc.202000273.
(106) Cuminet, F.; Caillol, S.; Dantras, É.; Leclerc, É.; Ladmiral, V. Neighboring Group Participation and Internal Catalysis Effects on Exchangeable Covalent Bonds: Application to the Thriving Field of Vitrimer Chemistry. *Macromolecules* **2021**, *54* (9), 3927–3961. https://doi.org/10.1021/acs.macromol.0c02706.
(107) Delahaye, M.; Tanini, F.; Holloway, J. O.; Winne, J. M.; Du Prez, F. E. Double Neighbouring Group Participation for Ultrafast Exchange in Phthalate Monoester Networks. *Polym. Chem.* **2020**, *11* (32), 5207–5215. https://doi.org/10.1039/D0PY00681E.
(108) Zhang, H.; Majumdar, S.; van Benthem, R. A. T. M.; Sijbesma, R. P.; Heuts, J. P. A. Intramolecularly Catalyzed Dynamic Polyester Networks Using Neighboring Carboxylic and Sulfonic Acid Groups. *ACS Macro Lett.* **2020**, *9* (2), 272–277. https://doi.org/10.1021/acsmacrolett.9b01023.
(109) Delahaye, M.; Winne, J. M.; Du Prez, F. E. Internal Catalysis in Covalent Adaptable Networks: Phthalate Monoester Transesterification As a Versatile Dynamic Cross-Linking Chemistry. *J. Am. Chem. Soc.* **2019**, *141* (38), 15277–15287. https://doi.org/10.1021/jacs.9b07269.
(110) Rossegger, E.; Höller, R.; Reisinger, D.; Fleisch, M.; Strasser, J.; Wieser, V.; Griesser, T.; Schlögl, S. High Resolution Additive Manufacturing with Acrylate Based Vitrimers Using Organic Phosphates as Transesterification Catalyst. *Polymer* **2021**, *221*, 123631. https://doi.org/10.1016/j.polymer.2021.123631.
(111) Moazzen, K.; Rossegger, E.; Alabiso, W.; Shaukat, U.; Schlögl, S. Role of Organic Phosphates and Phosphonates in Catalyzing Dynamic Exchange Reactions in Thiol-Click Vitrimers. *Macromol. Chem. Phys.* **2021**, *222* (12), 2100072. https://doi.org/10.1002/macp.202100072.
(112) Guerre, M.; Taplan, C.; Nicolaÿ, R.; Winne, J. M.; Du Prez, F. E. Fluorinated Vitrimer Elastomers with a Dual Temperature Response. *J. Am. Chem. Soc.* **2018**, *140* (41), 13272–13284. https://doi.org/10.1021/jacs.8b07094.
(113) Bakkali-Hassani, C.; Berne, D.; Bron, P.; Irusta, L.; Sardon, H.; Ladmiral, V.; Caillol, S. Polyhydroxyurethane Covalent Adaptable Networks: Looking for Suitable Catalysts. *Polym. Chem.* **2023**, *14* (31), 3610–3620. https://doi.org/10.1039/D3PY00579H.
(114) Porath, L. E.; Evans, C. M. Importance of Broad Temperature Windows and Multiple Rheological Approaches for Probing Viscoelasticity and Entropic Elasticity in Vitrimers. *Macromolecules* **2021**, *54* (10), 4782–4791. https://doi.org/10.1021/acs.macromol.0c02800.
(115) Soman, B.; Evans, C. M. Effect of Precise Linker Length, Bond Density, and Broad Temperature Window on the Rheological Properties of Ethylene Vitrimers. *Soft Matter* **2021**, *17* (13), 3569–3577. https://doi.org/10.1039/D0SM01544J.
(116) Ricarte, R. G.; Shanbhag, S. Unentangled Vitrimer Melts: Interplay between Chain Relaxation and Cross-Link Exchange Controls Linear Rheology. *Macromolecules* **2021**, *54* (7), 3304–3320. https://doi.org/10.1021/acs.macromol.0c02530.
(117) Lijsebetten, F. V.; Bruycker, K. D.; Ruymbeke, E. V.; Winne, J. M.; Du Prez, F. E. Characterising Different Molecular Landscapes in Dynamic Covalent Networks. *Chem. Sci.* **2022**, *13* (43), 12865–12875. https://doi.org/10.1039/D2SC05528G.
(118) Fortman, D. J.; Brutman, J. P.; Cramer, C. J.; Hillmyer, M. A.; Dichtel, W. R. Mechanically Activated, Catalyst-Free Polyhydroxyurethane Vitrimers. *J. Am. Chem. Soc.* **2015**, *137* (44), 14019–14022. https://doi.org/10.1021/jacs.5b08084.
(119) van't Hoff, J. H.; Cohen, E.; Ewan, T. *Studies in Chemical Dynamics*; Amsterdam : F. Muller ; London : Williams & Norgate, 1896.
(120) Podgórski, M.; Spurgin, N.; Mavila, S.; Bowman, C. N. Mixed Mechanisms of Bond Exchange in Covalent Adaptable Networks: Monitoring the Contribution of Reversible Exchange and Reversible Addition in Thiol–Succinic Anhydride Dynamic Networks. *Polym. Chem.* **2020**, *11* (33), 5365–5376. https://doi.org/10.1039/D0PY00091D.

(121) Thostenson, E. T.; Li, C.; Chou, T.-W. Nanocomposites in Context. *Compos. Sci. Technol.* **2005**, *65* (3), 491–516. https://doi.org/10.1016/j.compscitech.2004.11.003.
(122) Kato, M.; Usuki, A.; Becker, O.; Simon, G.; Sinha Ray, S.; Bousmina, M.; Jayaraman, K.; Kumar, S.; Yei, D.-R.; Fu, H.-K.; Chang, F.-C.; Tang, T.; Tong, X.; Feng, Z.; Huang, B.; Decker, C.; Strawhecker, K. E.; Manias, E.; Ha, C.-S.; Zanetti, M.; Vittoria, V.; Sorrentino, A.; Gorrasi, G.; Tortora, M.; Mohammad, A.; Liao, K.; Ren, Y.; Xiao, T.; Kuzumaki, T.; Ok Park, O.; Park, J. H.; Kim, T.-H.; Lu, X.; Liu, T.; Millan, A.; Palacio, F.; Snoeck, E.; Serin, V.; Lecante, P.; Chiang, C.; Ma, C.-C. M.; Meng, Y.; Zhang, M. Q.; Rong, M. Z.; Friedrich, K. *Polymer Nanocomposites*; Mai, Y.-W., Yu, Z.-Z., Eds.; Woodhead Publishing Series in Composites Science and Engineering; Woodhead Publishing, 2006. https://doi.org/10.1016/B978-1-85573-969-7.50023-4.
(123) Kakisawa, H.; Sumitomo, T. The Toughening Mechanism of Nacre and Structural Materials Inspired by Nacre. *Sci. Technol. Adv. Mater.* **2012**, *12* (6), 064710. https://doi.org/10.1088/1468-6996/12/6/064710.
(124) Sun, J.; Bhushan, B. Hierarchical Structure and Mechanical Properties of Nacre: A Review. *RSC Adv.* **2012**, *2* (20), 7617–7632. https://doi.org/10.1039/C2RA20218B.
(125) Katouzian, M.; Vlase, S.; Marin, M.; Öchsner, A. Creep Response of Fiber-Reinforced Composites: A Review. *Discov. Mech. Eng.* **2022**, *1* (1), 3. https://doi.org/10.1007/s44245-022-00003-2.
(126) Kasraei, S.; Sami, L.; Hendi, S.; AliKhani, M.-Y.; Rezaei-Soufi, L.; Khamverdi, Z. Antibacterial Properties of Composite Resins Incorporating Silver and Zinc Oxide Nanoparticles on Streptococcus Mutans and Lactobacillus. *Restor. Dent. Endod.* **2014**, *39* (2), 109–114. https://doi.org/10.5395/rde.2014.39.2.109.
(127) Zhang, B.; Li, Z.; Wu, H.; Nie, J. Research on Damping Performance and Strength of the Composite Laminate. *Sci. Rep.* **2021**, *11* (1), 18281. https://doi.org/10.1038/s41598-021-97933-w.
(128) Zheng, X.; Zhang, H.; Liu, Z.; Jiang, R.; Zhou, X. Functional Composite Electromagnetic Shielding Materials for Aerospace, Electronics and Wearable Fields. *Mater. Today Commun.* **2022**, *33*, 104498. https://doi.org/10.1016/j.mtcomm.2022.104498.
(129) Ahmed, K. K.; Muheddin, D. Q.; Mohammed, P. A.; Ezat, G. S.; Murad, A. R.; Ahmed, B. Y.; Hussen, S. A.; Ahmed, T. Y.; Hamad, S. M.; Abdullah, O. Gh.; Aziz, S. B. A Brief Review on Optical Properties of Polymer Composites: Insights into Light-Matter Interaction from Classical to Quantum Transport Point of View. *Results Phys.* **2024**, *56*, 107239. https://doi.org/10.1016/j.rinp.2023.107239.
(130) Snow, M. R.; Pring, A.; Self, P.; Losic, D.; Shapter, J. The Origin of the Color of Pearls in Iridescence from Nano-Composite Structures of the Nacre. *Am. Mineral.* **2004**, *89* (10), 1353–1358. https://doi.org/10.2138/am-2004-1001.
(131) Poryvai, A.; Šmahel, M.; Švecová, M.; Nemati, A.; Shadpour, S.; Ulbrich, P.; Ogolla, T.; Liu, J.; Novotná, V.; Veverka, M.; Vejpravová, J.; Hegmann, T.; Kohout, M. Chiral, Magnetic, and Photosensitive Liquid Crystalline Nanocomposites Based on Multifunctional Nanoparticles and Achiral Liquid Crystals. *ACS Nano* **2022**, *16* (8), 11833–11841. https://doi.org/10.1021/acsnano.1c10594.
(132) Ahn, H.-Y.; Le, K. Q.; Narushima, T.; Yamanishi, J.; Kim, R. M.; Nam, K. T.; Okamoto, H. Highly Chiral Light Emission Using Plasmonic Helicoid Nanoparticles. *Adv. Opt. Mater.* **2024**, *12* (22), 2400699. https://doi.org/10.1002/adom.202400699.
(133) Hiremath, A.; Murthy, A. A.; Thipperudrappa, S.; K N, B. Nanoparticles Filled Polymer Nanocomposites: A Technological Review. *Cogent Eng.* **2021**, *8* (1), 1991229. https://doi.org/10.1080/23311916.2021.1991229.
(134) Islam, M. S.; Masoodi, R.; Rostami, H. The Effect of Nanoparticles Percentage on Mechanical Behavior of Silica-Epoxy Nanocomposites. *J. Nanosci.* **2013**, *2013* (1), 275037. https://doi.org/10.1155/2013/275037.
(135) Soni, D.; Sharma, A. K.; Narwariya, M.; Chauhan, P. S. Effect of Low Weight Fraction of Nano-Reinforcement on Tensile Properties of Polymer Nanocomposites. In *Recent Advances in Mechanical Engineering*; Muzammil, M., Chandra, A., Kankar, P. K., Kumar, H., Eds.; Springer: Singapore, 2021; pp 729–735. https://doi.org/10.1007/978-981-15-8704-7_90.
(136) Yao, H.-B.; Fang, H.-Y.; Wang, X.-H.; Yu, S.-H. Hierarchical Assembly of Micro-/Nano-Building Blocks: Bio-Inspired Rigid Structural Functional Materials. *Chem. Soc. Rev.* **2011**, *40* (7), 3764–3785. https://doi.org/10.1039/C0CS00121J.
(137) Nepal, D.; Kang, S.; Adstedt, K. M.; Kanhaiya, K.; Bockstaller, M. R.; Brinson, L. C.; Buehler, M. J.; Coveney, P. V.; Dayal, K.; El-Awady, J. A.; Henderson, L. C.; Kaplan, D. L.; Keten, S.; Kotov, N. A.;

Schatz, G. C.; Vignolini, S.; Vollrath, F.; Wang, Y.; Yakobson, B. I.; Tsukruk, V. V.; Heinz, H. Hierarchically Structured Bioinspired Nanocomposites. *Nat. Mater.* **2023**, *22* (1), 18–35. https://doi.org/10.1038/s41563-022-01384-1.

(138) Lossada, F.; Hoenders, D.; Guo, J.; Jiao, D.; Walther, A. Self-Assembled Bioinspired Nanocomposites. *Acc. Chem. Res.* **2020**, *53* (11), 2622–2635. https://doi.org/10.1021/acs.accounts.0c00448.

(139) Benítez, A. J.; Walther, A. Cellulose Nanofibril Nanopapers and Bioinspired Nanocomposites: A Review to Understand the Mechanical Property Space. *J. Mater. Chem. A* **2017**, *5* (31), 16003–16024. https://doi.org/10.1039/C7TA02006F.

(140) Walther, A.; Bjurhager, I.; Malho, J.-M.; Pere, J.; Ruokolainen, J.; Berglund, L. A.; Ikkala, O. Large-Area, Lightweight and Thick Biomimetic Composites with Superior Material Properties via Fast, Economic, and Green Pathways. *Nano Lett.* **2010**, *10* (8), 2742–2748. https://doi.org/10.1021/nl1003224.

(141) Zhao, H.; Yang, Z.; Guo, L. Nacre-Inspired Composites with Different Macroscopic Dimensions: Strategies for Improved Mechanical Performance and Applications. *NPG Asia Mater.* **2018**, *10* (4), 1–22. https://doi.org/10.1038/s41427-018-0009-6.

(142) Zhou, T.; Zhao, C.; Liu, Y.; Huang, J.; Zhou, H.; Nie, Z.; Fan, M.; Zhao, T.; Cheng, Q.; Liu, M. Large-Area Ultrastrong and Stiff Layered MXene Nanocomposites by Shear-Flow-Induced Alignment of Nanosheets. *ACS Nano* **2022**, *16* (8), 12013–12023. https://doi.org/10.1021/acsnano.2c02062.

(143) Yu, Y.; Kong, K.; Tang, R.; Liu, Z. A Bioinspired Ultratough Composite Produced by Integration of Inorganic Ionic Oligomers within Polymer Networks. *ACS Nano* **2022**, *16* (5), 7926–7936. https://doi.org/10.1021/acsnano.2c00663.

(144) Xie, W.; Tadepalli, S.; Park, S. H.; Kazemi-Moridani, A.; Jiang, Q.; Singamaneni, S.; Lee, J.-H. Extreme Mechanical Behavior of Nacre-Mimetic Graphene-Oxide and Silk Nanocomposites. *Nano Lett.* **2018**, *18* (2), 987–993. https://doi.org/10.1021/acs.nanolett.7b04421.

(145) Wan, S.; Chen, Y.; Wang, Y.; Li, G.; Wang, G.; Liu, L.; Zhang, J.; Liu, Y.; Xu, Z.; Tomsia, A. P.; Jiang, L.; Cheng, Q. Ultrastrong Graphene Films via Long-Chain π-Bridging. *Matter* **2019**, *1* (2), 389–401. https://doi.org/10.1016/j.matt.2019.04.006.

(146) Martin, J. J.; Fiore, B. E.; Erb, R. M. Designing Bioinspired Composite Reinforcement Architectures via 3D Magnetic Printing. *Nat. Commun.* **2015**, *6* (1), 8641. https://doi.org/10.1038/ncomms9641.

(147) Gao, H.-L.; Zhao, R.; Cui, C.; Zhu, Y.-B.; Chen, S.-M.; Pan, Z.; Meng, Y.-F.; Wen, S.-M.; Liu, C.; Wu, H.-A.; Yu, S.-H. Bioinspired Hierarchical Helical Nanocomposite Macrofibers Based on Bacterial Cellulose Nanofibers. *Natl. Sci. Rev.* **2020**, *7* (1), 73–83. https://doi.org/10.1093/nsr/nwz077.

(148) Meyers, M. A.; Chen, P.-Y.; Lopez, M. I.; Seki, Y.; Lin, A. Y. M. Biological Materials: A Materials Science Approach. *J. Mech. Behav. Biomed. Mater.* **2011**, *4* (5), 626–657. https://doi.org/10.1016/j.jmbbm.2010.08.005.

(149) Meyers, M. A.; Chen, P.-Y.; Lin, A. Y.-M.; Seki, Y. Biological Materials: Structure and Mechanical Properties. *Prog. Mater. Sci.* **2008**, *53* (1), 1–206. https://doi.org/10.1016/j.pmatsci.2007.05.002.

(150) Jones, P.; Wegner, T. H. Wood and Paper as Materials for the 21st Century. *MRS Online Proc. Libr. OPL* **2009**, *1187*, 1187. https://doi.org/10.1557/PROC-1187-KK04-06.

(151) Lossada, F.; Jiao, D.; Hoenders, D.; Walther, A. Recyclable and Light-Adaptive Vitrimer-Based Nacre-Mimetic Nanocomposites. *ACS Nano* **2021**, *15* (3), 5043–5055. https://doi.org/10.1021/acsnano.0c10001.

(152) Lossada, F.; Jiao, D.; Guo, J.; Hoenders, D.; Eckert, A.; Walther, A. Outstanding Synergies in Mechanical Properties of Bioinspired Cellulose Nanofibril Nanocomposites Using Self-Cross-Linking Polyurethanes. *ACS Appl. Polym. Mater.* **2019**, *1* (12), 3334–3342. https://doi.org/10.1021/acsapm.9b00774.

(153) Benítez, A. J.; Lossada, F.; Zhu, B.; Rudolph, T.; Walther, A. Understanding Toughness in Bioinspired Cellulose Nanofibril/Polymer Nanocomposites. *Biomacromolecules* **2016**, *17* (7), 2417–2426. https://doi.org/10.1021/acs.biomac.6b00533.

(154) Das, P.; Schipmann, S.; Malho, J.-M.; Zhu, B.; Klemradt, U.; Walther, A. Facile Access to Large-Scale, Self-Assembled, Nacre-Inspired, High-Performance Materials with Tunable Nanoscale Periodicities. *ACS Appl. Mater. Interfaces* **2013**, *5* (9), 3738–3747. https://doi.org/10.1021/am400350q.

(155) Das, P.; Malho, J.-M.; Rahimi, K.; Schacher, F. H.; Wang, B.; Demco, D. E.; Walther, A. Nacre-Mimetics with Synthetic Nanoclays up to Ultrahigh Aspect Ratios. *Nat. Commun.* **2015**, *6* (1), 5967. https://doi.org/10.1038/ncomms6967.

(156) Wang, B.; Torres-Rendon, J. G.; Yu, J.; Zhang, Y.; Walther, A. Aligned Bioinspired Cellulose Nanocrystal-Based Nanocomposites with Synergetic Mechanical Properties and Improved Hygromechanical Performance. *ACS Appl. Mater. Interfaces* **2015**, *7* (8), 4595–4607. https://doi.org/10.1021/am507726t.

(157) Aoki, D.; Lossada, F.; Hoenders, D.; Ajiro, H.; Walther, A. Efficient Softening and Toughening Strategies of Cellulose Nanofibril Nanocomposites Using Comb Polyurethane. *Biomacromolecules* **2022**, *23* (4), 1693–1702. https://doi.org/10.1021/acs.biomac.1c01625.

(158) Benítez, A. J.; Walther, A. Counterion Size and Nature Control Structural and Mechanical Response in Cellulose Nanofibril Nanopapers. *Biomacromolecules* **2017**, *18* (5), 1642–1653. https://doi.org/10.1021/acs.biomac.7b00263.

(159) Möller, M. W.; Kunz, D. A.; Lunkenbein, T.; Sommer, S.; Nennemann, A.; Breu, J. UV-Cured, Flexible, and Transparent Nanocomposite Coating with Remarkable Oxygen Barrier. *Adv. Mater.* **2012**, *24* (16), 2142–2147. https://doi.org/10.1002/adma.201104781.

(160) Walther, A.; Bjurhager, I.; Malho, J.-M.; Ruokolainen, J.; Berglund, L.; Ikkala, O. Supramolecular Control of Stiffness and Strength in Lightweight High-Performance Nacre-Mimetic Paper with Fire-Shielding Properties. *Angew. Chem. Int. Ed.* **2010**, *49* (36), 6448–6453. https://doi.org/10.1002/anie.201001577.

(161) Das, P.; Thomas, H.; Moeller, M.; Walther, A. Large-Scale, Thick, Self-Assembled, Nacre-Mimetic Brick-Walls as Fire Barrier Coatings on Textiles. *Sci. Rep.* **2017**, *7* (1), 39910. https://doi.org/10.1038/srep39910.

(162) Mäkiniemi, R. O.; Das, P.; Hönders, D.; Grygiel, K.; Cordella, D.; Detrembleur, C.; Yuan, J.; Walther, A. Conducting, Self-Assembled, Nacre-Mimetic Polymer/Clay Nanocomposites. *ACS Appl. Mater. Interfaces* **2015**, *7* (29), 15681–15685. https://doi.org/10.1021/acsami.5b04676.

(163) Hu, B.; Zhang, W.; Guo, H.; Xu, S.; Li, Y.; Li, M.; Li, B. Nacre-Mimetic Elastomer Composites with Synergistic Alignments of Boron Nitride/Graphene Oxide towards High through-Plane Thermal Conductivity. *Compos. Part Appl. Sci. Manuf.* **2022**, *156*, 106891. https://doi.org/10.1016/j.compositesa.2022.106891.

(164) Zhu, H.; Cao, H.; Liu, X.; Wang, M.; Meng, X.; Zhou, Q.; Xu, L. Nacre-like Composite Films with a Conductive Interconnected Network Consisting of Graphene Oxide, Polyvinyl Alcohol and Single-Walled Carbon Nanotubes. *Mater. Des.* **2019**, *175*, 107783. https://doi.org/10.1016/j.matdes.2019.107783.

(165) Guo, J.; Haehnle, B.; Hoenders, D.; Creusen, G.; Jiao, D.; Kuehne, A. J. C.; Walther, A. Biodegradable Laser Arrays Self-Assembled from Plant Resources. *Adv. Mater.* **2020**, *32* (29), 2002332. https://doi.org/10.1002/adma.202002332.

(166) Yeom, J.; Choe, A.; Lee, J.; Kim, J.; Kim, J.; Oh, S. H.; Park, C.; Na, S.; Shin, Y.-E.; Lee, Y.; Ro, Y. G.; Kwak, S. K.; Ko, H. Photosensitive Ion Channels in Layered MXene Membranes Modified with Plasmonic Gold Nanostars and Cellulose Nanofibers. *Nat. Commun.* **2023**, *14* (1), 359. https://doi.org/10.1038/s41467-023-36039-5.

(167) Kumar, A.; Jyske, T.; Petrič, M. Delignified Wood from Understanding the Hierarchically Aligned Cellulosic Structures to Creating Novel Functional Materials: A Review. *Adv. Sustain. Syst.* **2021**, *5* (5), 2000251. https://doi.org/10.1002/adsu.202000251.

(168) *Wood Polymer Composites: Recent Advancements and Applications*; Mavinkere Rangappa, S., Parameswaranpillai, J., Kumar, M. H., Siengchin, S., Eds.; Composites Science and Technology; Springer: Singapore, 2021. https://doi.org/10.1007/978-981-16-1606-8.

(169) Wang, S.; Li, L.; Zha, L.; Koskela, S.; Berglund, L. A.; Zhou, Q. Wood Xerogel for Fabrication of High-Performance Transparent Wood. *Nat. Commun.* **2023**, *14* (1), 2827. https://doi.org/10.1038/s41467-023-38481-x.

(170) Li, Y.; Vasileva, E.; Sychugov, I.; Popov, S.; Berglund, L. Optically Transparent Wood: Recent Progress, Opportunities, and Challenges. *Adv. Opt. Mater.* **2018**, *6* (14), 1800059. https://doi.org/10.1002/adom.201800059.

(171) Zhu, M.; Song, J.; Li, T.; Gong, A.; Wang, Y.; Dai, J.; Yao, Y.; Luo, W.; Henderson, D.; Hu, L. Highly Anisotropic, Highly Transparent Wood Composites. *Adv. Mater.* **2016**, *28* (26), 5181–5187. https://doi.org/10.1002/adma.201600427.

(172) Frey, M.; Schneider, L.; Masania, K.; Keplinger, T.; Burgert, I. Delignified Wood–Polymer Interpenetrating Composites Exceeding the Rule of Mixtures. *ACS Appl. Mater. Interfaces* **2019**, *11* (38), 35305–35311. https://doi.org/10.1021/acsami.9b11105.

(173) Jungstedt, E.; Montanari, C.; Östlund, S.; Berglund, L. Mechanical Properties of Transparent High Strength Biocomposites from Delignified Wood Veneer. *Compos. Part Appl. Sci. Manuf.* **2020**, *133*, 105853. https://doi.org/10.1016/j.compositesa.2020.105853.

(174) Koch, S. M.; Pillon, M.; Keplinger, T.; Dreimol, C. H.; Weinkötz, S.; Burgert, I. Intercellular Matrix Infiltration Improves the Wet Strength of Delignified Wood Composites. *ACS Appl. Mater. Interfaces* **2022**, *14* (27), 31216–31224. https://doi.org/10.1021/acsami.2c04014.

(175) Montanari, C.; Li, Y.; Chen, H.; Yan, M.; Berglund, L. A. Transparent Wood for Thermal Energy Storage and Reversible Optical Transmittance. *ACS Appl. Mater. Interfaces* **2019**, *11* (22), 20465–20472. https://doi.org/10.1021/acsami.9b05525.

(176) Yu, Z.-L.; Yang, N.; Zhou, L.-C.; Ma, Z.-Y.; Zhu, Y.-B.; Lu, Y.-Y.; Qin, B.; Xing, W.-Y.; Ma, T.; Li, S.-C.; Gao, H.-L.; Wu, H.-A.; Yu, S.-H. Bioinspired Polymeric Woods. *Sci. Adv.* **2018**, *4* (8), eaat7223. https://doi.org/10.1126/sciadv.aat7223.

(177) Zhang, Y.; Chen, Z.; Du, K.; Bi, Y.; Su, J.; Zhang, Y.; Shen, Y.; Zhang, S. Functional Natural Wood-Plastic Composites: A Review of Antimicrobial Properties and Their Influencing Factors. *Ind. Crops Prod.* **2023**, *201*, 116705. https://doi.org/10.1016/j.indcrop.2023.116705.

(178) Li, T.; Song, J.; Zhao, X.; Yang, Z.; Pastel, G.; Xu, S.; Jia, C.; Dai, J.; Chen, C.; Gong, A.; Jiang, F.; Yao, Y.; Fan, T.; Yang, B.; Wågberg, L.; Yang, R.; Hu, L. Anisotropic, Lightweight, Strong, and Super Thermally Insulating Nanowood with Naturally Aligned Nanocellulose. *Sci. Adv.* **2018**, *4* (3), eaar3724. https://doi.org/10.1126/sciadv.aar3724.

(179) Yang, Y.; Boom, R.; Irion, B.; van Heerden, D.-J.; Kuiper, P.; de Wit, H. Recycling of Composite Materials. *Chem. Eng. Process. Process Intensif.* **2012**, *51*, 53–68. https://doi.org/10.1016/j.cep.2011.09.007.

(180) Frey, M.; Biffi, G.; Adobes-Vidal, M.; Zirkelbach, M.; Wang, Y.; Tu, K.; Hirt, A. M.; Masania, K.; Burgert, I.; Keplinger, T. Tunable Wood by Reversible Interlocking and Bioinspired Mechanical Gradients. *Adv. Sci.* **2019**, *6* (10), 1802190. https://doi.org/10.1002/advs.201802190.

(181) Grönquist, P.; Wood, D.; Hassani, M. M.; Wittel, F. K.; Menges, A.; Rüggeberg, M. Analysis of Hygroscopic Self-Shaping Wood at Large Scale for Curved Mass Timber Structures. *Sci. Adv.* **2019**, *5* (9), eaax1311. https://doi.org/10.1126/sciadv.aax1311.

(182) Frey, M.; Zirkelbach, M.; Dransfeld, C.; Faude, E.; Trachsel, E.; Hannus, M.; Burgert, I.; Keplinger, T. Fabrication and Design of Wood-Based High-Performance Composites. *J. Vis. Exp. JoVE* **2019**, No. 153. https://doi.org/10.3791/60327.

(183) Kumar, V.; Kuang, W.; Fifield, L. S. Carbon Fiber-Based Vitrimer Composites: A Path toward Current Research That Is High-Performing, Useful, and Sustainable. *Materials* **2024**, *17* (13), 3265. https://doi.org/10.3390/ma17133265.

(184) Debsharma, T.; Amfilochiou, V.; Wróblewska, A. A.; De Baere, I.; Van Paepegem, W.; Du Prez, F. E. Fast Dynamic Siloxane Exchange Mechanism for Reshapable Vitrimer Composites. *J. Am. Chem. Soc.* **2022**, *144* (27), 12280–12289. https://doi.org/10.1021/jacs.2c03518.

(185) Lossada, F.; Guo, J.; Jiao, D.; Groeer, S.; Bourgeat-Lami, E.; Montarnal, D.; Walther, A. Vitrimer Chemistry Meets Cellulose Nanofibrils: Bioinspired Nanopapers with High Water Resistance and Strong Adhesion. *Biomacromolecules* **2019**, *20* (2), 1045–1055. https://doi.org/10.1021/acs.biomac.8b01659.

(186) Wang, K.; Zhang, T.; Li, C.; Xiao, X.; Tang, Y.; Fang, X.; Peng, H.; Liu, X.; Dong, Y.; Cai, Y.; Tian, D.; Li, Y.; Li, J. Shape-Reconfigurable Transparent Wood Based on Solid-State Plasticity of Polythiourethane for Smart Building Materials with Tunable Light Guiding, Energy Saving, and Fire Alarm Actuating Functions. *Compos. Part B Eng.* **2022**, *246*, 110260. https://doi.org/10.1016/j.compositesb.2022.110260.

(187) Lossada, F.; Zhu, B.; Walther, A. Dry Processing and Recycling of Thick Nacre–Mimetic Nanocomposites. *Adv. Funct. Mater.* **2021**, *31* (30), 2102677. https://doi.org/10.1002/adfm.202102677.

(188) Tan, Y.; Wang, K.; Dong, Y.; Gong, S.; Shi, S. Q.; Li, J. High Performance, Shape Manipulatable Transparent Wood Based on Delignified Wood Framework and Exchangeable Dynamic Covalent Vitrimers. *Chem. Eng. J.* **2022**, *448*, 137487. https://doi.org/10.1016/j.cej.2022.137487.
(189) Wang, K.; Dong, Y.; Ling, Z.; Liu, X.; Shi, S. Q.; Li, J. Transparent Wood Developed by Introducing Epoxy Vitrimers into a Delignified Wood Template. *Compos. Sci. Technol.* **2021**, *207*, 108690. https://doi.org/10.1016/j.compscitech.2021.108690.
(190) Vasileva, E.; Chen, H.; Li, Y.; Sychugov, I.; Yan, M.; Berglund, L.; Popov, S. Light Scattering by Structurally Anisotropic Media: A Benchmark with Transparent Wood. *Adv. Opt. Mater.* **2018**, *6* (23), 1800999. https://doi.org/10.1002/adom.201800999.
(191) Pereira Oliveira Moreira, R. L.; Simão, J. A.; Gouveia, R. F.; Strauss, M. Exploring the Hierarchical Structure and Alignment of Wood Cellulose Fibers for Bioinspired Anisotropic Polymeric Composites. *ACS Appl. Bio Mater.* **2020**, *3* (4), 2193–2200. https://doi.org/10.1021/acsabm.0c00038.
(192) Szycher, M. *Szycher's Handbook of Polyurethanes, Second Edition*; CRC Press, 2012.

Chapter 2. Tunable Waterborne Aspartic Acid-Based Covalent Adaptable Networks with Internal Catalysis and Incorporation in Bioinspired Nanocomposites

Affiliation

Life-Like Materials and Systems, Department of Chemistry, University of Mainz, Duesbergweg 10-14, 55128 Mainz, Germany.

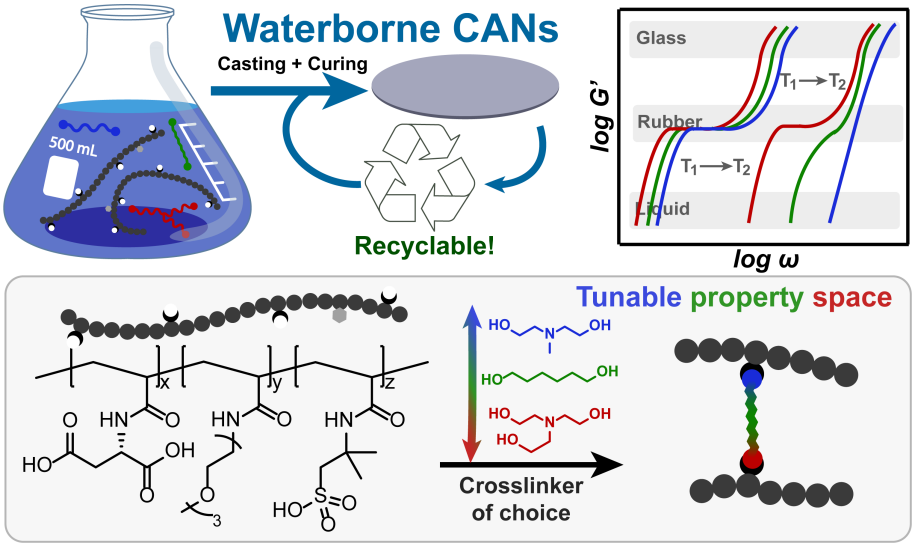

Note, this chapter is adapted with minor formatting changes from the scientific publication: ''**Sjoerd Engels**, Andreas Walther, Tunable Waterborne Aspartic Acid-Based Covalent Adaptable Networks with Internal Catalysis and Incorporation in Bioinspired Nanocomposites, *Macromolecules* 2024, 57, 16, 7701-7712. DOI: https://doi.org/10.1021/acs.macromol.4c00666''

Author contributions: S.E. and A.W. conceptualized the core ideas. **S.E.** planned and conducted the experiments. **S.E.** wrote the manuscript. A.W. edited and finalized the manuscript.

2.1 Abstract

Waterborne resins are important for coatings and adhesives, yet the field of reprocessable covalent adaptable networks (CANs) is dominated by hydrophobic materials. Here, we introduce waterborne CANs that feature dual internal catalysis, dissociative bond exchange and customizable properties through specific selection of different crosslinkers. The system uses random copolymers based on aspartic acid, which can catalyze formation and exchange of dynamic covalent ester bonds. Crosslinker variation enables vast differences in thermoresponsive properties: Diols with a tertiary amine feature fastest bond exchange and stress relaxation, and enable ductile mechanical behavior in ambient conditions. Amine-containing triols instead lead to high nonelastic deformation resistance, linked to *e.g.* creep, by slowing stress relaxation until high temperatures. Aliphatic diols exhibit low exchange kinetics, while affording glassy mechanical behavior. Our CAN-prepolymer/crosslinker systems offer great potential for aqueous applications due to their good recyclability and excellent tunability, as is further demonstrated by incorporation in waterborne bioinspired nanocomposites.

2.2 Introduction

In a global context, there is an ever increasing demand for plastics[1], which necessitates to develop versatile and economical high-performance (crosslinked) polymer materials that can function in a sustainable circular economy.[2] Commonly employed thermosets possess vital heat and creep resistance together with excellent mechanical properties, but are highly intractable after initial production.[3,4] In contrast, the next generation of polymer materials requires more adaptability, no matter whether in lightweight-engineering (*e.g.*, aerospace and automotive industries), for ultrahigh-performance mechanical parts (*e.g.*, composites in spacecraft or windmill applications) or for coatings, paints, and adhesives.[3] One solution is to make the structural constituents of a polymer material responsive to a certain trigger (usually temperature, but lately also chemicals). In this way, materials can access faster dynamic properties when required for adaptability, but in operating conditions they remain resilient against the drawbacks (*e.g.*, creep, flow, solubility).[5–7] Noncovalent strategies to achieve this involve supramolecular interactions, such as hydrogen bonds, or π-π and ionic interactions, thereby yielding highly dynamic but often also thermally and structurally labile networks.[8–11] Covalent adaptable networks (CANs) exhibit analogous dynamic properties based on a covalent crosslinking strategy, but with a potential for higher resilience to creep or solvents under operating conditions.[12–15]

CANs are a broad set of networks that can differ based on the chemistry of bond exchange (*e.g.*, transesterification, disulfide exchange, transamination, and the Diels Alder reaction), mechanistic pathway (*e.g.*, associative versus dissociative), nature of catalysis, network topology, and more, all of which can in turn influence one another.[14,16–19] The associative pathway typically involves a degenerate reaction going through an addition-reaction transition state whereby the crosslinking degree is maintained. In contrast, dissociative pathways involve reaction intermediates that are lower in crosslinking degree. Such intermediates are of low lifetime at functional temperatures, thereby maintaining network cohesion almost completely. However, increasing the temperature shifts the equilibrium towards the dissociated state. Hence, dissociative CANs often differ in their temperature response compared to associative CANs, indicated by decreasing plateau modulus and enhanced viscous flow. It should be noted that this idealized theoretical description often does not reflect the full complexity of CANs in real settings.[18] Depending on the bond enthalpy, the equilibrium can be shifted towards association to such a degree that decrosslinking becomes only relevant at very high temperature. Hence, there are examples of dissociative CANs that display quasi-constant crosslink densities and Arrhenius-like temperature responses, just like associative CANs.[20] Additionally, for many bond exchange chemistries (*e.g.*, transesterification), both associative and dissociative mechanisms have been identified, which can occur in parallel and often with different dependencies on conditions such as catalysis or temperature.[18,21,22] In addition, more complex exchange mechanisms that depend on more than one reactive step are often feasible as well.[23,24]

The use of internal catalysts eliminates the reliance on external additives, which often face problems like instability, incompatibility or bearing allergic potential due to migration in a final material. Moreover, internal catalysts can lead to much larger rate enhancements of the dynamic chemistries.[15] Neighboring group participation in particular has been used to increase chemical reactivity and thereby macroscopic flow of the network to such drastic levels that extrusion of fully crosslinked networks becomes feasible.[25,26]

In the context of this article, it is important to mention that most CANs investigated in the field are incompatible with water or waterborne processes. While this is desirable in some cases, a body of applications can benefit from waterborne systems, as is demonstrated for highly reinforced, bioinspired nanocomposite materials whose hierarchical structure formation requires water for proper self-assembly.[27,28] Additionally, paint and coating industries favor usage of water as a green and non-toxic solvent, especially indoors.[29]

Here, we demonstrate the development of a highly crosslinked tunable waterborne CAN system, featuring dual internal catalysis and customizable properties through specific selection of different crosslinkers. The system uses linear random copolymers, created through free radical polymerization, comprising three different monomers, including an L-aspartic acid derivative which is chosen for its ability to form dynamic covalent ester bonds and catalyze bond exchange reactions. Five CAN networks are created with variable dynamic and mechanical behaviors via simple variation of copolymer and crosslinker used. The vast differences in thermoresponsive properties are characterized extensively. This approach results in a material system with good recyclability and excellent potential for applications requiring high performance materials with great and easy tunability for specific demands, specifically involving aqueous conditions. To demonstrate their unique usefulness further, the CANs are incorporated in bioinspired nanocomposites.

2.3 Results and Discussion

2.3.1 General System Design for Tunable Waterborne CANs based on Aqueous Prepolymers

Figure 1a-c gives a comprehensive overview of our aspartic acid-derived waterborne CAN system, which has dual internal catalysis and possesses a readily tunable range of properties based on the chosen components. It is based on a prepolymer (pre-CAN) system that can be crosslinked using different compounds. The pre-CANs are linear random copolymers prepared via free radical polymerization and are composed of three different monomer units: L-aspartic acid appended acrylamide (A3), methoxy triethylene glycol acrylamide (EG), and 2-acrylamido-2-methylpropane sulfonic acid (S). All monomers are chosen to provide high levels of water solubility to enable waterborne pre-CANs. Furthermore, this selection integrates three key design elements: (i) A3 is the functional component that can form dynamic covalent bonds with nucleophilic crosslinkers, specifically alcohols (**Figure 1d**).

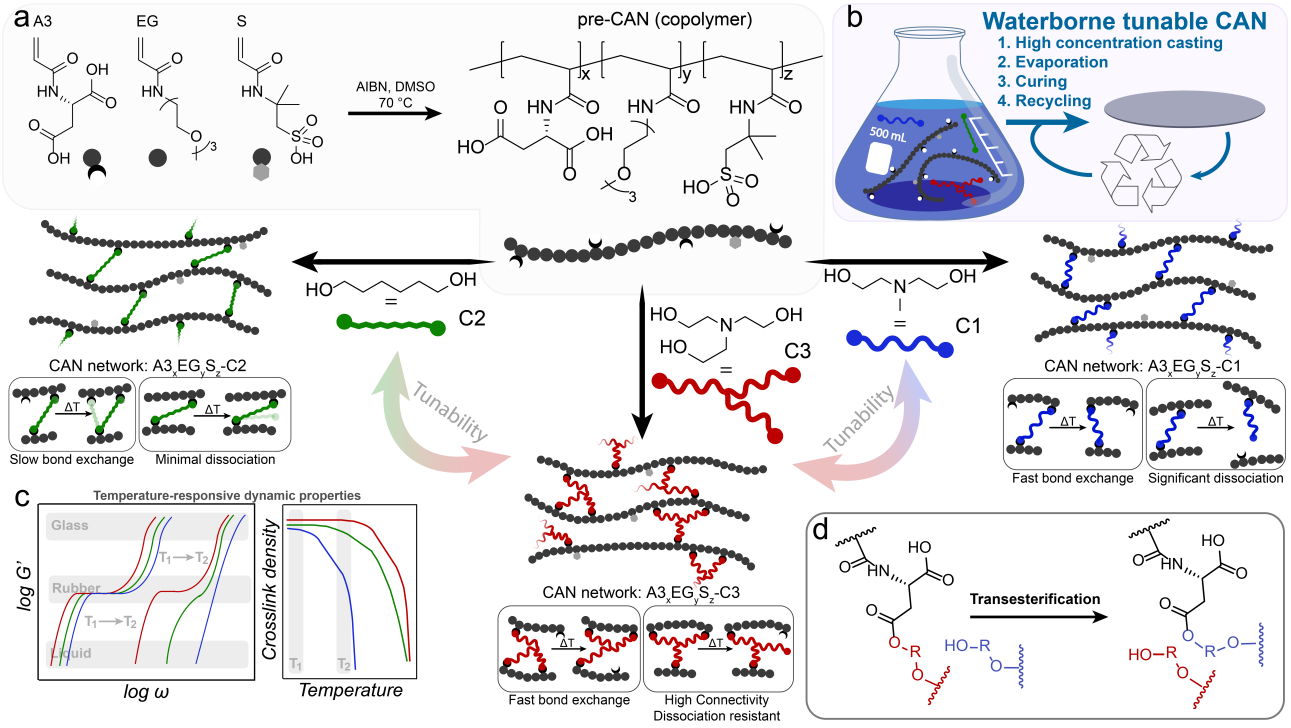

Figure 1. (a) Schematic preparation route of aspartic acid-derived waterborne tunable CANs via free radical polymerization and subsequent network formation via addition of crosslinkers, with differing dynamic profiles based on crosslinkers utilized. (b) Preparation, processing, and recycling of the CANs under aqueous conditions. (c) Schematic representation of the temperature-dependence of the CANs. (d) The net reaction for the transesterification bond exchange.

Analogous to CANs shown in literature, A3 is expected to catalyze transesterification via dissociative cyclization to form an intermediate 5-membered anhydride to enhance the rate of dissociation and subsequent association with crosslinker alcohols (**Figure 2**).[17,26,30] Besides, A3 ensures high crosslink density and high fractions of dynamic crosslinks, associated with mechanical stiffness and

strength, on account of having two carboxylic acid groups per repeating unit.[4,31] (ii) Incorporation of a sulfonic acid via monomer S is known to catalyze esterification and transesterification in both small molecules and polymers to further enhance the bond exchange process.[32–34](iii) Lastly, EG is a covalently tethered water-soluble plasticizer to ensure both ductility and the possibility for viscous flow to occur at elevated temperatures, which is required for efficient network bond reshuffling.[4,13]

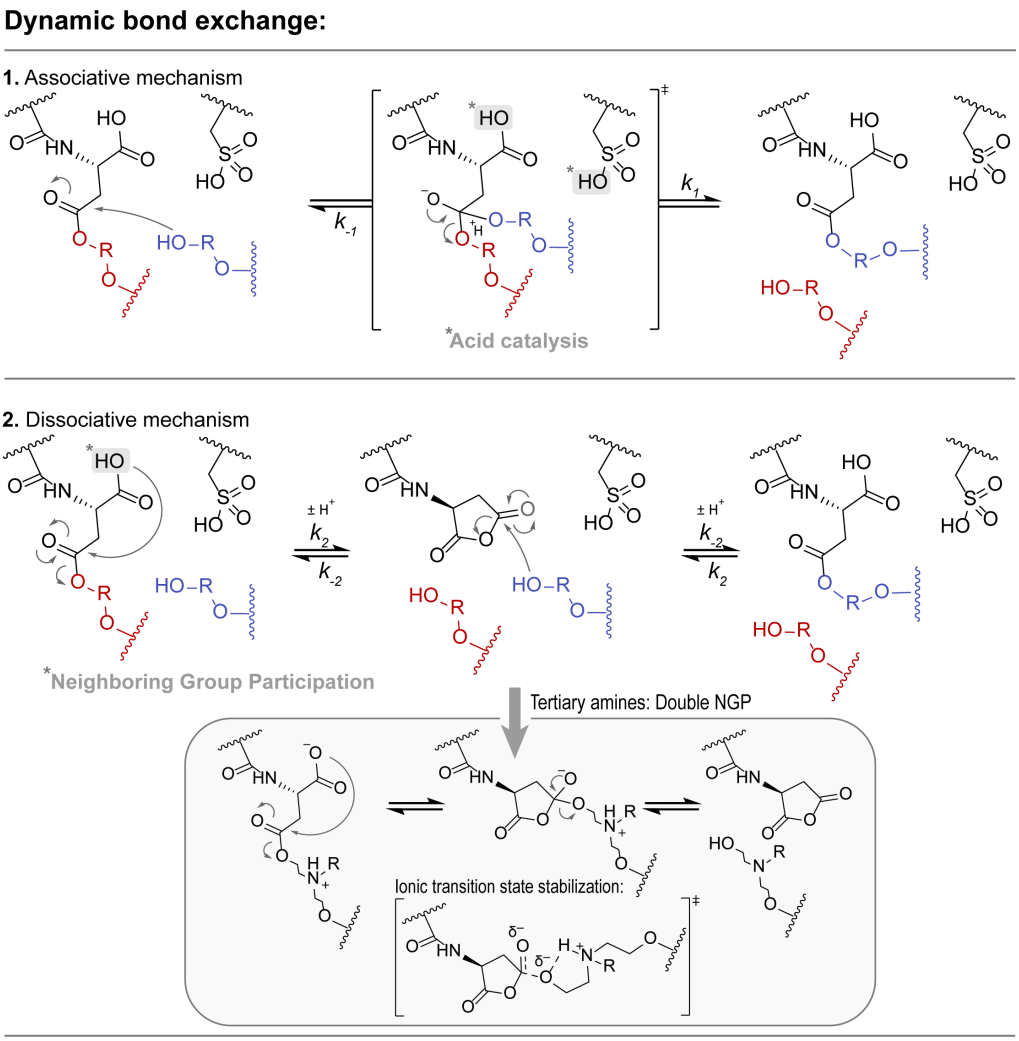

Figure 2. Proposed mechanisms for associative and dissociative transesterification respectively of the $A3_xEG_yS_z$ based CAN networks. The general proposed mechanism of how tertiary amine-containing crosslinkers (C1 and C3) enhance the transesterification via double neighboring group participation is depicted below.

A combination of the pre-CANs with nucleophilic crosslinking units, such as alcohols, provides a wide parameter space for tuning the CAN by choosing from a variety of simple (often commercial) small molecules. This strategy enables the preparation of highly distinct CAN networks, both in terms of dynamic and mechanical properties, based on simple aqueous mixing, evaporation, and heat-induced crosslinking. In this study, we selected three crosslinkers with distinctly different properties: (i) *N*-methyldiethanolamine (C1) as a diol containing a tertiary amine group, (ii) 1,6-hexanediol (C2) as an aliphatic diol of similar size but without the amine group, and (iii) triethanolamine (C3) as a trivalent analogue of C1. C1 has been shown in literature to improve dissociative bond exchange

rates via double internal catalysis of carboxylate and ammonium groups, via a charge stabilization and transfer mechanism (**Figure 2**).[26,35] Such an effect is also anticipated for C3 but not for C2, indicating a distinction in the catalytic capabilities for the different crosslinkers and thus the wide range of potential bond exchange pathways involved.[14,17,36]

2.3.2 Pre-CAN Synthesis and Network Formation

We synthesized three fully water-soluble pre-CAN copolymers via free radical polymerization with three molar ratios A3/EG/S at an aimed internal concentration of S of ca. 10 mol%, and with different fractions of A3 to EG. Analysis of the incremental monomer incorporation by ^{1}H-NMR shows a near-statistical incorporation of all three monomers with a small preference for EG (Figure S1). **Table 1** lists the number-average molecular weights (M_n) and the dispersity ($Đ$), as well as the final comonomer composition that is in line with the feed ratios (**Table 1**, Figure S2-3). The moderately broad range of $Đ$ from ca. 1.5 - 2.7 for the pre-CANs is not critical as these polymers are going to be crosslinked at a high density of crosslinks and it is hence unlikely that this dispersity has a substantial effect on the properties of the final CANs.[37–39]. We prepared the CAN networks by mixing the pre-CAN copolymers and crosslinker of choice in aqueous solution, whereby stoichiometry is based on the carboxylic acid groups of the A3 components and the alcohol group of the crosslinker (the functional groups in the crosslinking process): This molar ratio of carboxylic acid to alcohol is constant at 1 : 0.95. This is because literature shows that some free acids are necessary to form the anhydride intermediates for neighboring group participation.[30,32] After mixing, evaporation and heat-induced curing yielded the final CANs, abbreviated as $A3_xEG_yS_z$-Cw, where x, y, and z indicate the molar fraction of the corresponding monomer in the pre-CAN. Cw indicates the crosslinker (C1, C2, C3) (Table S1). We chose to prepare three CANs using C1 ($A3_3EG_6S_1$-C1, $A3_5EG_4S_1$-C1, and $A3_7EG_2S_1$-C1) to compare the effect of pre-CAN. Additionally, we prepared two more CANs ($A3_5EG_4S_1$-C2 and $A3_5EG_4S_1$-C3) to assess the impact of crosslinkers C1, C2, and C3 based on pre-CAN $A3_5EG_4S_1$.

Table 1. Overview of pre-CAN copolymers prepared by free radical polymerization.

Sample	Monomer ratio feed (A3/EG/S)	Molar fractions (A3/EG/S)[a)]	$M_{n,app}$ (kDa)	$Đ$[b)]
$A3_3EG_6S_1$	3/6/1	3.0/6.0/0.8	26	2.0
$A3_5EG_4S_1$	5/4/1	5.0/4.3/0.9	22	1.5
$A3_7EG_2S_1$	7/2/1	7.0/2.4/1.0	81	2.7

[a)] Molar fractions of the final polymers are determined by ^{1}H-NMR.

[b)] $M_{n,app}$ and $Đ$ of the methylated polymers are measured by gel permeation chromatography in 5 gL^{-1} LiBr in dimethylacetamide, calibrated against polymethylmethacrylate standard.

To understand the crosslinking kinetics of the CANs, we conducted small-amplitude oscillatory shear rheology at 130 °C. **Figure 3a** shows a comparison for the crosslinking of $A3_5EG_4S_1$ with different crosslinkers (C1, C2, C3), whereas Figure S4 additionally gives an overview of the crosslinking of the three different pre-CANs with C1. The gelation point, where the storage modulus (*G'*) is equal to the loss modulus (*G"*), occurs at early stages of the curing process for all CANs (< 100 s) because a significant number of crosslinking points is formed quickly, enabling percolation. Furthermore, all CANs exhibit similar curing kinetics. The curing process can be confirmed on a chemical level by Fourier-transform infrared spectroscopy. Characteristic bands can be attributed to various chemical groups present in the CAN: C=O stretch for amide (1645 cm^{-1}), carboxylic acid (1712 cm^{-1}), and ester groups (1734 cm^{-1}), O–H stretching for carboxylic acid (3065 cm^{-1}) and alcohol and H_2O (3300 cm^{-1}), and C–O stretching for esters, alcohols, and carboxylic acids (1300 - 1000 cm^{-1}) (**Figure 3b**).[40,41] The key observation is the shift of the C=O stretching signal from 1712 to 1734 cm^{-1} corresponding to the esterification upon curing. The small shift at 1180 cm^{-1} is a secondary indication of esterification.

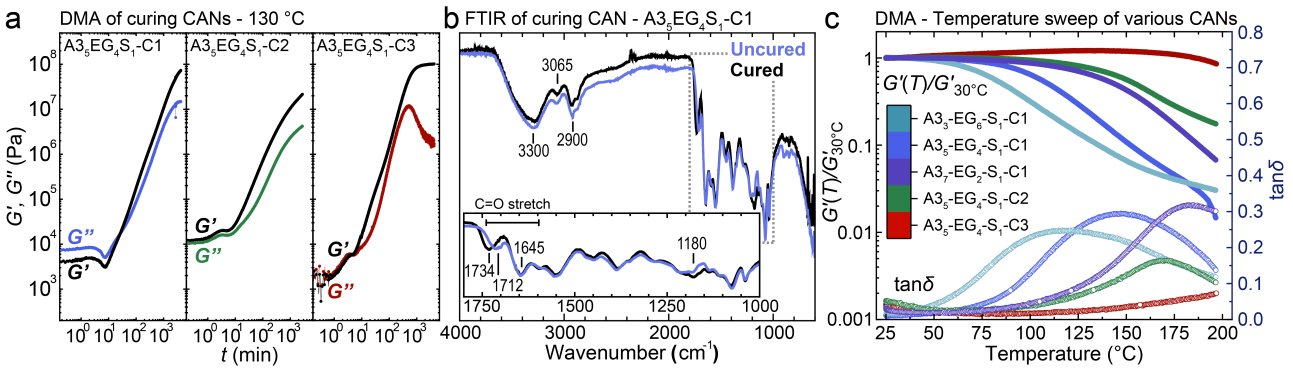

Figure 3. CAN network formation and characterization. (a) Curing kinetics (obtained by small-amplitude oscillatory shear) of $A3_5EG_4S_1$-C1, $A3_5EG_4S_1$-C2, and $A3_5EG_4S_1$-C3 when heated at 130 °C. (b) FTIR spectra of uncured and cured (70 h, 130 °C) samples of $A3_5EG_4S_1$-C1. (c) Temperature sweep spectra (obtained by small-amplitude oscillatory shear) of $A3_3EG_6S_1$-C1, $A3_5EG_4S_1$-C1, $A3_7EG_2S_1$-C1, $A3_5EG_4S_1$-C2, and $A3_5EG_4S_1$-C3 after curing (70 h, 130 °C) with normalized *G'*.

After curing (70 h, 130 °C), we determined the soluble fractions for each crosslinked CAN by immersion in H_2O and DMF for 48 h (Table S2) to be less than 10% for all CANs, except for ca. 15% for $A3_3EG_6S_1$-C1. These results further indicate the crosslinked nature of the networks as well as resilience against hydrolysis of the potentially dynamic ester bonds (internal catalysts) in H_2O, especially considering how, unlike thermosets, CANs can sometimes dissolve in good solvents.[42,43] Conditioning the CANs at 50% relative humidity (RH) followed by measurement of the water content reveals their water uptake (Table S2). The data indicate a trend: CANs with more tertiary amines contain more water ($A3_7EG_2S_1$-C1 > $A3_5EG_4S_1$-C1 > $A3_5EG_4S_1$-C3 > $A3_3EG_6S_1$-C1 > $A3_5EG_4S_1$-C2). Notably, $A3_5EG_4S_1$-C2 only contains ca. half as much water as $A3_5EG_4S_1$-C1, due to the lack of easily protonated tertiary amines in the crosslinker.

To obtain a first understanding of the effect of crosslinking on the thermomechanical properties, we investigated the linear elastic regimes via amplitude sweeps (Figure S5) and subsequently we conducted small-amplitude oscillatory temperature sweeps of the cured networks (cured for 70 h at 130 °C; **Figure 3c**). For a better comparison, the *G'* data were normalized for all CANs to be 1 at *T* = 30 °C. The temperature response varies with the degree of crosslinking (that is A3 content) in $A3_3EG_6S_1$-C1, $A3_5EG_4S_1$-C1, and $A3_7EG_2S_1$-C1, respectively: both the onset of the *G'* decrease and the maximum of tan*δ* shift to higher temperatures as the crosslink density increases (compare blue curves in **Figure 3c**).[44] The magnitude of the temperature response is similar for all three CANs based on C1. Such transitions spanning large temperature ranges (> 100 °C) have been related to either the onset of rapid bond exchange or bond dissociation in other CAN systems (or a combination of both).[16,44–48] Interestingly, $A3_5EG_4S_1$-C2, only shows a much smaller magnitude of the temperature-response and the maximum of tan*δ* is shifted by ca. 20 °C to a higher temperature compared to $A3_5EG_4S_1$-C1. This confirms our expectation that C2 does not contribute to internal catalysis due to a lack of a tertiary amine group. Such differences in the reactive environment impact the reaction kinetics and equilibria.[26,46]

In contrast to the C1 and C2-based systems, $A3_5EG_4S_1$-C3 exhibits no clear softening or maximum in tan*δ* within the temperature range up to 200 °C. This indicates that the trivalent crosslinker C3 plays a critical role in 'freezing' the temperature-induced network response. While the transesterification reaction is expected to follow an analogous mechanism as compared to CANs based on C1, C3 may correspond to a different equilibrium of dissociation or require a higher extent of dissociation for long-range network rearrangement, as has been observed in other work.[46] Lastly, $A3_5EG_4S_1$-C3 also displays a slight temperature-dependent increase of *G'*, visible in the range of 25 - 150 °C. Such an increase indicates contribution from entropic elasticity, which is commonly observed in highly crosslinked thermosets and some associative and even dissociative CANs.[20,49–51]

2.3.3 Tensile Mechanical Properties

We measured the mechanical properties at room temperature in tensile mode to understand the tunability of the property space as a function of the pre-CAN system with different crosslinkers. We performed these tensile tests for cured CANs (70 h, 130 °C) after conditioning at ambient conditions (50% RH) and at 20% RH to also investigate the role of hydrophilicity and water content in these networks. **Figure 4** and **Table 2** summarize the mechanical properties: stress (σ_b) and strain (ε_b) at break, yield stress (σ_y) and yield strain (ε_y), Young's modulus (E), and toughness (U_t). The tensile curves can be roughly divided into two different behaviors: C1-based CANs are relatively soft and ductile, whereas C2 and C3-based CANs are stiff and strong with limited ductility. For a more detailed discussion we first focus on the dependence of the mechanical properties as a function of degree of

crosslinking for the C1-based CANs, $A3_3EG_6S_1$-C1, $A3_5EG_4S_1$-C1, and $A3_7EG_2S_1$-C1 at 50% RH (**Figure 4a**). Here, E increases from 11.8 to 24.4 MPa as the degree of crosslinking increases. On the other hand, σ_b, ε_b, and U_t are the highest for $A3_5EG_4S_1$-C1, indicating good balance between crosslinks providing cohesion and the EG component enabling some dissipation. When changing from C1 to C3 for $A3_5EG_4S_1$, a vast increase in E and σ_b is observed. $A3_5EG_4S_1$-C3 reaches E = 380 MPa and σ_b = 14.7 MPa, and $A3_5EG_4S_1$-C2 continues this trend even further with values for E = 1.42 GPa and σ_b = 42.4 MPa. The latter also lacks an obvious plastic deformation regime, unlike the other four CANs. This change in mechanical properties can stem from both an increased crosslinking density and from a change in hydrophilicity and water-induced plasticization, as reflected by the differences in water absorption of the CANs (Table S2).

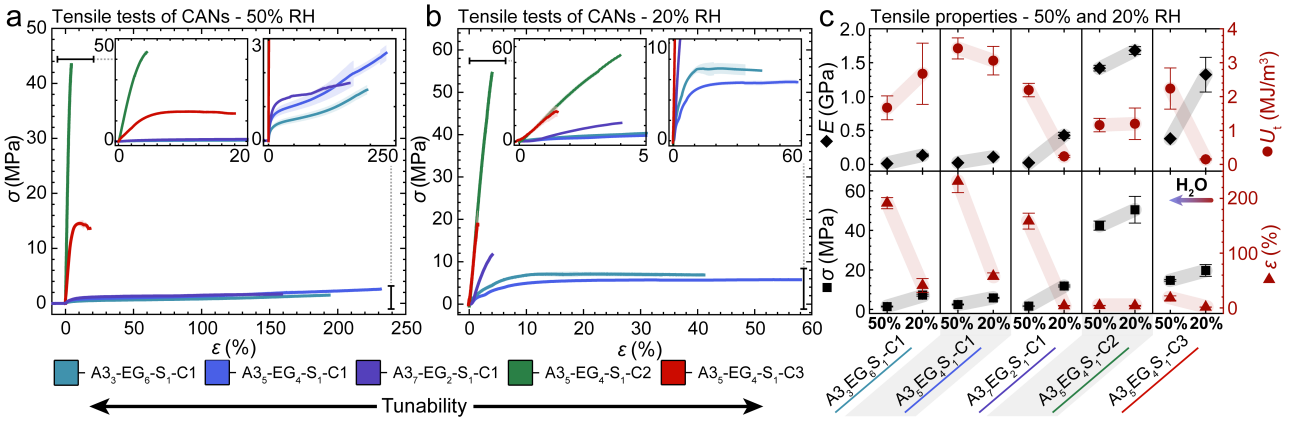

Figure 4. Tensile tests for CANs $A3_3EG_6S_1$-C1, $A3_5EG_4S_1$-C1, $A3_7EG_2S_1$-C1, $A3_5EG_4S_1$-C2, and $A3_5EG_4S_1$-C3 after conditioning at (a) 50% RH and (b) 20% RH. Plots for zoomed x-axis (top) and zoomed y-axis (bottom) are added. (c) Overview of the tensile properties for each CAN conditioned at 50% RH and 20% RH, respectively.

Table 2. Overview of tensile properties of CAN networks.

Sample	RH (%)[a)]	σ_b (MPa) ± SE[b)]	ε_b (%) ± SE[b)]	σ_y (MPa) ± SE[b)]	ε_y (%) ± SE[b)]	E (MPa) ± SE[b)]	U_t (MJm^{-3}) ± SE[b)]
$A3_3EG_6S_1$-C1	50	1.50 ± 0.21	191 ± 10	0.46 ± 0.08	4.0 ± 0.2	11.8 ± 2.2	1.7 ± 0.4
$A3_3EG_6S_1$-C1	20	7.27 ± 0.50	41.1 ± 13	7.2 ± 0.5	5.8 ± 1	134 ± 21	2.7 ± 1
$A3_5EG_4S_1$-C1	50	2.52 ± 0.24	231 ± 21	0.74 ± 0.1	3.1 ± 0.2	22.9 ± 3.5	3.4 ± 0.3
$A3_5EG_4S_1$-C1	20	5.84 ± 0.21	58.0 ± 6.0	5.4 ± 0.2	5.7 ± 0.3	109 ± 4.7	3.1 ± 0.4
$A3_7EG_2S_1$-C1	50	1.72 ± 0.02	159 ± 15	1.1 ± 0.04	6.2 ± 2	24.4 ± 6.8	2.2 ± 0.2
$A3_7EG_2S_1$-C1	20	11.9 ± 0.48	4.02 ± 0.41	-	-	429 ± 44	0.24 ± 0.03
$A3_5EG_4S_1$-C2	50	42.4 ± 2.3	4.39 ± 0.44	39 ± 2	2.9 ± 0.03	1419 ± 42	1.2 ± 0.2
$A3_5EG_4S_1$-C2	20	50.5 ± 6.7	3.98 ± 0.86	-	-	1680 ± 57	1.2 ± 0.5
$A3_5EG_4S_1$-C3	50	14.7 ± 0.45	18.0 ± 4.1	14 ± 0.3	4.6 ± 0.2	380 ± 5.3	2.2 ± 0.6
$A3_5EG_4S_1$-C3	20	19.7 ± 3.0	1.50 ± 0.093	-	-	1323 ± 26	0.15 ± 0.02

[a)] The samples are conditioned by storing them for 24 h at the indicated RH and immediately measured after.
[b)] SE refers to the standard error.

To further investigate this, we also measured the tensile properties after conditioning at 20% RH (**Figure 4b**). A strong shift towards higher σ_b and E, as well as lower ε_b can be observed for all C1-based networks ($A3_3EG_6S_1$-C1, $A3_5EG_4S_1$-C1, $A3_7EG_2S_1$-C1), most prominently for the most crosslinked one ($A3_7EG_2S_1$-C1), as well as for $A3_5EG_4S_1$-C3. In contrast, $A3_5EG_4S_1$-C2 only displays minute differences in these properties, because it already has the lowest water sorption at 50% RH. These observations show that the presence of water in CAN networks has significant plasticizing effects on the mechanical properties.[52,53] $A3_5EG_4S_1$-C3 displays a property-space somewhere in-between the other two, and balances water uptake due to the polar amine group with increased crosslinker valency. These results perfectly encapsulate the wide range of properties accessible in this CAN system via variation of the crosslinker.

2.3.4 Dynamic Exchange and Dissociation

Next, we focus our understanding on the exchange dynamics and potential dissociation of the crosslinks in these CANs. We first performed frequency sweeps for all CANs at 25 °C, 100 °C, and 140 °C after full curing (curing conditions: 70 h, 130 °C; **Figure 5**).

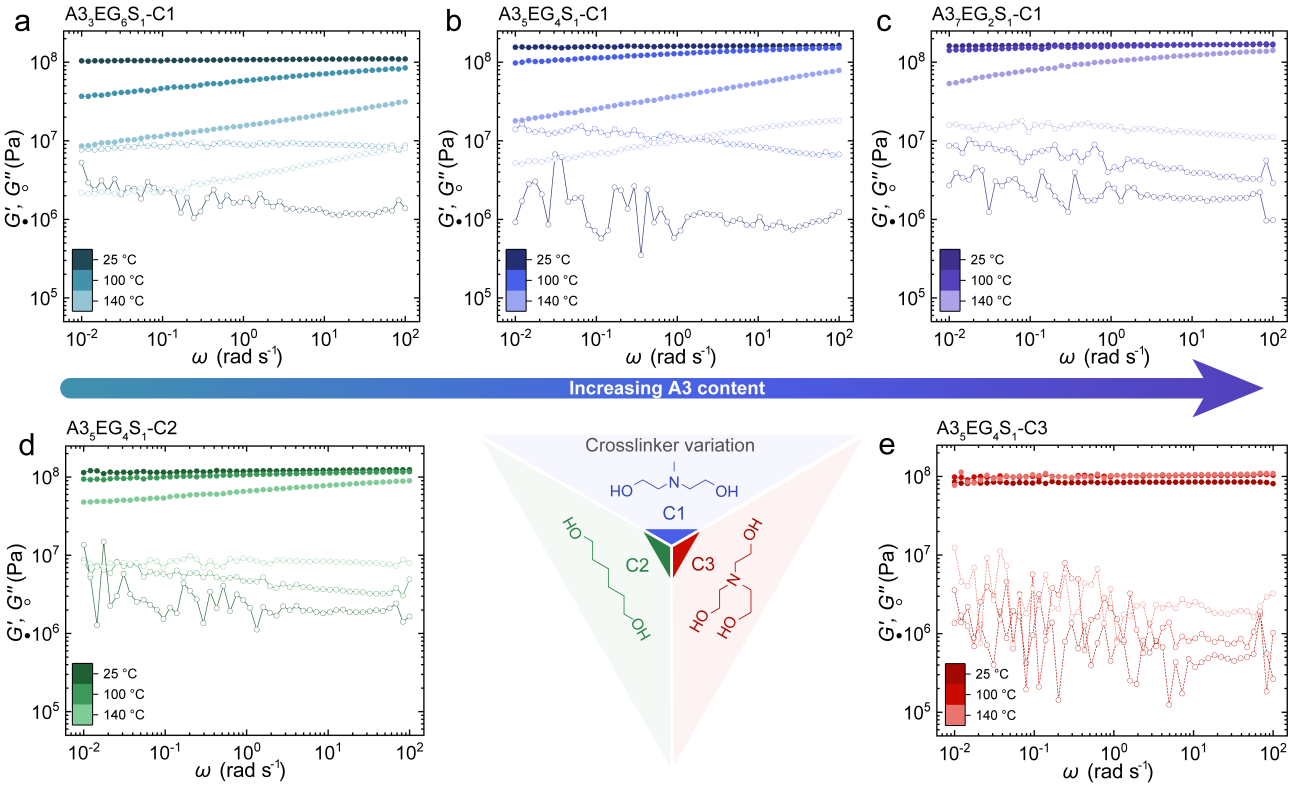

Figure 5. Frequency sweep spectra (obtained by small-amplitude oscillatory shear) taken at 25 °C, 100 °C, and 140 °C of (a) $A3_3EG_6S_1$-C1, (b) $A3_5EG_4S_1$-C1, (c) $A3_7EG_2S_1$-C1, (d) $A3_5EG_4S_1$-C2, and (e) $A3_5EG_4S_1$-C3.

At 25 °C the evolution of G' is independent of the frequency for all CANs due to their highly frozen bond dynamics and strong mechanical properties. However, at 100 °C and 140 °C, mild frequency-dependencies are observed for $A3_3EG_6S_1$-C1, $A3_5EG_4S_1$-C1, $A3_7EG_2S_1$-C1, and $A3_5EG_4S_1$-C2 with

a decrease of *G'* at smaller frequencies, indicating the occurrence of significant covalent bond exchange. The temperatures at which frequency-dependencies appear align well with the earlier observed transitions in the temperature sweeps (**Figure 3c**). The appearance of the temperature-dependent frequency dependency relates to two points: (i) lower degree of crosslinking ($A3_3EG_6S_1$-C1 < $A3_5EG_4S_1$-C1 < $A3_7EG_2S_1$-C1) leads to an earlier onset, and (ii) faster bond-exchange kinetics due to neighboring group participation of the tertiary amine is well visible comparing C1 and C2 (further shown below). $A3_5EG_4S_1$-C3 does not show significant frequency- or temperature-dependency despite the reactivity of the tertiary amine in C3, due to the high degree of connectivity and network immobilization afforded by the crosslink trivalency. Note that the general decrease of *G'* at higher temperatures, regardless of the frequency, can be indicative of thermally accessed bond dissociation.[20] CANs based on C1 and C2 both show signs of a drop in crosslink density when comparing between 25 °C and 140 °C, while C3 inhibits such network dissociation in this temperature range. This does not mean that no bond dissociation can occur for $A3_5EG_4S_1$-C3, but that the bond-equilibrium is such that network connectivity is maintained within this temperature range.[18,20]

To better understand mechanistic details of the temperature activated dynamization of the bonds, we subjected all CANs to stress relaxation experiments over a wide temperature range (**Figure 6a-e**). The C1-based CANs all display a relaxation response that involves two significant modes: stress relaxation at lower timeframes (ca. 50% relaxation or more for t < 10 s) and an additional decay at higher timeframes (ca. > 10 s). The latter decay exhibits a stronger temperature-dependence. Since our CANs are characterized by high crosslink density, numerous polar moieties, and multiple catalysts, we expect that that the first relaxation mode at lower timeframes corresponds to network contributions (*e.g.*, monomer friction, ionic interactions or hydrogen bonding), which has also been observed in other CAN systems, whereas the second relaxation mode corresponds to the covalent bond exchange.[54–56] Distinct differences are observed for the C2 and C3-based CANs (**Figure 6d,e**): For $A3_5EG_4S_1$-C2, the second relaxation mode is much slower and only a weak decay is observed for t > 3000 s, while the first relaxation mode appears similar to the C1-based CANs. This reflects how the networks are highly similar, but the covalent bond exchange is greatly suppressed when removing the tertiary amine for C2 compared to C1. For $A3_5EG_4S_1$-C3, the response is again different. The first relaxation mode is only observed above 180 °C, while the second relaxation mode is significant at longer timeframes (ca. t > 1000 s) like for the C1-based CANs. These results reflect how bond exchange is fast on account of the tertiary amine in C3, while the higher valency of the crosslinker impedes other forms of network relaxation. Thus, the C2 and C3-based CANs do a good job at emphasizing the two separate relaxation processes, which overlap significantly for the C1-based CANs. Furthermore, the C1 and C2-based CANs also display a strong temperature-dependence of their plateau modulus (G_0), whereby G_0 is lower at elevated temperatures. This observation indicates that these CANs undergo bond exchange via a dissociative mechanism: As the temperature increases, the equilibrium is pushed towards the entropically

favorable dissociation and thus the crosslink density decreases, which in turn lowers G_0 of the network.[20,57,58] When shifting focus to the C3-based CAN, such bond dissociation also occurs, but only significantly at ca. 190 °C. $A3_5EG_4S_1$-C3 shows a remarkable resilience up to 190 °C, due to the more connective crosslinking arresting network motion at lower temperatures even as some bonds dissociate.

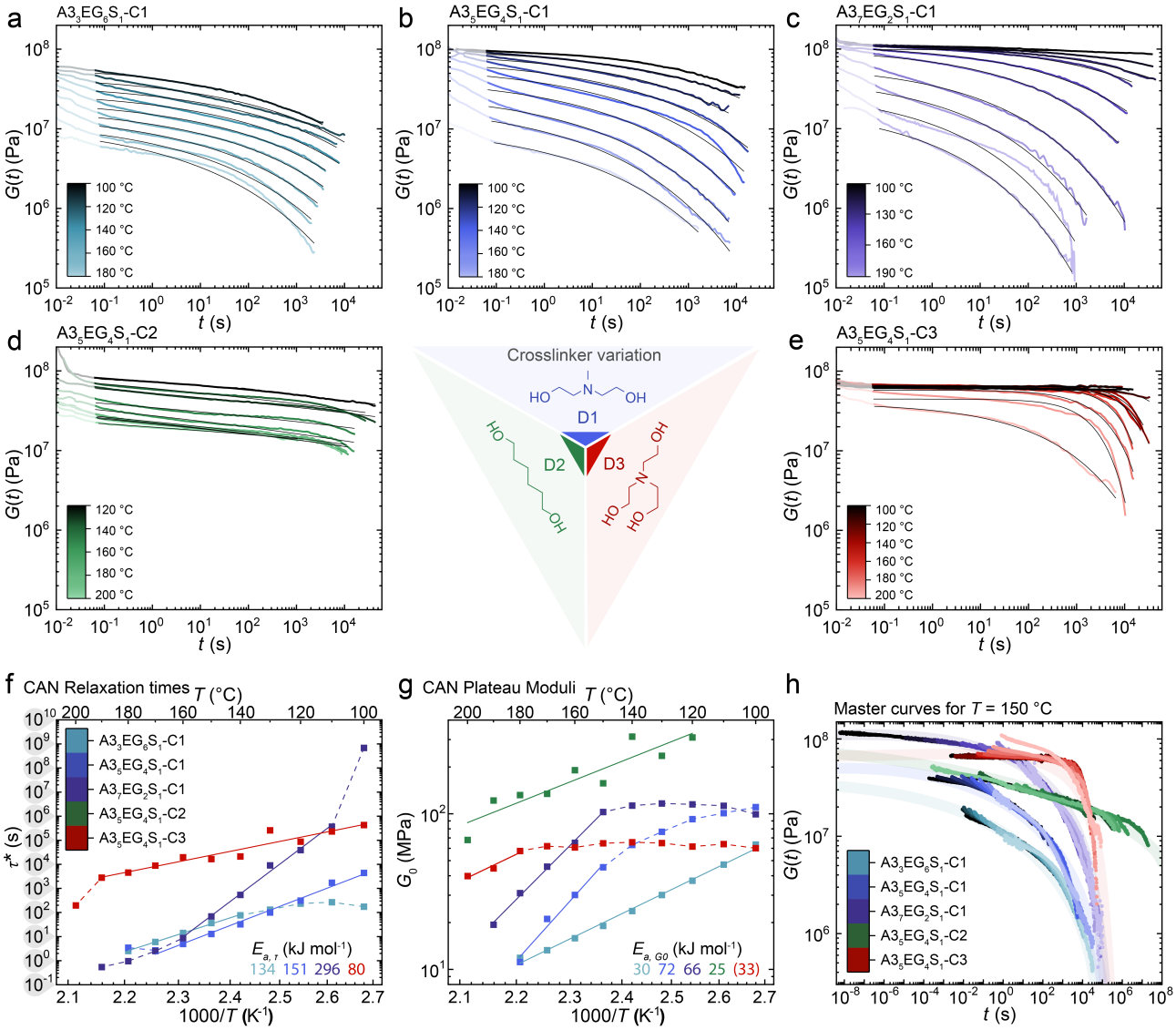

Figure 6. Stress Relaxation data obtained at a wide range of temperatures (colored lines) and corresponding stretched exponential fits (thin black lines) of (a) $A3_3EG_6S_1$-C1, (b) $A3_5EG_4S_1$-C1, (c) $A3_7EG_2S_1$-C1, (d) $A3_5EG_4S_1$-C2, and (e) $A3_5EG_4S_1$-C3. Measurement intervals before constant strain is reached (ca. 0.1 s) are indicated transparently. Based on the fitted data, Arrhenius plots of (f) τ^* and (g) G_0 were constructed as well as (h) time-temperature superposition master curves at a reference temperature of 150 °C.

None of these stress relaxation data can be described well by a simple exponential function. They are also not described well by a two-element Prony series on account of different temperature-dependencies of the relaxation modes (Figure S6).[50,55] Hence, to better quantify the data and allow for comparison, we fitted the stress relaxation data with stretched exponential decay functions.[50,55] All fits are presented together with the stress relaxation data (**Figure 6a-e** and Table S3-7).

$$G(t) = G_0 e^{-(t/\tau^*)^\beta} \quad (1)$$

therein, G_0 is the plateau modulus, τ^* is the characteristic relaxation time, and β is the stretching exponent. τ^* does not correspond to the intrinsic relaxation times of the individual relaxation modes, but instead provides a way to quantify a combined measure of relaxation modes. Thus, the stretched exponential function conveys information on all relaxation modes, combined into one decay function, which allows for comparison of the relaxation behavior of the different CANs.

Let us first consider in more detail the temperature dependence of G_0 for the C1-based CANs (**Figure 6g**). All of them show distinct temperature thresholds after which they enter a linear Arrhenius behavior, which is indicative of temperature-dependent bond dissociation. For $A3_3EG_6S_1$-C1, G_0 decreases from 100 °C, whereas $A3_5EG_4S_1$-C1 and $A3_7EG_2S_1$-C1 have largely constant G_0 up to threshold temperatures of 120 °C and 150 °C, respectively. Afterwards, their G_0s also decrease as a function of temperature. The activation energies corresponding to the changes in G_0 ($E_{a,G0}$) in the linear regime above the threshold temperature are bigger for $A3_5EG_4S_1$-C1 and $A3_7EG_2S_1$-C1 than for $A3_3EG_6S_1$-C1. This might be related to the different physical environment, that is highest EG content, and lowest degree of crosslinking. When shifting attention towards the different crosslinkers, $A3_5EG_4S_1$-C2 similarly displays bond dissociation across the entire temperature range, while $A3_5EG_4S_1$-C3 displays a constant G_0 up to 180 °C. This indicates that the trivalent C3 protects the network connectivity up to a certain point even as bond dissociation occurs, whereas the bivalent C1 and C2 are more sensitive to the softening effects of bond dissociation. The corresponding $E_{a,G0}$s for $A3_5EG_4S_1$-C2 and $A3_5EG_4S_1$-C3 are relatively low compared the C1-based CANs, reflecting how the C1-based CANs are more prone to thermally induced bond dissociation. These conclusions align well with the temperature responses seen before in temperature sweep (**Figure 3c**) and frequency sweep data (**Figure 5**).

The values of τ^* corresponding to each of the networks are summarized in **Figure 6f**, along with the derived kinetic activation energies ($E_{a,\tau}$). Note that $E_{a,G0}$ signifies activation energy for a change in G_0 (*i.e.*, bond dissociation), whereas $E_{a,\tau}$ corresponds to kinetic activation energy of the relaxation process (*i.e.*, network rearrangement).[20] Overall, stress relaxation for $A3_3EG_6S_1$-C1, $A3_5EG_4S_1$-C1, and $A3_7EG_2S_1$-C1 is fast with relaxations times $\tau^* < 100$ s above 150 °C and even showing significant relaxation at relatively low temperatures (*e.g.*, 120 °C). Relaxation for $A3_5EG_4S_1$-C3 is relatively slow up to 180 °C, above which it increases. τ^*s for $A3_5EG_4S_1$-C2 derived from the fits are unreliable as they only convey the first relaxation mode (Figure S7), while not corresponding to the slow covalent bond exchange. Based on direct comparison of the relaxation curves, it is clear how the second relaxation mode is much slower for $A3_5EG_4S_1$-C2 compared to the other networks (**Figure 6a-e**). As expected for CANs, $E_{a,\tau}$ increases as the crosslink density goes up (compare C1-based systems for

similar networks). Interestingly, τ^* only correlates inversely with crosslink density up to 130 °C, above which $A3_5EG_4S_1$-C1 and $A3_7EG_2S_1$-C1 gradually overtake $A3_3EG_6S_1$-C1 and display faster relaxation, which is uncommon behavior for CANs.[46,49,50,55] We speculate that with sufficient bond dissociation, untethered C1 can plasticize the network, depending on how much C1 is present, and offset the impact crosslink density might have. Furthermore, the CANs (with the exception of $A3_5EG_4S_1$-C2) display Arrhenius type temperature-dependence for τ^* throughout most of the probed temperatures, which is typically the temperature-dependence of covalent bond exchange.[13,15,31,46,55,59,60] However, $A3_3EG_6S_1$-C1 and $A3_7EG_2S_1$-C1 display deviation from their Arrhenius regions below 120 °C and above 160 °C, respectively. These deviations indicate alterations in the mechanism governing network dynamics or bond exchange, potentially signifying that a certain threshold of bond dissociation has been reached in this scenario.[50] $A3_5EG_4S_1$-C3 displays comparatively low $E_{a,\tau}$, even as temperature increases, and at ca. 190 °C shows a shift from the Arrhenius behavior towards stronger temperature-dependence of τ^*. This matches the temperature where G_0 drops due to bond dissociation, indicating that the shift from Arrhenius behavior of τ^* stems from changes in network topology. These results indicate how $A3_5EG_4S_1$-C3 possesses resistance against stress relaxation and flow below a temperature threshold on account of a rigid network topology, above which an onset of higher responsiveness is reached. Such behavior is highly sought after for CANs that require creep resistance at service temperatures, but need to possess good processability at elevated temperature.[61] In contrast, the C1-based CANs are highly temperature-responsive across a wide temperature range and can thus access significant processability at relatively low temperatures while possessing high network connectivity. C2 yields a CAN with much slower stress relaxation on account of lacking a tertiary amine that catalyzes transesterification, which can be utilized in applications where only moderate processability is required in return for superior strength and stiffness.

Finally, to compare the thermodynamic behaviors across a wide temperature range for these CANs, each with different viscoelastic properties, we further used time-temperature superpositions (TTS) to construct master curves with 150 °C as a reference temperature (**Figure 6h**), based on the definition:

$$G^*(t, T_{\mathrm{ref}}) = (1/b_T)G(t/a_T, T) \quad (2)$$

Therein, b_T shift factors ($b_T = G_0(T)/G_0(T_{\mathrm{ref}})$) describe the temperature-dependence of G_0 and a_T shift factors ($a_T = \tau^*(T)/\tau^*(T_{\mathrm{ref}})$) describe variations in τ^* (Figure S8).[20] We constructed master curves for all CANs using TTS (**Figure 6h**). Based on the two distinct relaxation modes with different temperature-dependencies and bond dissociation in the system, the TTSs do not accurately cover the entire temperature range.[55,62] For C1 and C3-based CANs, deviations can be seen at shorter relaxation times where the single-exponential fit fails to accurately describe the first relaxation mode

In contrast, TTS fits the first relaxation mode well for $A3_5EG_4S_1$-C2, however it underestimates the second mode. Despite these limitations, the TTS curves visualize the different relaxation behaviors of our CANs over many orders of magnitude of *t*: for C1-based CANs, increasing crosslink density increases both G_0 and τ^*. Secondly, the vastly different profiles relating to C1, C2, and C3 reflect the difference in temperature-dependence, where $A3_5EG_4S_1$-C3 is more resilient at lower temperature, while at higher temperatures both $A3_5EG_4S_1$-C1 and $A3_5EG_4S_1$-C3 show much more rapid relaxation compared to $A3_5EG_4S_1$-C2.

2.3.5 Recycling

To understand to what extent the different relaxation behaviors impact the ability for reprocessing, we used compression molding of mechanically obtained powders of cured networks (70 h, 130 °C) to reform smooth samples (**Figure 7a**). Except for $A3_5EG_4S_1$-C2, efficient and complete reshaping is possible at moderate temperature (130 °C) and in short timeframes (15 - 45 min), which is in accordance with the fast stress relaxation observed in prior experiments (**Figure 6a-e**). $A3_5EG_4S_1$-C3 requires longer times for preparing a coherent film as compared to the C1-based CANs. For $A3_5EG_4S_1$-C2, reprocessing was only partly possible as demonstrated by the higher temperature (180 °C) needed and the poor quality of the resulting film. Using higher temperatures is unwise as they might cause significant network degradation, so much larger timeframes would be required to effectively reform the CAN.

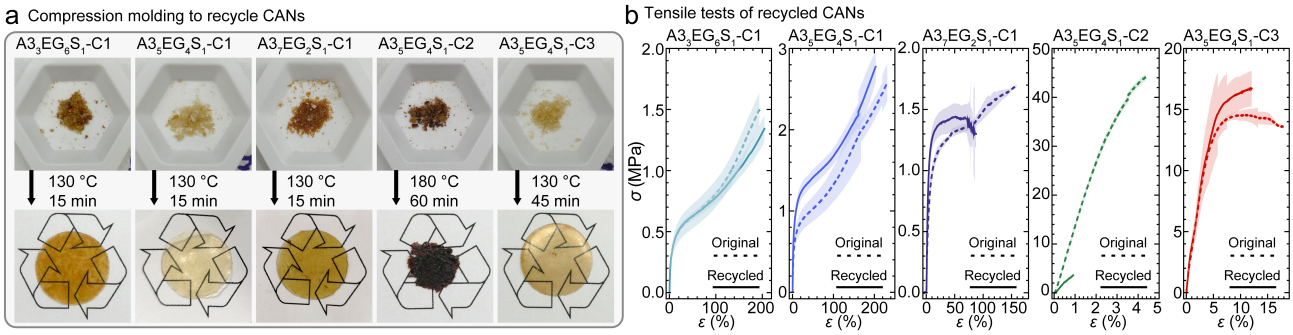

Figure 7. (a) Recycling cured CANs by compression molding at ~ 8 MPa and 130 °C for $A3_3EG_6S_1$-C1, $A3_5EG_4S_1$-C1, $A3_7EG_2S_1$-C1, and $A3_5EG_4S_1$-C3 and 180 °C for $A3_5EG_4S_1$-C2. (b) Tensile tests of recycled CANs compared to original CANs.

We performed tensile tests of the recycled CANs to gauge the network integrity after the compression molding process (**Figure 7b**, Table S8). Except for $A3_5EG_4S_1$-C2, the CANs display similar tensile properties after being recycled when compared to the original cured CANs, indicating that the recycling process does not adversely affect the networks. Small increases in *E* and σ_b and decreases in ε_b can be attributed to minimal additional curing of the networks upon exposure to the heating in the compression molding process. For $A3_5EG_4S_1$-C2, the recycling procedure yields a material with

poor mechanical properties compared to the original, in line with what was noted above, while still displaying relatively high *E* and σ_b of 488 MPa and 3.7 MPa respectively.

2.3.6 Waterborne Nanocomposites

Finally, as a demonstration of the unique applicability of these waterborne CANs, we prepared bioinspired nanocomposites (NCs) by mixing aqueous dispersions of sodium fluorohectorite (NHT) nanoclay platelets (0.5 wt%; average diameter ca. 750 nm, thickness ca. 1 nm)[63] with aqueous solutions of pre-CAN and crosslinker (stochiometric ratio of carboxylic acid to alcohol of 1:0.95; combined 0.5 wt%) to obtain dispersions containing polymer-coated nanoparticles (**Figure 8a**).[28,64,65] Subsequently, the mixtures were cast into films. During evaporation, the high aspect ratio CAN-coated nanoclays self-assemble into lamellar nacre-mimetic NC films with 50 wt% of nanoclay separated by nm-scale layers of the CAN (**Figure 8c**). Finally, a curing step (70 h, 130 °C) to crosslink the CAN phase yields the final NCs that are macroscopically homogeneous and transparent (**Figure 8b**).

Next, we discuss the tensile properties of uncured and cured NCs based on all CANs at 50 wt% and conditioned at 50% RH (**Figure 8f**, Table S9). A significant stiffening and strengthening occurs for all films upon curing. Before curing, the softest and most ductile NCs are formed by the C1-based CANs with the highest content of C1 ($A3_5EG_4S_1$-C1/NHT and $A3_7EG_2S_1$-C1/NHT). All cured NCs display similar behavior, whereby the stress-strain curve is fully linearly elastic and σ_b ranges between 100-120 MPa with very high *E* values of ca. 23 GPa. Considering this, the CAN capable of introducing significant dynamic properties to the NC is the ideal candidate for further experiments. We chose $A3_5EG_4S_1$-C1 based on the strong dynamic character. To investigate whether the thermal dynamization associated with CANs are accessible in these NCs, we subjected $A3_5EG_4S_1$-C1/NHT(1/1 w/w) to small-amplitude dynamic mechanical analysis and shape-locking experiments (**Figure 8d,g**). The temperature sweep reveals a thermoresponsive material that displays changes in *G'* and *G"* of almost an order of magnitude over a temperature range of ca. 200 °C. While *G'* remains an order of magnitude higher than *G"*, the decline in *G'* and the increase in *G"* are characteristic of a softening response of the highly reinforced material. Using these thermoresponsive properties, the cured NC was reshaped into a spiral by reconfiguring the CAN network topology as stress dissipates under strain.

After, we investigated whether the surfaces of CAN-based NCs have adhesive properties by performing tensile single lap shear tests of $A3_5EG_4S_1$-C1/NHT with different CAN weight percentages (30 wt% and 50 wt%) (**Figure 8e,h**). The welding was done by hot pressing (ca. 29 MPa) two pre-cut parts of cured NC film with a 5 mm overlap and with no added chemicals for 20 h at 120 °C. The welded samples are compared to their pristine counterparts as controls. NCs with 30 wt% CAN, can

be welded to regain almost identical stiffness and behave in a similar manner to pristine samples up to a certain force. However, the ultimate strength is lower as the sample fails at the adhesion junction at ca. 50% of the force of a pristine sample. In contrast, the NCs with 50 wt% CAN display higher toughness by dissipating energy in the lap-shear test through a 'slipping'-type failure instead of fracture at the junction, with an entirely different force-displacement curve compared to the pristine counterpart. The difference might be indicative of more pronounced CAN-CAN interaction at the welding interface for the latter rather than CAN-nanoparticle interaction. Both cases demonstrate the impressive ability of the CAN phase to create strong adhesion without addition of external compounds.

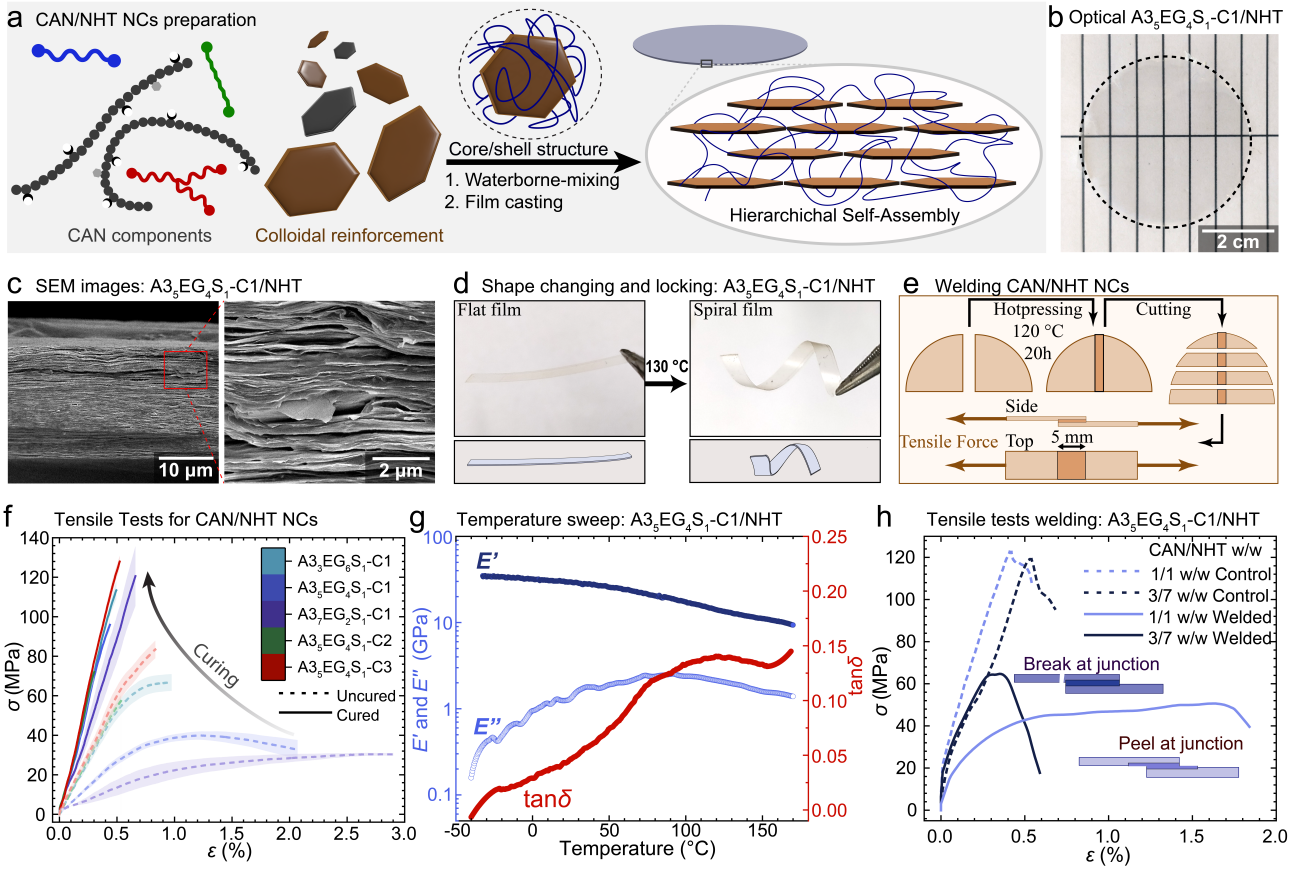

Figure 8. Bioinspired NCs by combination of waterborne CANs and NHT nanosheets. (a) Schematic overview of NC preparation via evaporative self-assembly to form hierarchical architecture. (b) Photograph of A3$_5$EG$_4$S$_1$-C1/NHT(50/50 w/w). (c) Cross section SEM micrograph of A3$_5$EG$_4$S$_1$-C1/NHT(1/1 w/w) NC displaying a homogeneous layered structure at two different degrees of magnification. (d) Shape changing and locking at 130 °C for A3$_5$EG$_4$S$_1$-C1/NHT(1/1 w/w) NC. (e, h) Stress-strain curves for single lap shear tests of A3$_5$EG$_4$S$_1$-C1/NHT(1/1 w/w) and A3$_5$EG$_4$S$_1$-C1/NHT(3/7 w/w) NCs adhered together via hot pressing. Tensile data for control samples are also displayed. (f) Tensile tests for CAN-based NCs with 1/1 w/w, both uncured and cured (70h, 130 °C). (g) Temperature sweep spectra (obtained by small-amplitude oscillatory shear) of cured A3$_5$EG$_4$S$_1$-C1/NHT(1/1 w/w) NC.

2.4 Conclusion

In conclusion, we demonstrated a new waterborne dissociative CAN system whereby an aspartic acid-derivative is incorporated in pre-CAN copolymers to facilitate internal catalysis. The fraction of this component can be varied to direct the crosslink density of the networks, yielding corresponding effects on the (dynamic) mechanical properties. Subsequently, these pre-CANs were combined with a variety of crosslinkers that impart unique properties to their respective CAN material, demonstrating the excellent tunability of the system. Diols involving a tertiary amine facilitate the largest degrees of bond exchange and thus stress relaxation, while enabling ductile mechanical behavior in ambient conditions. When using an amine-containing triol instead, a higher degree of nonelastic deformation resistance, linked to *e.g.* creep, is afforded by slowing stress relaxation up until high temperatures. Alternatively, CANs incorporating aliphatic diols trade off fast bond exchange kinetics with the capability to function as a glassy material with high stiffness and strength in ambient conditions. This platform further demonstrates its adaptability via combination with aqueous dispersions of clay nanosheets to prepare high-performance bioinspired nanocomposites, thereby imparting dynamic reprocessability, which is in high demand for future high-performance composite materials.

Our work on bringing highly crosslinked, fast-exchange CANs based on internal catalysis into the aqueous domain creates a wide array of possibilities for water-based applications. In addition, we demonstrated an effective strategy for preparing a whole library of CANs based on a single principal copolymer and via easy aqueous preparation by simply varying the crosslinker used. This enables vast tunability based on an extensive amount of commercial small molecule crosslinkers, which is potentially even expanded by combining two different crosslinkers to reach the property space in-between or by incorporating other components in conjunction, such as antibacterial, flame-retardant or pigment moieties.[15]

Supporting Information

Supporting information: Additional experimental details and methods, materials, and supplementary experimental data.

Acknowledgements

This project has received funding from the European Union's horizon research and innovation programme under the Marie Skłodowska-Curie Grant agreement no. 860911. AW acknowledges funding via a Gutenberg Research Professorship underpinning his Life-Like Materials Program.

Conflict of Interest

The authors declare no conflict of interest.

Data Availability Statement

The data that support the findings of this study are available from the corresponding author upon reasonable request.

Keywords

covalent adaptable networks, waterborne polymers, bioinspired nanocomposites, internal catalysis, vitrimers.

2.5 Supporting Information

Tunable Waterborne Aspartic Acid-Based Covalent Adaptable Networks with Internal Catalysis and Incorporation in Bioinspired Nanocomposites

*Sjoerd Engels[1], Andreas Walther[1]**

[1]Life-Like Materials and Systems, Department of Chemistry, University of Mainz, Duesbergweg 10-14, 55128 Mainz, Germany.

2.5.1 Instrumentation

2.5.1.1 Tensile Tests for CANs

Tensile tests for the CAN samples were performed at room temperature on a Shimadzu EZ-LX Long-Stroke Model tensile tester equipped with a 50 N load cell. Each of the CANs were prepared as rectangular samples (15 mm x 4 mm) with a thickness of around 200 µm. At least three measurements were performed for each material both at 50% relative humidity and 20% relative humidity respectively, with strain rates of 50 mm/min for more ductile samples ($A3_3EG_6S_1$-C1, $A3_5EG_4S_1$-C1, $A3_7EG_2S_1$-C1) and 5 mm/min for the less ductile samples ($A3_5EG_4S_1$-C2, $A3_5EG_4S_1$-C3) to ensure similar proportional strain rates. Subsequently, the mean was taken for each set. The Young's modulus (*E*) was determined from the slope of the linear region in the stress/strain curves.

2.5.1.2 Tensile Tests for Bioinspired Nanocomposites

Tensile tests for the bioinspired nanocomposite samples were performed at room temperature on a DEBEN minitester equipped with a 20 N load cell. Each of the CAN nanocomposites were prepared as rectangular samples (10 mm x 2 mm) with a thickness of around 20 µm. Six to eight measurements were performed for each material at 50% relative humidity, with a strain rate of 0.5 mm min^{-1}, then the mean was taken for each set. The Young's modulus (*E*) was determined from the slope of the linear region in the stress/strain curves. Tensile single lap shear tests were performed using the same parameters, with an adhesive area of 5 mm x 2 mm.

2.5.1.3 Nuclear Magnetic Resonance (NMR)

NMR spectra were recorded on a Bruker Avance II spectrometer operating at 400 MHz.

2.5.1.4 Dynamic Mechanical Analysis (DMA)

DMA measurements were performed on flat compression-molded disks (8 mm diameter, ca. 0.5 mm thickness) using a MCR702 MultiDrive from Anton Paar equipped with 8 mm parallel plate geometries and an oven attachment. For each measurement, a normal force of 0.4 N was used unless specified otherwise. For the **curing experiments**, small-amplitude oscillatory sweeps were performed at 0.5 Hz, 0.1% strain, and 130 °C. **The temperature sweeps** were performed from 25 to 200 °C at a rate of 2.4 °C min^{-1}, 0.1% strain using a frequency of 1 Hz. **Amplitude tests** were performed at 1 Hz and temperatures of 25 °C and 100 °C to determine the linear elastic regime for each CAN. **Frequency sweep tests** were performed at temperatures of 25 °C, 100 °C, and 140 °C at 0.1% strain over a frequency range of 0.01-100 Hz. **Stress relaxation tests** were performed at temperatures ranging from 100 °C to 200 °C at 0.1% strain.

2.5.1.5 Gel Permeation Chromatography (GPC)

GPC with dimethylacetamide (DMAc) with 5 g L^{-1} LiBr as eluent was performed using an Agilent 1260 Infinity II system. For separation, a GRAM high speed linear column system (molar mass range:

500–1000 kDa) was used. With a flow rate of 1 mL min^{-1} at 50 °C. The traces were calibrated with narrowly distributed poly(methyl methacrylate). Average relative molecular weights and dispersities of the polymers obtained by free radical polymerization were determined by GPC with a sample concentration between 0.5 and 1.5 mg mL^{-1}. Polymers containing carboxylate groups were methylated prior to measurement by dissolving in 3/1 v/v toluene/MeOH and adding an excess of (trimethylsilyl)diazomethane.

2.5.1.6 Fourier Transform Infrared Spectroscopy (FTIR).

FTIR spectra were acquired using a Jasco FT/IR-4100 spectrometer with a frequency range from 4000 to 600 cm^{-1}.

2.5.1.7 Scanning Electron Microscopy (SEM)

The fracture surface of a $A3_5$-EG_4-S_1-C1/NHT(50 wt%) nanocomposite was imaged using a FEI Nova NanoSEM equipped with a field emission emitter (5 kV) after sputter-coating an ultrathin Au layer (ca. 20 nm).

2.5.1.8 Compression Molding

Compression molding was performed on a Collin P 200 E press.

2.5.2 Materials

2-(2-(2-Methoxyethoxy)ethoxy)ethan-1-amine) and acryloyl chloride (= 96%; phenothiazine stabilized) were purchased from ABCR. L-Aspartic acid (≥ 98%) and hexanediol (= 97%) were purchased from Alfa Aesar. 2-Acrylamido-2-methylpropane sulfonic acid (S) (≥ 98%) was purchased from Fluka. Glacial acetic acid was purchased from VWR chemicals. Azobisisobutyronitrile (AIBN) (= 98%) was purchased from Acros Organics. Dichloromethane (≥ 99.8%), Dimethylsulfoxide (DMSO) (= 99.9%), Sodium hydrogen carbonate (≥ 99.7%), Sodium hydroxide (analytical grade), Ethyl Acetate (≥ 99.5%), and Toluene (≥ 99.8%) were purchased from Fisher Chemical. Dimethylformamide (DMF) (≥ 99%), Methanol (≥ 99.9%), N-methyl diethanolamine (≥ 99%), Triethanolamine (≥ 99.0%), and Triethylamine (TEA) (≥ 99.5%) were purchased from Sigma Aldrich (Merck). (Trimethylsilyl)diazomethane (1.8 - 2.4M in Hexane) was purchased from Thermo Fisher. Dialysis membranes (ZelluTrans, MWCO 3500) were purchased from Carl Roth. Sodium fluorohectorite (NHT) nanoclay was purchased from Kunimine Industries Co. Ltd. as dispersion and cleaned according to previous reports.[63]

2.5.3 Synthesis Procedures

2.5.3.1 Synthesis of N-(2-(2-(2-methoxyethoxy)ethoxy)ethyl)acrylamide (EG)

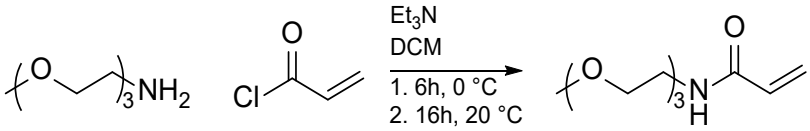

2-(2-(2-methoxyethoxy)ethoxy)ethan-1-amine (6.462 g, 0.03959 mol, 1 eq.) and triethylamine (7.17 mL, 0.0515 mol, 1.3 eq.) were dissolved in dichloromethane (50 mL). The solution was then cooled to 0 °C and bubbled through with nitrogen gas for 30 min. Subsequently, a solution of acryloyl chloride (4.18 mL, 0.0515 mol, 1.3 eq.) in dichloromethane (50 mL) was added dropwise over a period of 30 min while stirring at 0 °C under nitrogen atmosphere. After stirring for 6 h at 0 °C and then for another 16 h at room temperature, the mixture was filtrated and the organic phase was washed with an aqueous sodium bicarbonate solution (0.1 N, 3 x 30 mL). The aqueous phase was subsequently extracted with dichloromethane (3 x 30 mL) and the organic phases were combined and evaporated *in vacuo* to yield the product as a light-yellow oil (4.900 g, 0.02257 mol, 57%).
^{1}H NMR (400 MHz, $CDCl_3$ D_2O, 25 °C): δ = 6.34 (s, 1H; NH), 6.28 (dd, $^3J_{trans}$ = 17.0; ^2J = 1.6 Hz, 1H; Hβ), 6.12 (dd, $^3J_{trans}$ = 17.0; $^3J_{cis}$ = 10.2 Hz, 1H; Hα), 5.61 (dd, $^3J_{cis}$ = 10.2; ^2J = 1.6 Hz, 1H; Hβ), 3.66-3.50 (m, 12H; CH_2), 3.37 (s, 3H; CH_3).

2.5.3.2 Synthesis of acryloyl-L-aspartic acid (A3)

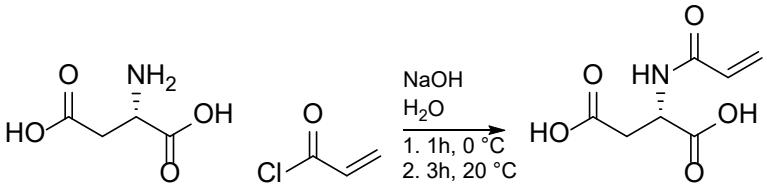

L-Aspartic acid-(S)-(+) (8.2058g, 0.061651mol, 1 eq.) and sodium hydroxide (8.63 g, 0.218 mol, 3.5 eq.) were dissolved in distilled water (100 mL). The solution was then cooled to 0 °C and acryloyl chloride (6.138 g, 0.06782 mol, 1.1 eq.) was added in dropwise fashion over a period of 30 min while stirring. Subsequently, the mixture was stirred for 1 h at 0 °C and for 3 h more at room temperature. Then, the mixture was adjusted to pH = 2 using hydrochloric acid. The aqueous phase was extracted with ethyl acetate (5 x 300 mL). The organic phase was subsequently dried over magnesium sulfate and concentrated *in vacuo*. The concentrate was then left to crystallize in the fridge over the weekend. Finally, the mixture was filtered and the residue was air dried to yield white crystals (6.803 g, 0.03637 mol, 59%).
^{1}H NMR (400 MHz, D_2O, 25 °C): δ = 6.31 (dd, $^3J_{trans}$ = 17.1; $^3J_{cis}$ = 9.8 Hz, 1H; Hα), 6.23 (dd, $^3J_{trans}$ = 17.1; ^2J = 1.8 Hz, 1H; Hβ), 5.80 (dd, $^3J_{cis}$ = 9.8; ^2J = 1.8 Hz, 1H; Hβ), 4.83 (t, ^3J = 6.0 Hz, 1H; CH), 3.03 - 2.92 (m, 2H; CH_2).

2.5.3.3 Synthesis of pre-CAN Copolymers: $A3_3EG_6S_1$, $A3_5EG_4S_1$ and $A3_7EG_2S_1$

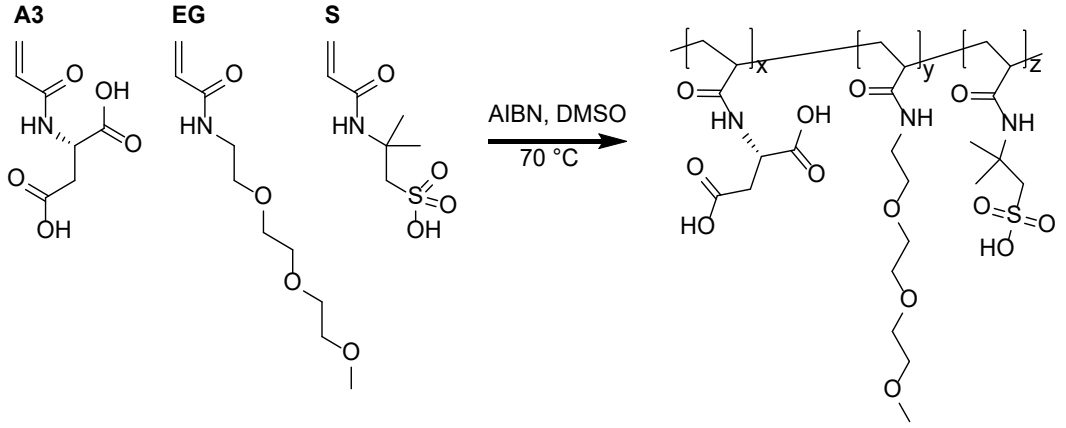

Three copolymers were prepared via free radical polymerization based on molar ratios for monomers A3/EG/S of 0.3/0.6/0.1, 0.5/0.4/0.1 and 0.7/0.2/0.1 respectively. The monomers and initiator azobisisobutyronitrile (AIBN) were used in a ratio of 400:1 for all copolymers. As a general procedure, the monomers (20 wt%) and catalyst were dissolved in dimethyl sulfoxide (DMSO) and subsequently dimethyl formamide was added (2 wt%) as an internal standard. The mixture was then degassed using nitrogen gas with the freeze-pump-thaw method (four cycles). The reaction flask was then heated to 75 °C under constant stirring, while reaction progress was followed via ^{1}H-NMR. When roughly 90% monomer conversion was observed (ca. 2 days), the reaction was terminated, and the reaction mixture was dialyzed (3.5k cellulose membrane) against water for 5 days, with the water being refreshed daily. Finally, the resulting solution was freeze-dried to obtain the solid light-yellow copolymer (52.0%/43.1%/64.1% yield for $A3_3EG_6S_1$/$A3_5EG_4S_1$/$A3_7EG_2S_1$ respectively).

2.5.4 Covalent Adaptable Network (CAN) Preparation

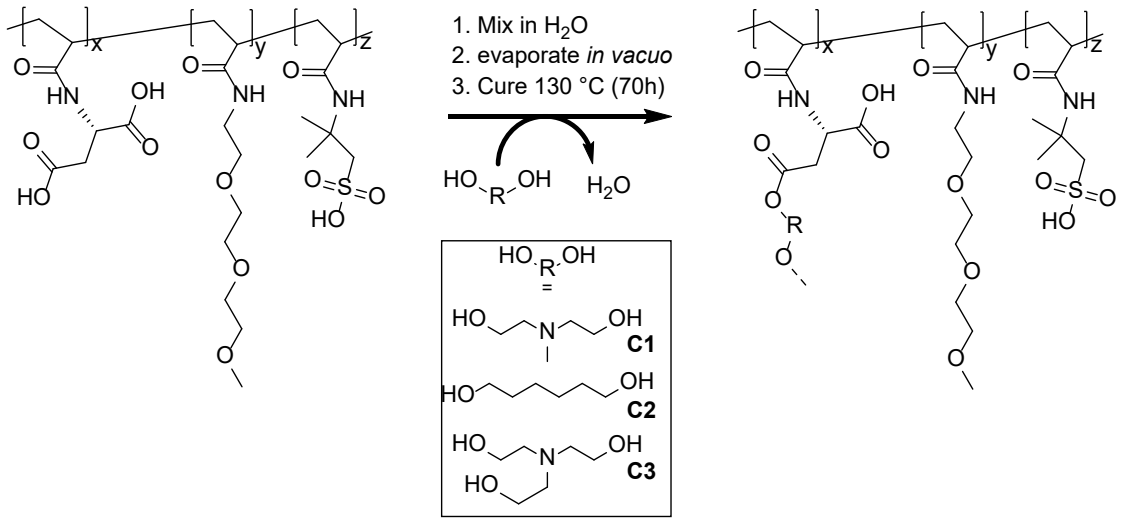

The pre-CAN copolymer was dissolved in H_2O and subsequently the crosslinker (C1, C2, or C3) was added, whereby the crosslinker amount was chosen in a molar ratio of crosslinker alcohol group to A3 carboxylic acid group of 0.95:1.00. The mixture was then stirred for a few minutes and

subsequently evaporated *in vacuo*. The resulting crude product was cured at 130 °C for ~ 48 - 70 h to yield the CAN network. The material can be reshaped via compression molding (conditions dependent on network) to yield smooth flat films for further analysis.

2.5.5 Bioinspired Nanocomposite Preparation

2.5.5.1 Preparation of CAN-NHT Bioinspired Nanocomposites

An aqueous solution was prepared of the pre-CAN and crosslinker (with composition corresponding to one of the CANs: $A3_3EG_6S_1$-C1, $A3_5EG_4S_1$-C1, $A3_7EG_2S_1$-C1, $A3_5EG_4S_1$-C2 or $A3_5EG_4S_1$-C3) so that the combined components represent 0.5 wt% of the solution. Subsequently, an NHT nanoclay dispersion (0.5 wt%) was added in dropwise fashion to the pre-CAN solution while stirring vigorously to ensure a homogeneous combination of both components. Depending on the volume added for either, the weight fractions of the CANs can be controlled. Next, the mixture is mixed for 16 h and then cast in a Petri dish to evaporate the water in ambient conditions. This results in transparent and homogeneous nanocomposite films with a thickness of around 10 - 25 µm.

2.5.5.2 Preparation of Welded Nanocomposite Samples

The welded samples of $A3_5EG_4S_1$-C1/NHT(50 wt%) nanocomposites were obtained by overlapping two cured films, with a parallel overlapped region with 5 mm width. The two films were welded by hot-pressing at 5 bar for 20 h at 120 °C.

2.5.6 Swelling Tests

The insoluble fractions were determined by swelling the fully cured CAN networks (ca. 50 - 100 mg) in both water and in dimethyl formamide (10 mL) for each of the five different CANs ($A3_3$-EG_6-S_1-C1, $A3_5$-EG_4-S_1-C1, $A3_7$-EG_2-S_1-C1, $A3_5$-EG_4-S_1-C2, $A3_5$-EG_4-S_1-C3) for 48 h. Then, the insoluble fractions were weighed after the liquid phases were removed and the samples were dried by vacuum.

2.5.7 Water Content Determination

Flat films of the fully cured CAN networks (ca. 50 - 100 mg) were conditioned at 50% relative humidity for 48 h and subsequently weighed. Next, the films were heated to 120 °C under vacuum for 24 h and subsequently weighed again to determine their dry weight.

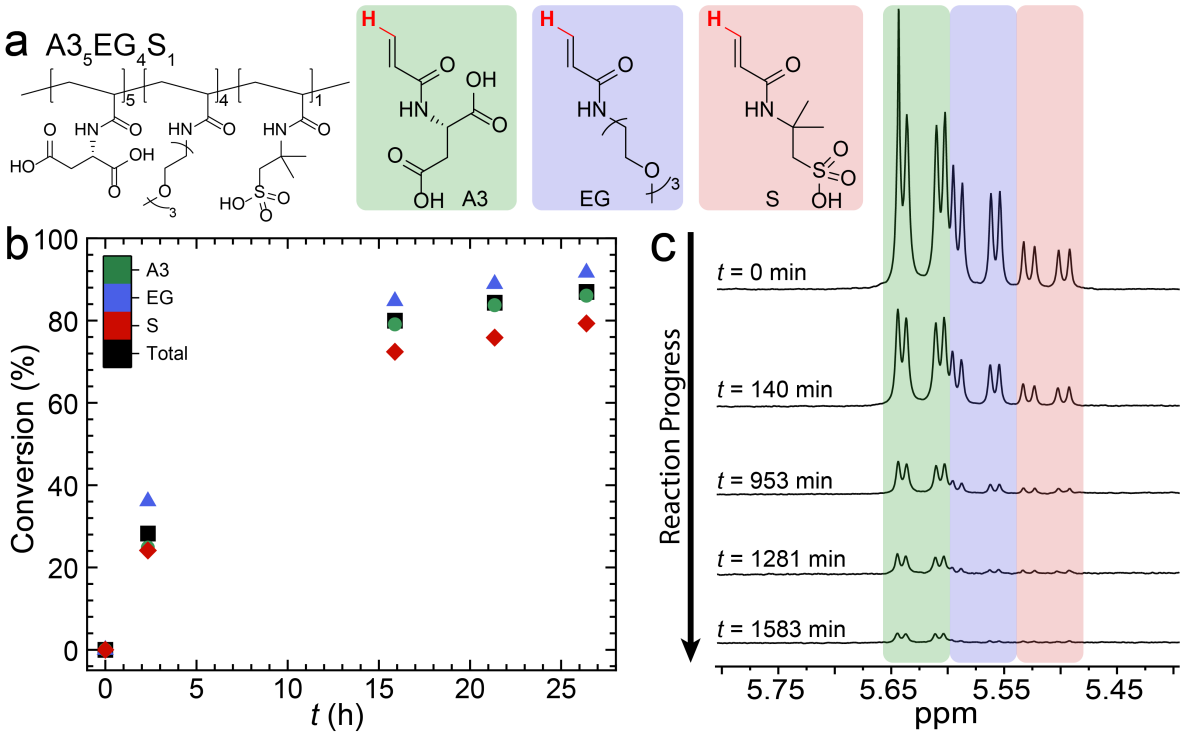

Figure S1. pre-CAN $A3_5EG_4S_1$ copolymer kinetic analysis via ^{1}H-NMR (400 MHz, D_2O, 25 °C, TMS). (a) Chemical structures of the copolymer and feed monomers. (b) Conversion of monomers over time, determined via integration of respective peaks. (c) ^{1}H-NMR of vinylogous protons in the polymerization mixture at different times after the start of the polymerization reaction. The protons of the monomers corresponding to each of the ^{1}H-NMR signals are highlighted.

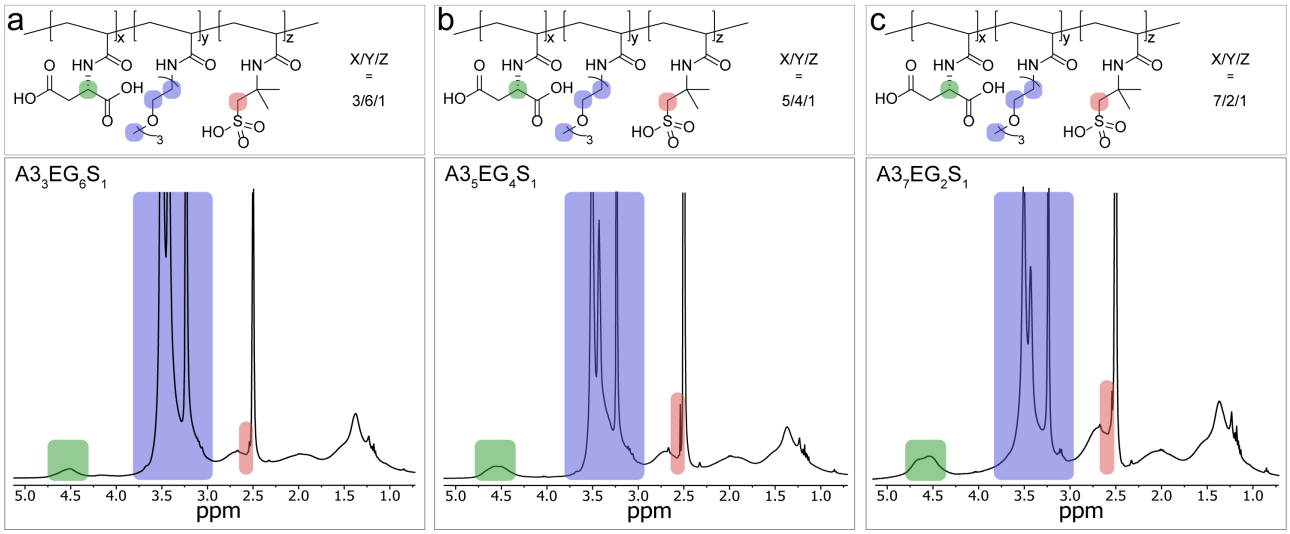

Figure S2. pre-CAN copolymer analysis via ^{1}H-NMR (400 MHz, D_2O, 25 °C, TMS). ^{1}H-NMR spectra with corresponding structures of (a) pre-CAN $A3_3EG_6S_1$, (b) pre-CAN $A3_5EG_4S_1$, (c) pre-CAN $A3_7EG_2S_1$. The protons corresponding to the NMR signals are highlighted for each monomer.

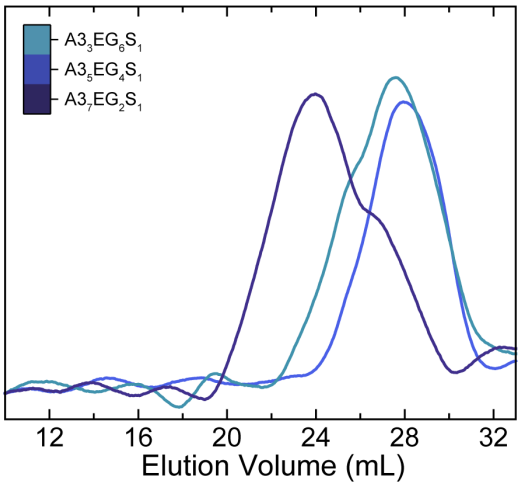

Figure S3. Normalized GPC plots of pre-CAN copolymers.

Table S1. Overview of the components of the CAN networks.

Pre-CAN[a)]	Crosslinker[a)]	Sample name
A3$_3$EG$_6$S$_1$	C1	A3$_3$EG$_6$S$_1$-C1
A3$_5$EG$_4$S$_1$	C1	A3$_5$EG$_4$S$_1$-C1
A3$_5$EG$_4$S$_1$	C2	A3$_5$EG$_4$S$_1$-C2
A3$_5$EG$_4$S$_1$	C3	A3$_5$EG$_4$S$_1$-C3
A3$_7$EG$_2$S$_1$	C1	A3$_7$EG$_2$S$_1$-C1

[a)] Added with molar ratio [crosslinker-alcohol]:[A3-carboxylic acid] of 0.95:1.

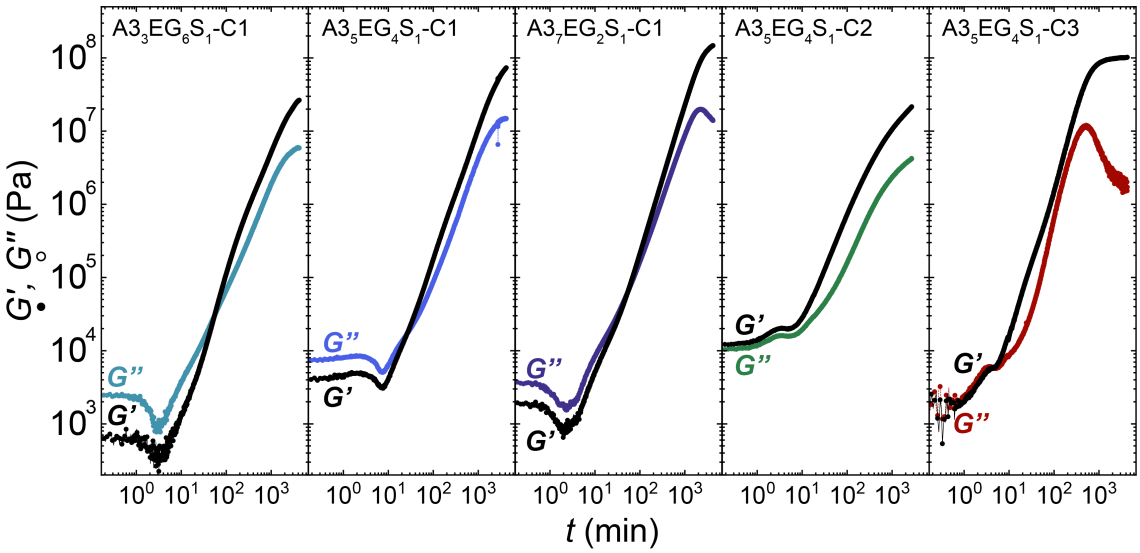

Figure S4. Curing kinetics via small-amplitude oscillatory sweeps of A3$_3$EG$_6$S$_1$-C1, A3$_5$EG$_4$S$_1$-C1, A3$_7$EG$_2$S$_1$-C1, A3$_5$EG$_4$S$_1$-C2, and A3$_5$EG$_4$S$_1$-C3 taken at 130 °C with *G'* (black) and *G"* (colored) indicated.

Table S2. Solubility and water content.

Sample[a)]	Insoluble Fraction H_2O (48 h)	Insoluble Fraction DMF (48 h)	Water content (50% RH)
$A3_3EG_6S_1$-C1	85%	84%	11%
$A3_5EG_4S_1$-C1	94%	90%	14%
$A3_7EG_2S_1$-C1	89%	100%	15%
$A3_5EG_4S_1$-C2	93%	97%	8.6%
$A3_5EG_4S_1$-C3	95%	95%	13%

[a)] Cured for 72 h at 130 °C

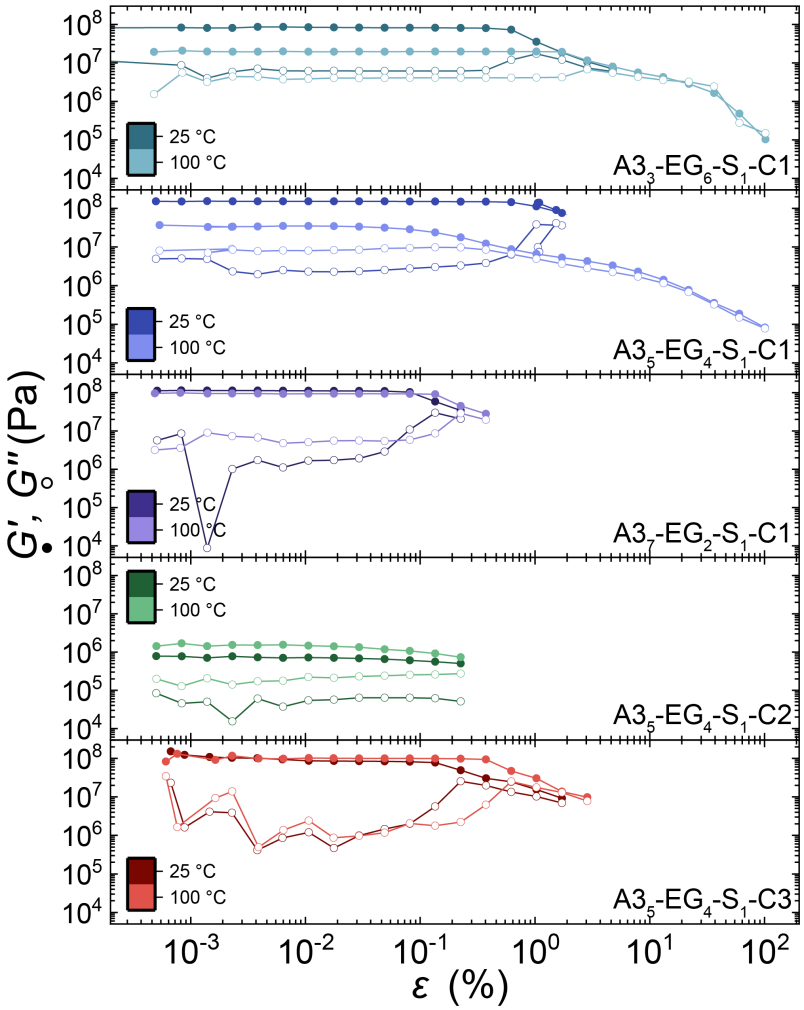

Figure S5. Amplitude sweep spectra obtained by oscillatory shear DMA at 25 °C and 100 °C of $A3_3EG_6S_1$-C1, $A3_5EG_4S_1$-C1, $A3_7EG_2S_1$-C1, $A3_5EG_4S_1$-C2, and $A3_5EG_4S_1$-C3. The linear elastic regimes are indicated as the ε range where values for *G'* and *G"* are constant.

2.5.8 Fitting Stress Relaxation Data

It has been demonstrated recently how stress relaxation data that display more than one relaxation process can be fitted using multiple element Prony series, whereby the individual contributing pathways can be deconvoluted in the case of dual covalent bond exchange.[58] In contrast however, in another study it has been shown how this does not always lead to more meaningful interpretation of the experimental data, with shift factor sets that are difficult to correlate to the material system, especially if the relaxation modes overlap significantly in time.[50,55] To demonstrate this, we fitted the stress relaxation of $A3_5EG_4S_1$-C1 at 150 °C via a variety of methods: single element exponential decay, single-element stretched exponential decay, 2-element Maxwell exponential decay and, 3-element Maxwell exponential decay (figure S6). The resulting comparison demonstrates how the single-element stretched exponential can fit the data relatively well, while the 2-element and 3-element Maxwell cannot. This is on account of the different temperature dependencies of the two relaxation modes. As such, we relied on the simple and adequate single-element stretched exponentials to analyze the material properties (Table S3-7).

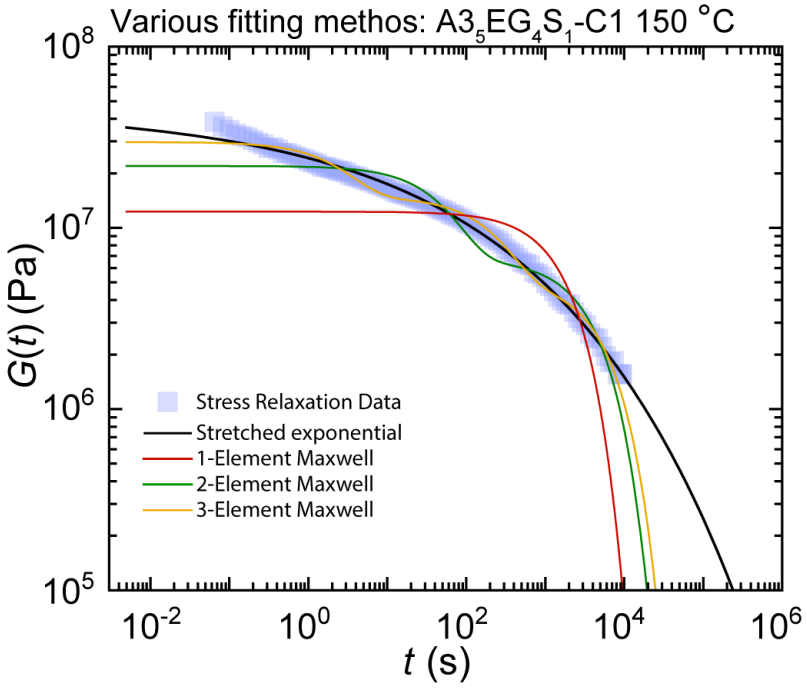

Figure S6. Comparison of a variety of fitting methods applied to stress relaxation data from $A3_5EG_4S_1$-C1 at 150 °C.

Table S3. Parameters of stress relaxation and fitting of $A3_3EG_6S_1$-C1.

Temperature (°C)	G_0 (MPa)	τ (s)	β	a_T	b_T
100	63.4	174	0.183	4.77	3.33
110	47.2	267	0.183	7.29	2.48
120	37.2	235	0.183	6.43	1.95
130	30.1	131	0.183	3.58	1.58
140	23.7	76.7	0.183	2.10	1.25
150	19.0	36.6	0.183	1	1
160	15.8	14.3	0.183	0.390	0.833
170	13.3	5.98	0.183	0.163	0.698
180	11.9	2.53	0.183	0.0691	0.624

Table S4. Parameters of stress relaxation and fitting of $A3_5EG_4S_1$-C1.

Temperature (°C)	G_0 (MPa)	τ (s)	β	a_T	b_T
100	110	4413	0.184	0.00292	0.410
110	101	1733	0.184	0.00743	0.448
120	92.5	313	0.184	0.0412	0.490
130	76.7	100	0.184	0.128	0.591
140	63.1	32.3	0.184	0.398	0.718
150	45.3	12.9	0.184	1	1
160	30.1	4.94	0.184	2.61	1.50
170	21.1	2.67	0.184	4.82	2.15
180	11.2	3.47	0.184	3.71	4.06

Table S5. Parameters of stress relaxation and fitting of $A3_7EG_2S_1$-C1.

Temperature (°C)	G_0 (MPa)	τ (s)	β	a_T	b_T
100	99.4	$6.87*10^8$	0.215	0.0000001	1.03
110	113	$3.67*10^5$	0.215	0.000187	0.912
120	115	39152 ($3.92*10^4$)	0.215	0.00176	0.893
130	117	9072 ($9.07*10^3$)	0.215	0.00758	0.881
140	113	540	0.215	0.127	0.910
150	103	68.7 ($6.87*10^1$)	0.215	1	1
160	65.1	8.71	0.215	7.89	1.58
170	45.8	2.51	0.215	27.4	2.24
180	30.9	0.959	0.215	71.7	3.32
190	19.4	0.544	0.215	126	5.30

Table S6. Parameters of stress relaxation and fitting of $A3_5EG_4S_1$-C2.

Temperature (°C)	G_0 (MPa)	τ (s)	β	a_T	b_T
120	310	0.0000264	0.0347	0.264	0.507
130	236	0.00000771	0.0347	0.907	0.666
140	313	0.000000585	0.0347	12.0	0.501
150	157	0.00000699	0.0347	1	1
160	191	0.00000000524	0.0347	1334	0.823
170	134	0.0000000422	0.0347	165.833	1.17
180	132	0.000000107	0.0347	65.2	1.19
190	122	0.000000149	0.0347	46.8	1.29
200	67.9	0.00208	0.0347	0.00336	2.31

Table S7. Parameters of stress relaxation and fitting of $A3_5EG_4S_1$-C3.

Temperature (°C)	G_0 (MPa)	τ (s)	β	a_T	b_T
100	60.2	428321	0.970	0.0388	1.08
110	63.9	233243	0.970	0.0712	1.01
120	61.6	87486	0.970	0.190	1.05
130	64.9	259730	0.970	0.0640	0.997
140	65.6	21301	0.970	0.780	0.986
150	64.7	16611	0.970	1	1
160	60.8	19680	0.970	0.844	1.06
170	62.0	8852	0.970	1.88	1.04
180	57.7	4540	0.714	2.95	1.19
190	44.6	2806	0.844	5.18	1.50
200	39.8	197	0.290	13.5	2.85

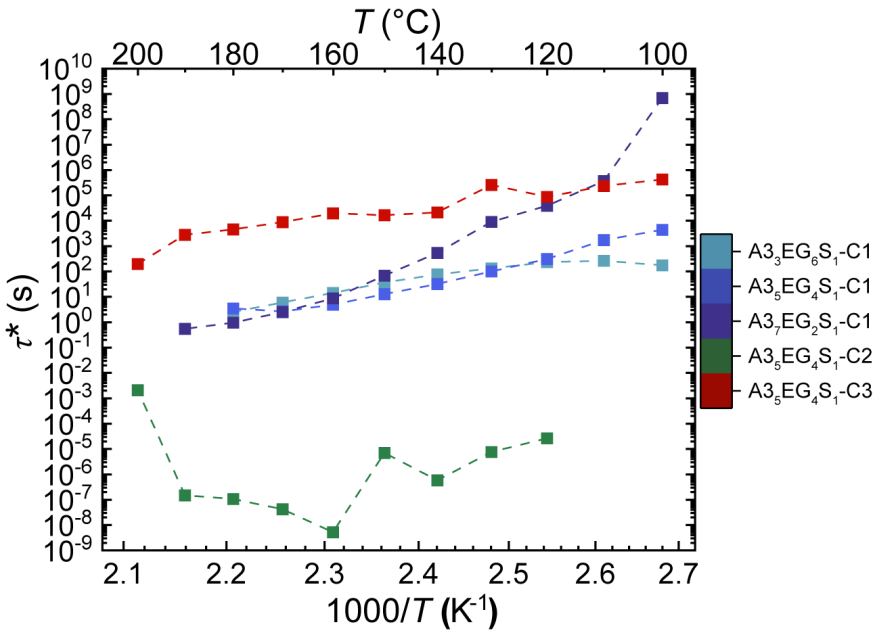

Figure S7. Arrhenius plots of τ obtained via stretched exponential fitting of the stress relaxation data. The plot includes data of $A3_3EG_6S_1$-C1, $A3_5EG_4S_1$-C1, $A3_7EG_2S_1$-C1, $A3_5EG_4S_1$-C2, and $A3_5EG_4S_1$-C3.

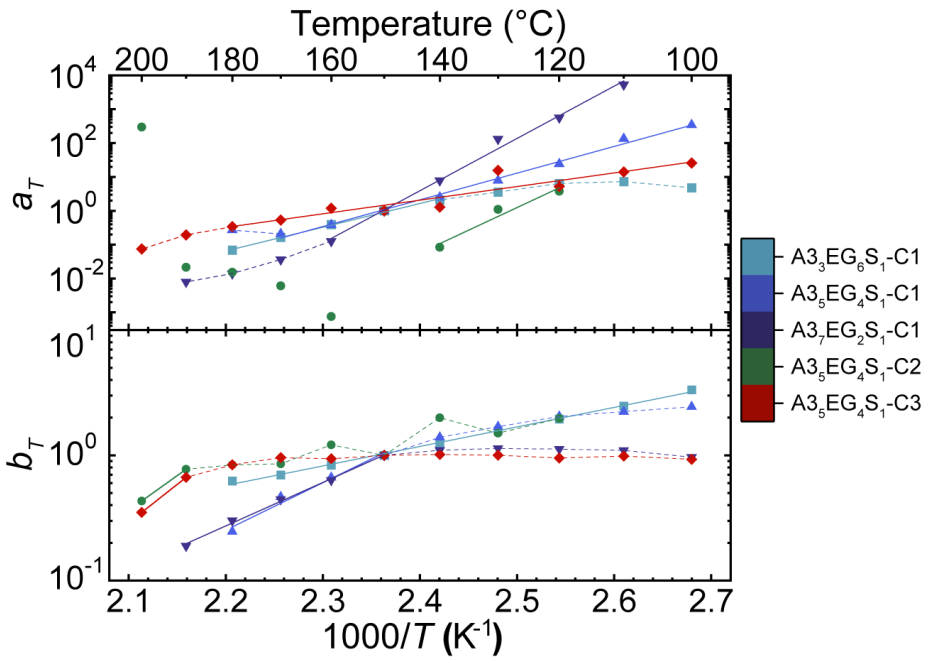

Figure S8. Temperature dependence of shift factors a_T (top) and b_T (bottom). The shift factors are obtained via TTS of the stretched exponential fits corresponding to the stress relaxation data for CANs $A3_3EG_6S_1$-C1 (turquoise), $A3_5EG_4S_1$-C1 (blue), $A3_7EG_2S_1$-C1 (purple), $A3_5EG_4S_1$-C2 (green), and $A3_5EG_4S_1$-C3 (red).

Table S8. Overview of mechanical properties of recycled CAN networks.

Sample	RH (%)[a]	σ_b (MPa) ± SE[b]	ε_b (%) ± SE[b]	σ_y (MPa) ± SE[b]	ε_y (%) ± SE[b]	E (MPa) ± SE[b]	U_t (MJm^{-3}) ± SE[b]
$A3_3EG_6S_1$-C1	50	1.34 ± 0.09	204 ± 23	0.56 ± 0.03	5.5 ± 0.2	13.6 ± 1.1	1.7 ± 0.2
$A3_5EG_4S_1$-C1	50	2.64 ± 0.28	199 ± 19	1.2 ± 0.06	5.7 ± 0.3	39.0 ± 2.7	3.5 ± 0.5
$A3_7EG_2S_1$-C1	50	1.45 ± 0.11	86.0 ± 4.5	1.3 ± 0.09	5.3 ± 0.25	34.0 ± 3.1	1.2 ± 0.1
$A3_5EG_4S_1$-C2	50	3.70 ± 0.55	0.913 ± 0.218	-	-	488 ± 83	0.02 ± 0.006
$A3_5EG_4S_1$-C3	50	16.0 ± 3.0	12.0 ± 3.3	9.7 ± 1.4	4.9 ± 1.1	369 ± 68	1.1 ± 0.2

[a] The samples are conditioned by storing them for 24 h at the indicated RH and immediately measured after.
[b] SE refers to the standard error.

Table S9. Overview of mechanical properties of NHT-CAN nanocomposites.

Sample	σ_b (MPa) ± SE[b)]	ε_b (%) ± SE[b)]	σ_y (MPa) ± SE[b)]	ε_y (%) ± SE[b)]	E (GPa) ± SE[b)]	U_t (MJm^{-3}) ± SE[b)]
$A3_3EG_6S_1$-C1 (U)[a]	67 ± 4	0.97 ± 0.10	66 ± 4	0.62 ± 0.1	10.8 ± 0.8	0.42 ± 0.06
$A3_3EG_6S_1$-C1 (C)[a]	113 ± 9	0.49 ± 0.05	-	-	23.7 ± 1.0	0.30 ± 0.06
$A3_5EG_4S_1$-C1 (U)	41 ± 2	2.07 ± 0.37	38 ± 2	0.73 ± 0.2	5.6 ± 0.4	0.70 ± 0.2
$A3_5EG_4S_1$-C1 (C)	97 ± 5	0.44 ± 0.03	-	-	22.9 ± 0.6	0.22 ± 0.03
$A3_7EG_2S_1$-C1 (U)	30 ± 0.7	2.90 ± 0.73	30 ± 0.4	1.45 ± 0.8	2.1 ± 0.8	0.47 ± 0.2
$A3_7EG_2S_1$-C1 (C)	114 ± 14	0.66 ± 0.04	-	-	17.8 ± 2.4	0.39 ± 0.08
$A3_5EG_4S_1$-C2 (U)	60 ± 7	0.53 ± 0.06	-	-	11.4 ± 0.5	0.18 ± 0.04
$A3_5EG_4S_1$-C2 (C)	72 ± 2	0.30 ± 0.02	-	-	24.3 ± 1.2	0.11 ± 0.007
$A3_5EG_4S_1$-C3 (U)	82 ± 5	0.83 ± 0.09	-	-	12.1 ± 1.1	0.46 ± 0.08
$A3_5EG_4S_1$-C3 (C)	127 ± 6	0.52 ± 0.02	-	-	24.7 ± 0.6	0.34 ± 0.03

[a)] U and C refer to uncured and cured samples, respectively.
[b)] SE refers to the standard error.

2.6 References

(1) Geyer, R.; Jambeck, J. R.; Law, K. L. Production, Use, and Fate of All Plastics Ever Made. *Sci. Adv.* **2017**, *3* (7), e1700782. https://doi.org/10.1126/sciadv.1700782.

(2) *Circular economy action plan - European Commission*. https://environment.ec.europa.eu/strategy/circular-economy-action-plan_en (accessed 2024-01-05).

(3) Biron, M. *Thermosets and Composites*; Elsevier, 2003.

(4) Walton, D.; Lorimer, P. *Polymers*; Oxford University Press: Oxford, 2000.

(5) Skene, W. G.; Lehn, J.-M. P. Dynamers: Polyacylhydrazone Reversible Covalent Polymers, Component Exchange, and Constitutional Diversity. *Proc. Natl. Acad. Sci.* **2004**, *101* (22), 8270–8275. https://doi.org/10.1073/pnas.0401885101.

(6) Samanta, S.; Kim, S.; Saito, T.; Sokolov, A. P. Polymers with Dynamic Bonds: Adaptive Functional Materials for a Sustainable Future. *J. Phys. Chem. B* **2021**, *125* (33), 9389–9401. https://doi.org/10.1021/acs.jpcb.1c03511.

(7) Wemyss, A. M.; Ellingford, C.; Morishita, Y.; Bowen, C.; Wan, C. Dynamic Polymer Networks: A New Avenue towards Sustainable and Advanced Soft Machines. *Angew. Chem. Int. Ed.* **2021**, *60* (25), 13725–13736. https://doi.org/10.1002/anie.202013254.

(8) Burattini, S.; Greenland, B. W.; Merino, D. H.; Weng, W.; Seppala, J.; Colquhoun, H. M.; Hayes, W.; Mackay, M. E.; Hamley, I. W.; Rowan, S. J. A Healable Supramolecular Polymer Blend Based on Aromatic Π−π Stacking and Hydrogen-Bonding Interactions. *J. Am. Chem. Soc.* **2010**, *132* (34), 12051–12058. https://doi.org/10.1021/ja104446r.

(9) Seiffert, S.; Sprakel, J. Physical Chemistry of Supramolecular Polymer Networks. *Chem. Soc. Rev.* **2012**, *41* (2), 909–930. https://doi.org/10.1039/C1CS15191F.

(10) Wojtecki, R. J.; Meador, M. A.; Rowan, S. J. Using the Dynamic Bond to Access Macroscopically Responsive Structurally Dynamic Polymers. *Nat. Mater.* **2011**, *10* (1), 14–27. https://doi.org/10.1038/nmat2891.

(11) Cordier, P.; Tournilhac, F.; Soulié-Ziakovic, C.; Leibler, L. Self-Healing and Thermoreversible Rubber from Supramolecular Assembly. *Nature* **2008**, *451* (7181), 977–980. https://doi.org/10.1038/nature06669.

(12) Montarnal, D.; Capelot, M.; Tournilhac, F.; Leibler, L. Silica-Like Malleable Materials from Permanent Organic Networks. *Science* **2011**, *334* (6058), 965–968. https://doi.org/10.1126/science.1212648.

(13) Denissen, W.; Winne, J. M.; Du Prez, F. E. Vitrimers: Permanent Organic Networks with Glass-like Fluidity. *Chem. Sci.* **2016**, *7* (1), 30–38. https://doi.org/10.1039/C5SC02223A.

(14) Guerre, M.; Taplan, C.; Winne, J. M.; Du Prez, F. E. Vitrimers: Directing Chemical Reactivity to Control Material Properties. *Chem. Sci.* **2020**, *11* (19), 4855–4870. https://doi.org/10.1039/D0SC01069C.

(15) Van Zee, N. J.; Nicolaÿ, R. Vitrimers: Permanently Crosslinked Polymers with Dynamic Network Topology. *Prog. Polym. Sci.* **2020**, *104*, 101233. https://doi.org/10.1016/j.progpolymsci.2020.101233.

(16) Scheutz, G. M.; Lessard, J. J.; Sims, M. B.; Sumerlin, B. S. Adaptable Crosslinks in Polymeric Materials: Resolving the Intersection of Thermoplastics and Thermosets. *J. Am. Chem. Soc.* **2019**, *141* (41), 16181–16196. https://doi.org/10.1021/jacs.9b07922.

(17) Cuminet, F.; Caillol, S.; Dantras, É.; Leclerc, É.; Ladmiral, V. Neighboring Group Participation and Internal Catalysis Effects on Exchangeable Covalent Bonds: Application to the Thriving Field of Vitrimer Chemistry. *Macromolecules* **2021**, *54* (9), 3927–3961. https://doi.org/10.1021/acs.macromol.0c02706.

(18) Winne, J. M.; Leibler, L.; Du Prez, F. E. Dynamic Covalent Chemistry in Polymer Networks: A Mechanistic Perspective. *Polym. Chem.* **2019**, *10* (45), 6091–6108. https://doi.org/10.1039/c9py01260e.

(19) Zou, W.; Jin, B.; Wu, Y.; Song, H.; Luo, Y.; Huang, F.; Qian, J.; Zhao, Q.; Xie, T. Light-Triggered Topological Programmability in a Dynamic Covalent Polymer Network. *Sci. Adv.* **2020**, *6* (13), eaaz2362. https://doi.org/10.1126/sciadv.aaz2362.

(20) Jourdain, A.; Asbai, R.; Anaya, O.; Chehimi, M. M.; Drockenmuller, E.; Montarnal, D. Rheological Properties of Covalent Adaptable Networks with 1,2,3-Triazolium Cross-Links: The Missing Link between Vitrimers and Dissociative Networks. *Macromolecules* **2020**, *53* (6), 1884–1900. https://doi.org/10.1021/acs.macromol.9b02204.

(21) Denissen, W.; Droesbeke, M.; Nicolaÿ, R.; Leibler, L.; Winne, J. M.; Du Prez, F. E. Chemical Control of the Viscoelastic Properties of Vinylogous Urethane Vitrimers. *Nat. Commun.* **2017**, *8* (1), 14857. https://doi.org/10.1038/ncomms14857.

(22) Guerre, M.; Taplan, C.; Nicolaÿ, R.; Winne, J. M.; Du Prez, F. E. Fluorinated Vitrimer Elastomers with a Dual Temperature Response. *J. Am. Chem. Soc.* **2018**, *140* (41), 13272–13284. https://doi.org/10.1021/jacs.8b07094.
(23) Otera, J. Transesterification. *Chem. Rev.* **1993**, *93* (4), 1449–1470. https://doi.org/10.1021/cr00020a004.
(24) Reinoso, D. M.; Ferreira, M. L.; Tonetto, G. M. Study of the Reaction Mechanism of the Transesterification of Triglycerides Catalyzed by Zinc Carboxylates. *J. Mol. Catal. Chem.* **2013**, *377*, 29–41. https://doi.org/10.1016/j.molcata.2013.04.024.
(25) Taplan, C.; Guerre, M.; Winne, J. M.; Du Prez, F. E. Fast Processing of Highly Crosslinked, Low-Viscosity Vitrimers. *Mater. Horiz.* **2020**, *7* (1), 104–110. https://doi.org/10.1039/C9MH01062A.
(26) Delahaye, M.; Tanini, F.; Holloway, J. O.; Winne, J. M.; Du Prez, F. E. Double Neighbouring Group Participation for Ultrafast Exchange in Phthalate Monoester Networks. *Polym. Chem.* **2020**, *11* (32), 5207–5215. https://doi.org/10.1039/D0PY00681E.
(27) Lossada, F.; Guo, J.; Jiao, D.; Groeer, S.; Bourgeat-Lami, E.; Montarnal, D.; Walther, A. Vitrimer Chemistry Meets Cellulose Nanofibrils: Bioinspired Nanopapers with High Water Resistance and Strong Adhesion. *Biomacromolecules* **2019**, *20* (2), 1045–1055. https://doi.org/10.1021/acs.biomac.8b01659.
(28) Lossada, F.; Jiao, D.; Hoenders, D.; Walther, A. Recyclable and Light-Adaptive Vitrimer-Based Nacre-Mimetic Nanocomposites. *ACS Nano* **2021**, *15* (3), 5043–5055. https://doi.org/10.1021/acsnano.0c10001.
(29) Freitag, W.; Stoye, D. *Paints, Coatings and Solvents*; John Wiley & Sons, 2008.
(30) Delahaye, M.; Winne, J. M.; Du Prez, F. E. Internal Catalysis in Covalent Adaptable Networks: Phthalate Monoester Transesterification As a Versatile Dynamic Cross-Linking Chemistry. *J. Am. Chem. Soc.* **2019**, *141* (38), 15277–15287. https://doi.org/10.1021/jacs.9b07269.
(31) Soman, B.; Evans, C. M. Effect of Precise Linker Length, Bond Density, and Broad Temperature Window on the Rheological Properties of Ethylene Vitrimers. *Soft Matter* **2021**, *17* (13), 3569–3577. https://doi.org/10.1039/D0SM01544J.
(32) Zhang, H.; Majumdar, S.; van Benthem, R. A. T. M.; Sijbesma, R. P.; Heuts, J. P. A. Intramolecularly Catalyzed Dynamic Polyester Networks Using Neighboring Carboxylic and Sulfonic Acid Groups. *ACS Macro Lett.* **2020**, *9* (2), 272–277. https://doi.org/10.1021/acsmacrolett.9b01023.
(33) McKinnis, A. C. Aromatic Phosphonic Acid Esterification Catalysts. US2776985A, January 8, 1957. https://patents.google.com/patent/US2776985A/en (accessed 2024-01-05).
(34) Rossegger, E.; Höller, R.; Reisinger, D.; Strasser, J.; Fleisch, M.; Griesser, T.; Schlögl, S. Digital Light Processing 3D Printing with Thiol–Acrylate Vitrimers. *Polym. Chem.* **2021**, *12* (5), 639–644. https://doi.org/10.1039/D0PY01520B.
(35) Lijsebetten, F. V.; Holloway, J. O.; Winne, J. M.; Du Prez, F. E. Internal Catalysis for Dynamic Covalent Chemistry Applications and Polymer Science. *Chem. Soc. Rev.* **2020**, *49* (23), 8425–8438. https://doi.org/10.1039/D0CS00452A.
(36) Bakkali-Hassani, C.; Berne, D.; Bron, P.; Irusta, L.; Sardon, H.; Ladmiral, V.; Caillol, S. Polyhydroxyurethane Covalent Adaptable Networks: Looking for Suitable Catalysts. *Polym. Chem.* **2023**, *14* (31), 3610–3620. https://doi.org/10.1039/D3PY00579H.
(37) Zhou, Y.; Goossens, J. G. P.; Sijbesma, R. P.; Heuts, J. P. A. Poly(Butylene Terephthalate)/Glycerol-Based Vitrimers via Solid-State Polymerization. *Macromolecules* **2017**, *50* (17), 6742–6751. https://doi.org/10.1021/acs.macromol.7b01142.
(38) Niu, X.; Wang, F.; Kui, X.; Zhang, R.; Wang, X.; Li, X.; Chen, T.; Sun, P.; Shi, A.-C. Dual Cross-Linked Vinyl Vitrimer with Efficient Self-Catalysis Achieving Triple-Shape-Memory Properties. *Macromol. Rapid Commun.* **2019**, *40* (19), 1900313. https://doi.org/10.1002/marc.201900313.
(39) Tran, T. N.; Rawstron, E.; Bourgeat-Lami, E.; Montarnal, D. Formation of Cross-Linked Films from Immiscible Precursors through Sintering of Vitrimer Nanoparticles. *ACS Macro Lett.* **2018**, *7* (3), 376–380. https://doi.org/10.1021/acsmacrolett.8b00173.
(40) Pavia, D. L.; Lampman, G. M.; Kriz, G. S. *Introduction to Spectroscopy: A Guide for Students of Organic Chemistry*; Harcourt College Publishers, 2001.
(41) Morris, N. M.; Catalano, E. A.; Andrews, B. A. K. FT-IR Determination of Degree of Esterification in Polycarboxylic Acid Cross-Link Finishing of Cotton. *Cellulose* **1995**, *2* (1), 31–39. https://doi.org/10.1007/BF00812770.

(42) Schoustra, S. K.; Asadi, V.; Smulders, M. M. J. Probing the Solubility of Imine-Based Covalent Adaptable Networks. *ACS Appl. Polym. Mater.* **2023**, *6* (1), 79–89. https://doi.org/10.1021/acsapm.3c01472.
(43) Breuillac, A.; Kassalias, A.; Nicolaÿ, R. Polybutadiene Vitrimers Based on Dioxaborolane Chemistry and Dual Networks with Static and Dynamic Cross-Links. *Macromolecules* **2019**, *52* (18), 7102–7113. https://doi.org/10.1021/acs.macromol.9b01288.
(44) Porath, L.; Soman, B.; Jing, B. B.; Evans, C. M. Vitrimers: Using Dynamic Associative Bonds to Control Viscoelasticity, Assembly, and Functionality in Polymer Networks. *ACS Macro Lett.* **2022**, *11* (4), 475–483. https://doi.org/10.1021/acsmacrolett.2c00038.
(45) Jing, B. B.; Evans, C. M. Catalyst-Free Dynamic Networks for Recyclable, Self-Healing Solid Polymer Electrolytes. *J. Am. Chem. Soc.* **2019**, *141* (48), 18932–18937. https://doi.org/10.1021/jacs.9b09811.
(46) Zhang, L.; Rowan, S. J. Effect of Sterics and Degree of Cross-Linking on the Mechanical Properties of Dynamic Poly(Alkylurea–Urethane) Networks. *Macromolecules* **2017**, *50* (13), 5051–5060. https://doi.org/10.1021/acs.macromol.7b01016.
(47) Fang, H.; Ye, W.; Ding, Y.; Winter, H. H. Rheology of the Critical Transition State of an Epoxy Vitrimer. *Macromolecules* **2020**, *53* (12), 4855–4862. https://doi.org/10.1021/acs.macromol.0c00843.
(48) Zhang, H.; Wang, D.; Wu, N.; Li, C.; Zhu, C.; Zhao, N.; Xu, J. Recyclable, Self-Healing, Thermadapt Triple-Shape Memory Polymers Based on Dual Dynamic Bonds. *ACS Appl. Mater. Interfaces* **2020**, *12* (8), 9833–9841. https://doi.org/10.1021/acsami.9b22613.
(49) Saed, M. O.; Terentjev, E. M. Siloxane Crosslinks with Dynamic Bond Exchange Enable Shape Programming in Liquid-Crystalline Elastomers. *Sci. Rep.* **2020**, *10* (1), 6609. https://doi.org/10.1038/s41598-020-63508-4.
(50) Porath, L. E.; Evans, C. M. Importance of Broad Temperature Windows and Multiple Rheological Approaches for Probing Viscoelasticity and Entropic Elasticity in Vitrimers. *Macromolecules* **2021**, *54* (10), 4782–4791. https://doi.org/10.1021/acs.macromol.0c02800.
(51) Wu, Y.-C. M.; Chyr, G.; Park, H.; Makar-Limanov, A.; Shi, Y.; M. DeSimone, J.; Bao, Z. Stretchable, Recyclable Thermosets via Photopolymerization and 3D Printing of Hemiacetal Ester-Based Resins. *Chem. Sci.* **2023**, *14* (44), 12535–12540. https://doi.org/10.1039/D3SC03623E.
(52) Emri, I.; Pavsek, V. On the Influence of Moisture on the Mechanical-Properties of Polymers. *Mater. Forum* **1992**, *16* (2), 123–131.
(53) Li, L.; Xu, X.; Liu, L.; Song, P.; Cao, Q.; Xu, Z.; Fang, Z.; Wang, H. Water Governs the Mechanical Properties of Poly(Vinyl Alcohol). *Polymer* **2021**, *213*, 123330. https://doi.org/10.1016/j.polymer.2020.123330.
(54) Snijkers, F.; Pasquino, R.; Maffezzoli, A. Curing and Viscoelasticity of Vitrimers. *Soft Matter* **2016**, *13* (1), 258–268. https://doi.org/10.1039/C6SM00707D.
(55) Ricarte, R. G.; Shanbhag, S. Unentangled Vitrimer Melts: Interplay between Chain Relaxation and Cross-Link Exchange Controls Linear Rheology. *Macromolecules* **2021**, *54* (7), 3304–3320. https://doi.org/10.1021/acs.macromol.0c02530.
(56) Stukenbroeker, T.; Wang, W.; Winne, J. M.; Du Prez, F. E.; Nicolaÿ, R.; Leibler, L. Polydimethylsiloxane Quenchable Vitrimers. *Polym. Chem.* **2017**, *8* (43), 6590–6593. https://doi.org/10.1039/C7PY01488K.
(57) Anaya, O.; Jourdain, A.; Antoniuk, I.; Ben Romdhane, H.; Montarnal, D.; Drockenmuller, E. Tuning the Viscosity Profiles of High-Tg Poly(1,2,3-Triazolium) Covalent Adaptable Networks by the Chemical Structure of the N-Substituents. *Macromolecules* **2021**, *54* (7), 3281–3292. https://doi.org/10.1021/acs.macromol.0c02221.
(58) Lijsebetten, F. V.; Bruycker, K. D.; Ruymbeke, E. V.; Winne, J. M.; Du Prez, F. E. Characterising Different Molecular Landscapes in Dynamic Covalent Networks. *Chem. Sci.* **2022**, *13* (43), 12865–12875. https://doi.org/10.1039/D2SC05528G.
(59) Capelot, M.; Unterlass, M. M.; Tournilhac, F.; Leibler, L. Catalytic Control of the Vitrimer Glass Transition. *ACS Macro Lett.* **2012**, *1* (7), 789–792. https://doi.org/10.1021/mz300239f.
(60) Sharma, H.; Rana, S.; Singh, P.; Hayashi, M.; Binder, W. H.; Rossegger, E.; Kumar, A.; Schlögl, S. Self-Healable Fiber-Reinforced Vitrimer Composites: Overview and Future Prospects. *RSC Adv.* **2022**, *12* (50), 32569–32582. https://doi.org/10.1039/D2RA05103F.
(61) Van Lijsebetten, F.; Debsharma, T.; Winne, J. M.; Du Prez, F. E. A Highly Dynamic Covalent Polymer Network without Creep: Mission Impossible? *Angew. Chem. Int. Ed.* **2022**, *61* (48), e202210405. https://doi.org/10.1002/anie.202210405.

(62) Ricarte, R. G.; Shanbhag, S. A Tutorial Review of Linear Rheology for Polymer Chemists: Basics and Best Practices for Covalent Adaptable Networks. *Polym. Chem.* **2024**, *15*, 815–846. https://doi.org/10.1039/D3PY01367G.
(63) Das, P.; Malho, J.-M.; Rahimi, K.; Schacher, F. H.; Wang, B.; Demco, D. E.; Walther, A. Nacre-Mimetics with Synthetic Nanoclays up to Ultrahigh Aspect Ratios. *Nat. Commun.* **2015**, *6* (1), 5967. https://doi.org/10.1038/ncomms6967.
(64) Das, P.; Schipmann, S.; Malho, J.-M.; Zhu, B.; Klemradt, U.; Walther, A. Facile Access to Large-Scale, Self-Assembled, Nacre-Inspired, High-Performance Materials with Tunable Nanoscale Periodicities. *ACS Appl. Mater. Interfaces* **2013**, *5* (9), 3738–3747. https://doi.org/10.1021/am400350q.
(65) Walther, A.; Bjurhager, I.; Malho, J.-M.; Pere, J.; Ruokolainen, J.; Berglund, L. A.; Ikkala, O. Large-Area, Lightweight and Thick Biomimetic Composites with Superior Material Properties via Fast, Economic, and Green Pathways. *Nano Lett.* **2010**, *10* (8), 2742–2748. https://doi.org/10.1021/nl1003224.

Chapter 3. Three-Dimensional Shaping and Shape-Memory in Transparent Covalent Adaptable Network-Infused Wood Composites

Affiliation

[1]Life-Like Materials and Systems, Department of Chemistry, University of Mainz, Duesbergweg 10-14, 55128 Mainz, Germany.

[2]Wood Materials Science, Institute for Building Materials, ETH Zürich, 8093 Zürich, Switzerland.

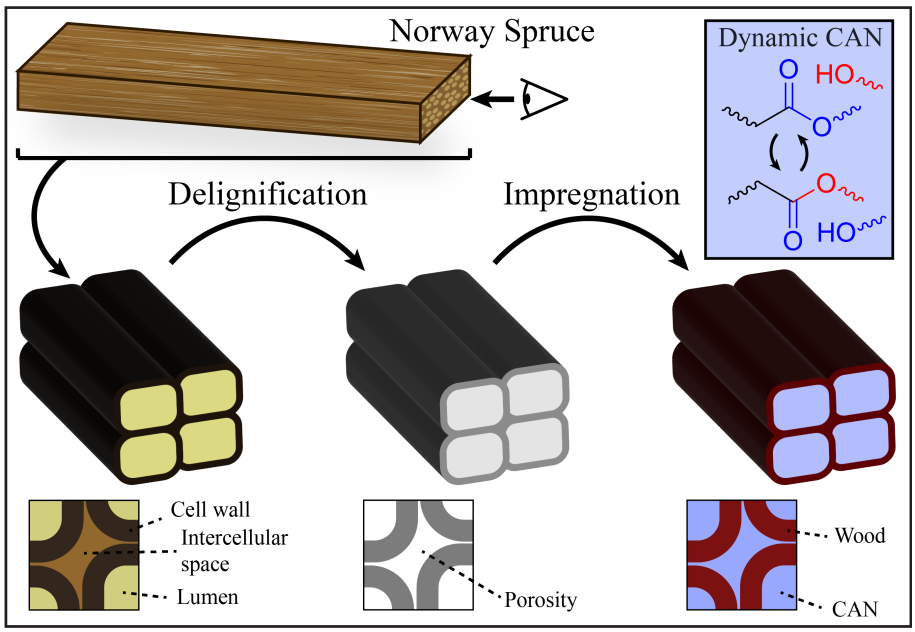

Note, an adapted version of this chapter will be submitted for scientific publication:
''**Sjoerd Engels**[1], Sophie Marie Koch[2], Ingo Burgert[2]*, Andreas Walther[1]*''

Author contributions: S.E., S.M.K., I.B., and A.W. conceptualized the core ideas. **S.E.** and S.M.K. planned the experiments. **S.E.** performed CAN synthesis, DMA, tensile testing, DSC, and FTIR alongside composite preparation, FTIR, DMA, shaping and shape-memory, and recycling and tensile tests of recycled 2nd life composites. S.M.K. performed the wood veneer delignification, composite tensile testing, SEM, and XRD. **S.E.** analyzed the results. **S.E.** wrote the manuscript. S.M.K., I.B., and A.W. edited and finalized the manuscript.

3.1 Abstract

The increasing demand for sustainable, lightweight, and high-performance materials drives innovation in renewable bioinspired composites based on wood, making use of its intricate hierarchical architecture. This work introduces transparent, highly shapeable, and dynamic wood-based composites with a high reinforcement content, enabled by the deep infiltration of a covalent adaptable network (CAN) phase into delignified wood scaffolds. The CAN was designed for low-viscosity impregnation, good mechanical and dynamic properties, and compatibility with the wood phase. By use of SEM and XRD, we demonstrate how the organometallic catalyst modifies the cellulosic structures by partial dissolution, enhancing interfacial interaction and shapeability while preserving the hierarchical architecture. This enables reversible shaping into complex three-dimensional geometries and shape-memory behavior. We also demonstrate end-of-life recycling into isotropic CAN/cellulose composites by way of milling and compression molding. These dynamic composites demonstrate the potential to meet processability and adaptability standards typically challenging for wood-based materials on account of their limited shaping.

3.2 Introduction

The growing demand for eco-friendly materials, especially in high-performance applications, signifies the need for sustainable alternatives to petroleum-based materials.[1,2] Wood is ubiquitous as a versatile and lightweight material class, characterized by its abundance and renewable nature.[1,2] The prevalence of wood in structural applications and its growing role in eco-friendly construction and production highlight the potential of renewable biomass to provide sustainable solutions across diverse applications.[1,2] Moreover, the intricate hierarchical structure of wood enables advanced and unique properties, unmatched by synthetic materials, and is overall responsible for incredible mechanical performance-to-weight ratios.[2–5] Fully and partially delignified woods, alongside composite materials prepared from them, constitute a relatively new strategy that preserves the complex cellulose architecture and corresponding advantages of wood, while providing additional opportunities (and pore size or space) for the incorporation of novel materials inside these porous scaffolds.[1,2,6–10]

Polymeric wood-based composites, particularly those in which the polymer phase infiltrates deeply into the wood scaffold, represent a promising class of sustainable high-performance materials.[1,3,10] This approach facilitates strong interfacial interactions, crucial for efficient stress transfer and enhanced mechanical performance, and combines advantages of both constituent phases into one material.[11] Whereas the wood components provide reinforcement and potential for anisotropic properties on account of their architecture, polymeric phases contribute their own benefits (*e.g.* transparency, defect reduction, and enhancement of mechanical performance, water and moisture resistance, thermal insulation, antimicrobial properties, corrosion resistance).[1,5,11–17] However, many wood-based composites face challenges related to their complex fabrication methods and limited (re)processability. Recycling is often unfeasible, and shaping into complex geometric shapes is constrained by the rigid architecture of wood. Previous approaches to overcome this and shape wood-based materials include using the soft, wet state of delignified wood scaffolds to shape the materials before being dried or leveraging multi-layered structures that can self-bend upon exposure to moisture.[5,8,18,19] However, these methods face limitations: wet-state processing is impractical for many applications as it can compromise mechanical performance and is frequently irreversible or restricted to the initial production phase.[20] Additionally, such procedures tend to be relatively complex, and unsuitable for rapid, on-site reshaping without disrupting the material functionality. Polymer-impregnated wood composites, specifically, can further exacerbate these issues due to the hydrophobicity or lack of porosity associated with the impregnated polymer phase.[21]

Covalent adaptable networks (CANs) are a class of crosslinked polymers that are thermoresponsive on account of dynamic chemistries that allow for network reorientation through covalent bond exchanges.[22–24] This enables the combination of chemical and mechanical benefits associated with crosslinked networks and (re)processability, leading to advanced options for recycling, shaping, and

on demand transitions between viscous flow and creep resistant elasticity. The impregnation of CANs into delignified wood scaffolds represents a novel approach for developing advanced wood-based composites with improved potential for shapeability, even into three-dimensional geometries, and recycling. This approach merges the remarkable hierarchical architecture, lightweight nature, eco-friendliness, and high reinforcement capabilities of the wood scaffold with enhanced shapeability and processability, enabling use in applications that require more complex geometries.

Literature examples of CANs in wood-based composites are rare, highlighting the potential for further exploration of this unique approach. Nevertheless, the concept has been demonstrated through the impregnation of delignified balsa wood with a variety of CANs that are well-established epoxy resin formulations designed for liquid processing and efficient thermal curing. These studies resulted in dynamic wood-based composites with good potential for shaping and, in addition, a variety of other features were incorporated into the materials, such as shape-memory properties, optical guiding and scattering properties, and thermal insulation properties.[25–28] However, a limitation of these examples is their low degree of reinforcement due to the low density of balsa wood. While this approach is sometimes necessary to enable the impregnation process and also enhances the expression of the dynamic properties of CANs, achieving the full mechanical potential of wood-based composites, requires preparing composites with higher levels of cellulose reinforcement.[11,13,28–30] Furthermore, the dynamic potential demonstrated is somewhat limited in terms of the extent to which the composites were shaped, particularly in the direction of the wood fibers, and the absence of any sort of recycling process. To elevate CAN-wood composites to a higher level of functionality, particularly in applications where other non-dynamic wood composites may fall short, further advancements in complex geometric shaping are necessary.

In this work, we present the development of transparent, highly shapeable (three-dimensional) wood-based composites, made from epoxy-based CANs and delignified spruce, a high-density softwood. These composites are designed as strongly reinforced structural materials with dynamic properties that can be accessed on demand via a thermal stimulus. We investigate a variety of CAN formulations via dynamic mechanical analysis. Subsequently, we use a liquid formulation, corresponding to a strong and stiff CAN with high crosslink density, and add a small quantity of acetone as a diluent to impregnate delignified wood scaffolds using a simple vacuum-assisted procedure. Moderate heating under mechanical pressure allows for efficient curing, followed by a post-curing step at 180 °C to enhance the mechanical performance of the composites. We demonstrate via scanning electron microscopy (SEM) and X-ray diffraction (XRD) that the CAN catalyst we use (tin(II) 2-ethylhexanoate) enables partial dissolution of the cellulosic structures. This phenomenon facilitates infiltration of the CAN into the hard-to-reach intercellular spaces, thereby enabling the transfer of dynamic properties from the CAN to the wood. Achieving such an effect typically requires a more complex approach involving ionic liquids to swell the scaffolds in, followed

by drying and potentially further sample preparation. The mechanical properties reveal that the wood architecture has a pronounced reinforcing effect in the fiber direction, while enabling higher ductility, even compared to the pure CAN, perpendicular to the fiber direction. Furthermore, we demonstrate shape-memory properties of the composite materials, with complete shape recovery in the ductile transverse direction and partial shape recovery in the more reinforced longitudinal direction. Finally, we demonstrate full recycling of the CAN-wood composites upon their end-of-life to yield 2nd life composites that are isotropic and dynamic materials reinforced with cellulose. The 2nd life composites possess mechanical behavior that is in between the property space of either anisotropic direction of the primary composites.

3.3 Results and Discussion

3.3.1 General CAN Design and Variation Based on Monomer Components

Before preparing bioinspired dynamic wood composites, we conducted extensive analysis of the CAN design to ensure the polymeric phase is compatible with the composite preparation process and can contribute significantly to the final product. Since impregnation of porous delignified wood is a vital step in the preparation of the wood composites, it is crucial to use a formulation that is fully liquid prior to curing into a polymer network structure. We utilize monomers that are widely considered for their properties in general thermoset design, and have also been used in the preparation of CANs with impressive mechanical properties, full transparency, and shape-memory as well as for polymer-impregnated wood composites.[21,29,31–33] However, their application in CAN/wood composites has so far been limited to low-density woods.[25,26] Our general CAN design combines a divalent epoxy with a thiol crosslinker of higher valency to form a polymer network. Upon curing, the epoxide and thiol groups undergo an efficient thiol-Michael addition to form a thioether linkage and a free hydroxy moiety.[31,34] By making use of thiol monomers that incorporate ester groups within their structure, the network can undergo transesterification bond-exchange between the esters and the formed hydroxyl groups. Via addition of an external Lewis acid catalyst, both the curing and bond-exchange processes are enhanced. In more detail, we combine bisphenol A diglycidyl ether (A), a widely used industrial epoxide for thermosetting and CAN resins, with either a trivalent thiol, trimethylolpropane tris(3-mercaptopropionate) (3S), or a tetravalent thiol, pentaerythritol tetrakis(3-mercaptopropionate) (4S). Tin(II) 2-ethylhexanoate (Sn(II)Oct) (5 mol% relative to ester groups) fills the function of catalyst to enable dynamic properties in the final materials.

We investigated the effect of using 4S compared to 3S for a CAN network with a higher crosslink density. We also explored the effects of adding neopentyl glycol diglycidyl ether (N) and glycidyl 2-methylphenyl ether (M) as alternative epoxy diluents. When combined with A, N and M lower the viscosity of the whole CAN formulation, which in turn can improve the wood impregnation process. CAN preparation involves carefully combining the components while rapidly and efficiently mixing in Sn(II)Oct to prevent aggregation, as 3S and 4S can form ligand-metal complexes with Sn(II)Oct at higher local concentrations. The resulting homogeneous mixtures cure into the crosslinked CAN networks. This curing process is rapid (~ 2 h) when heating to 120 °C, yielding the final CANs, abbreviated as AxNyMz-wS (**Table 1**, **Figure 1**). Here, x, y, and z represent the molar percentages of epoxide groups derived from the respective epoxy components (A, N, and M) relative to the total epoxide content, and w indicates the thiol crosslinker used (3S or 4S). Note that when any of x, y, or z is zero, we omit the corresponding component from the abbreviation. The thiols and epoxides are added in such a quantity that the molar contents of thiol and epoxide groups are equal, and Sn(II)Oct is added as 5 mol% relative to the amount of ester present. Based on these principles, we prepared

A100-3S and A100-4S as CANs with varied crosslink density and solely A as the epoxy. We also prepared A90N10-4S, A50N50-4S, and N100-4S to investigate the effect of increasing the ratio of N used as epoxy. Lastly, we prepared A50M50-4S to get an impression of M as a diluent as well.

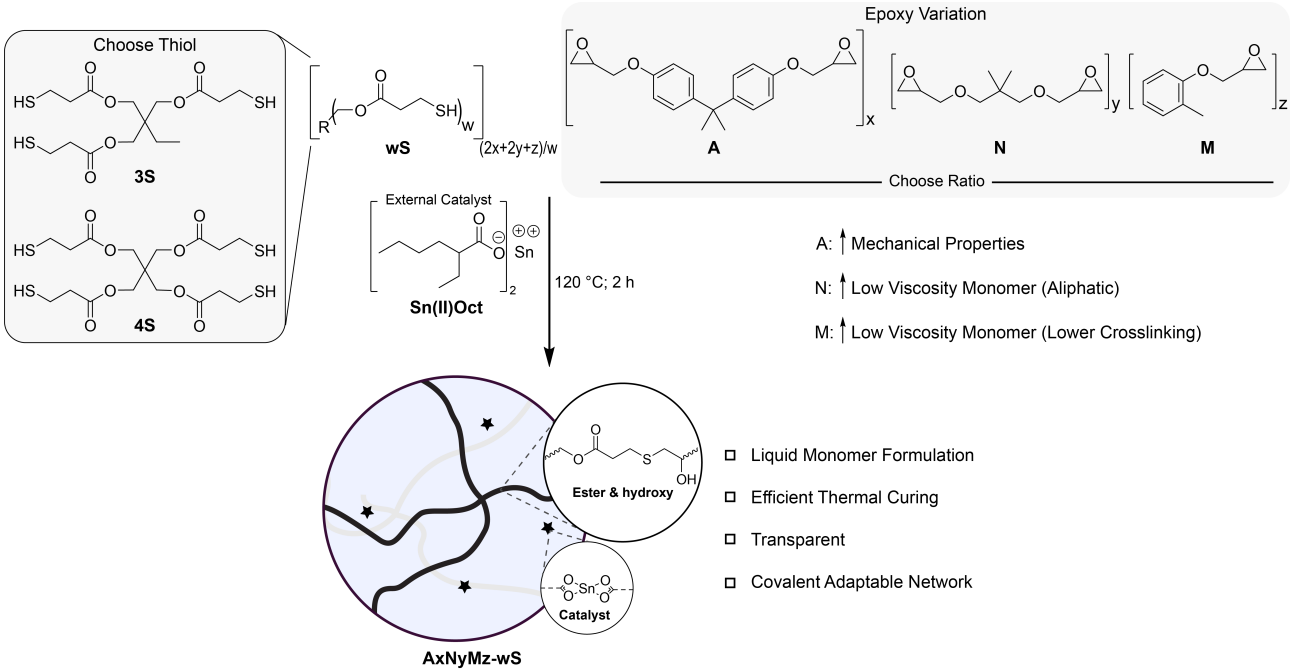

Figure 1. Schematic preparation of AxNyMz-wS via condensation of A, N, and M with 3S and 4S, including Sn(II)Oct as transesterification catalyst. The chemical groups formed during curing are depicted, along with groups relevant to the transesterification reaction and dynamic behavior. 4S results in networks with higher crosslink densities compared to networks based on 3S. N and M can be used in combination with or instead of A to ensure a lower viscosity of the CAN formulations.

Table 1. Overview of CAN compositions.

Sample name	Thiol used	A (mol% epoxide)[a)]	N (mol% epoxide)[a)]	M (mol% epoxide)[a]	Sn(II)Oct (mol% relative to ester)
A100-4S	4S	100	0	0	5
A100-3S	3S	100	0	0	5
A90N10-4S	4S	90	10	0	5
A50N50-4S	4S	50	50	0	5
N100-4S	4S	0	100	0	5
A50M50-4S	4S	50	0	50	5

[a)] 100 mol% is relative to the thiol compound (4S or 3S) so that the ratio of total epoxide to thiol is 1:1.

3.3.2 CAN Formulation Viscosities and Curing Behaviors

First, we focus on the viscosity of the various CAN formulations, both directly after mixing as well as the increase over a prolonged period as the curing process occurs. These factors are important to determine which candidate is preferable for composite preparation. We use small-amplitude

oscillatory shear experiments to analyze the complex viscosity as a function of time. The values of the storage modulus (*G'*) and the loss modulus (*G"*) relate to the complex modulus (*G**) as:[35]

$$G^* = G' + iG'' \tag{1}$$

following this, the complex viscosity (η^*) is defined as:

$$\eta^* = \frac{G^*}{\omega} \tag{2}$$

wherein the ω is the angular frequency of the experiment. The magnitude of the complex viscosity ($|\eta^*|$) is then given by:

$$|\eta^*| = \frac{\sqrt{G'^2 + G''^2}}{\omega} \tag{3}$$

making η^* a useful parameter for indicating the total resistance to flow under oscillatory shear, which relates to the ability of the material to impregnate a porous wood scaffold.

Initially, we investigate the formulations for A100-3S and A100-4S and their subsequent curing processes at three different temperatures (25 °C, 50 °C, and 120 °C) (**Table 2**, **Figure 2**). The initial values for *G'*, *G"*, and η^* reflect the state of the purely monomeric formulations, with values for *G"* that exceed *G'* by orders of magnitude as expected for viscoelastic liquids. It should be noted that a brief period (~ min) occurs prior to the start of the experiment, which particularly affects measurements performed at higher temperatures on account of faster curing reactions. As time progresses, both *G'* and *G"* increase, indicating the onset of polymerization. Notably, curing occurs at all three temperatures with higher temperatures corresponding to faster polymerization. The crossover points ($t_{G'=G''}$) mark the transition from predominantly liquid-like to predominantly solid-like behavior. These points also highlight further how curing accelerates at higher temperatures. For example, at 25 °C, 50 °C, and 120 °C, the crossover times for A100-4S are ca. 40 h, 13 h, and 42 min, respectively. Importantly, the timeframe of curing at 25 °C is wide enough to allow ample time for wood impregnation, whereas higher temperatures correspond to much more limited windows of opportunity. Towards the end of curing, the value for *G"* decreases, associated with a reduction in mobile chain segments, before both *G'* and *G"* reach a plateau when the curing is finished. The initial values for η^* at 25 °C and 50 °C indicate how increasing the temperature lowers the viscosity, as is known from literature.[36] However, at 120 °C, the curing process occurs so rapidly that η^* is already significantly higher by the time of the first data point. Beyond these general observations, the monomer formulation for A100-4S exhibits higher viscosity compared to A100-3S, and the network reaches a higher *G'* upon curing based on the higher crosslink density of A100-4S.

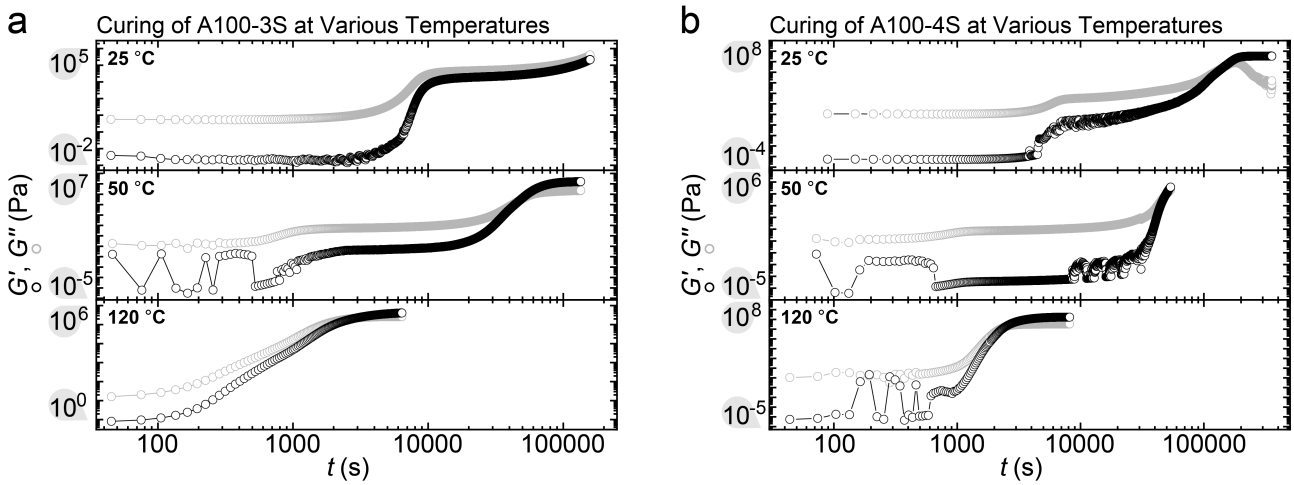

Figure 2. CAN network curing kinetics, obtained by small-amplitude oscillatory shear, of (a) A100-3S and (b) A100-4S when heated at 25 °C, 50 °C, and 120 °C.

Next, we investigate the usage of diluents N, M, and acetone to lower the initial viscosity. Starting with N, a range of formulations involve increasing the content of N compared to A100-4S to A90N10-4S, A50N50-4S, and N100-4S (**Table 2**, **Figure 3a**). Interestingly, all formulations exhibit similar curing rates and mechanical properties in the conditions investigated. However, it is important to note that while the crosslink density remains the same, A can in addition undergo supramolecular aromatic interactions (π- π stacking), whereas N does not. As such, the mechanical properties of the fully cured networks are remarkably different at room temperature, as discussed in more detail in section 3.3.3. As the N content increases, the initial η^* decreases by more than an order of magnitude (1793, 1192, 641, and 134 mPa·s for A100-4S, A90N10-4S, A50N50-4S, and N100-4S, respectively). This provides a strategy for precise tuning of the formulation viscosity within this range based on how much A and N are used.

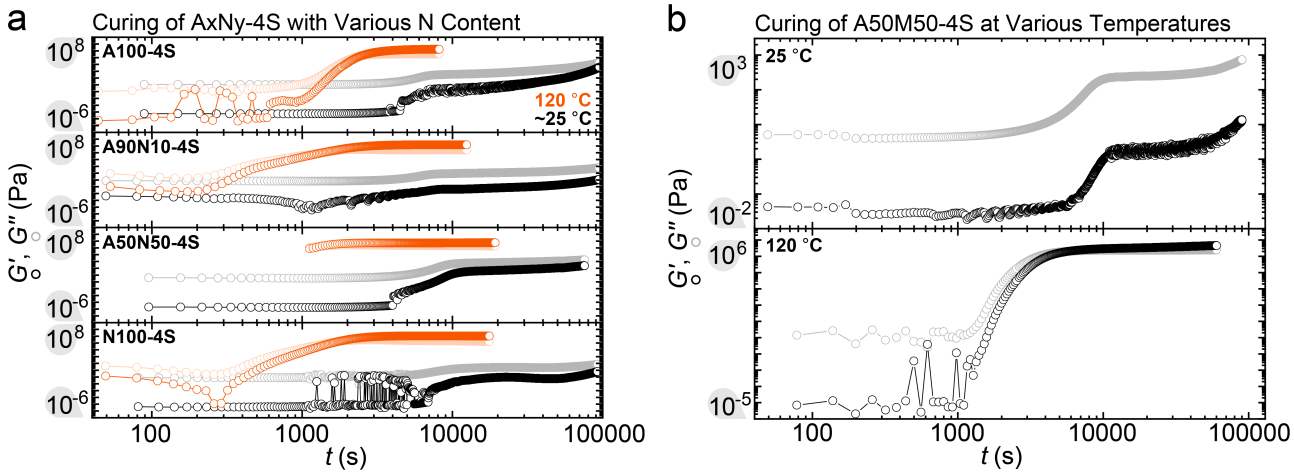

Figure 3. CAN network curing kinetics, obtained by small-amplitude oscillatory shear, of (a) A100-4S, A90N10-4S, A50N50-4S, N100-4S, and (b) A50M50-4S when heated at 25 °C and 120 °C.

Alternatively, M is a diluent that maintains the aromatic component within the network but lowers the crosslink density as a monofunctional chain terminator. We use A50M50-4S to determine the effectiveness of this approach, demonstrating an initial η^* value of 626 mPa·s, which is highly similar

to that of A50N50-4S (**Table 2**, **Figure 3b**). However, this approach comes with significant drawbacks. For instance, A50M50-4S has a significantly lower crosslink density because whereas A (and N) each contain two epoxide groups per molecule, M contains only one. As a result, in A50M50-4S, half of the total epoxide content that reacts with 4S does not contribute to chain extension, and therefore does not form covalent crosslinks. This significantly influences the mechanical properties of the materials, as we discuss in more detail in section 3.3.3. Additionally, it is not feasible to increase the M-content further as doing so would prevent the formation of a network.

We also investigate the effect of adding a small amount of acetone (10 wt%) to the formulation of A100-4S as a diluent (**Table 2**, **Figure 4a**). This mixture behaves similarly to A100-4S without acetone in terms of curing rate but shows a significant decrease in the initial values of *G'* and *G"* and thus in η^* (1793 to 398 mPa·s). This reduction suggests that acetone could be an effective additive to enhance the wood impregnation process. Additionally, this approach allows the formation of the A100-4S network itself, rather than an altered network, since acetone is not a monomer and evaporates upon curing. However, a drawback of this approach is the potential for bubble formation as the acetone evaporates.

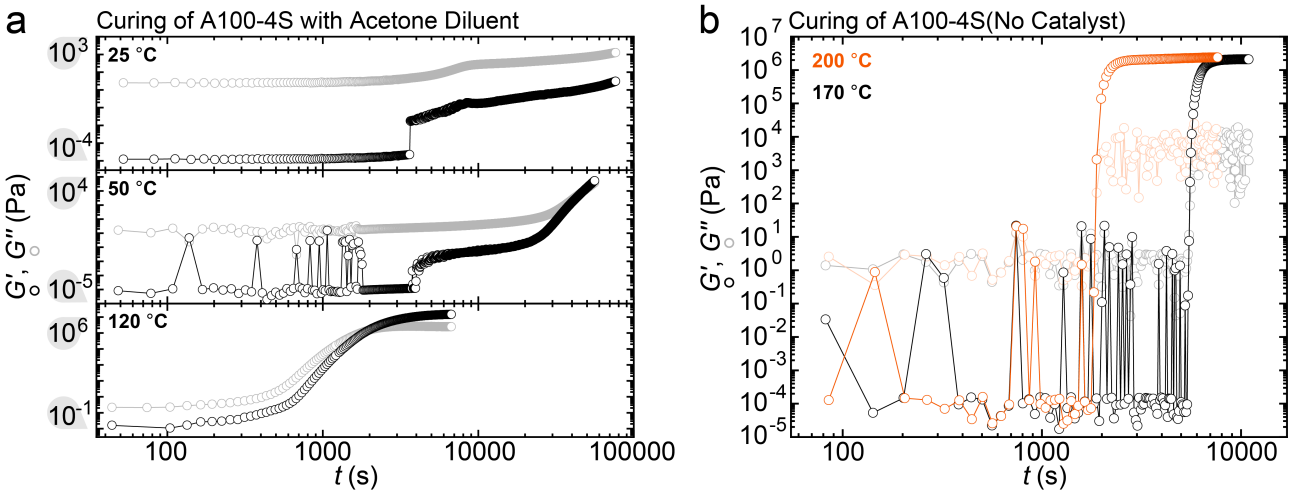

Figure 4. CAN network curing kinetics, obtained by small-amplitude oscillatory shear, of (a) A100-4S with 10wt% acetone as diluent, heated at 25 °C, 50 °C, and 120 °C and (b) A100-4S without catalyst (Sn(II)Oct) when heated at 170 °C and 200 °C.

Lastly, we investigate the curing kinetics of a network without catalyst (**Figure 4b**). While Sn(II)Oct mainly enables the transesterification in the CAN networks, it also plays a role in network formation through catalyzing the thiol-Michael addition reaction. A100-4S(No Catalyst) demonstrates network formation at 170 °C within 3 h and at 200 °C in ~ 1 h. Interestingly, there is no observable increase in *G'* and *G"* until a sudden onset of rapid curing once the reaction progresses, indicating a process driven by self-catalysis. The resulting networks are thermoset resins with no dynamic properties; however, the curing parameters are crucial for preparing control wood composite samples that do not contain Sn(II)Oct, as is detailed in section 3.3.5.

Table 2. Viscoelastic properties of CAN formulations.

Sample name	Temperature (°C)	Initial *G'* (Pa) [a]	Initial *G''* (Pa) [a]	Initial η^* (mPa·s) [a]	$t_{G'=G''}$ (s) [b]
A100-4S	25	0.000563	11.3	1793	~ 143200
	50	0.0000422	0.730	134	~ 48580
	120	0.0000545	1.09	173	~ 2492
A100-4S (10 wt% acetone)	25	0.000125	2.50	398	> 76340
	50	0.0000818	1.64	260	~ 47120
	120	0.166	2.17	347	~ 1993
A100-3S	25	0.0387	5.65	899	> 158200
	50	0.0000600	1.20	191	~ 47970
	120	0.808	16.2	2580	~ 2959
A90N10-4S	25	0.0427	7.49	1192	> 135100
	120	0.192	17.3	2757	~ 1451
A50N50-4S	25	0.000201	4.03	641	> 75640
	120	-	-	-	~ 1421
N100-4S	25	0.0000422	0.843	134	> 92240
	120	0.000117	2.33	371	~ 1766
A50M50-4S	25	0.0276	3.94	626	> 90140
	120	0.0000205	0.410	65.3	~ 5881
A100-4S (no Sn(II)Oct)	170	0.000149	2.97	473	~ 5542
	200	0.000146	2.91	464	~ 1885

[a] The initial value is taken as the lowest first measured data point.
[b] Since the precise crossover point falls between data points, the first data point where *G' > G''* is given. If the crossover point is not reached within the experiment time, the crossover point is said to exceed the last data point time.

3.3.3 Comparative CAN Characterization: Thermal, Chemical, and Mechanical Properties

We determined the soluble fractions for each cured network (curing for 2 h at 120 °C; hot pressed for 1 h at 180 °C at ca. 4 MPa) by immersion in acetone for 48 h (**Table 3**). A100-4S, A100-3S, A90N10-4S, and A50N50-4S exhibit insoluble fractions of over 90%, which demonstrates the high degree of crosslinking. N100-4S and especially A50M50-4S displayed slightly higher solubility, likely due to the lack of aromatic interactions and better solubility in acetone for N100-4S and lower crosslink density for A50M50-4S. Overall, part of the soluble fraction could correspond to Sn(II)Oct, which is not covalently tethered to the network. Additionally, CANs can sometimes (partly) dissolve

on account of their exchangeable crosslinks, which can further explain the small fraction of solubility.[37,38]

Table 3. Insoluble Fraction.

Sample[a)]	Insoluble fraction acetone (48 h)
A100-4S	94%
A100-3S	93%
A90N10-4S	95%
A50N50-4S	93%
N100-4S	89%
A50M50-4S	81%

[a)] Cured for 2 h at 120 °C + hot pressing for 1 h at 180 °C at ca. 4 MPa.

Next, we evaluated the T_g of each of the CANs via differential scanning calorimetry (DSC) (**Figure 5**). The data show that A100-4S displays an increased T_g compared to A100-3S (40.6 °C versus 27.0 °C) based on the higher crosslink density associated with the valency of the thiol monomer. A50M50-4S similarly has a lower T_g based on the greatly decreased crosslink density. Furthermore, using N instead of A also lowers the T_g, with a trend based on the amount of N used (A100-4S > A90N10-4S > A50N50-4S > N100-4S). Here, there is no difference in the (covalent) crosslink density, however the decreased T_g is associated with the lack of aromatic (π-π) interactions for N compared to A.

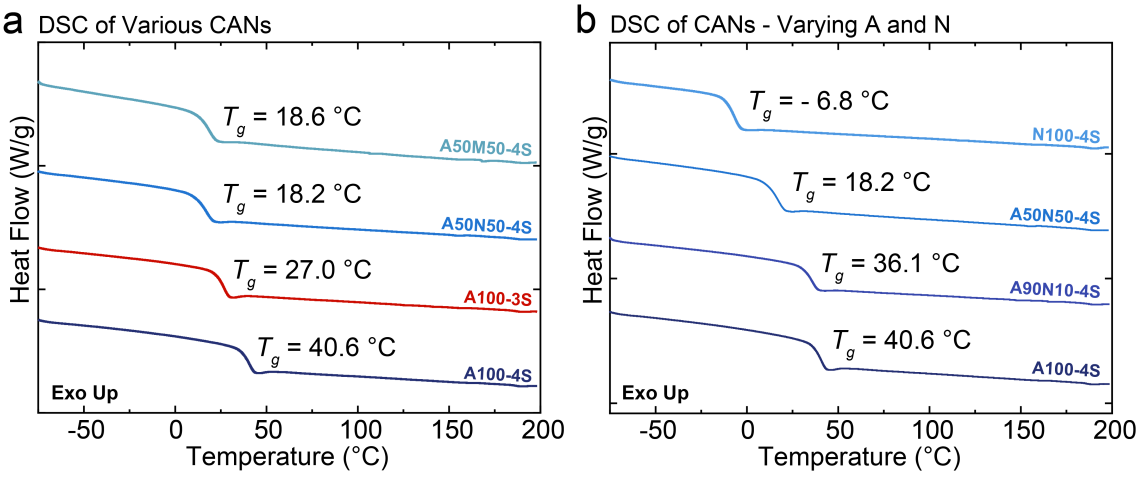

Figure 5. DSC thermograms of the second heating step of (a) A50M50-4S, A50N50-4S, A100-3S, A100-4S, and (b) N100-4S, A50N50-4S, A90N10-4S, and A100-4S measured at a heating rate of 10 °C·min^{-1}. Y-axis offset for clarity.

We further confirm curing on a chemical level by subjecting the formulation of A100-4S and the corresponding network to Fourier-transform infrared spectroscopy (FTIR) (**Figure 6**). Characteristic bands correspond to the chemical groups present: C–H aromatic bending for A (827 cm^{-1}), epoxide

ring deformation for A (914 cm^{-1}, 765 cm^{-1}), C–O stretching for alcohols, esters, and ethers (1000 - 1300 cm^{-1}), C=C aromatic stretching for A (1480 - 1635 cm^{-1}), C=O stretching for esters (1735 cm^{-1}), S–H stretching for 4S (2567 cm^{-1}), C–H stretching (2830 - 3000 cm^{-1}), and O–H stretching for opened epoxides for A (3430 cm^{-1}).[39] Crucially, the signals corresponding to the epoxide groups and the small signal for free thiols reduce upon curing, indicating the condensation reaction between epoxides and thiols. A signal at 3430 cm^{-1} emerges following this reaction, which corresponds to the formation of hydroxyl groups. We also performed a post-curing step of 3 h at 180 °C to ensure full completion of the thiol-epoxide condensation and found no observable shifts in the FTIR spectra. We discuss the impact of post-curing in the context of dynamic mechanical analysis in section 3.3.4 for the CANs and section 3.3.5 for the composites.

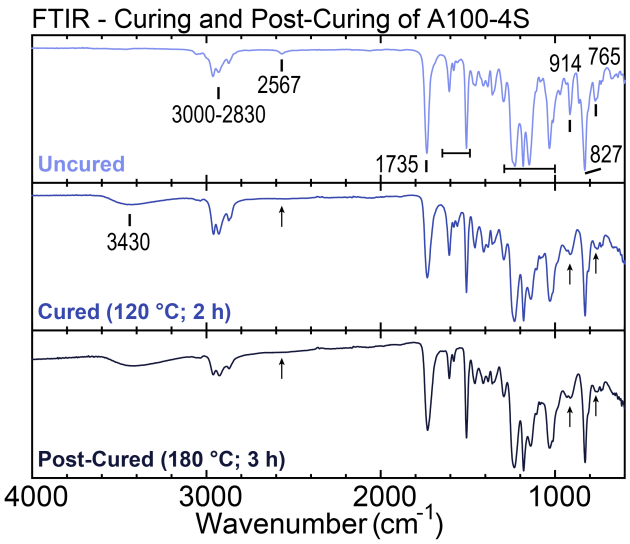

Figure 6. FTIR spectra of uncured, cured (2 h, 120 °C), and post-cured (3 h, 180 °C) samples of A100-4S.

We evaluated the mechanical properties in tensile mode at room temperature to assess the effect of composition variations. The CANs were cured for 2 h at 120 °C and hot pressed for 1 h at 180 °C, followed by conditioning under ambient conditions. **Table 4** and **Figure 7** summarize the mechanical properties: stress (σ_b) and strain (ε_b) at break, yield stress (σ_y) and yield strain (ε_y), Young's modulus (E), and toughness (U_t). We first focus on the comparison between A100-4S and A100-3S, where we observe a stark difference in σ_b, ε_b, and E. A100-4S possesses superior strength (37 MPa versus 9.8 MPa) and stiffness (1074 MPa versus 115 MPa), whereas A100-3S displays a much higher maximum strain (213% versus 6.2%). The higher crosslink density associated with A100-4S helps to explain part of these differences, however the T_g of the two networks is crucial to fully understand the results. Given its T_g of 40.6 °C, A100-4S is in the glassy state, whereas A100-3S exhibits more rubbery behavior. Although the T_g of A100-3S measured by DSC is also above room temperature (27.0 °C), the effects of the T_g are evident, as it is a gradual process that occurs over a temperature range rather than at a single, discrete phase transition.[40–42] This rubbery state of A100-3S is also associated with a much higher toughness compared to the glassy A100-4S. When switching focus to the effect of substituting A with increasing amounts of N, we observe a significant decline in both

stiffness and strength (**Figure 7b**). As previously noted, the increasing fraction of N in the CANs is associated with a decrease in T_g, which explains the enhanced ductility compared to A100-4S. However, beyond A90N10-4S, networks with higher N content show generally poorer mechanical properties without corresponding improvements in ductility. These findings demonstrate how usage of N as a diluent compromises the mechanical performance of the resulting CAN networks. Finally, A50M50-4S similarly displays relatively poor mechanical properties, indicating how using M as a diluent is also associated with a trade-off in mechanical properties. Interestingly, comparison with A50N50-4S allows for some conclusions on the impact of crosslink density and aromatic components, as both networks have almost identical T_g. A50N50-4S possesses a higher stiffness (4.6 MPa versus 2.5 MPa), which is associated with the crosslink density, while A50M50-4S displays a higher strength (2.3 MPa versus 2.1 MPa) despite the lower crosslink density, likely on account of enhanced supramolecular interactions of the aromatic components. The difference in ductility (99.8% vs. 59.2%) could stem from either lower crosslink density, which often increases ductility, or the influence of aromatic components. The latter is seen, for example, in A100-3S exhibiting higher ductility despite having a higher crosslink density compared to A50M50-4S. These results demonstrate clearly how in terms of mechanical performance A100-4S and A100-3S are the best candidates, with more glassy and rubbery behavior, respectively, at room temperature. We chose A100-4S as the CAN with higher stiffness and strength to go forward to analysis of the dynamic properties and preparation of bioinspired wood-based composites. We chose the addition of 10 wt% acetone as a diluent during the impregnation as it is unlikely to affect the final material properties or network structure.

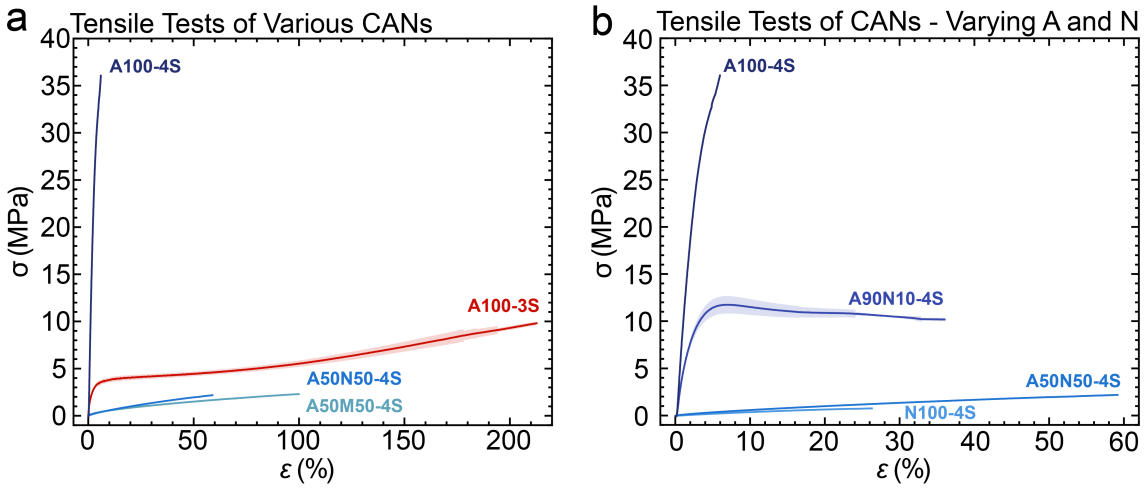

Figure 7. Tensile tests for cured and post-cured CANs (a) A100-4S, A100-3S, A50N50-4S, A50M50-4S, and (b) A100-4S, A90N10-4S, A50N50-4S, and N100-4S.

Table 4. Overview of mechanical properties of AxNyMz-wS.

Sample	σ_b (MPa) ± SE[a)]	ε_b (%) ± SE[a)]	σ_y (MPa) ± SE[a)]	ε_y (%) ± SE[a)]	E (MPa) ± SE[a)]	U_t (MJm^{-3}) ± SE[a)]
A100-4S	37.0 ± 2.0	6.19 ± 0.51	-	-	1074 ± 19	1.48 ± 0.20
A100-3S	9.78 ± 0.28	213 ± 13	3.67 ± 0.30	2.17 ± 0.16	115 ± 11	12.8 ± 0.56
A90N10-4S	11.9 ± 0.82	36.0 ± 8.9	11.5 ± 0.87	2.76 ± 0.12	448 ± 30	3.76 ± 0.96
A50N50-4S	2.14 ± 0.083	59.2 ± 3.3	-	-	4.55 ± 0.064	0.755 ± 0.068
N100-4S	0.745 ± 0.025	26.4 ± 1.7	-	-	3.72 ± 0.12	0.113 ± 0.013
A50M50-4S	2.28 ± 0.084	99.8 ± 8.4	-	-	2.54 ± 0.063	1.42 ± 0.14

[a)] SE refers to the standard error.

3.3.4 A100-4S Thermomechanical Properties and Dynamic Behavior

First, we determined the linear elastic regime of A100-4S for the temperatures 25 °C and 120 °C by small-amplitude oscillatory tests in tensile mode, displaying a small linear elastic regime at 25 °C of ~ 0.1% and a substantially larger regime at 120 °C of > 1% (**Figure 8a**). Both these values are relatively low, which is explained by the high crosslink density as well as the glassy state at 25 °C.

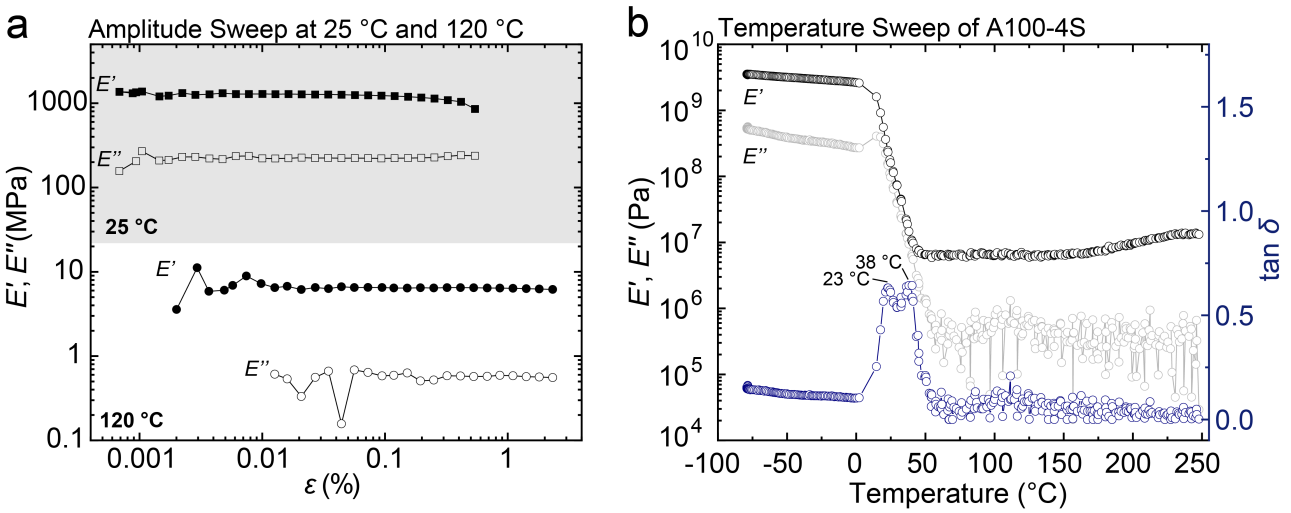

Figure 8. Dynamic mechanical properties of A100-4S. (a) Amplitude sweep measurements obtained by oscillatory experiments in tensile mode at 25 °C and 120 °C. The linear elastic regimes correspond to the ε range where *E'* and *E''* are constant. (b) Thermomechanical properties and glass transition obtained by small-amplitude oscillatory experiments in tensile mode

Next, we conducted a small-amplitude oscillatory temperature sweep experiment of cured (2 h at 120 °C) A100-4S to investigate the thermal response of the CAN at short timescales (frequency f = 1 Hz) where bond exchange likely plays a limited role (**Figure 8b**). The T_g of A100-4S is visible as a decrease of *E'* and *E''* spanning three orders of magnitude from the GPa range to the MPa range. We chose to consider the loss factor, which exhibited two maxima within this transition, to determine the T_g, although there are other methods, such as taking the inflection point of *E'*.[43] In the case of

A100-4S, the loss factor exhibits two maxima, which can indicate heterogeneity in the network due to regions with variable crosslink density, catalyst concentration, crystallinity, etc.[43] This means the T_g by DMA is somewhere in the range of 23 - 38 °C. This is lower than the value obtained from DSC analysis (40.6 °C). It is important to note that different experimental methods lead to different values, which is why it is important to indicate which method is used to determine the T_g.[43–45] For 100-4S, it is clear from both measurements that the material is in the glassy state at room temperature, while being far (100+ °C) above T_g during (re)processing. When shifting focus to the rubbery plateau (where T > 50 °C), we observe constant moduli, with E' ~ 7 MPa and E'' ~ 0.3 MPa, up to a temperature of roughly 164 °C. A constant rubbery plateau is typical for thermosets and indicates a constant crosslink density over the temperature range.[46] In the case of CANs, this indicates that no significant bond dissociation occurs in this range. [22,23,47] However, it does not mean that no bond exchange occurs, merely that the oscillation frequency is too fast to observe significant softening on account of bond exchange. Above a temperature of 164 °C, we observe a small increase in E' up to ~ 14 MPa, while E'' remains the same. This behavior is most likely related to post-curing effects, which is discussed in more detail in later sections. Alternatively, it is sometimes possible for side reactions to occur at higher temperatures or contributions from entropic elasticity, which can be observed in highly crosslinked thermosets and some CANs.[41,48–50]

Finally, it is important to understand the dynamic bond exchange properties of A100-4S before going forward with the preparation of dynamic wood composites. We performed stress relaxation experiments in tensile mode over a wide temperature range, while making sure to measure significantly above the T_g (120 - 220 °C) (**Figure 9**). To fit these data well, we use a stretched exponential function

$$E(t) = E_0 e^{-(t/\tau^*)^{\beta}} \tag{4}$$

wherein, E_0 is the plateau modulus, β is the stretching exponent, and τ^* is the characteristic relaxation time, which encapsulates all relaxation modes. This approach is advantageous in this case as it describes the data better than a single exponential model, while a multi-element approach is non-trivial in terms of its interpretation.[41,51] We present the fits together with the relaxation data (**Table 5**, **Figure 9a**). The CAN exhibits a relaxation response characteristic for materials where covalent bond exchange dominates, as there is a single perceivable relaxation mode, behavior common in many CANs.[32,52,53] Other potential modes of relaxation (*e.g.* monomer friction or supramolecular interactions) cannot be clearly distinguished in the relaxation response.[40,51,54] Similar to the temperature sweep, E_0 deviates only minimally with temperature variations in the stress relaxation experiments, indicating a largely constant crosslink density (**Figure 9b**).[22,23,47] This is indicated by the low activation energy ($E_{a,E0}$ = 2.2 KJmol^{-1}) associated with changes in E_0. Such behavior is typical for CANs that follow an associative mechanism, which is often the case for the standard transesterification reaction where esters undergo nucleophilic attack by hydroxyl groups.[22,23,47] While

some degree of bond dissociation is impossible to rule out, observed small decreases in plateau modulus could also stem from thermal softening via other processes, which even networks with constant crosslink densities (*e.g.* thermosets) can display.[55]

Next, we switch to discussing the temperature dependence of τ^*. Based on the data, the relaxation rates display an Arrhenius-like temperature dependence as is characteristic for CANs.[22,24,51] The activation energy ($E_{a,T}$ = 105 kJmol^{-1}) is within a typical range for catalyzed transesterification reactions.[31,32,56] Stress relaxation is relatively fast at temperatures above 160 °C with relaxations times τ^* < 10 min, while being in the range of hours at lower temperatures. Finally, we constructed a master curve with 160 °C as a reference temperature to visualize the thermodynamic behaviors across a wide temperature range (**Table 5**, **Figure 9c**). This process is based on time-temperature superpositions (TTS), following the definition:

$$E^*(t, T_{\mathrm{ref}}) = (1/b_T)E(t/a_T, T) \tag{5}$$

wherein, b_T shift factors ($b_T = E_0(T)/E_0(T_{\mathrm{ref}})$) convey the temperature-dependence of E_0 and a_T shift factors ($a_T = \tau^*(T)/\tau^*(T_{\mathrm{ref}})$) convey variations in τ^* (Figure S1).[49] The TTS covers the entire temperature range well, which further demonstrates that the stress relaxation is dominated by one relaxation mode corresponding to the covalent bond exchange.[40,51] These results indicate how A100-4S possesses dynamic properties, based predominantly on associative transesterification, which fit well within established epoxy CAN properties. These properties are ideal for applications that do not require ultrafast dynamic behavior, low viscosity, and melting behavior. As a trade-off A100-4S is highly connective and deformation resistant at moderate temperatures, with mechanical properties that are resilient towards moderate temperature changes.

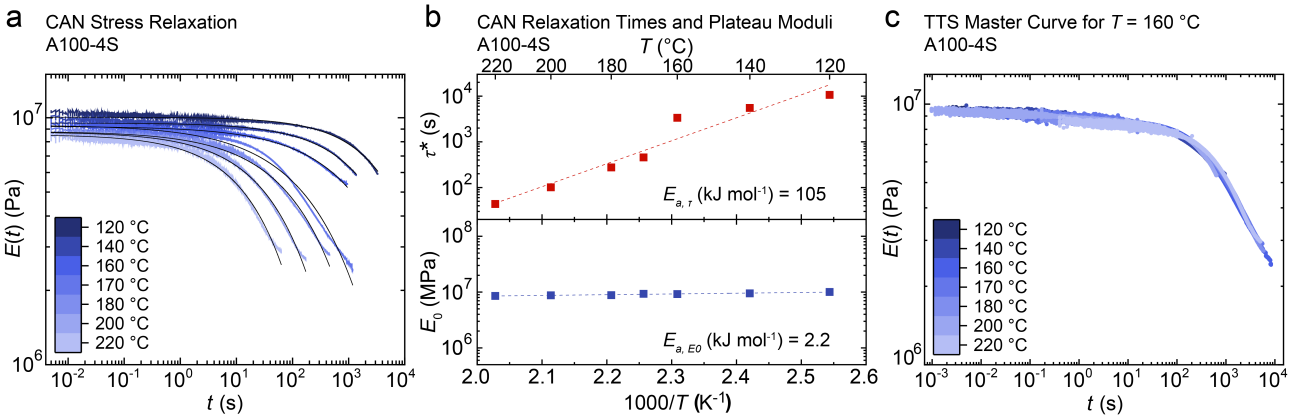

Figure 9. Stress relaxation data of A100-4S obtained across a wide range of temperatures. (a) Stress relaxation curves (colored lines) and corresponding stretched exponential fits (thin black lines) for A100-4S. (b) The fitted data generate Arrhenius plots of τ^* and E_0. (c) The data form a time-temperature superposition master curve at a reference temperature of 160 °C.

Table 5. Parameters of stress relaxation and fitting of A100-4S.

Temperature (°C)	E_0 (MPa)	τ (s)	β	a_T	b_T
120	10.1	10643	0.585	5.13	1.11
140	9.52	5514	0.530	2.25	1.05
160	9.22	3359	0.448	1	1
170	9.35	458	0.422	0.141	0.996
180	8.81	276	0.454	0.0819	0.958
200	8.76	101	0.497	0.0290	0.978
220	8.55	44	0.527	0.0123	0.973

Lastly, we investigate the impact of post-curing on A100-4S. Post-curing is a secondary step performed on cured networks, for example epoxy resins, to induce further crosslinking or improve the final properties of the network.[57,58] Post-curing is usually at higher temperatures than the original curing step, which might induce alternative curing reactions, such as etherification in epoxides. We performed small-amplitude oscillatory shear to follow the curing behavior of A100-4S formulation (**Figure 10**). The network formed at 120 °C, first indicated by the gelation point and then by a plateau in *G'* and *G''*. Next, we increased the temperature to 180 °C for the post-curing process. Immediately, small decreases in *G'* and *G''* were observed which relate to thermal softening or relaxation.[55] Over the next 3 h, *G'* increased from 1.81 to 2.77 MPa and *G''* decreased from 61 kPa to 5.8 kPa. This represents a significant shift towards more elastic behavior. It is important to keep in mind that A100-4S has fast bond exchange at 180 °C. It is conceivable that post-curing in CANs may lead to changes due to the reorganization of the network structure, rather than the formation of additional crosslinks, as no significant changes were observed in the FTIR spectra (**Figure 6**). For instance, network variations, such as backbone dispersity or crosslink distribution, impact the mechanical properties, which might be induced by dynamic bond exchanges.[59–62] Overall, these results demonstrate that a 2 h curing process at 120°C is insufficient to achieve optimal stiffness, which is addressed by a post-curing step (*e.g.* hot pressing for 1 h at 180 °C).

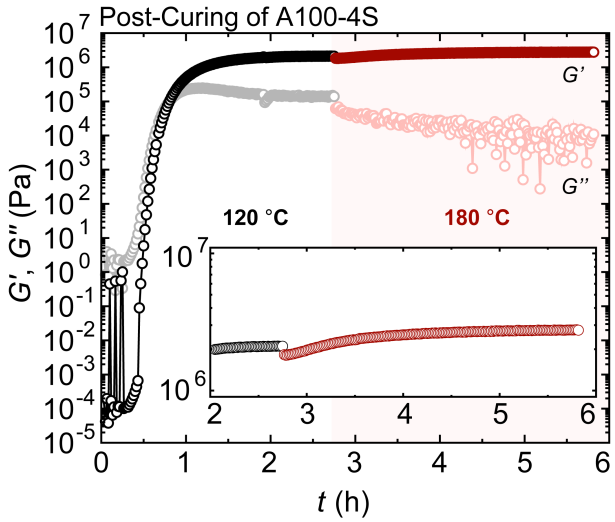

Figure 10. CAN network curing kinetics (obtained by small-amplitude oscillatory shear) of A100-4S when heated at 120 °C, followed by post-curing at 180 °C.

3.3.5 Impregnation of Delignified Wood with CANs to form Transparent Wood-based Composites

After extensive analysis of the pure CAN material, we proceed to the preparation of A100-4S/Wood composites (**Figure 11a-c**). We used spruce as a type of softwood with a high density (~ 450 kg/m^3), to allow for higher cellulose contents and thus large degrees of reinforcement compared to commonly used low density woods, such as balsa (~ 122 kg/m^3).[26–30,63] We delignified spruce veneers (1.3 mm thickness, 10 x 10 cm^2) for 6 h at 80 °C in a hydrogen peroxide and acetic acid solution, followed by aqueous washing steps until the washing solution reached pH > 5 (**Figure 11a,d**). The delignification process plays a major role in enabling the introduction of the CAN phase on account of its enhanced porosity.[2,7,9] The delignified veneers in the aqueous wet state then underwent solvent exchange to ethanol and subsequently to acetone to yield delignified wood soaked in acetone, where the resin is completely soluble to prevent miscibility issues. In addition, the wood must remain in solvent-soaked state to prevent collapse of the hierarchical cellulose structures, ensuring that the lumens, but specifically the intercellular spaces such as the middle lamella, are accessible to allow the resin to infiltrate these areas.[13,29,30] Ethanol and acetone are both sufficiently good swelling agents for wood, after water, so that the micro- and mesopores remain accessible for the CAN formulation.[64,65] Infiltration of A100-4S into the intercellular spaces is crucial for optimizing dynamic properties, as it facilitates effective stress transfer and interfacial interaction between the CAN phase and cellulose across multiple domains of the hierarchical architecture. In contrast, collapse of the intercellular spaces could result in overly rigid structures, limiting the shapeability of the final materials. Next, we carefully submersed the acetone soaked delignified wood veneers in a formulation of A100-4S with 10 wt% acetone as a diluent. Vacuum assisted infiltration

then enabled the combination of the wood and polymer phases, while also evaporating most of the acetone from the mixture.

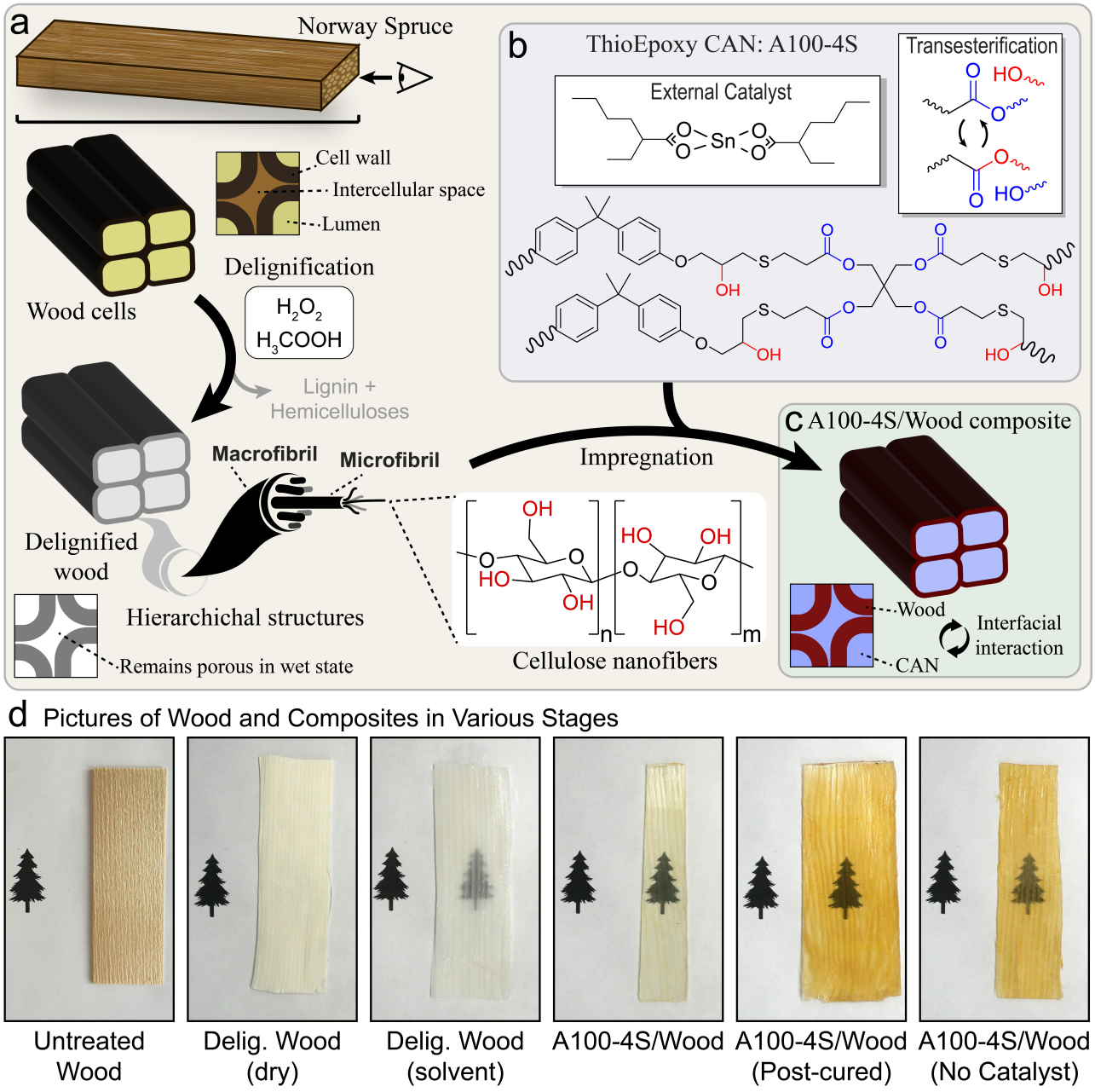

Figure 11. A100-4S/Wood composite preparation outline. (a) Schematic preparation route of delignified wood scaffolds with hierarchical architecture via delignification of Norway spruce. The cellular structures are prevented from collapsing in solvent-soaked state. Cellulose alcohol groups that can engage in transesterification are depicted in red. (b) Molecular depiction of the A100-4S CAN phase. Chemical groups that can participate in transesterification are depicted in blue (esters) and red (alcohols), as well as the net reaction of transesterification. (c) Schematic depiction of the CAN impregnated wood composite. The polymer phase is depicted in blue, infiltrating the lumens and intercellular spaces, whereas the cellulosic structures are depicted in red. (d) Images of the wood in various states of the procedure: untreated wood in the dry state, delignified wood in the dry state, delignified wood in the solvent-soaked state, A100-4S/Wood composite before post-curing, A100-4S/Wood composite after post-curing, and non-dynamic control A100-4S/Wood composite without Sn(II)Oct as catalyst.

Subsequently, the impregnated scaffolds underwent preliminary curing at room temperature (3 days) to allow for controlled acetone evaporation without bubble formation. This process also facilitates an

increase in viscosity that is crucial for preventing excessive flow during the curing step. We then cured the samples by applying heat (120 °C) and pressure (~ 0.4 MPa) for 2 h to yield transparent, smooth, and fully impregnated A100-4S/Wood composites with high content of reinforcement (26.1 wt% delignified wood). The transparency of the samples serves as an initial indicator of effective impregnation, as it suggests the absence of light-scattering interfaces within the wood structure, such as residual voids (**Figure 11d**).[12] Furthermore, the composites underwent a post-curing step (2 h, 180 °C) to obtain the final properties, as is detailed in the next section. In addition, we prepared non-dynamic control composites impregnated with an analogous A100-4S formulation, however crucially lacking any catalyst Sn(II)Oct content. We cured these composites at higher temperature (3 h, 180 °C, 0.4 MPa), followed by the same post-cure to yield non-dynamic polymer/wood composites (27.5 wt% delignified wood).

On a chemical level, we confirm successful impregnation of A100-4S into the delignified spruce veneers and subsequent curing by FTIR (**Figure 12a**). We attribute characteristic bands to various chemical groups in cellulose: O–H stretching for alcohols and acids (3345 cm^{-1}), C–H stretching (2890 cm^{-1}), C–O stretching for secondary alcohols, ethers, esters, and acids (918 - 1180 cm^{-1}), and C–H bending (1215 - 1487 cm^{-1}). By comparing the spectra of the delignified wood and pure A100-4S with the composite, the presence of both phases can be identified. Critically, the spectrum of the A100-4S/Wood composite exhibits the same indication of curing as the pure CANs based on the lacking signals at 914 cm^{-1} and 765 cm^{-1}, corresponding to epoxides, and 2567 cm^{-1}, corresponding to thiols. This demonstrates that the curing of the CAN phase is effective within the composite as well.

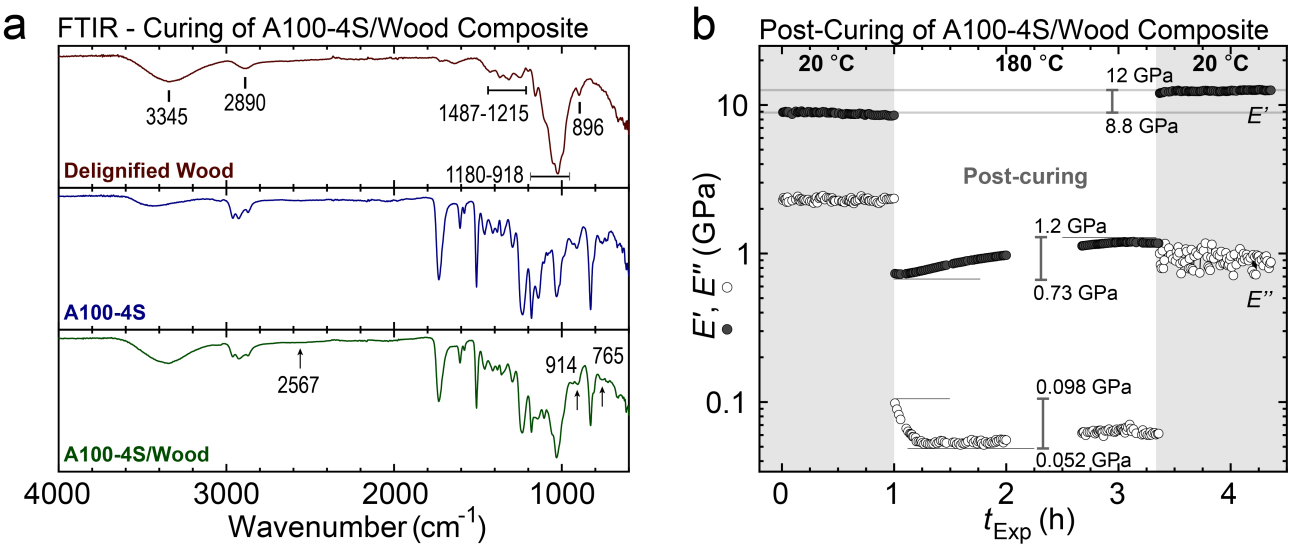

Figure 12. (a) FTIR spectra of delignified wood, A100-4S which is both cured (2 h, 120 °C) and post-cured (1 h, 180 °C), and A100-4S/Wood composite cured (2 h, 120 °C, 0.4 MPa) and then post-cured (3 h at 180 °C). (b) Post-curing of A100-4S/Wood composite measured via small amplitude oscillatory experiments in tensile mode at 20 °C and 180 °C to visualize the evolution of mechanical properties. Grey lines indicate changes in *E'* and *E''*.

We highlight the importance of the post-curing step by evaluating the dynamic mechanical properties of A100-4S/Wood composites after curing via DMA (**Figure 12b**). At 20 °C, both *E'* and *E"* possess large values of roughly 8.8 GPa and 2.3 GPa, respectively. We then proceeded with post-curing at 180 °C, observing substantial instantaneous reduction in *E'* and *E"* by about an order of magnitude. This response mainly reflects the glass transition of A100-4S, as well as potentially further thermal softening of both the polymer phase and wood reinforcement.[66] During the post-cure, *E'* exhibits an increase from 0.7 to 1.2 GPa, whereas *E"* decreases from 0.1 to 0.05 GPa. These changes indicate that the composites shift to a more elastic and resilient state. Subsequent analysis at 20 °C after post-curing, reveals that the changes in *E'* and *E"* are carried over to the rigid state under ambient conditions, with *E'* = 12 GPa and *E"* ~ 0.9 GPa. These changes correspond well with the effect of post-curing on pure A100-4S as previously described. It is crucial to highlight that transesterification proceeds rapidly at 180 °C, which suggests that the post-cure could lead to reorganization of the CAN network or even bond exchange between the CAN-esters and cellulose alcohols, thereby enhancing interfacial interactions. These results illustrate how a post-curing step imbues the A100-4S/Wood composites with higher stiffness and reduced viscosity.

3.3.6 CAN-Induced Cellulose Modification and Mechanical Implications

We used scanning electron microscopy (SEM) to visualize the hierarchical cellular structures of untreated wood, the A100-4S/Wood composites, and A100-4S/Wood(No Catalyst) composites as control samples for comparison (**Figure 13**). The untreated wood displays well-defined cellular structures with porous lumens encapsulated by the cellulose cell walls (**Figure 13a**). Importantly, the intercellular spaces are highly condensed in the dry state. Various cell walls also depict fibrous cellulose pullouts on account of the sample cutting process. Next we discuss the A100-4S/Wood(No Catalyst) composites that were prepared without the use of Sn(II)Oct (**Figure 13b**). The SEM micrographs depict a well impregnated polymer phase that permeates the lumens but also some of the intercellular spaces, indicating good compatibility of the wood and polymer phases. Critically, the cell walls are well-defined and fully intact, although some marks are visible across the samples on account of the sample cutting procedure. Overall, this indicates good polymer infiltration without affecting the cellulose significantly.

In contrast, the A100-4S/Wood composites exhibit even better polymer infiltration with large intercellular areas filled with the CAN phase, even in the condensed latewood areas (**Figure 13c**).

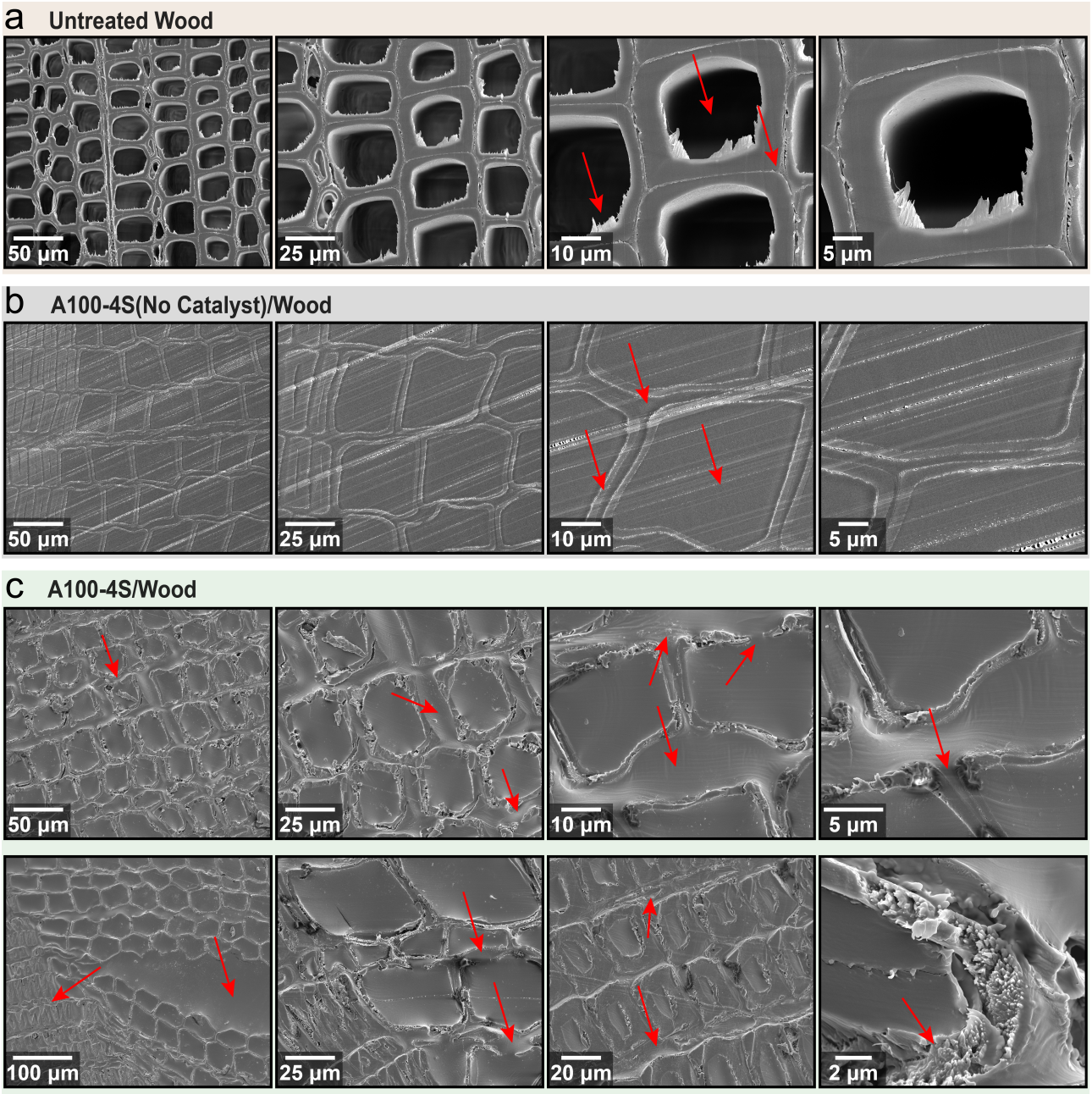

Figure 13. SEM micrographs of (a) untreated wood, (b) A100-4S/Wood(No Catalyst), and (c) A100-4S/Wood composites at various degrees of magnification, depicting cross sections of samples cut perpendicular to the wood fiber directions samples. Earlywood is characterized by larger structures with thinner cell walls, whereas latewood is comprised of more condensed cells with thicker cell walls. Red arrows indicate points of interest: porous lumen, nonporous connected intercellular spaces, and fibrous cellulose structures for untreated wood. For A100-4S/Wood(No Catalyst), red arrows indicate good infiltration of the polymer phase into the lumens and moderate infiltration into intercellular spaces with intact and well-defined cell walls. For A100-4S/Wood composites, red arrows indicate increased degrees of impregnation with big reservoirs of the CAN phase into both lumens and intercellular spaces. In addition, partial dissolution of the cellulose structures is indicated by distorted and dissociated cell walls and smoothened morphology of cellulose fibers.

Crucially, the SEM micrographs reveal evidence of partial dissolution of cellulose components, highlighted by disrupted structural organization, cell wall distortions, and occasional dissociation of cell walls as the CAN phase extends into intercellular spaces from the lumen.[67,68] Additionally, the cellulose morphology is altered, with a less distinct fibrous appearance and a smoother texture, further suggesting partial cellulose dissolution.[69–71] The absence of this phenomenon in the control

samples underscores the critical role of Sn(II)Oct in driving this effect. This observation aligns with the known ability of ionic liquids to dissolve cellulose, as Sn(II)Oct, a metal-organic complex, exhibits partial ionic character.[69,72] Additionally, 4S and A may contribute as cosolvents in facilitating this process, but only in the presence of Sn(II)Oct.[73] Generally, ionic liquids have been utilized to selectively partially dissolve cellulose within cellular wood structures, enabling the modification of wood for specific applications while preserving much of its anisotropic hierarchical architecture.[74–76]

Based on this, the high degree of CAN infiltration observed in A100-4S/Wood composites may be attributed to a combination of plasticizing effects on the cell walls and swelling action of the formulation, which further open the wood pores and enhance infiltration.[67,77] As a result of ionic liquid treatments, wood and cellulose materials with enhanced processability and shapeability have been prepared in the past.[76,78] In our case, partial cellulose dissolution likely also contributes to improved shapeability and shape-memory of A100-4S/Wood composites, as discussed in later sections. In addition to the direct plasticization of cellulose, the superior infiltration and dispersion of the CAN within the wood structure may further contribute by improving interfacial adhesion, allowing the dynamic properties of the CAN to more effectively transfer and relax stresses. Importantly, the SEM analysis shows that the anisotropic architecture of A100-4S/Wood composites is preserved.

To further investigate the effect of cellulose dissolution induced by the CAN formulation, we performed XRD analysis on A100-4S/Wood. As a comparison, we also performed XRD analysis on delignified wood and A100-4S as the individual components and on A100-4S(No Catalyst)/Wood and A100-4S(No Catalyst) as control samples (**Figure 14**, Figures S2-S6). First, we focus on the delignified wood, which exhibits crystallinity as indicated by the presence of multiple relatively sharp signals. The degree of crystallinity was estimated by using:

$$Crystallinity\ (\%) = 100 \times \frac{I_c}{I_a + I_c} = 100 \times \frac{I_{Total} - I_a}{I_{Total}} \quad (6)$$

where I_C is the integral of peaks related to crystallinity, I_a is the integral related to the amorphous halo, and I_{Total} is the total integral.[79] This procedure leads to an estimate of 66% crystallinity for the delignified wood scaffolds, consistent with the semi-crystalline nature of natural cellulose.[80,81] In contrast, the composite material A100-4S/Wood exhibits a broad amorphous halo with minimal crystallinity (ca. 4%). This pattern closely resembles the result of the pure CAN, although the latter bears no indication of any crystallinity. These observations suggest two key conclusions. First, the XRD pattern of the composite primarily reflects the CAN phase, which constitutes 73.9 wt% of the material. Second, the partial dissolution of the cellulose phase significantly reduces its crystallinity, to the point it is almost undetectable. Comparison with the XRD result of the control samples confirms these findings. The polymer control A100-4S(No Catalyst) is fully amorphous, but the control composite A100-4S(No Catalyst)/Wood shows significant crystallinity (27%) attributed to the cellulose phase, despite the material consisting predominantly of polymer (72.5 wt%). This further

demonstrates that the A100-4S, under influence of Sn(II)Oct, induces partial dissolution of the cellulose phase, thereby reducing its crystallinity.

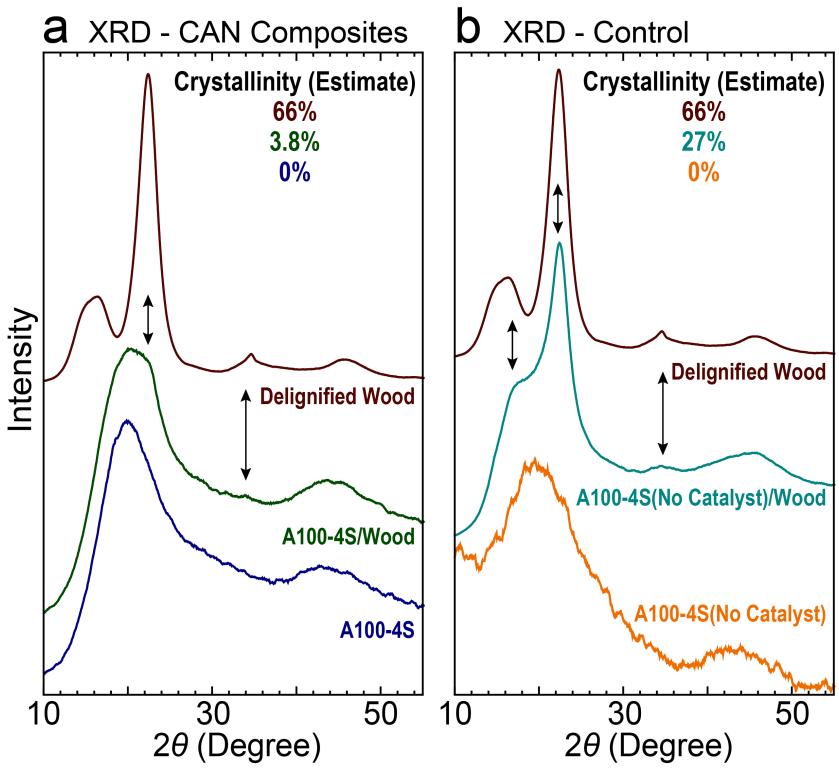

Figure 14. Determination of crystallinity via XRD. (a) XRD patterns of delignified wood, A100-4S/Wood, and A100-4S with crystallinity estimates, indicating reduction in crystallinity for the composite. (b) XRD patterns of delignified wood and the control samples A100-4S(No Catalyst)/Wood and A100-4S(No Catalyst) with crystallinity estimates, indicating cellulose crystallinity in the composite. The crystallinity was estimated by integration of crystallinity peaks and amorphous halo in the range of 10 - 30 2θ. Y-axis is offset for clarity.

We also investigated the mechanical properties in tensile mode for A100-4S/Wood composites in both longitudinal and transverse direction with respect to the wood fibers (**Table 6**, **Figure 15**). In the direction along wood-fibers, there is a significant reinforcing effect compared to the pure CAN material. Primarily, E increases from 1.1 GPa to 5.4 GPa and σ_b from 37 MPa to 49 MPa, accompanied by a reduction in ε_b from 6.2% to 1.1%. These results indicate how the composites in longitudinal direction can exhibit highly deformation-resistant properties, such as for cases that require high creep resistance. When shifting focus to the tensile properties perpendicular to the wood fibers, an entirely different result is obtained, with reductions in E (1.1 GPa to 0.3 GPa) and σ_b (37 MPa to 11 MPa) and a remarkable increase in ε_b from 6.2% to 17.4%. In transverse direction, the polymer matrix largely dictates the mechanical properties because the interaction between fibers is weak in this direction, leading to a softer, more ductile material. It is important to note that the CAN phase does not consist of a cohesive fully connected bulk structure either, but rather populates the pores in between wood fibers. This can explain why the stiffness and strength fall short of the bulk CAN material. Notably, the composite exhibits higher maximum strain than pure CAN, likely due to interfacial interactions between the wood and CAN, which help dissipate energy as wood fibers are strained and reorganized through plastic deformation rather than brittle failure. The mechanical

anisotropy is important to consider for shapeability, which might allow more complex geometries in certain directions, while allowing stiffer geometries in others.

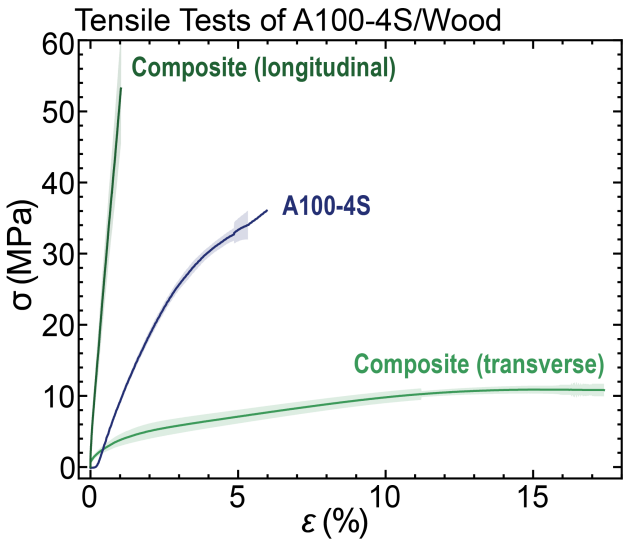

Figure 15. Tensile tests for cured and post-cured A100-4S/Wood composites in longitudinal and transverse direction with respect to the wood fibers. The tensile properties of the pure CAN phase are also depicted for comparison.

Table 6. Overview of mechanical properties of A100-4S and derived wood composites.

Sample	σ_b (MPa) ± SE[a)]	ε_b (%) ± SE[a)]	σ_y (MPa) ± SE[a)]	ε_y (%) ± SE[a)]	E (MPa) ± SE[a)]	U_t (MJm^{-3}) ± SE[a)]
A100-4S[b)]	37.0 ± 2.0	6.19 ± 0.51	-	-	1074 ± 19	1.48 ± 0.20
A100-4S/Wood Transverse	10.9 ± 0.80	17.4 ± 1.2	-	-	293 ± 77	1.43 ± 0.11
A100-4S/Wood Longitudinal	49.4 ± 2.6	1.14 ± 0.12	-	-	5434 ± 700	0.302 ± 0.027
A100-4S/Wood 2nd Life	47.7 ± 1.1	6.58 ± 0.67	-	-	1215 ± 43	2.03 ± 0.29

[a)] SE refers to the standard error.
[b)] Same results as in Table 4 added for comparison.

3.3.7 Thermal Shaping and Shape-Memory Behavior through Dynamic Bond Exchange

To ensure that the partial dissolution of the cellulose structures within the wood does not escalate upon repeated exposure to heat or stress, we investigated the evolution of the dynamic tensile properties over multiple cycles of heating to 140 °C and cooling to 20 °C (**Figure 16**). An instantaneous decrease in both *E′* and *E″* by an order of magnitude occurs upon heating, attributed to the combined effects of the glass transition and thermal softening. Beyond this, the composite retains its mechanical performance over six cycles of heating, totaling 13 hours at 140 °C. The slight decrease in *E″* during this process may indicate some final curing effect. Alternatively, covalent bond formation between CAN and cellulose could occur through bond exchange, affecting chain mobility

and consequently reducing energy dissipation and flow. Similarly, the slight increases observed for *E'* during individual cycles also reflect this. In contrast, *E'* exhibits small decreases when comparing the different cycles at 20 °C. This might relate to the sample's thermal history, which could lead to internal relaxation or reorientation during the heating steps, which then impacts the measurement thereafter. Alternatively, experimental effects due to sample expansion and contraction during heating and cooling may slightly influence the gripping in the DMA device, thereby affecting the results. These results are unlikely to reflect thermally induced network degradation as we see no adverse effects during the heated measurements themselves. Together with the property enhancing effects of the post-cure in **Figure 12b**, this suggests that further cellulose dissolution does not occur after curing when the network is formed. Instead, the liquid Sn(II)Oct formulation at early stages of the infiltration drives the process. Overall, these results indicate how heating the composite samples over multiple cycles does not impact their mechanical performance, allowing for reversible and repeatable shaping at higher temperatures.

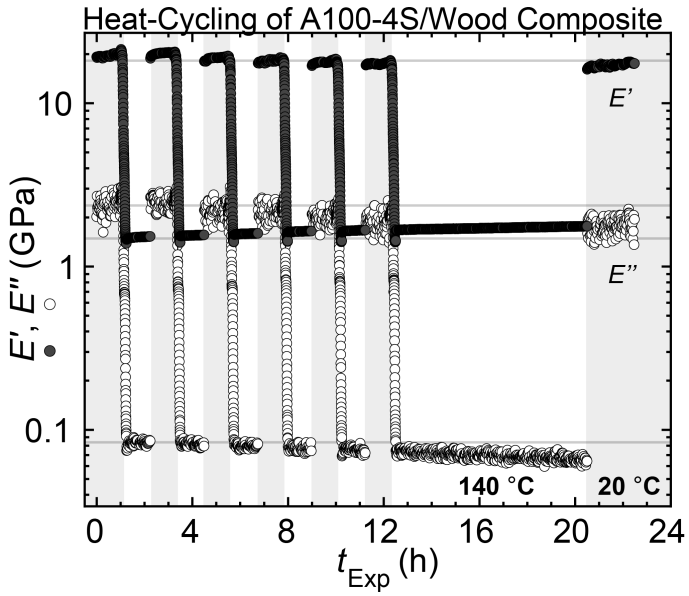

Figure 16. Heat-cycling of post-cured A100-4S/Wood composite measured via small amplitude oscillatory experiments in tensile mode at 20 °C and 140 °C to track the evolution of mechanical properties during repeated heating and cooling. Grey lines indicate initial values of *E'* and *E"* for both 20 °C and 140 °C.

Shaping A100-4S/Wood composites involves two key processes. Elevated temperatures (120 °C) soften the CAN phase by surpassing its T_g and thermally soften the cellulose phase, significantly increasing the strain the composite can endure without fracture. Sustained heating (180 °C) in the desired shape then relaxes internal stresses as the CAN network reorganizes, effectively locking in the new shape. Once cooled, the composite retains the imposed shape upon removal of external stresses. Repeating the process enables more extreme shaping via continuous relaxation of internal stresses, limited only by the maximum bending potential of the wood architecture. We demonstrate this by shaping the composites into full 360° circles in both the transverse and longitudinal directions, the latter being especially notable due to the rigidity of the fibers (**Figure 17a-b**). To push the shaping to more extreme geometries, we induced three-dimensional strains relying on bending in both

transverse and longitudinal directions (**Figure 17c-e**). In this manner, we configured flat composite samples into helix, corkscrew, and Möbius strip geometries, respectively. Such deformations are hard to achieve with other (impregnated) woods, demonstrating the high degree of shapeability of A100-4S/Wood composites on account of the dynamic CAN phase and the partial dissolution of the cellulose structures.

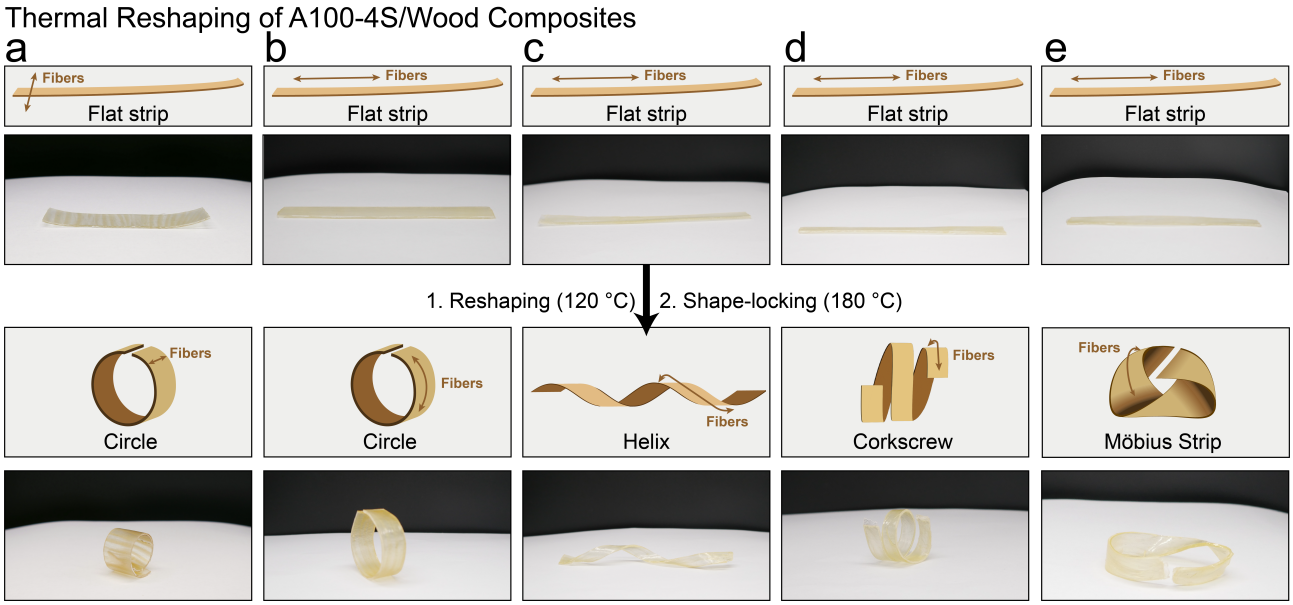

Figure 17. A100-4S/Wood composites after post-curing, formed into a variety of shapes via exposure to heat. Shaping into a circle for both (a) transverse and (b) longitudinal samples is depicted, as well as three-dimensional shaping into (c) helix, (d) corkscrew, and (e) Möbius strip geometries. Heating to 120 °C allows for the flexibility to reshape, whereas heating to 180 °C enables the bond exchange and network reorganization that locks the composite into the new shape permanently.

For the next step, we investigate whether the shape-memory properties associated with the pure CAN can be expressed in A100-4S/Wood composites. This behavior relies on a stable configuration (based on initial samples or adopted via network reorganization) that is subsequently deformed into a secondary shape while accumulating internal stress at an intermediate temperature above the polymer T_g (**Figure 18a**). Cooling to a temperature below the T_g locks the material into the metastable secondary shape while retaining internal stress on account of limited network mobility. When heating the network to a temperature above the T_g again, it dissipates internal stress by returning to the original stable shape. This process occurs at temperatures lower than those required for significant bond exchange within the relevant timeframe.

A100-4S/Wood composites possess shape-memory behavior, demonstrated by taking various shapes configured previously, and temporarily locking them into flat strips at 120 °C (**Figure 18b-f**). Upon exposure to heat the samples then regain their original geometry. For the transverse samples full shape-recovery is possible, whereas the longitudinal samples only regain part of their shape on account of the rigid anisotropic cellulose structures. These results are remarkable considering the high content of reinforcement in these composites (27.5 wt%).

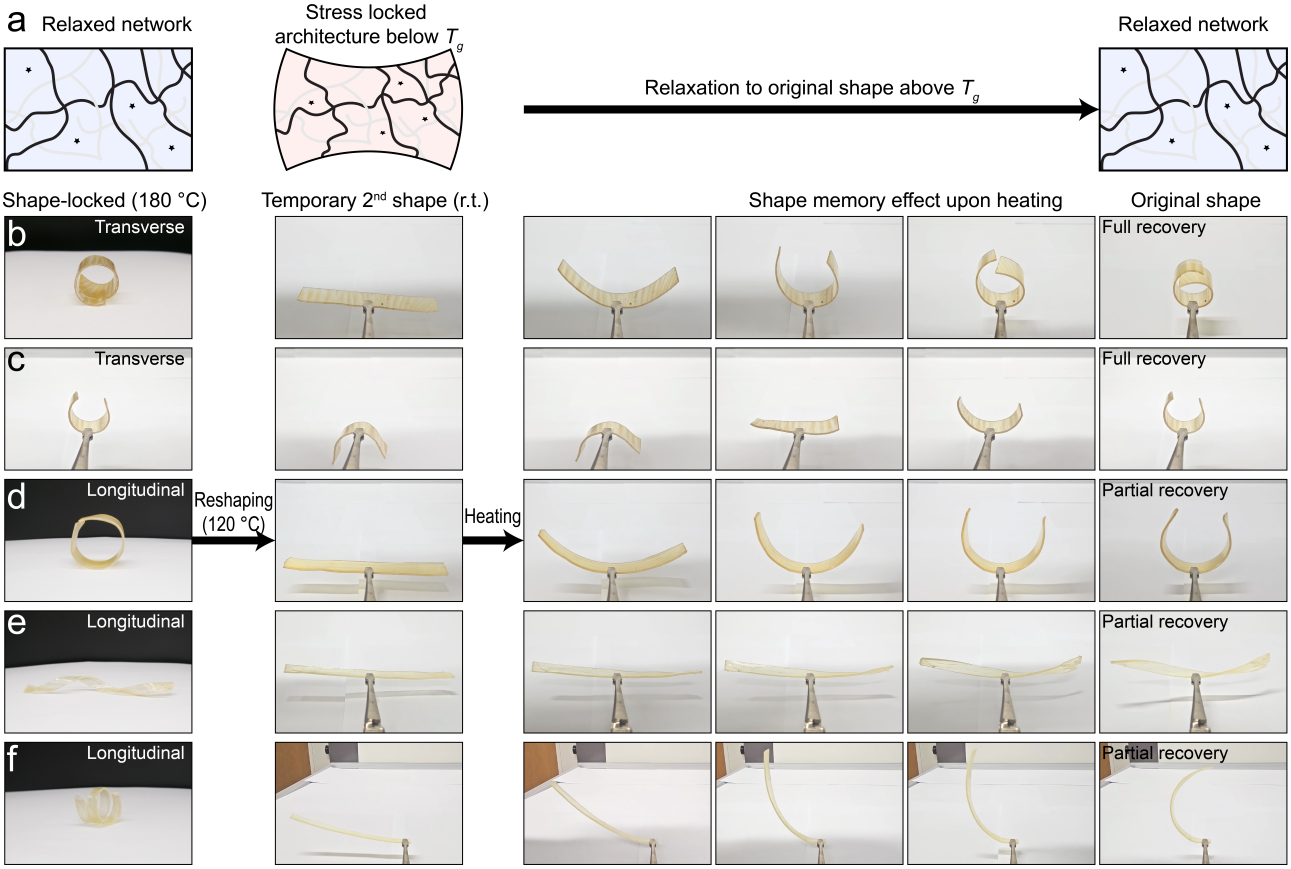

Figure 18. Shape-memory properties of A100-4S/Wood composites (post-cured). (a) Schematic depiction of shape-memory effect: the initial fixed shape is set via network reorganization at 180 °C. Subsequently, the network is deformed into a metastable secondary shape while accumulating internal stress at an intermediate temperature above the polymer phase's T_g, followed by cooling below the T_g to freeze network mobility. When the network is next heated above the T_g, it dissipates internal stress by returning to the original fixed shape. (b-f) Shape-memory effect of A100-4S/Wood composites, illustrated by inducing metastable secondary shape and subsequent (partial) recovery to the original shape. Examples include: (b) circle and strip with transverse fiber direction, (c) circle and inverted circle with transverse fiber direction, (d) circle and strip with longitudinal fiber direction, (e) helix and strip with longitudinal fiber direction, (f) corkscrew and strip with longitudinal fiber direction.

3.3.8 End-of-Life Recycling to form 2nd Life Composites

To make optimal use of the dynamic character of the A100-4S/Wood composite (cured and post-cured), we envision a procedure of end-of-life processing whereby damaged or used-up composites fulfill a 2nd life of application as isotropic CAN/cellulose composites (**Figure 19a**). The combination of efficient network reorientation of the CAN phase and the excellent compatibility of the CAN and cellulose make this form of recycling possible, potentially enhanced by the partial dissolution of the cellulose in the CAN phase by enabling excellent interfacial adhesion and preventing phase separation during the procedure. Ionic liquids are sometimes used in similar fashion to improve the preparation of particulate-based wood composites.[72] Here we can avoid such additives entirely. Our procedure follows the cryogenic milling of the composite parts to obtain a fine powder of the A100-4S and cellulose. We then use compression molding at 170 °C to form homogeneous isotropic

samples in a short timeframe (~ 45 min), in line with the kinetics of stress relaxation observed for A100-4S.

We performed tensile mechanical tests of the recycled 2nd life composites to determine the mechanical performance of the newly obtained materials (**Table 5**, **Figure 19b**). The first observation relates to the isotropic nature of the material as there is no directional dependence on the mechanical properties. By comparing the data with the transverse and longitudinal results from the A100-4S/Wood composites, a distinct pattern emerges, showing a material property space localized between these two extremes: E = 1.2 GPa, in between 0.29 GPa and 5.4 GPa, and ε_b = 6.6%, in between 17.4% and 1.1%, respectively. The strength of the 2nd life composite (σ_b = 48 MPa) is much closer to the A100-4S/Wood composite in the longitudinal direction. Interestingly, in terms of toughness it possesses a superior property (U_t = 2 MJm^{-3}) compared to any of the two original materials. Moreover, it also displays increased properties across the board compared to the pure CAN as well. These results indicate a dynamic CAN/cellulose composite material with improved mechanical properties, that can be recycled from the highly reinforced A100-4S composites at the end of their lifecycle.

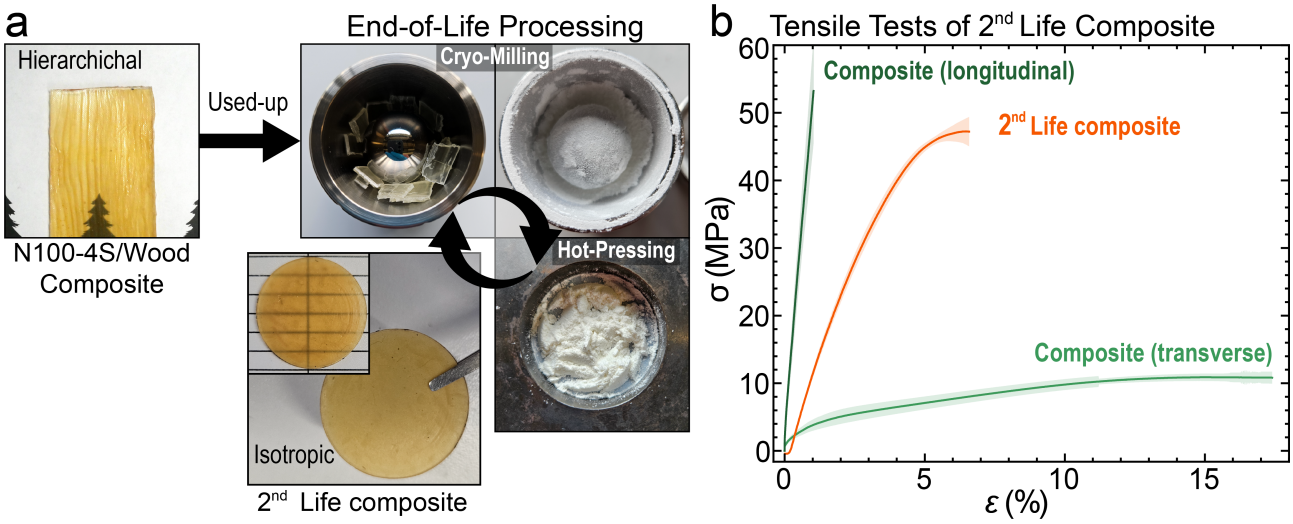

Figure 19. End-of-life recycling of CAN/Wood composites. (a) Images depicting the recycling procedure for A100-4S/Wood composites via cryomilling and subsequent hot-pressing to yield isotropic 2nd life composites. (b) Tensile tests for cured and post-cured CAN A100-4S, cured and post-cured A100-4S/Wood composite in both transverse and longitudinal directions, and for recycled 2nd life A100-4S/Wood composite.

3.4 Conclusion

In conclusion, this work presents transparent, highly shapeable, dynamic wood-based composites with high reinforcement content, achieved through deep infiltration of a CAN phase into delignified wood scaffolds. We optimized the CAN to exhibit low viscosity for effective impregnation prior to curing, good mechanical performance in the glassy state at room temperature, efficient stress relaxation when heated, and compatibility with cellulose. Upon impregnation, the organometallic CAN catalyst induces partial cellulose dissolution of the delignified wood, modifying the internal cellulose structures while retaining the unique hierarchical architecture. This process, akin to wood and cellulose dissolution via ionic liquids, can enhance impregnation, interfacial adhesion, and stress transfer and thus the shapeability of the material. We shaped fully cured composites into complex geometries, including three-dimensional configurations, by leveraging the CAN's dynamic network reorganization. To take full advantage of the dynamic composites, we also demonstrated shape-memory behavior, with full recovery transverse to the wood fibers and partial recovery in the longitudinal direction. Finally, we recycled broken composites into reinforced isotropic 2nd life materials with superior mechanical properties compared to the pure CAN, highlighting the system's compatibility with cellulose.

These wood-based composites represent a significant advancement in the field of anisotropic high-performance materials, offering high reinforcement content coupled with notable deformation resistance at room temperature, while being light weight materials. Moreover, they align with the ever-growing emphasis on sustainable materials, as they are derived from renewable and eco-friendly wood resources. Their advanced shapeability, encompassing fast and reversible reprocessing without reliance on the wet-state, enables the creation of highly curved or even complex three-dimensional geometries, significantly extending their potential use cases. This versatility supports designs requiring pronounced curvature while also enabling reversible on-site shaping for scenarios where materials must be tailored during application. The inclusion of shape-memory properties introduces potential for highly reinforced actuators or programmable reconfiguration. Crucially, this work introduces a novel method to modify internal cellulose structures via partial dissolution during polymer infiltration, thus eliminating the need for separate treatments methods, such as by using ionic liquids. To our knowledge, this is the first documented instance of organometallic catalysts within resin formulations achieving such an effect. The anisotropic hierarchy of wood can also be leveraged for unique properties not discussed in this study, such as optical properties like light scattering and guiding or directional conductivity or insulation properties, which could in turn benefit from advanced shaping, thus broadening the application potential.

Supporting Information

Supporting information: Additional experimental details and methods, materials, and supplementary experimental data.

Acknowledgements

This project has received funding from the European Union's horizon research and innovation programme under the Marie Skłodowska-Curie Grant agreement no. 860911. AW acknowledges funding via a Gutenberg Research Professorship underpinning his Life-Like Materials Program.

Conflict of Interest

The authors declare no conflict of interest.

3.5 Supporting Information

Chapter 3. Three-Dimensional Shaping and Shape-Memory in Transparent Covalent Adaptable Network-Infused Wood Composites

Sjoerd Engels[1], Sophie Marie Koch[2], Ingo Burgert[2] Andreas Walther[1]**

[1]Life-Like Materials and Systems, Department of Chemistry, University of Mainz, Duesbergweg 10-14, 55128 Mainz, Germany.

[2]Wood Materials Science, Institute for Building Materials, ETH Zürich, 8093 Zürich, Switzerland.

3.5.1 Instrumentation

3.5.1.1 Dynamic Mechanical Analysis (DMA)

Shear and tensile mode DMA measurements were performed using a MCR702 MultiDrive from Anton Paar equipped with an oven attachment and 8 mm parallel plate geometries (~ 0.3 mm gap) for shear mode or solid rectangular fixtures for tensile mode (~ 17 x 4 x 1.2 mm^3 for CANs and ~ 36 x 10 x 1.6 mm^3 for composites). For the **curing experiments**, pre-mixed liquid CAN formulations were applied to pre-heated DMA geometries. The gap was adjusted to ensure the formulation filled the cylindrical space. Next, when temperature equalized, small-amplitude oscillatory shear was performed at 1 Hz with 0 N normal force. The measurements were initially stress-controlled, at 10 Pa, until the strain dropped below 0.05%, after which the measurement continued being strain-controlled, at 0.05%. Measurements were performed at 25 °C, 50 °C, or 120 °C. Post-curing of A100-4S was analyzed in the same setup after curing by heating to 180 °C. **The temperature sweep** of A100-4S was performed in tensile mode from -80 to 250 °C at a rate of 1.9 °C min^{-1}, 0.025% strain, and using a frequency of 1 Hz. **Amplitude tests** were performed in tensile mode at 1 Hz and temperatures of 25 °C and 120 °C to determine the linear elastic regime for A100-4S. **Stress relaxation tests** were performed at temperatures ranging from 120 °C to 220 °C at 3% strain. **Composite post-curing** of A100-4S/Wood composites was performed in tensile mode starting at 20 °C, followed by heating to 180 °C, followed by cooling back to 20 °C with 0.2 MPa stress using a frequency of 1 Hz. **Composite heat cycling** of A100-4S/Wood composites was performed in tensile mode with repeated cycles of measurement at 20 °C, followed by heating to 180 °C with 0.2 MPa stress using a frequency of 1 Hz.

3.5.1.2 Differential Scanning Calorimetry (DSC)

Thermal analysis via DSC was performed using a TA Instruments DSC 250 in combination with a TA Instruments RCS 90 cooling system from Waters Corporation, United States. Experiments were performed using a heating rate of 10 K min^{-1}. The instrument was calibrated using indium and n-octane.

3.5.1.3 Fourier Transform Infrared Spectroscopy (FTIR).

FTIR spectra were acquired using a Jasco FT/IR-4100 spectrometer with a frequency range from 4000 to 600 cm^{-1}. The uncured formulation was measured as a liquid, while the cured and post-cured networks as well as the delignified woods and the composites were measured as a fine powder (by cryomilling).

3.5.1.4 Tensile Tests for CANs and for Recycled 2nd Life A100-4S/Wood Composites

Tensile tests for the CAN samples and 2nd life A100-4S/Wood composites were performed at room temperature on a Shimadzu EZ-LX Long-Stroke Model tensile tester equipped with either a 50 N (for A100-3S, A90N10-4S, A50N50-4S, N100-4S, and A50M50-4S) or a 500 N (for A100-4S and 2nd life

A100-4S/Wood composites) load cell. Each of the CANs were prepared as rectangular samples (~ 15 mm x 4 mm) with a thickness of ca. 700 µm. At least five measurements were performed for each material after the samples were conditioned at 50% relative humidity for 24 h, with a strain rate of 30 mm/min. Subsequently, the mean was taken for each set. The Young's modulus (*E*) was determined from the slope of the linear region in the stress/strain curves.

3.5.1.5 Tensile Tests for Bioinspired Wood Composites

The composites were cut to the dimensions of 80 × 10 mm^2 using a circular saw, and beech wood tabs (20 × 10 × 1 mm^3) were glued to the ends of the samples to reinforce the clamping area. The samples were conditioned at 65% relative humidity and 20 °C. Tensile testing was conducted using a Zwick Roell universal testing machine equipped with a 10 kN load cell. An initial clamp distance of 40 mm and a crosshead speed of 1 mm/min were applied, following ISO 527-3.[82] Length changes were measured using a Zwick Roell clip-on extensometer with an initial gauge length of 30 mm.

3.5.1.6 Scanning Electron Microscopy (SEM)

The samples were polished using a Leica UC7 ultramicrotome equipped with a Diatome diamond knife or a Leica RM2255 rotary microtome with a steel blade. The polished samples were then mounted onto SEM stubs, and their edges were coated with silver paint. A 6 nm-thick Pt/Pd sputter coating was applied using a Safematic CCU-010. Scanning electron microscopy (SEM) was performed using a Hitachi SU5000 microscope using 5 kV acceleration voltage and a secondary electron detector.

3.5.1.7 X-Ray Diffraction (XRD)

X-ray diffractograms were recorded in Bragg-Brentano geometry on a Panalytical X'Pert PRO MPD diffractometer using Cu Kα1 X-ray radiation (Ge monochromator). The wood and composite specimens (approx. 10 x 10 mm^2 and placed with the longitudinal-tangential plane facing upwards) were placed on a silicon zero-background sample holder using double-sided tape. The diffractograms were collected between the scattering angles 5° and 80° with a total acquisition time of 75 min and a step size of 0.0334°, while continuously rotating at 15 rpm. For the polymer samples, three measurements were collected and averaged using the HighScore Plus analysis software. The crystallinity of the samples was estimated by integration of the amorphous halo and crystalline peaks in the range of 10 - 30 2θ for each of the diffractograms.

3.5.1.8 Compression Molding (Hot Pressing)

Compression molding was performed on a Collin P 200 E press.

3.5.1.9 Cryomilling

Cryomilling was performed at -200 °C using a Retsch CryoMill to obtain finely powdered samples.

3.5.2 Materials

Bisphenol A diglycidyl ether (A), neopentyl glycol diglycidyl ether (N) (technical grade), glycidyl 2-methylphenyl ether (M) (90%), trimethylolpropane tris(3-mercaptopropionate) (3S) (> 95%), pentaerythritol tetrakis(3-mercaptopropionate) (4S) (> 95%), and tin(II) 2-ethylhexanoate (Sn(II)Oct) (92.5 - 100%) were purchased from Sigma Aldrich (Merck). Acetone (≥ 99.8%) and glacial acetic acid were purchased from Fisher Chemical. Ethanol (≥ 99.8%) was purchased from Carl Roth. Hydrogen peroxide solution (35 wt%) was purchased from Acros Organics. Radial cut norway spruce veneers (Picea abies) (1.3 mm thick, 10 × 10 cm²) were used for delignification.

3.5.3 Synthesis of CAN Networks: A100-3S, A100-4S, A90N10-4S, A50N50-4S, N100-4S, A50M50-4S, and A100-4S(No Catalyst)

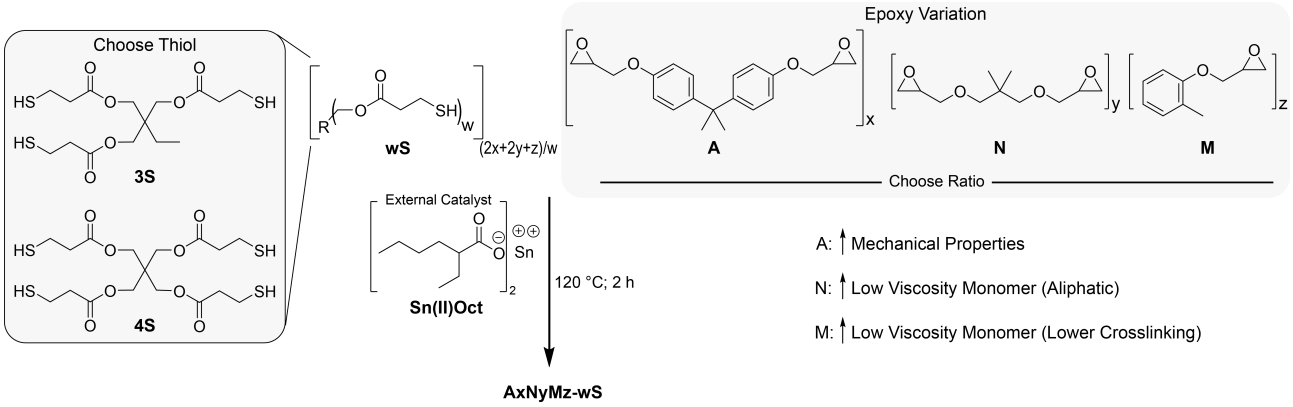

CANs were prepared by thorough mixing of the three types of components: epoxies, thiols, and catalysts. The epoxies used to prepare the various networks are bisphenol A diglycidyl ether (A), neopentyl glycol diglycidyl ether (N) and glycidyl 2-methylphenyl ether (M), where the latter two were used as diluents. The thiols used are trimethylolpropane tris(3-mercaptopropionate) (3S) or pentaerythritol tetrakis(3-mercaptopropionate) (4S). The catalyst used in all networks is tin(II) 2-ethylhexanoate (Sn(II)Oct). Special care was taken to avoid contact between the thiols and catalyst before mixing to prevent aggregation. The general ratios of components used for all networks were chosen so that they contain 5 mol% Sn(II)Oct relative to the ester groups (in 3S or 4S) and so that they have equal quantities of epoxide groups and thiol groups. Upon thorough mixing, it was optional to add acetone (10wt%) as a diluent in dropwise fashion, followed by curing at 120 °C for 2 h and post-curing at 180 °C for 1 h. Post-curing was often done during compression molding (~ 4 MPa) to simultaneously prepare flat disk samples for further analysis. In the case of the control (nondynamic) networks, no Sn(II)Oct was added, and the curing was performed at 170 °C for 3 h.

Based on this general procedure, seven different networks were prepared based on using either 3S or 4S as a thiol and varying the ratios of epoxies A, N, and M: A100-3S, A100-4S, A90N10-4S, A50N50-4S, N100-4S, A50M50-4S, and A100-4S(No Catalyst) as described in **Table 1**.

3.5.4 Delignification of Wood Scaffolds

Radially cut Norway spruce (*Picea abies*) veneers (1.3 mm-thick and measuring 10 × 10 cm²) were delignified using an equal-volume mixture of aqueous hydrogen peroxide (35 wt%) and glacial acetic acid, following the method described by Frey et al.[8] The veneers were soaked in the delignification solution overnight, then subjected to delignification at 80 °C for 6 hours. Afterward, the samples were washed with deionized water until the washing solution reached a neutral pH (pH = 7). Following washing, the veneers were stored submerged in deionized water while never being dried.

3.5.5 Delignified Wood Solvent Exchange

The never-dried delignified wood scaffolds were taken from their water storage and submerged in a mixture of water and ethanol (1/1 v/v) while stirring for ca. 2 h. Next, the scaffolds were transferred to pure ethanol and again stirred for ca. 2 h. This process was repeated for a mixture of ethanol and acetone (1/1 v/v) and three times for pure acetone, finally being stored in the last acetone wash until impregnation to prevent drying.

3.5.6 Preparation of Bioinspired A100-4S/Wood Composites

A100-4S/Wood composites were prepared by first preparing the mixed formulation for A100-4S following the procedure described above, including the addition of 10wt% acetone as a diluent. Next, delignified wood scaffolds in the acetone-soaked state were submerged in CAN formulation, weighing them down with a metal mesh to ensure they remained submerged. Subsequently, impregnation was assisted by applying reduced pressure (~ 100 mbar) for ca. 10 min and then repressurizing to allow infiltration. This process was repeated for four cycles. The scaffolds were precured for 3 days at room temperature to allow controlled viscosity increases, resin shrinkage, and evaporation of the acetone. Afterwards, excess formulation was removed from the scaffolds, and they were cured by heating under mechanical pressure (2 h, 120 °C, 0.4 MPa). Afterwards the samples were also post-cured to enhance the mechanical properties further (2 h, 180 °C). In the case of the nondynamic control composites, A100-4S(No Catalyst) was used for impregnation, and the curing process was done for 3 h, 180 °C, 0.4 MPa.

3.5.7 Preparation of 2nd Life Composites

To prepare 2nd life composites, broken samples of A100-4S/Wood composites were cut into square pieces (~ 10 x 10 mm^2) and cryomilled to obtain fine CAN/cellulose powders. These powders were then compression molded (~ 1 h, 170 °C, 0.4 MPa) to form smooth and flat isotropic samples.

3.5.8 Swelling Tests (Insoluble Fraction Determination)

The insoluble fractions were determined by swelling the fully cured and post-cured CAN networks (ca. 100 mg) in acetone (10 mL) for each of the six different CANs (A100-4S, A100-3S, A90N10-4S, A50N50-4S, N100-4S, A50M50-4S) for 48 h. Then, the insoluble fractions were weighed after the liquid phases were removed and the samples were dried by vacuum.

3.5.9 Composite Weight Content Determination

The weight fraction of the delignified wood component in A100-4S/Wood composites was determined by taking the dry weight of the delignified wood scaffolds and comparing it to the dry weight of cured composites.

3.5.10 Composite Shaping

A100-4S/Wood composites were shaped by oven heating samples (~ 120 °C) to allow shaping to a desired configuration and fixing it in place. Next, a heating step at 180 °C was performed for 1 h to lock in the shape. The process was repeated to form more extreme shapes.

3.5.11 Shape-Memory Tests

Shape-memory tests were performed on previously shaped samples. They were heated to ~ 100 °C and strained into flat configurations, after which they were cooled down to room temperature while fixed in this position. Then by heating above T_g they regained their original shape.

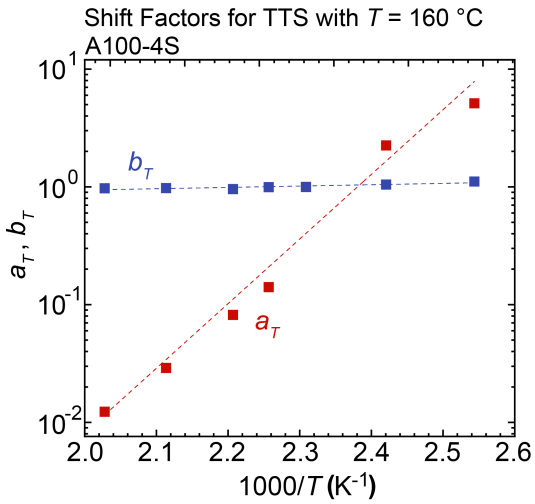

Figure S1. Temperature dependence of shift factors a_T and b_T, obtained via TTS of the stretched exponential fits corresponding to the stress relaxation data for A100-4S.

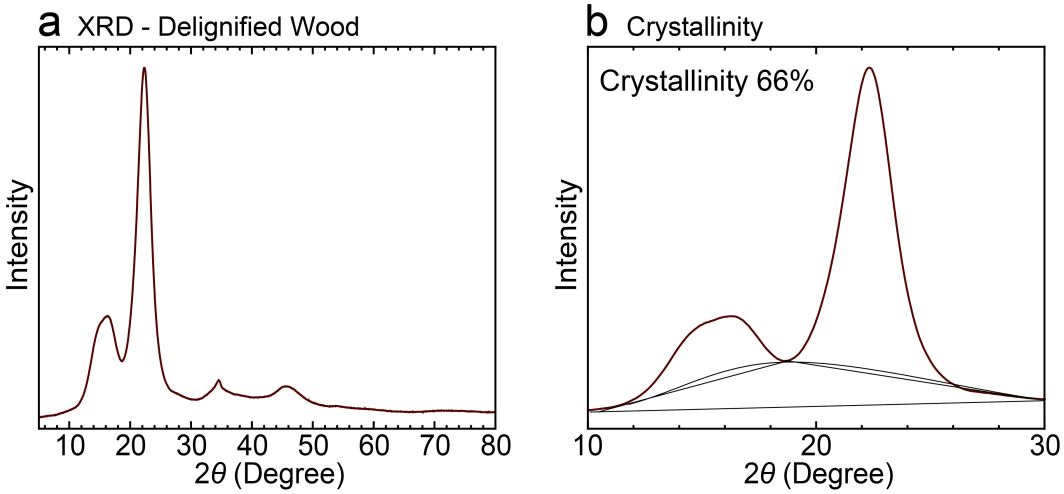

Figure S2. (a) XRD pattern of delignified wood sample illustrating the crystalline peaks. (b) The crystallinity was estimated by integration of amorphous halo and crystalline peaks in the range of 10 - 30 2θ.

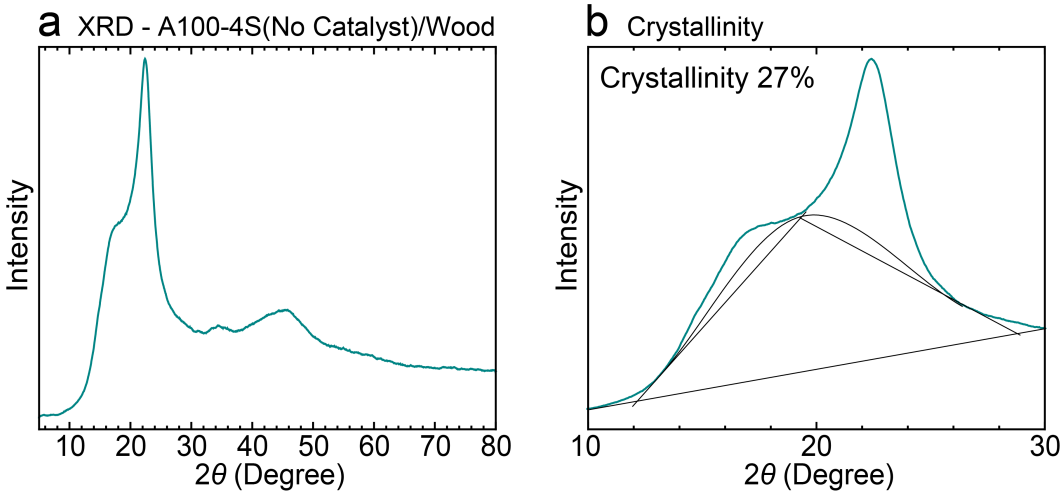

Figure S3. (a) XRD pattern of A100-4S(No Catalyst)/Wood composite sample illustrating the crystalline peaks and amorphous halo. (b) The crystallinity was estimated by integration of amorphous halo and crystalline peaks in the range of 10 - 30 2θ.

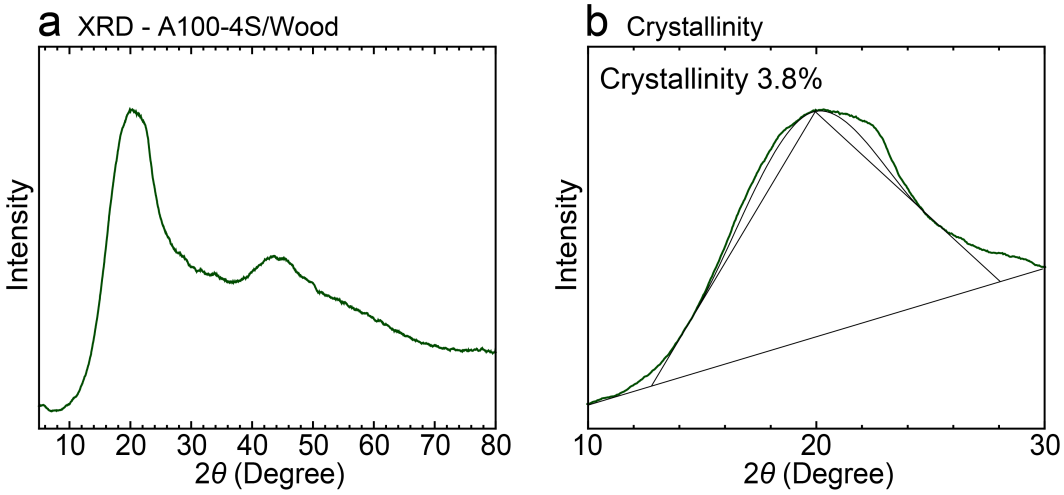

Figure S4. (a) XRD pattern of A100-4S/Wood composite sample illustrating the big amorphous halo with slight crystallinity. (b) The crystallinity was estimated by integration of amorphous halo and crystalline peaks in the range of 10 - 30 2θ.

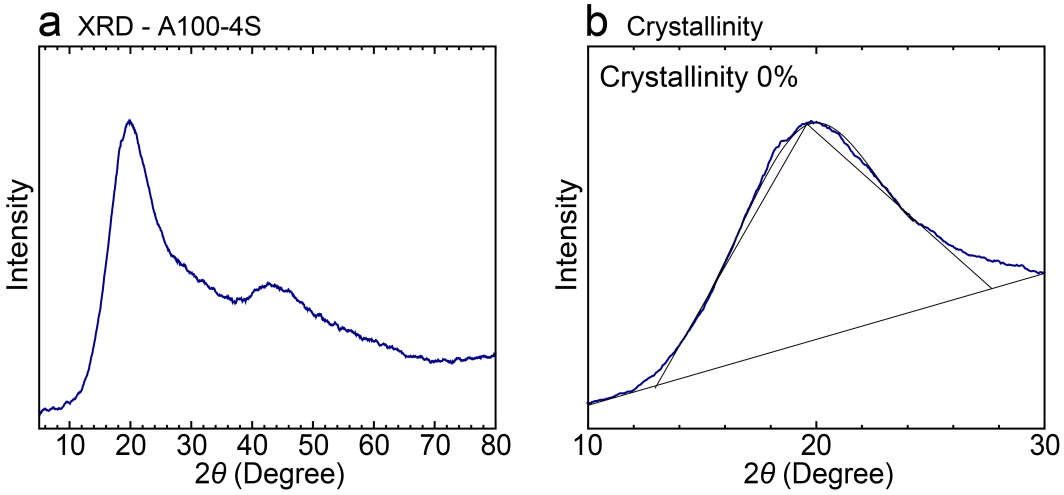

Figure S5. (a) XRD pattern of A100-4S polymer sample illustrating the big amorphous halo. (b) The crystallinity was estimated by integration of amorphous halo (no crystalline peaks) in the range of 10 - 30 2θ.

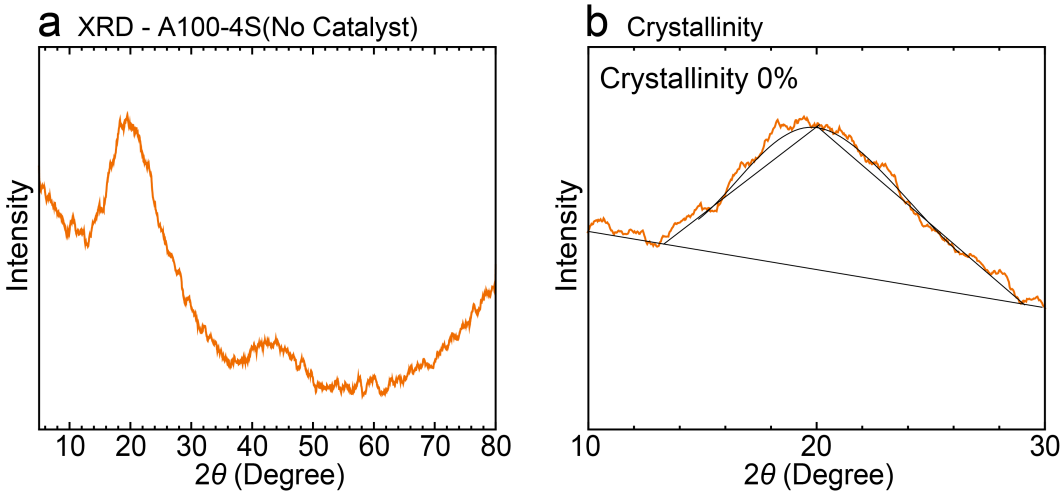

Figure S6. (a) XRD pattern of A100-4S(No Catalyst) polymer sample illustrating the amorphous halo. (b) The crystallinity was estimated by integration of amorphous halo (no crystalline peaks) in the range of 10 - 30 2θ.

3.6 References

(1) Titirici, M.; Baird, S. G.; Sparks, T. D.; Yang, S. M.; Brandt-Talbot, A.; Hosseinaei, O.; Harper, D. P.; Parker, R. M.; Vignolini, S.; Berglund, L. A.; Li, Y.; Gao, H.-L.; Mao, L.-B.; Yu, S.-H.; Díez, N.; Ferrero, G. A.; Sevilla, M.; Szilágyi, P. Á.; Stubbs, C. J.; Worch, J. C.; Huang, Y.; Luscombe, C. K.; Lee, K.-Y.; Luo, H.; Platts, M. J.; Tiwari, D.; Kovalevskiy, D.; Fermin, D. J.; Au, H.; Alptekin, H.; Crespo-Ribadeneyra, M.; Ting, V. P.; Fellinger, T.-P.; Barrio, J.; Westhead, O.; Roy, C.; Stephens, I. E. L.; Nicolae, S. A.; Sarma, S. C.; Oates, R. P.; Wang, C.-G.; Li, Z.; Loh, X. J.; Myers, R. J.; Heeren, N.; Grégoire, A.; Périssé, C.; Zhao, X.; Vodovotz, Y.; Earley, B.; Finnveden, G.; Björklund, A.; Harper, G. D. J.; Walton, A.; Anderson, P. A. The Sustainable Materials Roadmap. *J. Phys. Mater.* **2022**, *5* (3), 032001. https://doi.org/10.1088/2515-7639/ac4ee5.

(2) Kumar, A.; Jyske, T.; Petrič, M. Delignified Wood from Understanding the Hierarchically Aligned Cellulosic Structures to Creating Novel Functional Materials: A Review. *Adv. Sustain. Syst.* **2021**, *5* (5), 2000251. https://doi.org/10.1002/adsu.202000251.

(3) Chen, C.; Kuang, Y.; Zhu, S.; Burgert, I.; Keplinger, T.; Gong, A.; Li, T.; Berglund, L.; Eichhorn, S. J.; Hu, L. Structure–Property–Function Relationships of Natural and Engineered Wood. *Nat. Rev. Mater.* **2020**, *5* (9), 642–666. https://doi.org/10.1038/s41578-020-0195-z.

(4) Fratzl, P.; Weinkamer, R. Nature's Hierarchical Materials. *Prog. Mater. Sci.* **2007**, *52* (8), 1263–1334. https://doi.org/10.1016/j.pmatsci.2007.06.001.

(5) Xiao, S.; Chen, C.; Xia, Q.; Liu, Y.; Yao, Y.; Chen, Q.; Hartsfield, M.; Brozena, A.; Tu, K.; Eichhorn, S. J.; Yao, Y.; Li, J.; Gan, W.; Shi, S. Q.; Yang, V. W.; Lo Ricco, M.; Zhu, J. Y.; Burgert, I.; Luo, A.; Li, T.; Hu, L. Lightweight, Strong, Moldable Wood via Cell Wall Engineering as a Sustainable Structural Material. *Science* **2021**, *374* (6566), 465–471. https://doi.org/10.1126/science.abg9556.

(6) Shams, M. I.; Yano, H.; Endou, K. Compressive Deformation of Wood Impregnated with Low Molecular Weight Phenol Formaldehyde (PF) Resin III: Effects of Sodium Chlorite Treatment. *J. Wood Sci.* **2005**, *51* (3), 234–238. https://doi.org/10.1007/s10086-004-0638-y.

(7) Yano, H.; Hirose, A.; Collins, P. J.; Yazaki, Y. Effects of the Removal of Matrix Substances as a Pretreatment in the Production of High Strength Resin Impregnated Wood Based Materials. *J. Mater. Sci. Lett.* **2001**, *20* (12), 1125–1126. https://doi.org/10.1023/A:1010992307614.

(8) Frey, M.; Widner, D.; Segmehl, J. S.; Casdorff, K.; Keplinger, T.; Burgert, I. Delignified and Densified Cellulose Bulk Materials with Excellent Tensile Properties for Sustainable Engineering. *ACS Appl. Mater. Interfaces* **2018**, *10* (5), 5030–5037. https://doi.org/10.1021/acsami.7b18646.

(9) Grönquist, P.; Frey, M.; Keplinger, T.; Burgert, I. Mesoporosity of Delignified Wood Investigated by Water Vapor Sorption. *ACS Omega* **2019**, *4* (7), 12425–12431. https://doi.org/10.1021/acsomega.9b00862.

(10) Keplinger, T.; Wittel, F. K.; Rüggeberg, M.; Burgert, I. Wood Derived Cellulose Scaffolds—Processing and Mechanics. *Adv. Mater.* **2021**, *33* (28), 2001375. https://doi.org/10.1002/adma.202001375.

(11) Jungstedt, E.; Montanari, C.; Östlund, S.; Berglund, L. Mechanical Properties of Transparent High Strength Biocomposites from Delignified Wood Veneer. *Compos. Part Appl. Sci. Manuf.* **2020**, *133*, 105853. https://doi.org/10.1016/j.compositesa.2020.105853.

(12) Li, Y.; Vasileva, E.; Sychugov, I.; Popov, S.; Berglund, L. Optically Transparent Wood: Recent Progress, Opportunities, and Challenges. *Adv. Opt. Mater.* **2018**, *6* (14), 1800059. https://doi.org/10.1002/adom.201800059.

(13) Frey, M.; Schneider, L.; Masania, K.; Keplinger, T.; Burgert, I. Delignified Wood–Polymer Interpenetrating Composites Exceeding the Rule of Mixtures. *ACS Appl. Mater. Interfaces* **2019**, *11* (38), 35305–35311. https://doi.org/10.1021/acsami.9b11105.

(14) Yu, Z.-L.; Yang, N.; Zhou, L.-C.; Ma, Z.-Y.; Zhu, Y.-B.; Lu, Y.-Y.; Qin, B.; Xing, W.-Y.; Ma, T.; Li, S.-C.; Gao, H.-L.; Wu, H.-A.; Yu, S.-H. Bioinspired Polymeric Woods. *Sci. Adv.* **2018**, *4* (8), eaat7223. https://doi.org/10.1126/sciadv.aat7223.

(15) Zhang, Y.; Chen, Z.; Du, K.; Bi, Y.; Su, J.; Zhang, Y.; Shen, Y.; Zhang, S. Functional Natural Wood-Plastic Composites: A Review of Antimicrobial Properties and Their Influencing Factors. *Ind. Crops Prod.* **2023**, *201*, 116705. https://doi.org/10.1016/j.indcrop.2023.116705.

(16) Li, T.; Song, J.; Zhao, X.; Yang, Z.; Pastel, G.; Xu, S.; Jia, C.; Dai, J.; Chen, C.; Gong, A.; Jiang, F.; Yao, Y.; Fan, T.; Yang, B.; Wågberg, L.; Yang, R.; Hu, L. Anisotropic, Lightweight, Strong, and Super Thermally Insulating Nanowood with Naturally Aligned Nanocellulose. *Sci. Adv.* **2018**, *4* (3), eaar3724. https://doi.org/10.1126/sciadv.aar3724.

(17) Yang, Z.; Meng, X.; Zeng, G.; Wei, J.; Wang, C.; Yu, W. Effect of Resin Content on the Structure, Water Resistance and Mechanical Properties of High-Density Bamboo Scrimbers. *Polymers* **2024**, *16* (6), 797. https://doi.org/10.3390/polym16060797.
(18) Frey, M.; Biffi, G.; Adobes-Vidal, M.; Zirkelbach, M.; Wang, Y.; Tu, K.; Hirt, A. M.; Masania, K.; Burgert, I.; Keplinger, T. Tunable Wood by Reversible Interlocking and Bioinspired Mechanical Gradients. *Adv. Sci.* **2019**, *6* (10), 1802190. https://doi.org/10.1002/advs.201802190.
(19) Grönquist, P.; Wood, D.; Hassani, M. M.; Wittel, F. K.; Menges, A.; Rüggeberg, M. Analysis of Hygroscopic Self-Shaping Wood at Large Scale for Curved Mass Timber Structures. *Sci. Adv.* **2019**, *5* (9), eaax1311. https://doi.org/10.1126/sciadv.aax1311.
(20) Xia, Q.; Chen, C.; Yao, Y.; He, S.; Wang, X.; Li, J.; Gao, J.; Gan, W.; Jiang, B.; Cui, M.; Hu, L. In Situ Lignin Modification toward Photonic Wood. *Adv. Mater.* **2021**, *33* (8), 2001588. https://doi.org/10.1002/adma.202001588.
(21) Koch, S. M.; Pillon, M.; Keplinger, T.; Dreimol, C. H.; Weinkötz, S.; Burgert, I. Intercellular Matrix Infiltration Improves the Wet Strength of Delignified Wood Composites. *ACS Appl. Mater. Interfaces* **2022**, *14* (27), 31216–31224. https://doi.org/10.1021/acsami.2c04014.
(22) Van Zee, N. J.; Nicolaÿ, R. Vitrimers: Permanently Crosslinked Polymers with Dynamic Network Topology. *Prog. Polym. Sci.* **2020**, *104*, 101233. https://doi.org/10.1016/j.progpolymsci.2020.101233.
(23) Scheutz, G. M.; Lessard, J. J.; Sims, M. B.; Sumerlin, B. S. Adaptable Crosslinks in Polymeric Materials: Resolving the Intersection of Thermoplastics and Thermosets. *J. Am. Chem. Soc.* **2019**, *141* (41), 16181–16196. https://doi.org/10.1021/jacs.9b07922.
(24) Denissen, W.; Winne, J. M.; Du Prez, F. E. Vitrimers: Permanent Organic Networks with Glass-like Fluidity. *Chem. Sci.* **2016**, *7* (1), 30–38. https://doi.org/10.1039/C5SC02223A.
(25) Wang, K.; Dong, Y.; Ling, Z.; Liu, X.; Shi, S. Q.; Li, J. Transparent Wood Developed by Introducing Epoxy Vitrimers into a Delignified Wood Template. *Compos. Sci. Technol.* **2021**, *207*, 108690. https://doi.org/10.1016/j.compscitech.2021.108690.
(26) Wang, K.; Liu, X.; Dong, Y.; Ling, Z.; Cai, Y.; Tian, D.; Fang, Z.; Li, J. Editable Shape-Memory Transparent Wood Based on Epoxy-Based Dynamic Covalent Polymer with Excellent Optical and Thermal Management for Smart Building Materials. *Cellulose* **2022**, *29* (14), 7955–7972. https://doi.org/10.1007/s10570-022-04754-9.
(27) Wang, K.; Zhang, T.; Li, C.; Xiao, X.; Tang, Y.; Fang, X.; Peng, H.; Liu, X.; Dong, Y.; Cai, Y.; Tian, D.; Li, Y.; Li, J. Shape-Reconfigurable Transparent Wood Based on Solid-State Plasticity of Polythiourethane for Smart Building Materials with Tunable Light Guiding, Energy Saving, and Fire Alarm Actuating Functions. *Compos. Part B Eng.* **2022**, *246*, 110260. https://doi.org/10.1016/j.compositesb.2022.110260.
(28) Tan, Y.; Wang, K.; Dong, Y.; Gong, S.; Shi, S. Q.; Li, J. High Performance, Shape Manipulatable Transparent Wood Based on Delignified Wood Framework and Exchangeable Dynamic Covalent Vitrimers. *Chem. Eng. J.* **2022**, *448*, 137487. https://doi.org/10.1016/j.cej.2022.137487.
(29) Höglund, M.; Johansson, M.; Sychugov, I.; Berglund, L. A. Transparent Wood Biocomposites by Fast UV-Curing for Reduced Light-Scattering through Wood/Thiol–Ene Interface Design. *ACS Appl. Mater. Interfaces* **2020**, *12* (41), 46914–46922. https://doi.org/10.1021/acsami.0c12505.
(30) Li, Y.; Fu, Q.; Yu, S.; Yan, M.; Berglund, L. Optically Transparent Wood from a Nanoporous Cellulosic Template: Combining Functional and Structural Performance. *Biomacromolecules* **2016**, *17* (4), 1358–1364. https://doi.org/10.1021/acs.biomac.6b00145.
(31) Hayashi, M.; Katayama, A. Preparation of Colorless, Highly Transparent, Epoxy-Based Vitrimers by the Thiol-Epoxy Click Reaction and Evaluation of Their Shape-Memory Properties. *ACS Appl. Polym. Mater.* **2020**, *2* (6), 2452–2457. https://doi.org/10.1021/acsapm.0c00397.
(32) Montarnal, D.; Capelot, M.; Tournilhac, F.; Leibler, L. Silica-Like Malleable Materials from Permanent Organic Networks. *Science* **2011**, *334* (6058), 965–968. https://doi.org/10.1126/science.1212648.
(33) Canadell, J.; Goossens, H.; Klumperman, B. Self-Healing Materials Based on Disulfide Links. *Macromolecules* **2011**, *44* (8), 2536–2541. https://doi.org/10.1021/ma2001492.
(34) Nair, D. P.; Podgórski, M.; Chatani, S.; Gong, T.; Xi, W.; Fenoli, C. R.; Bowman, C. N. The Thiol-Michael Addition Click Reaction: A Powerful and Widely Used Tool in Materials Chemistry. *Chem. Mater.* **2014**, *26* (1), 724–744. https://doi.org/10.1021/cm402180t.
(35) Ferry, J. D. *Viscoelastic Properties of Polymers*, 3rd ed.; John Wiley & Sons, 1980.

(36) Peleg, M. Temperature–Viscosity Models Reassessed. *Crit. Rev. Food Sci. Nutr.* **2018**, *58* (15), 2663–2672. https://doi.org/10.1080/10408398.2017.1325836.
(37) Schoustra, S. K.; Asadi, V.; Smulders, M. M. J. Probing the Solubility of Imine-Based Covalent Adaptable Networks. *ACS Appl. Polym. Mater.* **2023**, *6* (1), 79–89. https://doi.org/10.1021/acsapm.3c01472.
(38) Breuillac, A.; Kassalias, A.; Nicolaÿ, R. Polybutadiene Vitrimers Based on Dioxaborolane Chemistry and Dual Networks with Static and Dynamic Cross-Links. *Macromolecules* **2019**, *52* (18), 7102–7113. https://doi.org/10.1021/acs.macromol.9b01288.
(39) Pavia, D. L.; Lampman, G. M.; Kriz, G. S. *Introduction to Spectroscopy: A Guide for Students of Organic Chemistry*; Harcourt College Publishers, 2001.
(40) Ricarte, R. G.; Shanbhag, S. A Tutorial Review of Linear Rheology for Polymer Chemists: Basics and Best Practices for Covalent Adaptable Networks. *Polym. Chem.* **2024**, *15*, 815–846. https://doi.org/10.1039/D3PY01367G.
(41) Porath, L. E.; Evans, C. M. Importance of Broad Temperature Windows and Multiple Rheological Approaches for Probing Viscoelasticity and Entropic Elasticity in Vitrimers. *Macromolecules* **2021**, *54* (10), 4782–4791. https://doi.org/10.1021/acs.macromol.0c02800.
(42) Flory, P. J. *Principles of Polymer Chemistry*; Cornell University Press, 1953.
(43) Whitcomb, K. *TA Instruments - Measurement of Glass Transition Temperatures by Dynamic Mechanical Analysis and Rheology*; RH100; TA Instruments; pp 1–5. https://www.tainstruments.com/pdf/literature/RH100.pdf (accessed 2024-11-19).
(44) *TA Instruments - Overview of Glass Transition Analysis by Differential Scanning Calorimetry*; TA443; TA Instruments; pp 1–5. https://www.tainstruments.com/pdf/literature/TA443.pdf (accessed 2024-11-19).
(45) Gracia-Fernández, C. A.; Gómez-Barreiro, S.; López-Beceiro, J.; Tarrío Saavedra, J.; Naya, S.; Artiaga, R. Comparative Study of the Dynamic Glass Transition Temperature by DMA and TMDSC. *Polym. Test.* **2010**, *29* (8), 1002–1006. https://doi.org/10.1016/j.polymertesting.2010.09.005.
(46) Chen, T. T. *TA Instruments - Quantifying Polymer Crosslinking Density Using Rheology and DMA*; RH102; TA Instruments. https://www.tainstruments.com/pdf/literature/RH102.pdf (accessed 2024-11-19).
(47) Winne, J. M.; Leibler, L.; Du Prez, F. E. Dynamic Covalent Chemistry in Polymer Networks: A Mechanistic Perspective. *Polym. Chem.* **2019**, *10* (45), 6091–6108. https://doi.org/10.1039/c9py01260e.
(48) Saed, M. O.; Terentjev, E. M. Siloxane Crosslinks with Dynamic Bond Exchange Enable Shape Programming in Liquid-Crystalline Elastomers. *Sci. Rep.* **2020**, *10* (1), 6609. https://doi.org/10.1038/s41598-020-63508-4.
(49) Jourdain, A.; Asbai, R.; Anaya, O.; Chehimi, M. M.; Drockenmuller, E.; Montarnal, D. Rheological Properties of Covalent Adaptable Networks with 1,2,3-Triazolium Cross-Links: The Missing Link between Vitrimers and Dissociative Networks. *Macromolecules* **2020**, *53* (6), 1884–1900. https://doi.org/10.1021/acs.macromol.9b02204.
(50) Wu, Y.-C. M.; Chyr, G.; Park, H.; Makar-Limanov, A.; Shi, Y.; M. DeSimone, J.; Bao, Z. Stretchable, Recyclable Thermosets via Photopolymerization and 3D Printing of Hemiacetal Ester-Based Resins. *Chem. Sci.* **2023**, *14* (44), 12535–12540. https://doi.org/10.1039/D3SC03623E.
(51) Ricarte, R. G.; Shanbhag, S. Unentangled Vitrimer Melts: Interplay between Chain Relaxation and Cross-Link Exchange Controls Linear Rheology. *Macromolecules* **2021**, *54* (7), 3304–3320. https://doi.org/10.1021/acs.macromol.0c02530.
(52) Denissen, W.; Rivero, G.; Nicolaÿ, R.; Leibler, L.; Winne, J. M.; Du Prez, F. E. Vinylogous Urethane Vitrimers. *Adv. Funct. Mater.* **2015**, *25* (16), 2451–2457. https://doi.org/10.1002/adfm.201404553.
(53) Anaya, O.; Jourdain, A.; Antoniuk, I.; Ben Romdhane, H.; Montarnal, D.; Drockenmuller, E. Tuning the Viscosity Profiles of High-Tg Poly(1,2,3-Triazolium) Covalent Adaptable Networks by the Chemical Structure of the N-Substituents. *Macromolecules* **2021**, *54* (7), 3281–3292. https://doi.org/10.1021/acs.macromol.0c02221.
(54) Snijkers, F.; Pasquino, R.; Maffezzoli, A. Curing and Viscoelasticity of Vitrimers. *Soft Matter* **2016**, *13* (1), 258–268. https://doi.org/10.1039/C6SM00707D.
(55) Biron, M. *Thermosets and Composites*; Elsevier, 2003.
(56) Shi, Q.; Yu, K.; Kuang, X.; Mu, X.; Dunn, C. K.; Dunn, M. L.; Wang, T.; Qi, H. J. Recyclable 3D Printing of Vitrimer Epoxy. *Mater. Horiz.* **2017**, *4* (4), 598–607. https://doi.org/10.1039/C7MH00043J.
(57) Moller, J. C.; Berry, R. J.; Foster, H. A. On the Nature of Epoxy Resin Post-Curing. *Polymers* **2020**, *12* (2), 466. https://doi.org/10.3390/polym12020466.

(58) Carraher, C. E. Jr.; Carraher, C. E.; Seymour, R. B. *Seymour/Carraher's Polymer Chemistry*, 7th ed.; CRC Press: Boca Raton, 2007. https://doi.org/10.1201/9781420051032.
(59) Miao, W.; Yang, B.; Jin, B.; Ni, C.; Feng, H.; Xue, Y.; Zheng, N.; Zhao, Q.; Shen, Y.; Xie, T. An Orthogonal Dynamic Covalent Polymer Network with Distinctive Topology Transformations for Shape- and Molecular Architecture Reconfiguration. *Angew. Chem. Int. Ed.* **2022**, *61* (11), e202109941. https://doi.org/10.1002/anie.202109941.
(60) Zou, W.; Jin, B.; Wu, Y.; Song, H.; Luo, Y.; Huang, F.; Qian, J.; Zhao, Q.; Xie, T. Light-Triggered Topological Programmability in a Dynamic Covalent Polymer Network. *Sci. Adv.* **2020**, *6* (13), eaaz2362. https://doi.org/10.1126/sciadv.aaz2362.
(61) Parada, G. A.; Zhao, X. Ideal Reversible Polymer Networks. *Soft Matter* **2018**, *14* (25), 5186–5196. https://doi.org/10.1039/C8SM00646F.
(62) Raji, I. O.; Dodo, O. J.; Saha, N. K.; Eisenhart, M.; Miller, K. M.; Whitfield, R.; Anastasaki, A.; Konkolewicz, D. Network Polymer Properties Engineered Through Polymer Backbone Dispersity and Structure. *Angew. Chem. Int. Ed.* **2024**, *63* (21), e202315200. https://doi.org/10.1002/anie.202315200.
(63) Gryc, V.; Horáček, P. Variability in Density of Spruce (Picea Abies [L.] Karst.) Wood with the Presence of Reaction Wood. *J. For. Sci.* **2007**, *53* (3), 129–137. https://doi.org/10.17221/2146-JFS.
(64) Mantanis, G. I.; Young, R. A.; Rowell, R. M. Swelling of Wood. Part II. Swelling in Organic Liquids. *Holzforschung* **1994**, *48* (6), 480–490. https://doi.org/10.1515/hfsg.1994.48.6.480.
(65) Hill, C. A. S. *Wood Modification Chemical, Thermal and Other Processes*; Wiley Series in Renewable Resources; John Wiley & Sons, Ltd, 2006. https://doi.org/10.1002/0470021748.ch7.
(66) Östman, B. A.-L. Wood Tensile Strength at Temperatures and Moisture Contents Simulating Fire Conditions. *Wood Sci. Technol.* **1985**, *19* (2), 103–116. https://doi.org/10.1007/BF00353071.
(67) Abushammala, H.; Pontes, J. F.; Gomes, G. H.; Osorio-Madrazo, A.; Thiré, R. M. S. M.; Pereira, F. V.; Laborie, M.-P. G. Swelling, Viscoelastic, and Anatomical Studies on Ionic Liquid-Swollen Norway Spruce as a Screening Tool toward Ionosolv Pulping. *Holzforschung* **2015**, *69* (9), 1059–1067. https://doi.org/10.1515/hf-2014-0292.
(68) Kanbayashi, T.; Miyafuji, H. Influence of Ionic Liquid Treatment on Wood Cell Walls: Anatomical Changes in Opposite Wood. *Eur. J. Wood Wood Prod.* **2016**, *74* (6), 905–908. https://doi.org/10.1007/s00107-016-1097-z.
(69) Swatloski, R. P.; Spear, S. K.; Holbrey, J. D.; Rogers, R. D. Dissolution of Cellose with Ionic Liquids. *J. Am. Chem. Soc.* **2002**, *124* (18), 4974–4975. https://doi.org/10.1021/ja025790m.
(70) Sun, N.; Rahman, M.; Qin, Y.; Maxim, M. L.; Rodríguez, H.; Rogers, R. D. Complete Dissolution and Partial Delignification of Wood in the Ionic Liquid 1-Ethyl-3-Methylimidazolium Acetate. *Green Chem.* **2009**, *11* (5), 646–655. https://doi.org/10.1039/B822702K.
(71) Duchemin, B. J. C.; Mathew, A. P.; Oksman, K. All-Cellulose Composites by Partial Dissolution in the Ionic Liquid 1-Butyl-3-Methylimidazolium Chloride. *Compos. Part Appl. Sci. Manuf.* **2009**, *40* (12), 2031–2037. https://doi.org/10.1016/j.compositesa.2009.09.013.
(72) Abushammala, H.; Mao, J. A Review on the Partial and Complete Dissolution and Fractionation of Wood and Lignocelluloses Using Imidazolium Ionic Liquids. *Polymers* **2020**, *12* (1), 195. https://doi.org/10.3390/polym12010195.
(73) Ci, Y.; Ma, Y.; Chen, T.; Li, F.; Tang, Y. Facile Dissolution of Cellulose by Superbase-Derived Ionic Liquid Using Organic Solvents as Co-Solvents at Mild Temperatures. *Carbohydr. Polym.* **2024**, *330*, 121836. https://doi.org/10.1016/j.carbpol.2024.121836.
(74) Garemark, J.; Yang, X.; Sheng, X.; Cheung, O.; Sun, L.; Berglund, L. A.; Li, Y. Top-Down Approach Making Anisotropic Cellulose Aerogels as Universal Substrates for Multifunctionalization. *ACS Nano* **2020**, *14* (6), 7111–7120. https://doi.org/10.1021/acsnano.0c01888.
(75) Shibata, M.; Teramoto, N.; Nakamura, T.; Saitoh, Y. All-Cellulose and All-Wood Composites by Partial Dissolution of Cotton Fabric and Wood in Ionic Liquid. *Carbohydr. Polym.* **2013**, *98* (2), 1532–1539. https://doi.org/10.1016/j.carbpol.2013.07.062.
(76) Khakalo, A.; Tanaka, A.; Korpela, A.; Hauru, L. K. J.; Orelma, H. All-Wood Composite Material by Partial Fiber Surface Dissolution with an Ionic Liquid. *ACS Sustain. Chem. Eng.* **2019**, *7* (3), 3195–3202. https://doi.org/10.1021/acssuschemeng.8b05059.

(77) Ou, R.; Xie, Y.; Wang, Q.; Sui, S.; Wolcott, M. P. Material Pocket Dynamic Mechanical Analysis: A Novel Tool to Study Thermal Transition in Wood Fibers Plasticized by an Ionic Liquid (IL). *Holzforschung* **2015**, *69* (2), 223–232. https://doi.org/10.1515/hf-2014-0080.

(78) Adak, B.; Mukhopadhyay, S. Effect of the Dissolution Time on the Structure and Properties of Lyocell-Fabric-Based All-Cellulose Composite Laminates. *J. Appl. Polym. Sci.* **2016**, *133* (19). https://doi.org/10.1002/app.43398.

(79) Uzun, İ. Methods of Determining the Degree of Crystallinity of Polymers with X-Ray Diffraction: A Review. *J. Polym. Res.* **2023**, *30* (10), 394. https://doi.org/10.1007/s10965-023-03744-0.

(80) Hildén, L.; Johansson, G. Recent Developments on Cellulases and Carbohydrate-Binding Modules with Cellulose Affinity. *Biotechnol. Lett.* **2004**, *26* (22), 1683–1693. https://doi.org/10.1007/s10529-004-4579-8.

(81) Abhilash, V.; Rajender, N.; Suresh, K. Chapter 14 - X-Ray Diffraction Spectroscopy of Polymer Nanocomposites. In *Spectroscopy of Polymer Nanocomposites*; Thomas, S., Rouxel, D., Ponnamma, D., Eds.; William Andrew Publishing, 2016; pp 410–451. https://doi.org/10.1016/B978-0-323-40183-8.00014-8.

(82) *Plastics—Determination of Tensile Properties—Part 3: Test Conditions for Films and Sheets*; ISO 527-3:2018; International Organization for Standardization: Geneva, Switzerland, 2018. https://www.iso.org/standard/70307.html (accessed 2024-12-14).

Chapter 4. Polyurethane Covalent Adaptable Networks: Unlocking Superior Mechanical Properties in Dynamic Cellulose Nanofiber-Based Bioinspired Nanocomposites

Affiliation

[1]Life-Like Materials and Systems, Department of Chemistry, University of Mainz, Duesbergweg 10-14, 55128 Mainz, Germany.

[2]POLYMAT, University of the Basque Country UPV/EHU, Joxe Mari korta Center, Avda. Tolosa 72, Donostia-San Sebastián 20018, Spain.

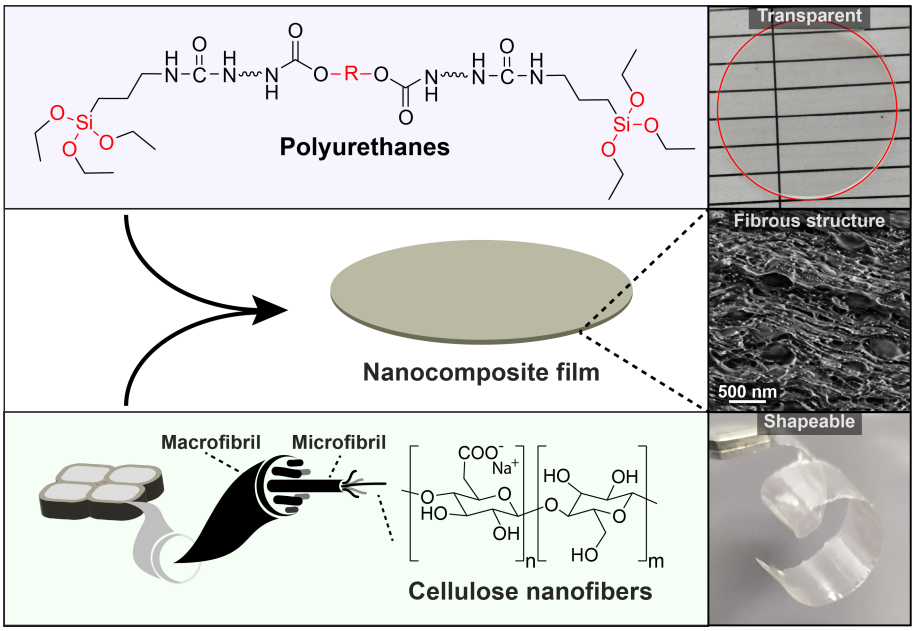

Note, this chapter is based on a collaboration with the POLYMAT institute in the context of the EU Marie Skłodowska-Curie consortium: VITRIMAT.

‘’**Sjoerd Engels**[1], Haritz Sardon[2]*, Andreas Walther[1]*’’

Author contributions: S.E., H.S., and A.W. conceptualized the core ideas. **S.E.** planned and performed the experiments. **S.E.** wrote the manuscript. A.W. edited and finalized the manuscript.

4.1 Abstract

This work presents a library of polyurethane (PU) and polyhydroxyurethane (PHU) materials with diverse properties, synthesized from amorphous and semi-crystalline polyols, including linear and crosslinked networks with siloxane and disulfide dynamic bonds. For the networks, the bond exchanges of both siloxane and disulfide components facilitate effective stress relaxation. A phase inversion procedure after polymer synthesis allows preparation of aqueous dispersions, so that the polymers can be integrated into cellulose nanofiber (CNF)-based nanocomposites (NCs), yielding dynamic films with high strength and stiffness. The dynamic properties enable effective reshaping and thick laminate formation through moderate heating. Notably, NCs with 10 wt% PU/PHU demonstrate the best mechanical properties, with strengths up to 550 MPa and Young's moduli of 32 GPa, although there are big discrepancies in tensile performance between different samples, likely stemming from factors involving the dispersion.

4.2 Introduction

Cellulose is the primary reinforcing component in plant cell walls and plays a crucial role in the structural properties of materials like wood or plant fibers. This structural performance arises from the intricate hierarchical organization, spanning from nanofibrils to microfibrils and mesostructures.[1,2] Cellulose-based fillers have traditionally been used mainly for their low cost and eco-friendliness, however when taking inspiration from nature's design strategies, cellulose can be used to develop renewable advanced materials with excellent mechanical performance and multifunctionality.[3] The controlled ordering of cellulose, in a fibrillar or hierarchical manner, can enable distinctive advantages, such as unique optical properties or directional conductivity and insulation.[4–7] For structural applications, cellulose nanofibrils (CNFs) exhibit outstanding mechanical properties while remaining versatile as they are efficient to prepare and functionalize.[8–10] There are multiple strategies to process CNFs from cellulose pulp so that they can be used to prepare high-performance materials.[11–16] One such approach involves TEMPO-mediated oxidation, a pretreatment of pulp conducted in aqueous NaOCl conditions at room temperature, which produces colloidally stable CNFs with surface carboxylate groups after homogenization.[17–19] The presence of carboxylates makes the TEMPO-oxidized CNFs more hydrophilic, thereby preventing their aggregation in aqueous dispersions. These dispersions can then be used in the preparation of nanocomposites (NCs), by combination with various other waterborne materials.

Even small amounts of CNFs can significantly improve the mechanical properties of synthetic polymer matrices in NCs, thanks to interfibrillar hydrogen bonding that forms strong and resilient supramolecular networks.[20,21] However, pure CNF nanopapers demonstrate the potential of NCs with much higher CNF fractions, achieving high toughness, strength, and stiffness and surpassing earlier cellulose-based materials.[3] Following a similar high-CNF-content strategy, NCs have been prepared with an interconnected network of CNFs combined with various synthetic polymer phases.[22,23] Bioinspired NCs in particular incorporate design elements with structures organized on different length scales, enabling a wide range of properties and functionalities.[24–29] However, while the incorporation of synthetic polymers often enhances specific properties, such as dynamic properties through incorporation of a covalent adaptable network (CAN), it typically leads to a reduction in mechanical strength and stiffness compared to pure CNF films.[8,24,30,31] This trade-off arises from mixing the CNF with the softer synthetic polymers, following a pattern similar to the rule of mixtures. An exception to this trend, reported in an earlier study, demonstrated that the introduction of a commercial polyurethane (PU) formulation could enhance the mechanical strength and stiffness of CNF films to unprecedented levels, surpassing even pure CNF films.[32]

PUs are a class of polymers, characterized by the urethane group that is formed during synthesis.[33–36] PUs are versatile polymers known for their tunable properties, including the ability to form both linear and crosslinked networks. They exhibit relatively high polarity and deliver strong performance

characteristics, such as excellent abrasion resistance, adjustable flexibility or hardness, and durability.[37,38] These attributes make PUs suitable for a wide range of applications, including surface and textile coatings, adhesives, elastomers, foams, and for preparing aqueous dispersions.[36,39] Moreover, these properties of PUs are key to the aforementioned synergy in CNF-based NCs, something that is not seen for other polymers.[32] PUs are generally synthesized by reacting polyols with diisocyanates, making their preparation inherently incompatible with water due to the reactivity of isocyanates with water.[40,41] However, aqueous PU dispersions have attracted attention as non-toxic, environmentally friendly alternatives to solvent-based systems.[41,42] One common approach involves a phase inversion from an organic solvent to water after PU synthesis.[43–47] This process requires precise optimization of the system and the incorporation of hydrophilic internal emulsifiers, which facilitate the formation of highly stable water-based PU dispersions. In addition to PUs, polyhydroxyurethanes (PHUs), produced via isocyanate-free methods, offer a complementary option for aqueous systems.[48–50] PHUs are a more hydrophilic polymer class, relying on urethane bond formation through the ring opening of carbonate-type moieties, which introduces hydroxyl groups into their backbone. While PHUs represent a distinct material class, they can complement aqueous PU dispersions as hydroxy-containing analogs. Preparing aqueous dispersions of PUs and PHUs facilitate their use in waterborne systems, such as the preparation of bioinspired CNF-based NCs.

To advance the use of PUs in CNF-based NCs, we prepared waterborne PU and PHU dispersions based on literature procedures.[43,44,48] Understanding the structure and functionality of these PUs and their dispersions is essential to elucidate the synergistic interactions between the polymers and the CNFs, which is why we created a library of PU and PHU materials with diverse properties, architectures, and functionalities. Given the tunable nature of PUs and the inherently mild dynamic properties of urethane bonds, we incorporated two additional dynamic chemistries into some of their designs to enable their use as hydrophilic CANs: siloxane crosslinks, dynamic in combination with acids or bases, and aromatic disulfide chain extenders.[51–55] We incorporated these PUs and PHUs into bioinspired CNF NCs, enabling both the unique PU-CNF synergy and dynamic properties to obtain materials stronger and stiffer than CNF films, capable of undergoing advanced (re)processing options, such as reshaping or laminate formation. Importantly, however, the results showed inconsistency: tensile properties varied widely for the same films, with strengths reaching up to 550 MPa and Young's modulus values up to 32 GPa in the most extreme cases, unprecedented for such materials. Similar measurement discrepancies across different PUs and PHUs suggest that the inconsistency might not be entirely dependent on molecular structure. The discrepancies may arise from variations in PU dispersion properties, such as particle size and dispersity, which could influence integration into the CNF matrix. Although promising, further optimization of PU dispersions is required to improve consistency and fully realize the mechanical potential of these materials.

4.3 Results and Discussion

4.3.1 PU and PHU Synthesis and Dispersion in Water by Phase Inversion

Waterborne PUs were prepared as described in **Figure 1**. PU synthesis involves isophorone diisocyanate (IPDI), a commonly used isocyanate, which undergoes a condensation reaction with hydroxyl groups to form the characteristic urethane bond. The polyol used to react with IPDI primarily defines the polymer backbone, providing the first opportunity to tailor the PU properties. We selected polypropylene glycol with M_n = 1000 g/mol (PPG_{1000}) as an amorphous polyol, while polycaprolactone diol with M_n = 2000 g/mol (PCl_{2000}) served as a semi-crystalline polyol. We improved the hydrophilicity of the PUs via addition of dimethylolpropionic acid (DMPA) as an internal emulsifier (ca. 0.3 mmol/g). Subsequently adding an equimolar amount of triethylamine increased the ionic group content of the PU to allow for formation of stable aqueous dispersions. Upon addition of dibutyltin dilaurate (DBTDL) as catalyst and acetone as solvent, the mixture was heated to 60 °C for four hours to initiate prepolymerization.

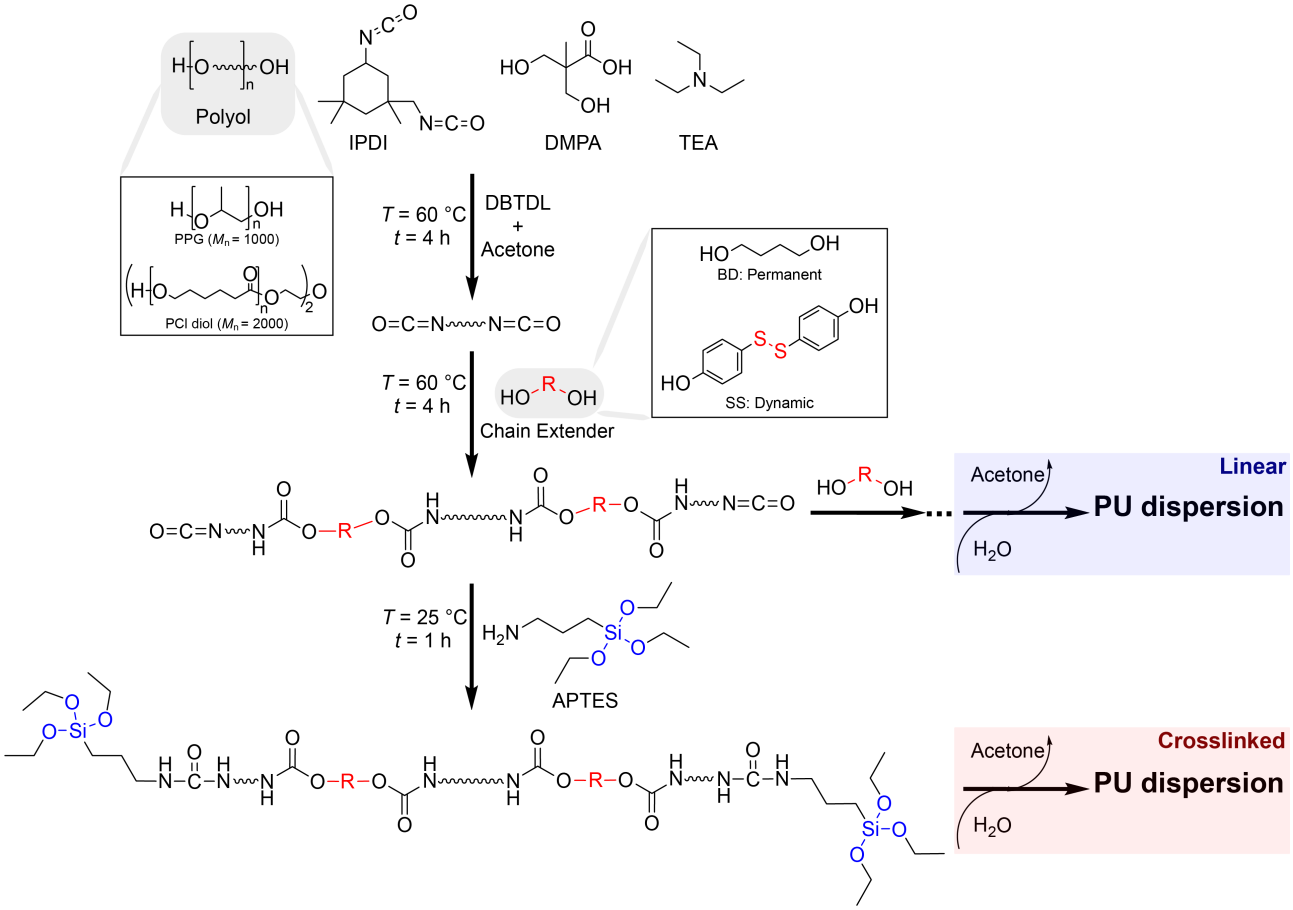

Figure 1. Preparation of aqueous PU dispersions via acetone-based PU synthesis and subsequent phase inversion using water. After initial prepolymerization, linear polymers (blue) are prepared by reacting all remaining isocyanate groups with chain extender diol, while crosslinked polymers (red) are prepared by reacting part of the remaining isocyanate groups with APTES. Either an amorphous or a semi-crystalline polyol is used to diversify polymer properties. Dynamic disulfide bonds are introduced by using a chain extender with a disulfide in between.

Since there is a stochiometric excess of IPDI isocyanate groups compared to the hydroxyl groups of polyols and DMPA, prepolymers with active isocyanate end groups can react further in the next step. Here, the commonly used 1,4-butanediol (BD) functions as a permanent chain extender, whereas 4,4'-dihydroxy diphenyl disulfide (SS) functions as a dynamic chain extender that can undergo disulfide exchange.[56–59] For linear PUs, we added the chain extender in slight excess compared to the remaining isocyanate groups so that complete condensation is achieved. To form crosslinked networks, we introduced the chain extender in lower stochiometric amount, resulting in PU chains with reactive isocyanate end groups, followed by reaction with 3-aminopropyl triethoxysilane (APTES). This aminosilane can self-cure to form siloxane crosslinks between different polymer chains.[44] In the context of waterborne PUs, the curing process primarily initiates when the water evaporates from the dispersion. Siloxane bonds are also capable of bond exchange and have been shown to enable stress relaxation in siloxane-based CANs in the presence of catalysts such as Lewis or Brønsted acids and bases.[51–55] These crosslinks therefore serve not only as structural elements but also as dynamic bonds within the final PU materials. Additionally, APTES functions as a coupling agent to various substrates, such as cellulose or glass, potentially enhancing interactions between the PU and CNFs in the NCs discussed later.[60–62]

We introduced water only after synthesis was complete to prevent formation of urea crosslinks through reaction with isocyanates. We prepared aqueous dispersions via phase inversion from acetone to water, carefully controlling stirring parameters, water addition rate and content, acetone content, and triethylamine concentration. Only with the right conditions can stable dispersions be formed instead of PU flocculation.[43] Finally, we removed acetone under reduced pressure, which also relies on precise parameters, to yield the final dispersions with high weight content of PU (ca. 30 wt%).

We prepared six PU dispersions to explore various design elements (**Table 1**).

Table 1. Overview of PU compositions.

Sample name	IPDI (eq.)	PPG_{1000} (eq.)	PCl_{2000} (eq.)	DMPA (eq.)	BD (eq.)	SS (eq.)	APTES (eq.)
PU-PPG_{1000}	1	0.40	-	0.23	0.44	-	-
PU-PPG_{1000}-SiO	1	0.40	-	0.23	0.19	-	0.34
PU-PPG_{1000}-SiO-SS	1	0.40	-	0.20	-	0.12	0.57
PU-PCl_{2000}	1	-	0.30	0.30	0.47	-	-
PU-PCl_{2000}-SiO	1	-	0.25	0.25	0.27	-	0.43
PU-PCl_{2000}-SiO-SS	1	-	0.25	0.25	-	0.16	0.73

Using PPG_{1000} as the polyol, we synthesized (i) a nondynamic linear PU with BD as the chain extender (PU-PPG_{1000}), (ii) a network with dynamic siloxane linkages using APTES and BD (PU-PPG_{1000}-SiO), and (iii) a crosslinked PU incorporating both siloxane and disulfide chemistries using APTES and SS as chain extender (PU-PPG_{1000}-SiO-SS). Similarly, three corresponding dispersions were prepared with semi-crystalline PCl_{2000} as the polyol (PU-PCl_{2000}, PU-PCl_{2000}-SiO, and PU-PCl_{2000}-SiO-SS, respectively). The dispersions could visually appear as transparent and almost colorless liquids, or milky white or yellow liquids, depending on the particle sizes and distribution (Figure S1).

An important method to follow the reaction progress is Fourier-transform infrared spectroscopy (FTIR), as the isocyanate signal (2265 cm^{-1}) is strong and isolated (**Figure 2**). Changes in signal intensity indicate reaction progress, with the completion of the synthesis signaled by the absence of the isocyanate peak. Further characteristic bands in the spectrum of PU-PPG_{1000}-SiO-SS are: C–O stretching for urethanes and ethers (1000 - 1300 cm^{-1}), potentially C–N stretching for triethylamine (1363 cm^{-1}), C=O stretching (1713 cm^{-1}), C–H stretching (2925 cm^{-1}), and O–H stretching (3348 cm^{-1}).[63]

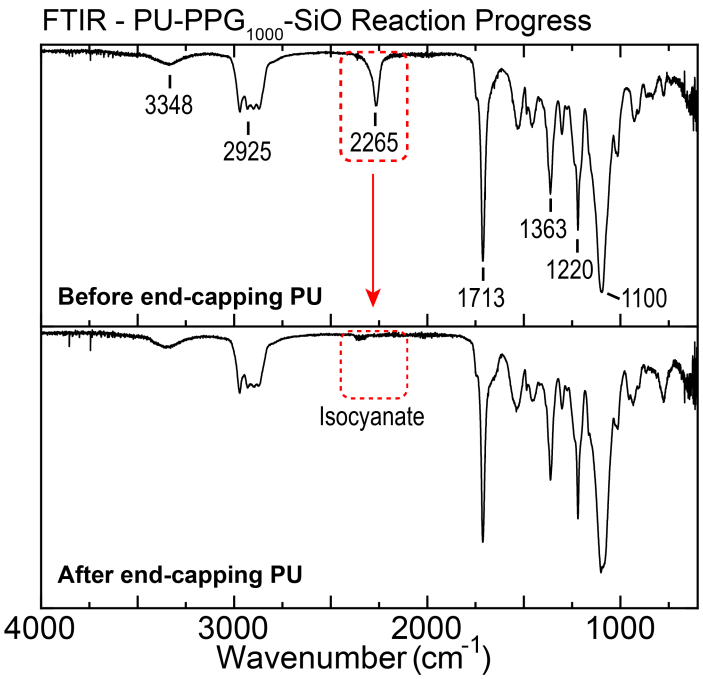

Figure 2. FTIR spectra of PU-PPG_{1000}-SiO-SS during synthesis, before and after end-capping with APTES.

Additionally, we also prepared one PHU dispersion via a non-isocyanate-based procedure (**Figure 3**). The solvent-free synthesis involves reacting bis(3-aminopropyl) terminated poly(dimethyl siloxane) with M_n = 2500 g/mol, 1,4-dibutanol dicarbonate, and bis-N-8-Ce at 80 °C to yield linear PHU. In this synthesis, strained 5-membered and 7-membered carbonate rings undergo ring-opening addition with primary amines, forming urethane bonds and pendant hydroxyl groups. Incorporation of bis-N-8-Ce introduces tertiary amines into the polymer backbone, which improve

water dispersibility when combined with acetic acid. The aqueous dispersion is prepared via an adapted phase-inversion process using acetone and water. This PHU avoids the need for toxic isocyanates during synthesis and provides additional hydrophilicity by incorporating hydroxyl functionalities. As such, it could enhance compatibility with hydrophilic substrates like cellulose through hydrogen bonding or even esterification.

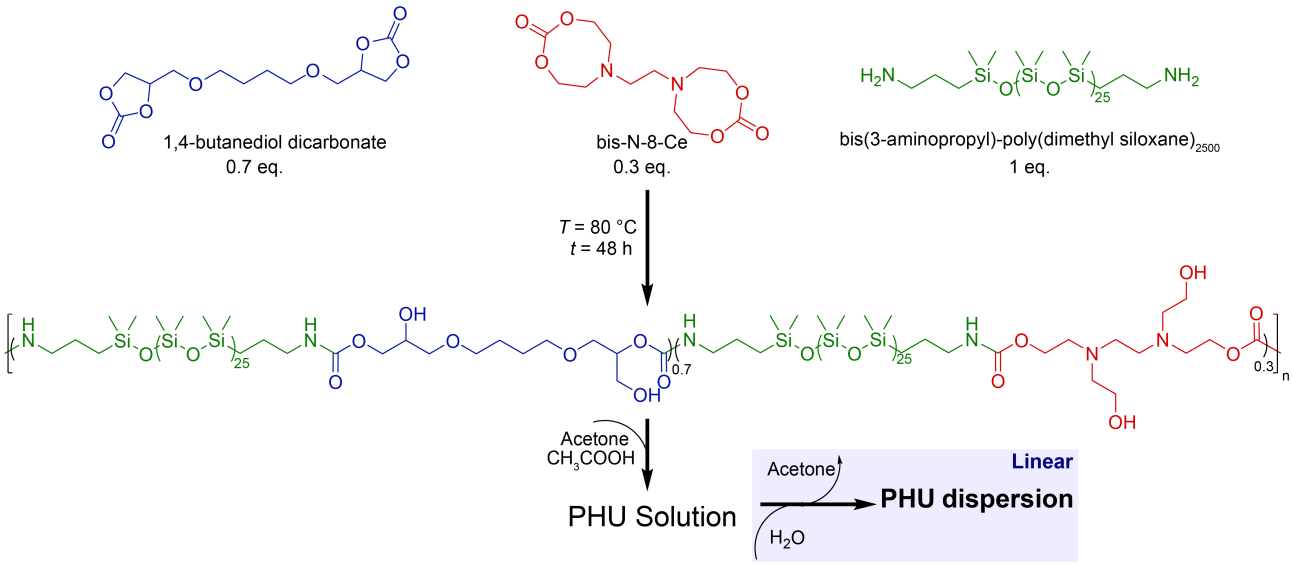

Figure 3. Preparation of PHU based on an isocyanate-free synthesis. Amine-terminated poly(dimethyl siloxane) reacts with strained 5-membered and 7-membered carbonates to form linear PHU polymers, followed by dissolution in acetone and addition of acetic acid and subsequent phase-inversion to aqueous dispersion.

4.3.2 Characterization of PU and PHU Dispersions and their Mechanical Properties

Next, we determined the polymer weight content for each dispersion and measured the average particle size via dynamic light scattering (DLS) (**Table 2**). All PU dispersions except for PU-PCl_{2000}-SiO-SS had a polymer weight content of ca. 30 wt%, while the latter had a much lower content of 7 wt%. This discrepancy arose from phase separation, which caused a gradual reduction in the polymer content over time after initial preparation. Unfortunately, this polymer cannot be redispersed afterwards on account of its crosslinks.

The DLS data reveal that most dispersions contain nanoscale particles with relatively narrow size distributions, a characteristic essential for high dispersion stability. PUs incorporating SS posed greater challenges for achieving stable dispersions, likely due to the higher hydrophobicity of SS compared to BD on account of the aromatic rings. For this reason, no accurate DLS data could be obtained for the PU-PCl_{2000}-SiO-SS dispersion, while the PU-PPG_{1000}-SiO-SS dispersion possessed greater particle sizes and dispersity. Increasing the amount of DMPA as an emulsifying agent could potentially enhance dispersion stability, but for the purposes of this project the dispersions were used without further changes. We also encountered challenges in obtaining reliable data for the dispersion

of PHU. As this dispersion procedure was adapted from a different synthesis process, additional optimization may be required to achieve more stable dispersions. Nevertheless, the dispersion was suitable for subsequent NC preparation.

Table 2. Weight contents and particles sizes of dispersions.

Dispersions	PU in aqueous dispersion (wt%)	Particle size, D_p (nm)[a)]
PU-PPG_{1000}	33.0	42 ± 1
PU-PPG_{1000}-SiO	24.5	130 ± 1
PU-PPG_{1000}-SiO-SS	32.6	239 ± 7
PU-PCl_{2000}	28.5	81 ± 1
PU-PCl_{2000}-SiO	29.7	71 ± 2
PU-PCl_{2000}-SiO-SS	7.1	-
PHU	23.1	20400 ± 12140

[a)] Determined via DLS

We determined the soluble fractions for the various PUs after drying of the dispersions by immersion in acetone for 48 h (**Table 3**). PU-PPG_{1000}, PU-PCl_{2000}, and PHU completely dissolve in acetone because they are linear polymer chains without crosslinks. PU-PCl_{2000}-SiO-SS, PU-PCl_{2000}-SiO, and PU-PCl_{2000}-SiO-SS are largely insoluble, indicating their crosslinked nature, whereas PU-PPG_{1000}-SiO displays a higher degree of solubility with an insoluble fraction of 64%. The soluble fraction may include leached triethylamine. More importantly, since the PUs form small particles in dispersion, the bulk material may lack overall connectivity between particles after drying. This connectivity, primarily dependent on covalent bond exchanges, could potentially increase by heating, thereby increasing the insoluble fraction. Crosslinked CANs are known to sometimes demonstrate solubility in good solvents on account of creating such small particles.[64,65]

Table 3. Insoluble fractions of dried PUs.

Sample[a)]	Insoluble fraction acetone (48 h)
PU-PPG_{1000}	0%
PU-PPG_{1000}-SiO	64%
PU-PPG_{1000}-SiO-SS	84%
PU-PCl_{2000}	0%
PU-PCl_{2000}-SiO	92%
PU-PCl_{2000}-SiO-SS	79%
PHU	0%

[a)] Dried under vacuum prior to swelling in acetone.

To gain a first understanding of the mechanical properties of the solid PUs (PU-PPG$_{1000}$-SiO, PU-PPG$_{1000}$-SiO-SS, PU-PCl$_{2000}$, PU-PCl$_{2000}$-SiO, and PU-PCl$_{2000}$-SiO-SS), we subjected them to tensile tests at room temperature. The PUs were obtained by drying the dispersions in ambient conditions prior to testing. The mechanical properties: stress (σ_b) and strain (ε_b) at break, yield stress (σ_y) and yield strain (ε_y), Young's modulus (E), and toughness (U_t) are summarized in **Figure 4** and **Table 4**.

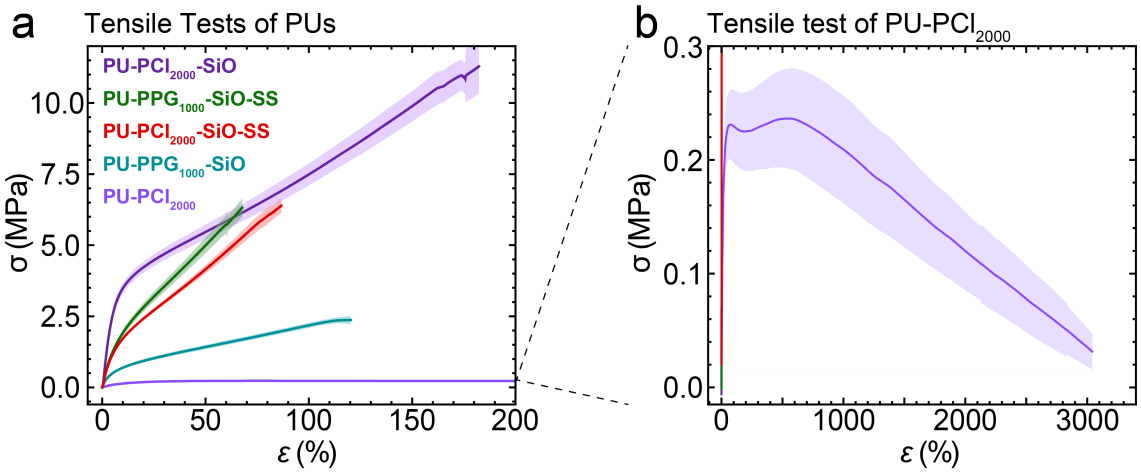

Figure 4. (a) Tensile tests for PU materials PU-PPG$_{1000}$-SiO, PU-PPG$_{1000}$-SiO-SS, PU-PCl$_{2000}$, PU-PCl$_{2000}$-SiO, and PU-PCl$_{2000}$-SiO-SS, with (b) zoomed in plot to depict PU-PCl$_{2000}$.

Table 4. Overview of mechanical properties of PU materials.

Sample	σ_b (MPa) ± SE[a)]	ε_b (%) ± SE[a)]	σ_y (MPa) ± SE[a)]	ε_y (%) ± SE[a)]	E (MPa) ± SE[a)]	U_t (MJm^{-3}) ± SE[a)]
PU-PPG$_{1000}$-SiO	2.42 ± 0.13	120 ± 2.8	0.78 ± 0.14	6.63 ± 0.24	10.9 ± 0.84	1.86 ± 0.15
PU-PPG$_{1000}$-SiO-SS	6.39 ± 0.48	67.8 ± 4.9	5.98 ± 0.17	1.75 ± 0.11	24.8 ± 1.6	2.55 ± 0.29
PU-PCl$_{2000}$	0.389 ± 0.17	3042 ± 279	0.248 ± 0.040	34.0 ± 0.71	0.363 ± 0.054	4.78 ± 1.1
PU-PCl$_{2000}$-SiO	11.4 ± 0.51	182 ± 3.4	3.70 ± 0.15	7.93 ± 0.033	54.9 ± 2.9	13.1 ± 0.60
PU-PCl$_{2000}$-SiO-SS	6.35 ± 0.088	86.7 ± 4.2	6.05 ± 0.12	1.60 ± 0.039	23.6 ± 0.60	3.23 ± 0.17

[a)] SE refers to the standard error.

As a linear polymer, PU-PCl$_{2000}$ possesses very different properties compared to the PU networks, with relatively low σ_b and E values of 0.39 and 0.36 MPa, respectively, and ductility of more than an order of magnitude higher (ε_b = 3042 %). In contrast, PU-PPG$_{1000}$ is a liquid on account of the amorphous backbone structure. The addition of siloxane crosslinks results in significant increases in σ_b and E (11 and 55 MPa, respectively) and reduction in ε_b (182 %) for PU-PCl$_{2000}$-SiO. Interestingly, all these properties are superior to those of PU-PPG$_{1000}$-SiO (2.4 MPa, 11 MPa, and 120 %, respectively), indicating better synergy with the APTES crosslinks on account of the semi-crystalline nature of PCl$_{2000}$. When comparing the PU CANs incorporating disulfide bonds, the properties of PU-PPG$_{1000}$-SiO-SS and PU-PCl$_{2000}$-SiO-SS are similar, with almost identical σ_b and E, and similar ε_b (6.4 versus 6.4 MPa, 25 versus 24 MPa, and 68 versus 87 %, respectively). For PU-PPG$_{1000}$-SiO-SS, this is a stronger and stiffer material compared to PU-PPG$_{1000}$-SiO, likely on account of

interactions between the aromatic components of SS. Interestingly, for the PU based on PCl_{2000}, this is a significant reduction in properties compared to PU-PCl_{2000}-SiO, which potentially indicates how SS has a negative effect on the crystalline stacking of the PU backbone. These results provide insight into the properties of pure PU materials; however, they do not necessarily predict the mechanical properties of the derived NCs. Consequently, we chose to retain all PUs for subsequent experiments.

4.3.3 Thermal Behavior and Recycling of Dynamic Networks and Polymers

To understand the dynamic properties of the crosslinked PUs, we subjected PU-PPG_{1000}-SiO, PU-PPG_{1000}-SiO-SS, PU-PCl_{2000}-SiO, PU-PCl_{2000}-SiO-SS to stress relaxation experiments over a wide temperature range (**Figure 5**).

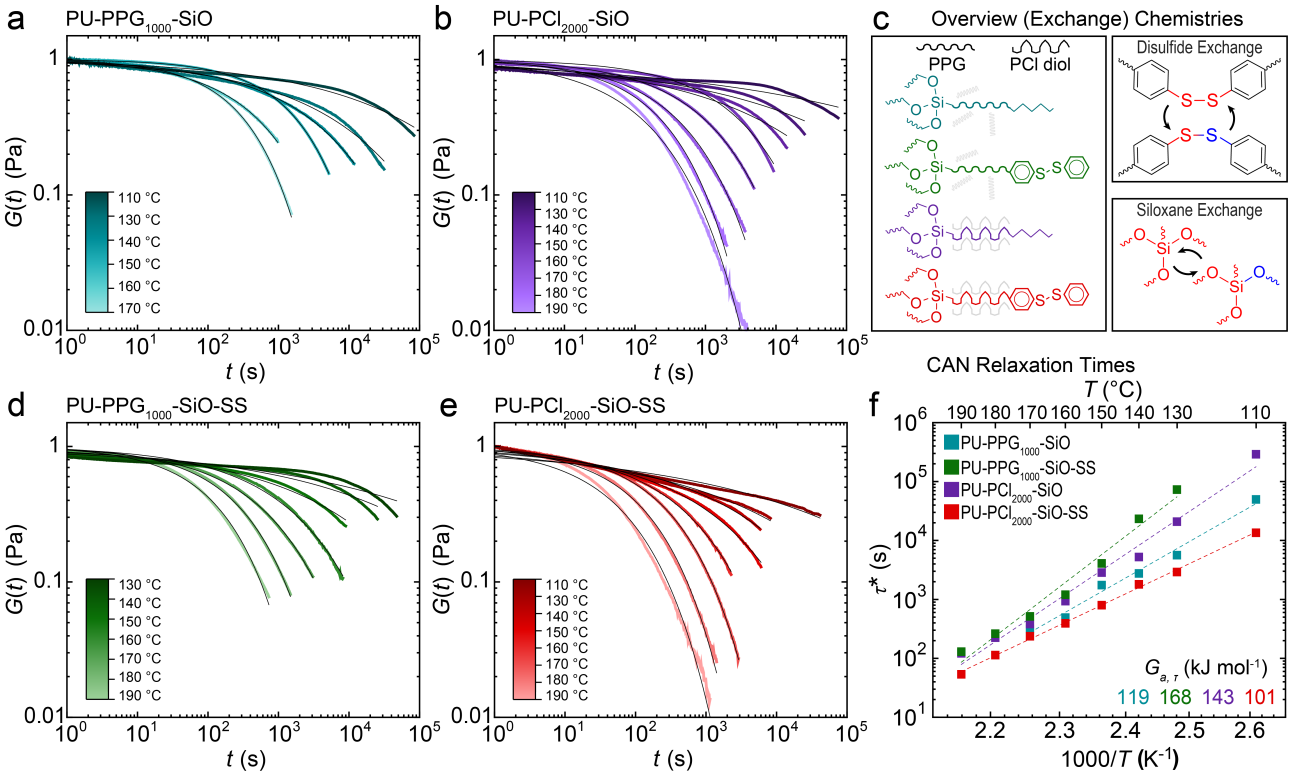

Figure 5. Stress Relaxation data (normalized) obtained at a wide range of temperatures (colored lines) and corresponding stretched exponential fits (thin black lines) of (a) PU-PPG_{1000}-SiO, (b) PU-PCl_{2000}-SiO, (d) PU-PPG_{1000}-SiO-SS, and (e) PU-PCl_{2000}-SiO-SS. (c) A schematic overview of the polymer backbones and exchange chemistries involved. (f) Based on the fitted data, Arrhenius plots of τ^* were constructed.

We normalized the stress relaxation data because the plateau moduli, G_0, change rapidly at t < 1 s, causing inconsistencies between the measurements at different temperatures. These inconsistencies can stem from experimental constraints such as instrument compliance or inertia effects, experimental conditions such as nonlinear viscoelasticity, or material-specific affects such as microstructural rearrangements. To improve future measurements, careful validation of instrument response at short timescales and ensuring that applied strains remain within the linear

viscoelastic range could help mitigate these issues. However, due to the complex dynamicity of these PUs, resolving these issues is not trivial. The materials exhibit a heterogeneous structure arising from hydrogen bonding, ionic interactions, and crosslinked microparticles with varying local environments. Additionally, multiple covalent bond exchange mechanisms are at play, including associative disulfide and siloxane exchanges and the possibility of dissociative urethane bond dynamics at higher temperatures. To sidestep the challenges of accurately measuring G_0, normalizing the data allows us to isolate and analyze the relaxation kinetics, providing insights into the overall bond exchange dynamics.

First, we observe the relaxation curves for the various CANs. All four PUs display stress relaxation rates in a comparable regime, with 90% relaxation at 190 °C for 100 s < *t* < 1000 s and 90% relaxation at 110 °C for *t* > 24 h. Differences in stress relaxation between PUs with an amorphous backbone (PPG_{1000}-based) and more semi-crystalline backbones (PCl_{2000}-based) are small. The introduction of disulfides mainly enhances the relaxation process at higher temperatures, as seen when comparing PU-PPG_{1000}-SiO and PU-PPG_{1000}-SiO-SS (**Figure 5a,d**) or PU-PCl_{2000}-SiO and PU-PCl_{2000}-SiO-SS (**Figure 5b,e**), respectively. The PUs involving disulfides exhibit their highest relaxation at t ~ 1000 s rather than *t* ~ 2000 s. Furthermore, some of the relaxation data deviate visibly from a single exponential decay, which is most visible in **Figure 5e** where there are secondary contributions, potentially with different temperature-dependences. Supramolecular interactions (*e.g.* hydrogen bonding or ionic interactions) and physical chain interactions, such as monomer friction, often result in deviations from simple exponential decay.[66–68] In PUs, a baseline level of dynamic properties are also often attributed to associative and dissociative urethane covalent bond exchange at higher temperatures.[69] In addition, the PUs with incorporated disulfides (**Figure 5d,e**) are expected to also exhibit contributions from disulfide exchange as a second covalent bond-exchange reaction, which is visible for PU-PCl_{2000}-SiO-SS, but harder to see for PU-PPG_{1000}-SiO-SS.

Based on these complexities, the data are fit with stretched exponential functions to encapsulate all ongoing processes that contribute to the stress relaxation.[67,70] The fits are presented with the stress relaxation data (**Figure 5a,b,d,e**), based on

$$G(t) = G_0 e^{-(t/\tau^*)^\beta} \quad (1)$$

wherein, G_0 is the plateau modulus, τ^* is the characteristic relaxation time, and β is the stretching exponent. τ^* represents a combined measure of all relaxation processes, which we analyze by constructing Arrhenius plots (**Figure 5f**).

Overall, the temperature response in all PUs results in linear Arrhenius plots, indicating that the temperature dependence of the various stress relaxation mechanisms aligns. This suggests that these processes either have similar activation energies or interact in a way that produces a combined

temperature dependence. Furthermore, the similarity in their stress relaxation kinetics suggests that siloxane exchange and the inherent polyurethane properties (*e.g.* potential urethane bond exchange, chain mobility, and polarity) are the primary contributors to stress relaxation.

However, comparing PU-PPG_{1000}-SiO and PU-PCl_{2000}-SiO reveals that relaxation times are shorter for the PUs based on PPG compared to those based on PCl diol, along with a lower activation energy (119 versus 143 kJ mol^{-1}). This is likely due to the higher chain mobility in the more amorphous PPG backbone compared to the semi-crystalline PCl diol backbone. Higher chain-mobility facilitates faster stress relaxation, even for identical bond exchange reactions. At higher temperatures, the relaxation times converge as the influence of crystallinity diminishes, in line with the different activation energies.

To assess the impact of the disulfide bond exchange, we first consider PU-PCl_{2000}-SiO and PU-PCl_{2000}-SiO-SS. Introducing the additional disulfide moiety reduces the stress relaxation times, especially at lower temperatures, and lowers the activation energy (143 versus 101 kJ mol^{-1}). This indicates that disulfide exchange significantly contributes to stress relaxation. However, this relation is not observed for PU-PPG_{1000}-SiO and PU-PPG_{1000}-SiO-SS, where the relaxation times and activation energy (119 versus 168 kJ mol^{-1}) increase upon introduction of the disulfide component. The slower stress relaxation observed in PU-PPG_{1000}-SiO-SS compared to PU-PPG_{1000}-SiO can likely be attributed to a reduction in chain mobility and phase separation. Despite the introduction of an additional bond exchange reaction, the aromatic nature of the disulfide moieties may cause aggregation or π-π stacking interactions within the network, thereby leading to localized rigid regions and hindering the stress relaxation process. In contrast, the more ordered PU-PCl_{2000}-SiO-SS, with its semi-crystalline backbone structure, might avoid significant phase separation and aggregation, maintaining a more uniform distribution of the disulfides. This would allow for more efficient stress transfer throughout the network, explaining the faster relaxation times and lower activation energy observed in PU-PCl_{2000}-SiO-SS. These results demonstrate how efficient stress relaxation relies on the network structure and mobility alongside the kinetics of the bond exchange reaction.

It is important to supplement stress relaxation data with (re)processing experiments to understand the full extent of the dynamic properties. We used heated compression molding of fractured PU pieces (130 °C, 45 min) to reform smooth discs (**Figure 6a-e**). We should note that PU-PPG_{1000} and PHU are not included as they are non-crosslinked liquids, while PU-PCl_{2000} is included as a solid but can be reformed simply on account of being a thermoplastic. More importantly, PU-PPG_{1000}-SiO, PU-PPG_{1000}-SiO-SS, and PU-PCl_{2000}-SiO-SS, demonstrated efficient and complete reshaping at moderate temperature (130 °C) and in a short timeframe (45 min), which is more rapid than the stress relaxation experiments performed at 130 °C might indicate (**Figure 5**). The high pressure applied during the experiment likely lowers the activation energy for covalent bond exchanges and other relaxation processes, induces plastic flow by pushing the material into the nonlinear regime,

and introduces additional mechanical energy into the system, all of which accelerate network reorganization. For PU-PCl_{2000}-SiO, the reprocessing is not fully complete, which can be remedied by adjusting the procedure to either t > 45 min or T > 130 °C.

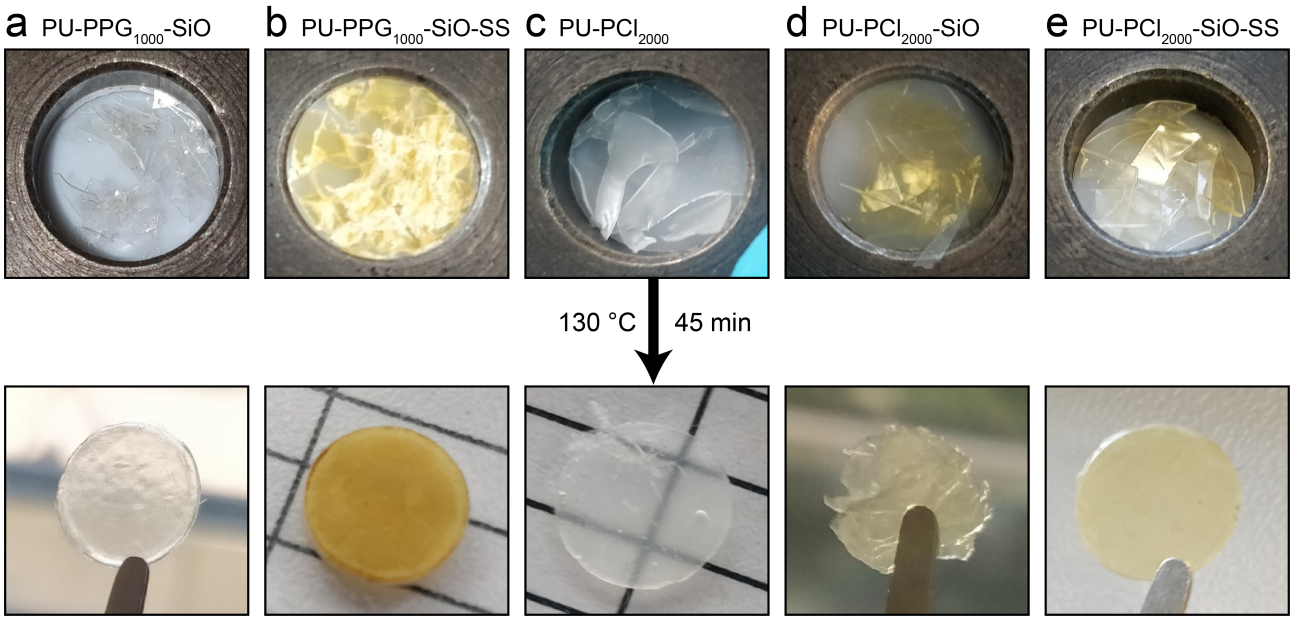

Figure 6. Recycling CAN PUs by compression molding at ~ 50 MPa and 130 °C for 45 min for (a) PU-PPG_{1000}-SiO, (b) PU-PPG_{1000}-SiO-SS, (c) PU-PCl_{2000}, (d) PU-PCl_{2000}-SiO, and (e) PU-PCl_{2000}-SiO-SS.

4.3.4 Preparation of Bioinspired NCs by Combining PU and PHU Dispersions and CNFs

Continuing to the preparation of bioinspired NCs based on the prepared PUs and CNF (COOH content of ca. 0.44 mmol/g, degree of polymerization of 725, degree of crystallinity of 77%)[24], we mixed diluted aqueous PU dispersions (0.25 wt%) with aqueous dispersions of CNF (0.25 wt%), after which we cast the mixtures into petri dishes (**Figure 7a**). The ratios of the PU and CNF dispersions control the weight content of CNF in the NCs. Evaporation of the water phase in ambient conditions yields thin transparent NC films (**Figure 7b**). During this process, the polymers and CNFs self-assemble into hierarchical structures, with cellulose fibers interspersed with polymer globules, corresponding to the polymer nanoparticles in dispersion (**Figure 7c**). APTES-end-capped PUs typically self-cure during water evaporation. Additionally, since APTES is known to bond effectively with fillers like cellulose, covalent interactions between the PU and CNFs may occur in the NC films. The SEM images also reveal fractured regions of CNFs, visible as brighter raised areas, as we fractured the samples in tensile mode (**Figure 7c**). This suggests that fracture rather than nanofiber pullout governs the failure mechanism.

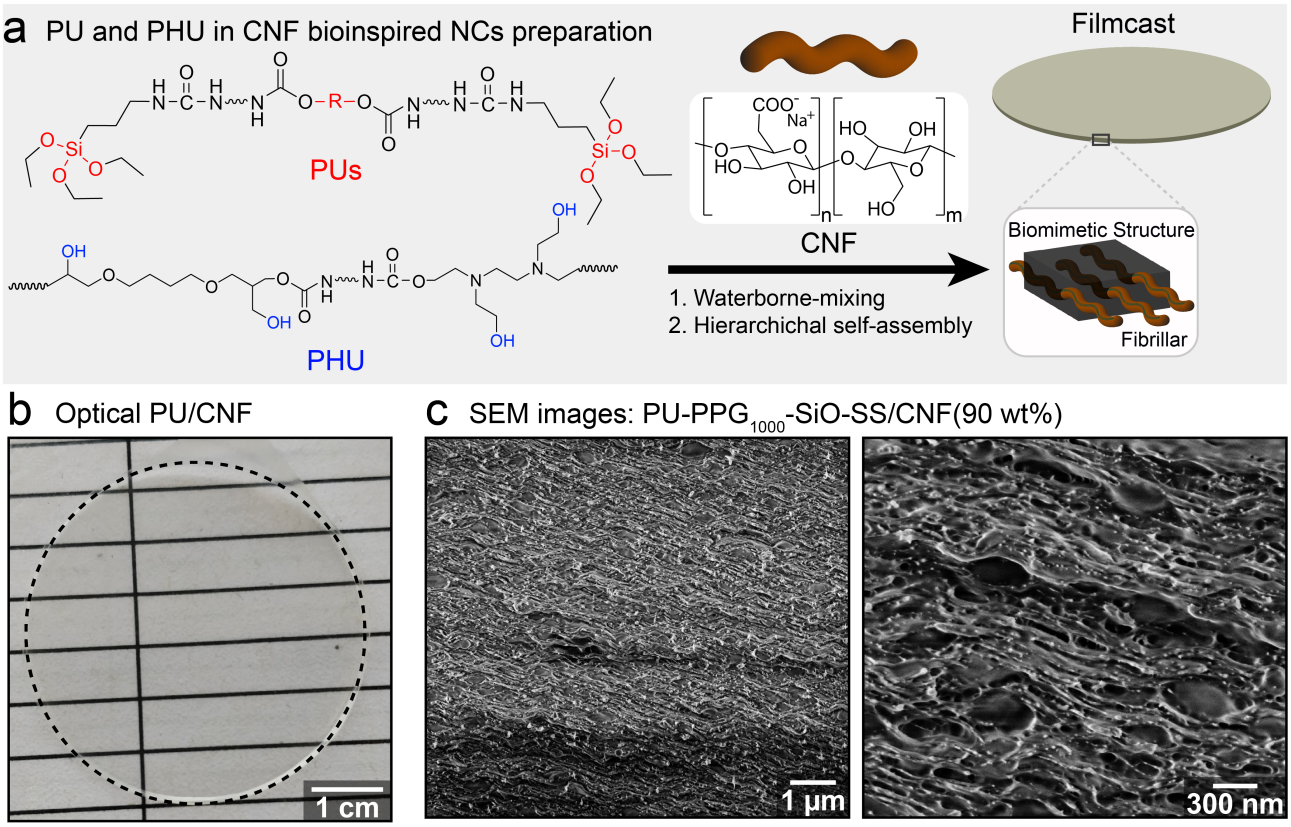

Figure 7. Bioinspired NCs by combination of waterborne PUs and CNFs. (a) Schematic overview of NC preparation via evaporative self-assembly to form hierarchical architecture. (b) Photograph of PU-PPG$_{1000}$-SiO-SS/CNF(90 wt%). (c) Cross section SEM micrograph of PU-PPG$_{1000}$-SiO-SS/CNF(90 wt%) NC displaying a fibrous structure with visible PU globules at two different degrees of magnification.

4.3.5 Dynamic Properties of Bioinspired NCs Enabled by Covalent Bond Exchange

To investigate the thermal dynamization associated with the PUs, and the PU CANs in particular, we subjected PU-PPG$_{1000}$-SiO-SS/CNF(90 wt%), PU-PPG$_{1000}$-SiO-SS/CNF(70 wt%), and PU-PPG$_{1000}$-SiO-SS/CNF(50 wt%) to small-amplitude dynamic mechanical analysis (**Figure 8**).

The three NCs displayed a similar temperature response, with a reduction in the tensile storage modulus (*E'*) of 30 - 40% over the temperature range of 30 to 195 °C. These results are indicative of highly reinforced materials that do not undergo significant transitions and maintain highly elastic behavior. The small degree of thermal softening is difficult to attribute to the dynamic properties of the CAN, as then we would likely see different responses depending on the weight fractions of CAN. However, it is important to note that these oscillatory experiments occur at a shearing frequency of 1 Hz, where dynamic bond exchange (significant for t >> 10s; see **Figure 5**) is unlikely to have an impact. The absolute values of *E'* vary with the CNF fraction in the NC, with higher CNF content correlating to increased stiffness, a typical behavior for polymer-CNF NCs.[30]

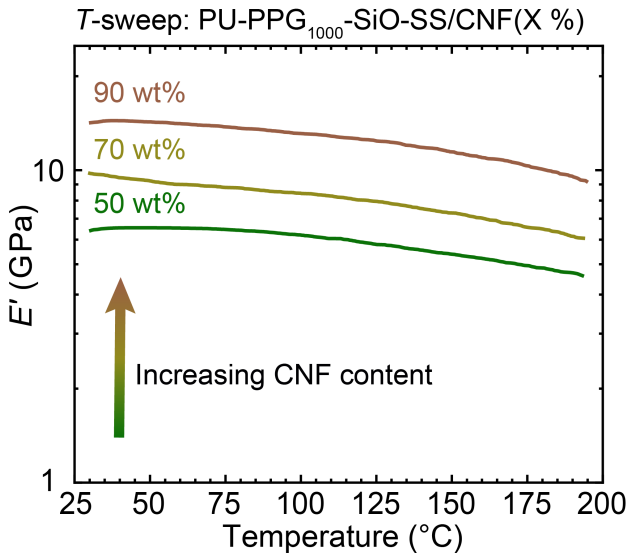

Figure 8. Dynamic mechanical properties of PU-PPG1000-SiO-SS/CNF NCs at various weight contents of CNF. Thermomechanical properties are obtained by small amplitude oscillatory experiments in tensile mode.

As a demonstration of the dynamic properties imparted on the bioinspired NCs, we investigated the capability for laminate formation and for reshaping of PU-PPG$_{1000}$-SiO-SS/CNF(50 wt%) (**Figure 9**). We selected composites with 50 wt% CAN to make optimal use of the covalent bond exchange properties. The laminate formed by stacking several NC films after coating each in concentrated aqueous dispersion of PU-PPG$_{1000}$-SiO-SS/CNF(50 wt%), which aids in the adhesion. Subsequently, the laminate was hot pressed at low pressure (130 °C, 0.5 MPa) to yield a sturdy disc shaped NC with a thickness that was ca. forty times that of the individual films. Despite being composed of 25 layers of NC film, no delamination or layer separation was observed. This strategy utilizes the dynamic chemistries of the PU CAN to enable the formation of thicker bioinspired NCs, which is a significant limitation in most cellulosic films. The process can conceivably be scaled to produce samples of significantly greater thickness, particularly with the appropriate equipment.

Composite films were reshaped simply by coiling the sample via external stress and subsequent moderate heating (120 °C) over a 30 min window. Stress relaxation induced by covalent bond exchange of the CAN phase allows the material to adopt the induced shape after removal of the external stress. Given the shapeability of the material, it is plausible to combine these two strategies to produce thicker laminates with shaped geometries, provided the samples are placed in suitable molds during hot pressing

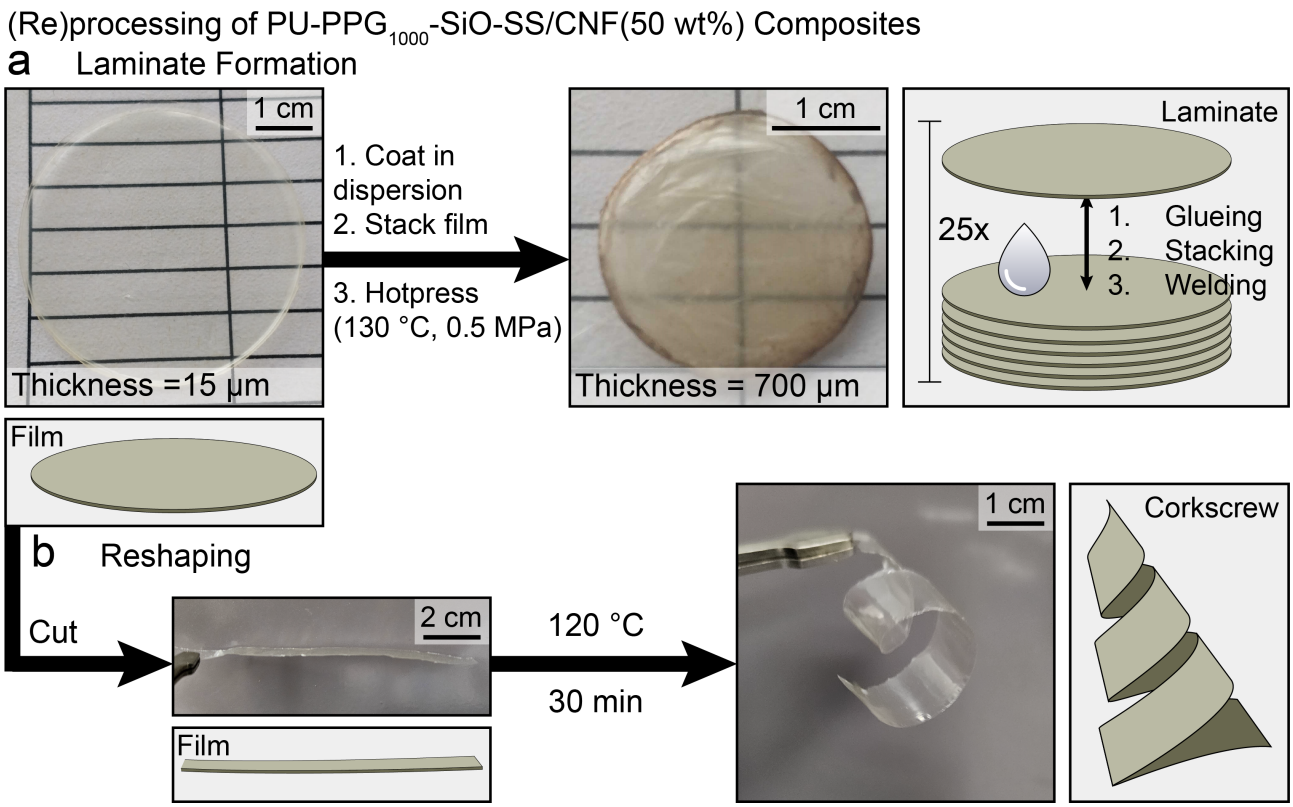

Figure 9. (Re)processing of PU-PPG-SiO-SS/CNF(50 wt%) composites. (a) Formation of thick laminate by the welding of individual composite films, through a process using aqueous dispersion as a glue and subsequent hot pressing (130 ℃, 0.5 MPa). (b) Rapid reshaping of NC by application of heat (120 ℃).

4.3.6 Tensile Properties of NCs: Variability and Influencing Factors

Finally, we analyzed the tensile mechanical properties of the prepared PU- and PHU-CNF NCs with 90 wt% CNF, together with pure CNF films as a reference (**Figure 10**). We noticed significant variability among the measurement results, even between "identical" specimens cut from the same films. While some variation is normal in tensile testing, especially for stiff and brittle NCs, the differences shown in in **Figure 10b,e,f,h** are unusual. To ensure not overlooking critical patterns, we chose not to use averaged properties or curves for the NCs. We do take the average of multiple measurements for the CNF control, as this is a known material that does not display the same discrepancies in the data.

The CNF control is a strong and tough material with σ_b of ca. 300 MPa, ε_b of ca. 5 %, and E of ca. 11 GPa (**Figure 10a**). Most of the measurement data on the NCs resemble the tensile properties of pure CNF film, which is expected given the high CNF content (90 wt%) in the NCs. In bioinspired CNF-based NCs, introducing a synthetic polymer phase typically reduces σ_b and E due to the lower strength and stiffness of the polymer compared to CNF, while ε_b can increase based on the polymer's ductility.[24,30,71] Toughness depends on the interplay of these properties and may increase or decrease with the addition of a new phase. This behavior can be roughly described by the rule of mixtures,

where composite properties fall between those of the individual components, weighted by their relative fractions.

As an outlier, PU-PPG_{1000}/CNF(90 wt%) shows inferior results on all properties compared to pure CNF. This could be a result of the PU being a liquid as opposed to a crosslinked network, which would explain mainly lower strength and stiffness (**Figure 10c**). Moreover, ductility did not improve compared to the CNF control. These data are limited, however, by there being only two measurement results, which should be expanded upon for more definitive conclusions. For all the other PU- and PHU-based NCs, the majority of measurements resemble the CNF properties on first glance (**Figure 10b,d-h**).

Next, we focus on measurements that deviate significantly from the properties of pure CNF films, showing superior σ_b and E values of up to 550 MPa and 32 GPa, respectively, demonstrating unprecedented mechanical performance. These results are observed for PU-PPG_{1000}-SiO-SS/CNF(90 wt%), PU-PCl_{2000}-SiO-SS/CNF(90 wt%), and PHU/CNF(90 wt%), and to a lesser degree for PU-PCl_{2000}/CNF(90 wt%) (**Figure 10b,e,f,h**). Similar but lesser synergies (σ_b ~ 340 MPa and E ~ 11 GPa) in CNF-based NCs have been reported in literature for PUs, where the PU phase enhances the NC strength, stiffness, and toughness beyond those of pure CNF films, despite the PU itself having lower strength and stiffness.[32] This effect relies on good interactions between the synthetic polymer and CNF phases, likely involving hydrogen or covalent bonding. However, the inconsistency of the results in this project presents a new challenge.

For a more quantitative analysis, we plotted σ_b versus E (**Figure 10i**) and ε_b versus U_t (**Figure 10j**) for all measurements. The first plot illustrates the strength and stiffness range for bioinspired CNF-based NCs, which would usually remain within the CNF zone, not surpassing the properties of pure CNF. However, for our data, the more extreme data points observed earlier fall far outside this box. Moreover, many of the other measurements also exceed the stiffness and sometimes also the strength of CNF films in a more moderate fashion. While this does not directly explain the large discrepancies, it demonstrates synergy between the PUs or PHU and CNF, enabling the composites to exceed the rule of mixtures. When we shift focus to the second plot, we observe that many samples also exceed the ε_b of CNF films (average ε_b = 5.07%; highest measured ε_b = 6.00%), reaching up to 8% elongation. Most results align along a pseudo-linear trend (fitted by eye), suggesting that toughness scales proportionally with ductility and that the stress-strain curves (strength and stiffness) share similar shapes. However, samples deviating from this trend show a much larger increase in toughness relative to ductility as a result of the vastly superior σ_b and E, which is not how NCs usually obtain improved toughness.[24,71] While this is a qualitative observation rather than rigorous analysis, it highlights deviations from general behavior.

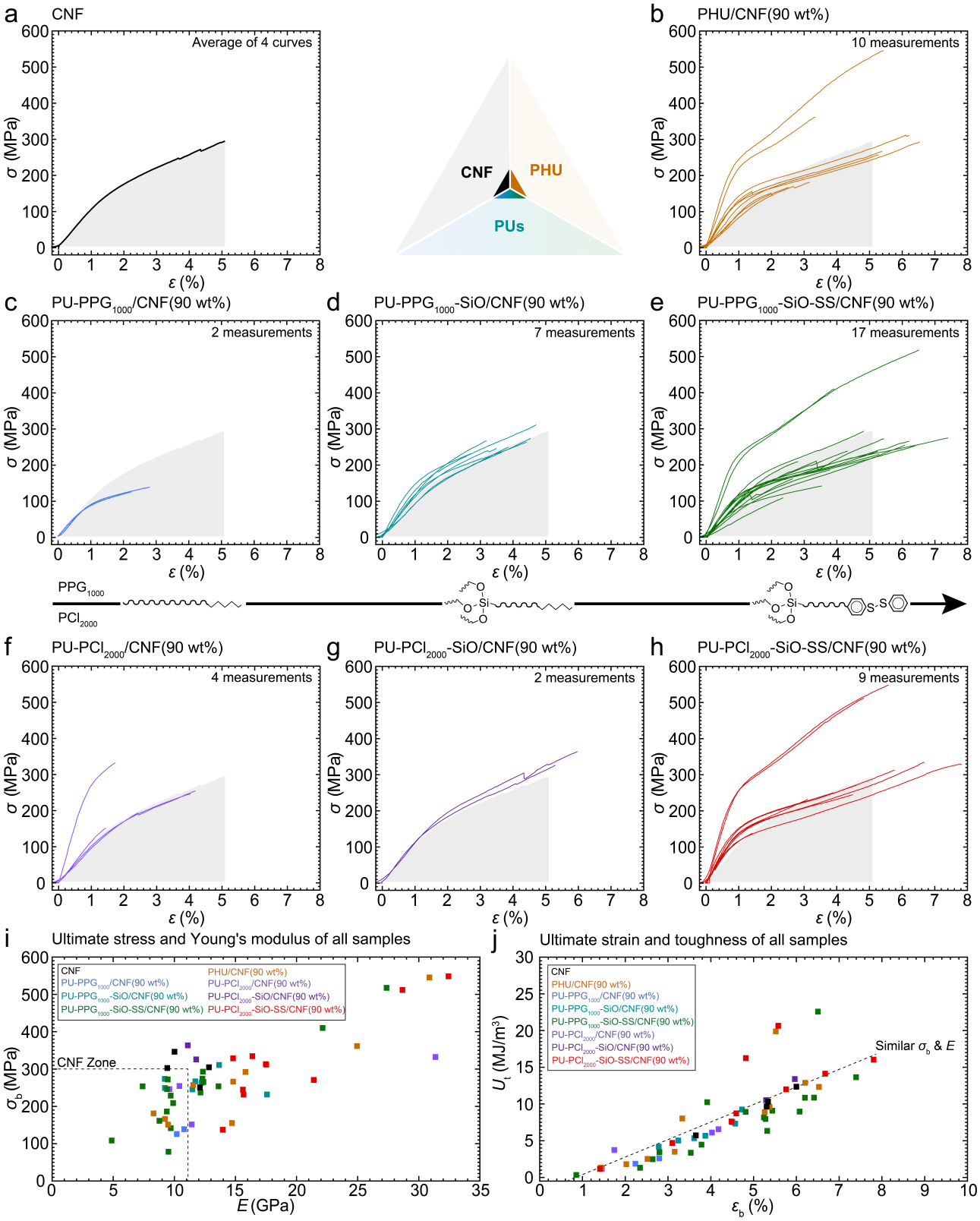

Figure 10. Tensile tests of CNF (averaged curve) and PU- and PHU-CNF NC films (individual measurements) for (a) CNF, (b) PHU/CNF(90 wt%), (c) PU-PPG$_{1000}$/CNF(90 wt%), (d) PU-PPG$_{1000}$-SiO/CNF(90 wt%), (e) PU-PPG$_{1000}$-SiO-SS/CNF(90 wt%), (f) PU-PCl$_{2000}$/CNF(90 wt%), (g) PU-PCl$_{2000}$-SiO/CNF(90 wt%), and (h) PU-PCl$_{2000}$-SiO-SS/CNF(90 wt%). The tensile results of CNF are depicted as greyed out areas for reference. Below, overview of (i) ultimate stress and Young's modulus and (j) ultimate strain and toughness is given for all samples. The CNF zone box and the linear dashed line (fitted by eye) are based on the properties of the pure CNF films.

The origin of the observed discrepancies remains unclear, so we focused further investigation on PU-PPG_{1000}-SiO-SS/CNF(90 wt%) and PU-PCl_{2000}-SiO-SS/CNF(90 wt%). We prepared multiple additional NC samples and conducted a larger quantity of measurements to rule out anomalies and attempt to replicate the results (**Figure 11a,b**). The analysis of the new data (**Figure 11c**) yielded similar findings: some measurements displayed the previously noted superior properties, while most aligned more closely with CNF properties, though many still showed improved stiffness. Strength was generally lower, and ductility higher across all samples (except CNF, which was not re-measured), potentially due to higher relative humidity during testing. Additionally, NCs based on PPG_{1000} and PCl_{2000} exhibited similar properties overall, with a slightly higher Young's modulus for the NCs based on PCl_{2000}.

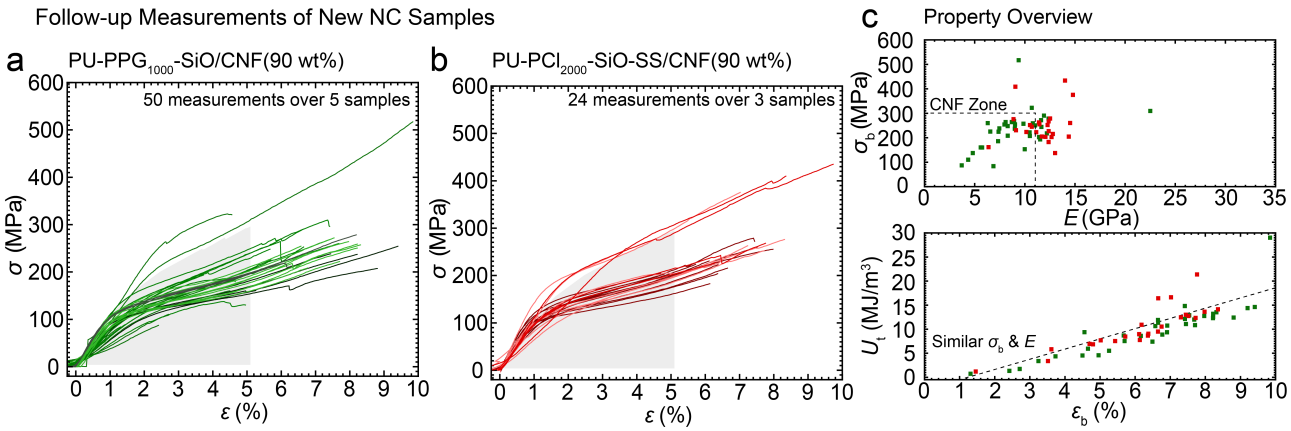

Figure 11. Follow-up tensile tests of (a) PU-PPG_{1000}-SiO-SS/CNF(90 wt%) and (b) PU-PCl_{2000}-SiO-SS/CNF(90 wt%) over multiple samples. (c) An overview of the ultimate stress versus Young's modulus and ultimate strain versus toughness is also given. The CNF zone box and the linear dashed line (fitted by eye) are based on the properties of the pure CNF films.

We explored various strategies to better understand and replicate the NC properties. First, we subjected PU-PPG_{1000}-SiO-SS/CNF(90 wt%) NCs to a curing protocol to potentially enhance bond exchange, crosslinking, polymer or fibrillar movement, and phase separation or mixing (**Figure 12a**). However, this resulted in no significant improvement, and strength appeared to decrease slightly, though this conclusion should be handled with some care on account of the relatively small number of measurements. This suggests that the high strength and stiffness observed in some results cannot be attributed to a thermally driven process. Next, we synthesized new PUs (PPG_{1000}-SiO-SS and PCl_{2000}-SiO-SS) and prepared fresh PU dispersions to test whether dispersion age influenced the results (**Figure 12b,c**). Again, no clear trends emerged. The two PUs produced similar properties, closely resembling those of CNF, though slightly lower than those in **Figure 10** and **Figure 11**. Due to the limited number of measurements, this is difficult to confirm. Across all tests, the most consistent observation was that nearly all samples exhibited superior stiffness compared to CNF films.

We next explored a strategy inspired by literature to enhance the properties of PU-based bioinspired CNF NCs.[19,32,72,73] We replaced the CNF counterion (sodium) with tetrabutylammonium (TBA), which alters the surfaces of the CNF and impacts the interactions with the polymer phase. This approach

slightly reduced the properties of pure CNF films, consistent with literature findings. However, unlike in literature, it also diminished the NC properties in our system, with similar ε_b and reductions in σ_b, E, and U_t. The impact on NC stiffness was particularly pronounced, disrupting the synergistic effect observed previously. The disparity with the literature results likely arises from differences in the molecular structure and functionality of the PUs. Additionally, the commercial PU formulation used in literature may have included additives that influenced the NC properties.

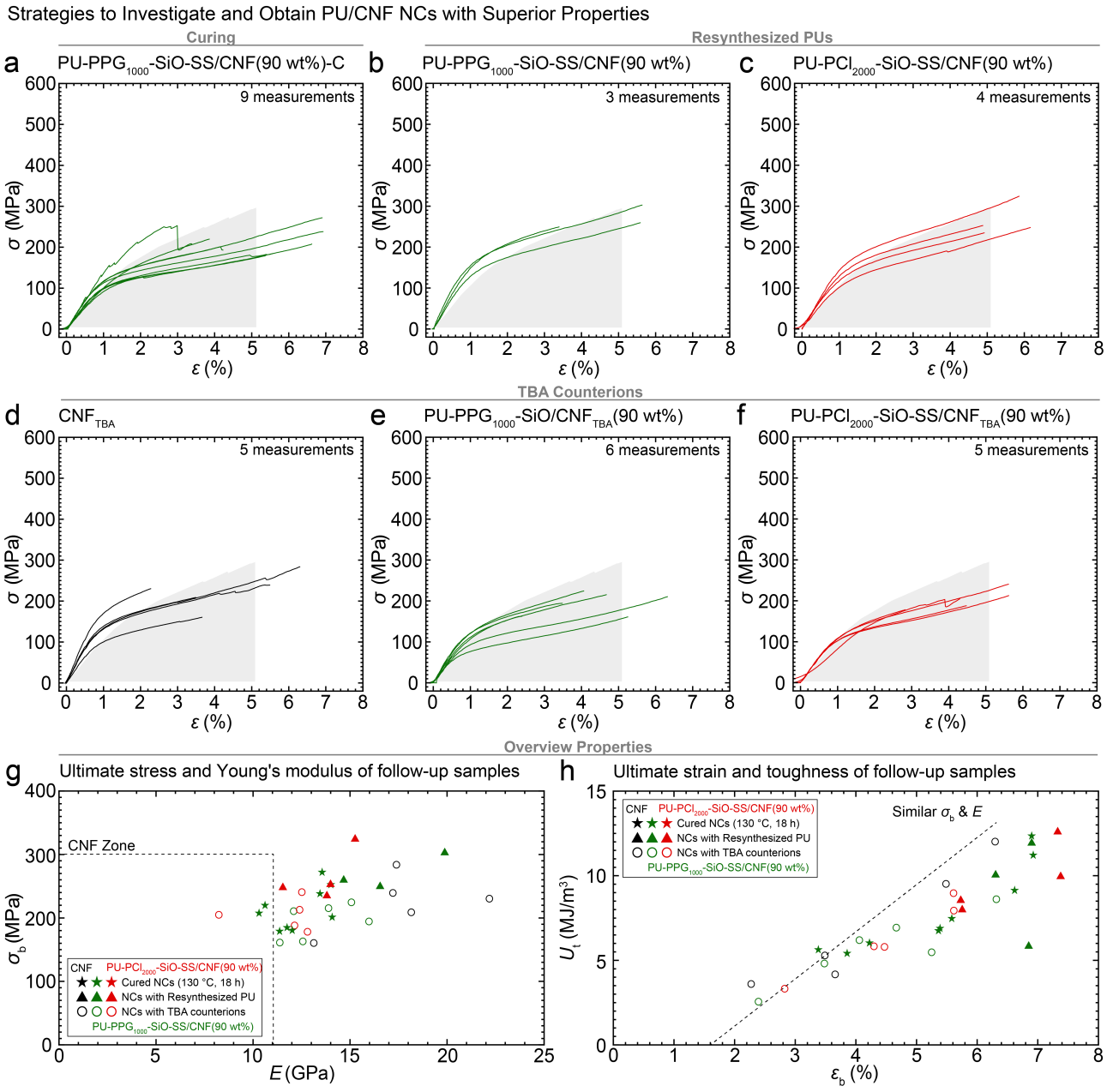

Figure 12. Variety of strategies to improve superior NC properties. Tensile tests of (a) cured PU-PPG$_{1000}$-SiO-SS/CNF(90 wt%), (b) PU-PPG$_{1000}$-SiO-SS/CNF(90 wt%) and (c) PU-PCl$_{2000}$-SiO-SS/CNF(90 wt%) prepared from resynthesized PUs, and NCs based on CNFs with TBA as a counterion for (d) CNF$_{TBA}$, (e) PU-PPG$_{1000}$-SiO-SS/CNF$_{TBA}$(90 wt%), and (f) PU-PCl$_{2000}$-SiO-SS/CNF$_{TBA}$(90 wt%). An overview of (g) ultimate stress and Young's modulus and (h) ultimate strain and toughness is also given. The CNF zone box and the linear dashed line (fitted by eye) are based on the properties of the pure CNF films.

Lastly, we visualized the effect of PU weight content on NC properties (**Figure 13**). To allow for optimal comparison, all measurements were conducted using the same PU and CNF dispersions, prepared and measured on the same day to minimize variations for taking average results.

The expected trend shows that strength and stiffness increase with higher CNF weight fractions, while ductility remains relatively constant across all NCs. This suggests that CNF failure occurs at a certain elongation, without significant changes based on the PU content present. Strong interphase interactions likely prevent energy dissipation, fibrillar movement or sacrificial bonding to improve ductility. Toughness generally increases with higher CNF content, reflecting these parameters. To highlight the discrepancies in the NC with 90 wt% CNF, we included two averages representing different result types.

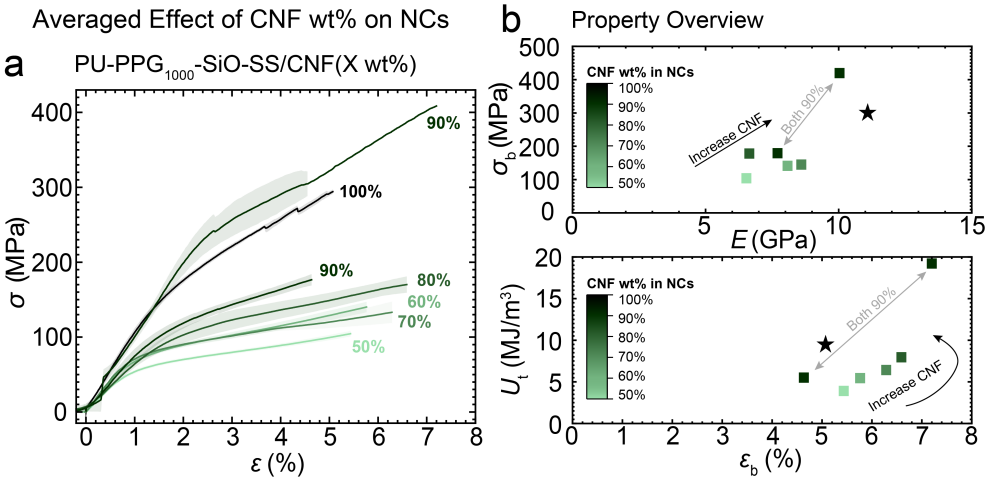

Figure 13. Effect of the CNF weight content for PU-PPG$_{1000}$-SiO-SS/CNF(X wt%). (a) Tensile test average curves for NCs with 50, 60, 70, 80, 90, and 100 wt% CNF. There are two curves for 90 wt% to indicate that superior properties were obtained only for some measurements. (b) An overview of the ultimate stress, Young's modulus, ultimate strain, and toughness is depicted.

Next we briefly discuss factors that could significantly influence NC properties. Interphase interaction may be critical to the synergistic effect, raising the question of whether certain samples with superior properties exhibit enhanced interactions.[74] Siloxane bonds can potentially form between PU (APTES) and CNF, but this cannot explain the superior properties observed in NCs based on PHU or PU-PCl$_{2000}$, which lack APTES. Hydrogen bonding, due to the hydrophilicity of PUs and PHU, likely contributes to the synergy in all NCs, but does not account for the observed discrepancies between measurements. Ester bond formation between PHU and CNF is theoretically possible but unlikely at room temperature. These discrepancies are particularly puzzling because the samples were cut from the same films, prepared under identical conditions, measured on the same device, and had similar thicknesses and appearances. Furthermore, the curing protocol shown in **Figure 12a** would likely have revealed such effects, as higher temperatures would accelerate the chemical reactions involved.

A plausible explanation relies on the nature of the PU and PHU dispersions, consisting of nano- or micro-aggregates rather than fully dissolved polymer chains, with variation in particle size. Complex structural entities in CNF-based NCs, such as aggregates or physical entanglements, can drastically affect the mechanical performance.[29] During or after mixing with CNFs in aqueous conditions, inconsistent dispersion or phase morphology across the cast film could lead to local variations in composition. Larger globules, as seen in SEM images (**Figure 7c**), might act as physical crosslinks within CNF bundles, increasing stiffness while enhancing stress transfer and reducing stress localization, thereby also improving strength. Such a mechanism would be akin to how nanoparticle introduction in polymer networks or even dual networks can display synergy.[75,76] This could improve strength and explain why the effect appears across different PU and PHU types, as all share a similar dispersion process. Additionally, we observed that the dispersions responsible for the superior type NC results (except for one measurement related to PU-PCl_{2000}-SiO) are those with the largest particle sizes (PU-PPG_{1000}-SiO-SS and PHU) or those that could not be measured via DLS on account of particle size or dispersities exceeding the limits (PU-PCl_{2000}-SiO-SS). This provides further evidence that parameters associated with the dispersion are largely responsible for the observed results.

4.4 Conclusion

This work presents a library of PU and PHU materials with diverse properties, architectures, and functionalities. We synthesized three PUs from the amorphous polyol PPG_{1000}, and three from the semi-crystalline polyol PCl_{2000}. For each polyol, the series includes a linear PU, a PU end-capped with APTES to introduce crosslinks and enable covalent bond exchange for CAN properties, and a PU incorporating both APTES and an aromatic disulfide chain extender to further enhance dynamic behavior. The PHU serves as a more hydrophilic alternative, featuring hydroxyl groups in the linear polymer backbone. All materials are functionalized with internal emulsifiers to facilitate the preparation of high polymer content aqueous dispersions via the phase inversion acetone process. DLS analysis revealed that the particle sizes are in the range of hundreds of nanometers, while solubility tests of the dry polymers show that the linear polymers fully dissolved in acetone, whereas the networks remain largely insoluble due to their crosslinking. The introduction of crosslinks also enhances the stiffness and strength of the materials, as confirmed by tensile testing. Stress relaxation and recycling experiments further revealed the dynamic nature of the crosslinked PUs, highlighting their capability to function as CAN materials through bond exchange mechanisms. Notably, while all networks exhibit dynamic behavior due to siloxane exchanges and the inherent dynamic character of urethane bonds, those incorporating disulfides possess an additional bond exchange process.

We integrated the prepared PUs and PHUs into bioinspired CNF NCs to develop dynamic, cellulose-based films with high strength and stiffness. Leveraging the dynamic properties of the PUs, we demonstrated effective reshaping of NCs and laminate formation by stacking and hot-pressing multiple films. This approach broadens the range of materials achievable with the unique bioinspired NC design, enabling the fabrication of thicker samples and potentially three-dimensional structures. The process is straightforward, requiring only moderate heating for brief periods, making it adaptable to various molding techniques. Moreover, the dynamic CAN properties could potentially enable NC recycling through milling or acetone swelling followed by hot pressing, offering a second life for these materials.

We evaluated the mechanical properties of the NCs through tensile testing. As with other CNF-based NCs, higher CNF content generally enhances strength, stiffness, and toughness. Notably, a synergistic effect emerges with 10 wt% PU and PHU, achieving superior properties compared to pure CNF or PU alone. While some results showed performance close to pure CNF films with only slightly higher stiffness, others demonstrated vastly superior tensile properties, including strengths up to 550 MPa and Young's modulus values reaching 32 GPa, unprecedented for such materials. These discrepancies might stem from the nature of the PU dispersions: varying particle sizes and dispersities influence their integration into the CNF matrix. Interestingly, we observed similar results across different PUs and PHUs, suggesting the effect may not be fully dependent on the molecular

structure. Future studies should focus on controlled variation of particle size and dispersity for the same PU in the preparation of bioinspired CNF NCs and how it affects mechanical properties.

Supporting Information

Supporting information: Additional experimental details and methods, materials, and supplementary experimental data.

Acknowledgements

This project has received funding from the European Union's horizon research and innovation programme under the Marie Skłodowska-Curie Grant agreement no. 860911. AW acknowledges funding via a Gutenberg Research Professorship underpinning his Life-Like Materials Program.

Conflict of Interest

The authors declare no conflict of interest.

4.5 Supporting Information

Chapter 4. Polyurethane Covalent Adaptable Networks: Unlocking Superior Mechanical Properties in Cellulose Nanofiber-Based Bioinspired Nanocomposites

Sjoerd Engels[1], Haritz Sardon[2], Andreas Walther[1]**

[1]Life-Like Materials and Systems, Department of Chemistry, University of Mainz, Duesbergweg 10-14, 55128 Mainz, Germany.

[2]POLYMAT, University of the Basque Country UPV/EHU, Joxe Mari korta Center, Avda. Tolosa 72, Donostia-San Sebastián 20018, Spain.

4.5.1 Instrumentation

4.5.1.1 Tensile tests for PUs

Tensile tests for the pure PU samples were performed at room temperature on a Shimadzu EZ-LX Long-Stroke Model tensile tester equipped with a 50 N load cell. The PUs were prepared as rectangular samples (~ 15 mm x 2 mm) with a thickness of ca. 1 mm. At least three measurements were performed for each PU after conditioning at 50% relative humidity for 24 h, with a strain rate of 144 mm/min for PU-PCl_{2000} and 50 mm/min for the other PUs. Subsequently, we took the mean for each measurement set. We determined the Young's modulus (*E*) from the slope of the linear region in the stress/strain curves.

4.5.1.2 Tensile tests for bioinspired NCs

Tensile tests for the bioinspired NC samples were performed at room temperature on a DEBEN minitester equipped with a 20 N load cell. The PU-CNF NCs were prepared as rectangular samples (10 mm x 2 mm) with a thickness of ca. 10 µm. Measurements were performed for each material after conditioning at 50% relative humidity for 24 h, with a strain rate of 0.5 mm min^{-1}. The Young's modulus (*E*) was determined from the slope of the linear region in the stress/strain curves.

4.5.1.3 Dynamic mechanical analysis (DMA)

Shear and tensile mode DMA measurements were performed using a MCR702 MultiDrive from Anton Paar equipped with an oven attachment and 8 mm parallel plate geometries (~ 0.5 mm gap) for shear mode or solid rectangular fixtures for tensile mode (~ 14 x 4 x 0.01 mm^3 for NCs). **The temperature sweeps** of PU-PPG_{1000}-SiO-SS/CNF(X wt%) were performed in tensile mode from 30 to 195 °C at a rate of 2.5 °C min^{-1}, 10 MPa stress, and using a frequency of 3.5 Hz. **Stress relaxation tests** were performed in shear mode at temperatures ranging from 110 °C to 190 °C at 3% strain.

4.5.1.4 Fourier transform infrared spectroscopy (FTIR).

FTIR spectra were acquired using a Jasco FT/IR-4100 spectrometer with a frequency range from 4000 to 600 cm^{-1}. The reaction progress of PUs were followed by measuring aliquots of the reaction mixtures and letting the acetone evaporate prior to starting the measurement.

4.5.1.5 Scanning Electron Microscopy (SEM)

SEM imaging was performed at 1 kV using a Gemini 1530 (Carl Zeiss AG Oberkochem, Germany) equipped with a Schottky FEG gun and InLens (SE) and Everhart-Thornley detectors. The samples were taken from NC films fractured in tensile mode and placed on the holder such that the cross section of fracture could be imaged. No external conductive coating was applied to the samples.

4.5.1.6 Compression Molding (Hot Pressing)

Compression molding was performed on a Collin P 200 E press.

4.5.1.7 Dynamic Light Scattering (DLS)

The particle size (D_p) and particle size distribution of the aqueous dispersions were measured using a Zetasizer Nano S from Malvern operating with a 4 mW He–Ne laser (633 nm wavelength) and a fixed detector angle of 173 (non-invasive backscattering geometry NIBSTM). The cell holder remained at constant temperature by use of a Peltier element. The samples were diluted with water before the measurements to avoid multiple light scattering.

4.5.2 Materials

Polypropylene glycol (M_n = 1000) (PPG_{1000}) and polycaprolactone diol (M_n = 2000) (PCl_{2000}), bis(3-aminopropyl)-poly(dimethyl siloxane) (M_n = 2500), and 1,4-butanediol (BD, 99%) were purchased from Sigma Aldrich. Isophorone diisocyanate (IPDI, 98%) and dimethylolpropionic acid (DMPA, > 98%) were sourced from Thermo Fisher Chemicals. Acetone, glacial acetic acid, and triethylamine (TEA, ≥ 99.5%) were obtained from Fisher Chemical. Dibutyltin dilaurate (DBTDL, > 95.0%) and 4,4'-dihydroxy diphenyl disulfide (SS) were supplied by TCI. (3-Aminopropyl)triethoxysilane (APTES, 98.0%) was purchased from Carl Roth. 1,4-dibutanol dicarbonate (4,4'-[1,4-Butanediylbis(oxymethylene)]bis[1,3-dioxolan-2-one) was obtained from the Polymat institute, synthesized following an adapted version of the method reported by Bossion, A. et al., where a diglycerol derivative is reacted with dimethyl carbonate.[77] Bis-N-8-Ce (6,6′-(ethane-1,2-diyl)bis(1,3,6-dioxazocan-2-one) was also obtained from the Polymat institute, synthesized following an adapted version of the method reported by Yuen, A. et al.[78] Cellulose nanofibrils (CNFs) were prepared by oxidizing TEMPO-oxidized Kraft pulp under neutral conditions, adjusting the pH to 9 with NaOH, and homogenizing the suspension using an LM10 Microfluidizer (Microfluidics) with four shear cycles (2 x 1400 bar, 2 x 1000 bar).[17,24] The resulting CNFs exhibited a carboxyl group content of 0.44 mmol/g, a degree of polymerization (DP_v) of 725 as determined by viscosimetry, and a crystallinity of 77% as measured by X-ray diffraction (XRD).

4.5.3 Synthesis of PUs and Preparation of Aqueous Dispersions via the Acetone Process ($PU\text{-}PPG_{1000}$, $PU\text{-}PPG_{1000}$-SiO, $PU\text{-}PPG_{1000}$-SiO-SS, $PU\text{-}PCl_{2000}$, $PU\text{-}PCl_{2000}$-SiO, $PU\text{-}PCl_{2000}$-SiO-SS).

PU dispersions were prepared following adapted versions of procedures outlined in literature.[43,44] The complete process involved two steps. In the first step the polymer synthesis was performed, and in the second step the dispersion was prepared via the acetone process. An overview of the individual components added for each synthesis is given in Table S1 (adjusted from Table 1).

Table S1. Overview of PU compositions (Adjusted from Table 1).

Sample name	IPDI (eq.)	PPG_{1000} (eq.)	PCl_{2000} (eq.)	DMPA (eq.)	BD (eq.)	SS (eq.)	APTES (eq.)	Acetone (mL g^{-1} PU)	Water (mL g^{-1} PU)
PU-PPG_{1000}	1	0.40	-	0.23	0.44	-	-	1.76	3.55
PU-PPG_{1000}-SiO	1	0.40	-	0.23	0.19	-	0.34	1.05	2.15
PU-PPG_{1000}-SiO-SS	1	0.40	-	0.20	-	0.12	0.57	0.972	1.98
PU-PCl_{2000}	1	-	0.30	0.30	0.47	-	-	1.00	2.04
PU-PCl_{2000}-SiO	1	-	0.25	0.25	0.27	-	0.43	0.863	1.77
PU-PCl_{2000}-SiO-SS	1	-	0.25	0.25	-	0.16	0.73	1.02	2.09

a)

4.5.3.1 Step 1 - Synthesis

The PUs were synthesized in a 250 mL jacket glass reactor equipped with a mechanical stirrer, nitrogen inlet, and a condenser. First, the polyol (polypropylene glycol with M_n = 1000 g/mol (PPG_{1000}) or polycaprolactone diol with M_n = 2000 g/mol (PCl_{2000})) was chosen (0.25 – 0.4 eq.) and mixed with dimethylolpropionic acid (DMPA; ca. 0.3 mmol/g or 0.23 – 0.3 eq.), triethylamine (equimolar to DMPA), dibutyltin dilaurate (DTBL; 700 ppm), and acetone (see Table S1). The reactor was heated to 60 °C upon mechanical stirring. Next, isophorone diisocyanate (IPDI; 1 eq.) was added dropwise at ca. 1 mL/min under nitrogen atmosphere and constant stirring (250 rpm) and subsequently reacted for 4 h under those conditions. Following this, the chain extender of choice (1,4-butanediol (BD) or 4,4'-dihydroxy diphenyl disulfide (SS)) was added (0.12 – 0.47 eq.) and the reaction was continued for another 4 h under the same conditions.

In the case of **linear PUs**, the amount of chain extender added was in small excess to the leftover NCO groups of IPDI, leading to complete reaction (monitored by FTIR) to yield the final PUs. Then the PUs were taken to the dispersion step.

In the case of the **PU networks**, chain extender was added in deficit so that the polymer chains are end-functionalized with reactive NCO group. Then, the reaction temperature was dropped to 25 °C while maintaining the mechanical stirring (250 rpm), and 3-aminopropyl triethoxysilane (APTES; 0.34 – 0.73 eq.) was added in small excess relative to the remaining NCO groups. The reaction was continued for ca. 1 h until completion (monitored by FTIR) to yield the PUs ready for the dispersion step.

4.5.3.2 Step 2 – Dispersion (Aqueous)

At the start of the dispersion process, the temperature was set to 25 °C and the PU concentration in acetone was determined by taking an aliquot and weighing it before and after drying. To compensate for solvent evaporation (unavoidable despite the condenser), fresh acetone and triethylamine were added to restore the mixture to its initial composition. Then, the mechanical stirring rate was set to

400 rpm, and water (see Table S1) was added dropwise to the reactor at ca. 2 mL/min. After complete addition, the stirring was continued for another 30 min and subsequently the acetone was removed under reduced pressure at 25 °C to obtain the final dispersions.

4.5.4 Synthesis of PHU and Preparation of Aqueous Dispersion via the Acetone Process.

PHU were synthesized and dispersed following adapted versions of procedures outlined in literature.[48] The solvent-free synthesis started by mixing bis(3-aminopropyl) terminated poly(dimethyl siloxane) with M_n = 2500 g/mol (1 eq.), 1,4-dibutanol dicarbonate (0.7 eq.), and bis-N-8-Ce at 80 °C (0.3 eq.). The mixture was then stirred at 80 °C for 48 h. Next, the aqueous dispersion was prepared by first adding acetone (40 wt%) and glacial acetic acid (0.45 eq.). Then, under mechanical stirring (400 rpm) water (1.5 mL/g PHU) was added in dropwise fashion at 1 mL/min, and subsequently the acetone was removed under reduced pressure at 25 °C.

4.5.5 Preparation of Bioinspired CNF NCs

Aqueous dispersion of PU or PHU were diluted to yield dispersions of 0.25 wt% polymer. Subsequently, a CNF dispersion (0.25 wt%) was added in dropwise fashion to the PU or PHU dispersion while stirring vigorously. Depending on the fractions added of both dispersions, the weight content of CNF in the final NCs can be controlled. Afterwards, the mixtures were mixed for ca. 20 h and then cast in Petri dishes to evaporate the water in ambient conditions, yielding transparent NCs with thicknesses of ca. 10 µm.

4.5.6 Swelling Tests (Insoluble Fraction Determination).

The insoluble fractions were determined by swelling the fully dried polymers (ca. 100 mg) in acetone (10 mL) for each of the six different polymers (PU-PPG1000, PU-PPG_{1000}-SiO, PU-PPG_{1000}-SiO-SS, PU-PCl_{2000}, PU-PCl_{2000}-SiO, PU-PCl_{2000}-SiO-SS, and PHU) for 48 h. Then, the insoluble fractions were weighed after the liquid phases were removed and the samples were dried by vacuum.

4.5.7 Dispersion Weight Content Determination

The weight fractions of polymer in the dispersions were determined by following the weight loss of 1 mL of dispersion upon drying. The fraction of dried weight compared to the initial weight gives the weight fraction of polymer.

4.5.8 Bioinspired CNF NC Reshaping

PU-PPG$_{1000}$-SiO-SS/CNF(50 wt%) NCs were reshaped by fixing the sample to a desired configuration and next heating the sample for 120 °C for 30 min to lock in the shape.

4.5.9 NC Laminate Preparation

Laminates of PU-PPG$_{1000}$-SiO-SS/CNF(50 wt%) were prepared by coating NC films in aqueous dispersion of the same composition, prior to stacking them on top of each other to the desired number of layers. Then the stack was hotpressed in an enclosed mold at a low pressure (130 °C, 0.5 MPa, 45 min).

Transparent and Milky Aqueous PU Dispersions

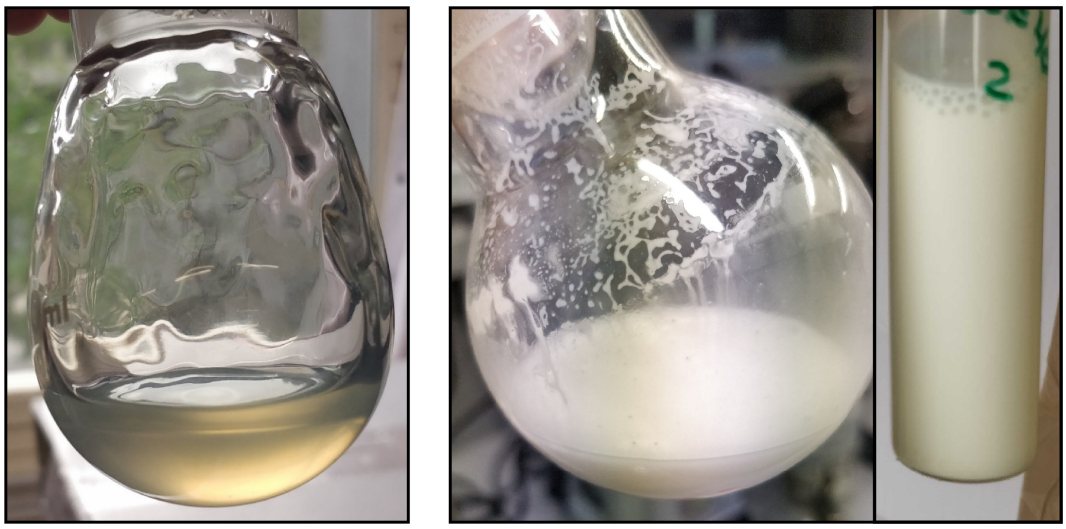

Figure S1. Optical images of aqueous PU dispersions. Two types of dispersions were obtained overall, transparent and milky white or yellow.

4.6 References

(1) Fratzl, P.; Weinkamer, R. Nature's Hierarchical Materials. *Prog. Mater. Sci.* **2007**, *52* (8), 1263–1334. https://doi.org/10.1016/j.pmatsci.2007.06.001.

(2) Kumar, A.; Jyske, T.; Petrič, M. Delignified Wood from Understanding the Hierarchically Aligned Cellulosic Structures to Creating Novel Functional Materials: A Review. *Adv. Sustain. Syst.* **2021**, *5* (5), 2000251. https://doi.org/10.1002/adsu.202000251.

(3) Henriksson, M.; Berglund, L. A.; Isaksson, P.; Lindström, T.; Nishino, T. Cellulose Nanopaper Structures of High Toughness. *Biomacromolecules* **2008**, *9* (6), 1579–1585. https://doi.org/10.1021/bm800038n.

(4) Reimer, M.; Zollfrank, C. Cellulose for Light Manipulation: Methods, Applications, and Prospects. *Adv. Energy Mater.* **2021**, *11* (43), 2003866. https://doi.org/10.1002/aenm.202003866.

(5) Guo, J.; Haehnle, B.; Hoenders, D.; Creusen, G.; Jiao, D.; Kuehne, A. J. C.; Walther, A. Biodegradable Laser Arrays Self-Assembled from Plant Resources. *Adv. Mater.* **2020**, *32* (29), 2002332. https://doi.org/10.1002/adma.202002332.

(6) Antlauf, M.; Boulanger, N.; Berglund, L.; Oksman, K.; Andersson, O. Thermal Conductivity of Cellulose Fibers in Different Size Scales and Densities. *Biomacromolecules* **2021**, *22* (9), 3800–3809. https://doi.org/10.1021/acs.biomac.1c00643.

(7) Li, T.; Song, J.; Zhao, X.; Yang, Z.; Pastel, G.; Xu, S.; Jia, C.; Dai, J.; Chen, C.; Gong, A.; Jiang, F.; Yao, Y.; Fan, T.; Yang, B.; Wågberg, L.; Yang, R.; Hu, L. Anisotropic, Lightweight, Strong, and Super Thermally Insulating Nanowood with Naturally Aligned Nanocellulose. *Sci. Adv.* **2018**, *4* (3), eaar3724. https://doi.org/10.1126/sciadv.aar3724.

(8) Benítez, A. J.; Walther, A. Cellulose Nanofibril Nanopapers and Bioinspired Nanocomposites: A Review to Understand the Mechanical Property Space. *J. Mater. Chem. A* **2017**, *5* (31), 16003–16024. https://doi.org/10.1039/C7TA02006F.

(9) Saito, T.; Uematsu, T.; Kimura, S.; Enomae, T.; Isogai, A. Self-Aligned Integration of Native Cellulose Nanofibrils towards Producing Diverse Bulk Materials. *Soft Matter* **2011**, *7* (19), 8804–8809. https://doi.org/10.1039/C1SM06050C.

(10) Azizi Samir, M. A. S.; Alloin, F.; Dufresne, A. Review of Recent Research into Cellulosic Whiskers, Their Properties and Their Application in Nanocomposite Field. *Biomacromolecules* **2005**, *6* (2), 612–626. https://doi.org/10.1021/bm0493685.

(11) Pääkkö, M.; Ankerfors, M.; Kosonen, H.; Nykänen, A.; Ahola, S.; Österberg, M.; Ruokolainen, J.; Laine, J.; Larsson, P. T.; Ikkala, O.; Lindström, T. Enzymatic Hydrolysis Combined with Mechanical Shearing and High-Pressure Homogenization for Nanoscale Cellulose Fibrils and Strong Gels. *Biomacromolecules* **2007**, *8* (6), 1934–1941. https://doi.org/10.1021/bm061215p.

(12) Henriksson, M.; Henriksson, G.; Berglund, L. A.; Lindström, T. An Environmentally Friendly Method for Enzyme-Assisted Preparation of Microfibrillated Cellulose (MFC) Nanofibers. *Eur. Polym. J.* **2007**, *43* (8), 3434–3441. https://doi.org/10.1016/j.eurpolymj.2007.05.038.

(13) Ansari, F.; Berglund, L. A. Toward Semistructural Cellulose Nanocomposites: The Need for Scalable Processing and Interface Tailoring. *Biomacromolecules* **2018**, *19* (7), 2341–2350. https://doi.org/10.1021/acs.biomac.8b00142.

(14) Walther, A.; Timonen, J. V. I.; Díez, I.; Laukkanen, A.; Ikkala, O. Multifunctional High-Performance Biofibers Based on Wet-Extrusion of Renewable Native Cellulose Nanofibrils. *Adv. Mater.* **2011**, *23* (26), 2924–2928. https://doi.org/10.1002/adma.201100580.

(15) Qi, Z.-D.; Saito, T.; Fan, Y.; Isogai, A. Multifunctional Coating Films by Layer-by-Layer Deposition of Cellulose and Chitin Nanofibrils. *Biomacromolecules* **2012**, *13* (2), 553–558. https://doi.org/10.1021/bm201659b.

(16) Jonoobi, M.; Oladi, R.; Davoudpour, Y.; Oksman, K.; Dufresne, A.; Hamzeh, Y.; Davoodi, R. Different Preparation Methods and Properties of Nanostructured Cellulose from Various Natural Resources and Residues: A Review. *Cellulose* **2015**, *22* (2), 935–969. https://doi.org/10.1007/s10570-015-0551-0.

(17) Isogai, A.; Saito, T.; Fukuzumi, H. TEMPO-Oxidized Cellulose Nanofibers. *Nanoscale* **2011**, *3* (1), 71–85. https://doi.org/10.1039/C0NR00583E.

(18) Saito, T.; Kimura, S.; Nishiyama, Y.; Isogai, A. Cellulose Nanofibers Prepared by TEMPO-Mediated Oxidation of Native Cellulose. *Biomacromolecules* **2007**, *8* (8), 2485–2491. https://doi.org/10.1021/bm0703970.

(19) Isogai, A.; Bergström, L. Preparation of Cellulose Nanofibers Using Green and Sustainable Chemistry. *Curr. Opin. Green Sustain. Chem.* **2018**, *12*, 15–21. https://doi.org/10.1016/j.cogsc.2018.04.008.
(20) Favier, V.; Canova, G. R.; Cavaillé, J. Y.; Chanzy, H.; Dufresne, A.; Gauthier, C. Nanocomposite Materials from Latex and Cellulose Whiskers. *Polym. Adv. Technol.* **1995**, *6* (5), 351–355. https://doi.org/10.1002/pat.1995.220060514.
(21) Favier, V.; Chanzy, H.; Cavaille, J. Y. Polymer Nanocomposites Reinforced by Cellulose Whiskers. *Macromolecules* **1995**, *28* (18), 6365–6367. https://doi.org/10.1021/ma00122a053.
(22) Svagan, A. J.; Azizi Samir, M. A. S.; Berglund, L. A. Biomimetic Polysaccharide Nanocomposites of High Cellulose Content and High Toughness. *Biomacromolecules* **2007**, *8* (8), 2556–2563. https://doi.org/10.1021/bm0703160.
(23) Hubbe, M. A.; Rojas, O. J.; Lucia, L. A.; Sain, M. Cellulosic Nanocomposites: A Review. *BioResources* **2008**, *3* (3), 929–980.
(24) Benítez, A. J.; Lossada, F.; Zhu, B.; Rudolph, T.; Walther, A. Understanding Toughness in Bioinspired Cellulose Nanofibril/Polymer Nanocomposites. *Biomacromolecules* **2016**, *17* (7), 2417–2426. https://doi.org/10.1021/acs.biomac.6b00533.
(25) Prakobna, K.; Galland, S.; Berglund, L. A. High-Performance and Moisture-Stable Cellulose–Starch Nanocomposites Based on Bioinspired Core–Shell Nanofibers. *Biomacromolecules* **2015**, *16* (3), 904–912. https://doi.org/10.1021/bm5018194.
(26) Wang, M.; Olszewska, A.; Walther, A.; Malho, J.-M.; Schacher, F. H.; Ruokolainen, J.; Ankerfors, M.; Laine, J.; Berglund, L. A.; Österberg, M.; Ikkala, O. Colloidal Ionic Assembly between Anionic Native Cellulose Nanofibrils and Cationic Block Copolymer Micelles into Biomimetic Nanocomposites. *Biomacromolecules* **2011**, *12* (6), 2074–2081. https://doi.org/10.1021/bm101561m.
(27) Walther, A.; Bjurhager, I.; Malho, J.-M.; Pere, J.; Ruokolainen, J.; Berglund, L. A.; Ikkala, O. Large-Area, Lightweight and Thick Biomimetic Composites with Superior Material Properties via Fast, Economic, and Green Pathways. *Nano Lett.* **2010**, *10* (8), 2742–2748. https://doi.org/10.1021/nl1003224.
(28) Wang, B.; Benitez, A. J.; Lossada, F.; Merindol, R.; Walther, A. Bioinspired Mechanical Gradients in Cellulose Nanofibril/Polymer Nanopapers. *Angew. Chem. Int. Ed.* **2016**, *55* (20), 5966–5970. https://doi.org/10.1002/anie.201511512.
(29) Benítez, A. J.; Torres-Rendon, J.; Poutanen, M.; Walther, A. Humidity and Multiscale Structure Govern Mechanical Properties and Deformation Modes in Films of Native Cellulose Nanofibrils. *Biomacromolecules* **2013**, *14* (12), 4497–4506. https://doi.org/10.1021/bm401451m.
(30) Lossada, F.; Hoenders, D.; Guo, J.; Jiao, D.; Walther, A. Self-Assembled Bioinspired Nanocomposites. *Acc. Chem. Res.* **2020**, *53* (11), 2622–2635. https://doi.org/10.1021/acs.accounts.0c00448.
(31) Lossada, F.; Guo, J.; Jiao, D.; Groeer, S.; Bourgeat-Lami, E.; Montarnal, D.; Walther, A. Vitrimer Chemistry Meets Cellulose Nanofibrils: Bioinspired Nanopapers with High Water Resistance and Strong Adhesion. *Biomacromolecules* **2019**, *20* (2), 1045–1055. https://doi.org/10.1021/acs.biomac.8b01659.
(32) Lossada, F.; Jiao, D.; Guo, J.; Hoenders, D.; Eckert, A.; Walther, A. Outstanding Synergies in Mechanical Properties of Bioinspired Cellulose Nanofibril Nanocomposites Using Self-Cross-Linking Polyurethanes. *ACS Appl. Polym. Mater.* **2019**, *1* (12), 3334–3342. https://doi.org/10.1021/acsapm.9b00774.
(33) Petrović, Z. S.; Ferguson, J. Polyurethane Elastomers. *Prog. Polym. Sci.* **1991**, *16* (5), 695–836. https://doi.org/10.1016/0079-6700(91)90011-9.
(34) Akindoyo, J. O.; Beg, M. D. H.; Ghazali, S.; Islam, M. R.; Jeyaratnam, N.; Yuvaraj, A. R. Polyurethane Types, Synthesis and Applications – a Review. *RSC Adv.* **2016**, *6* (115), 114453–114482. https://doi.org/10.1039/C6RA14525F.
(35) de Souza, F. M.; Kahol, P. K.; Gupta, R. K. Introduction to Polyurethane Chemistry. In *Polyurethane Chemistry: Renewable Polyols and Isocyanates*; ACS Symposium Series; American Chemical Society, 2021; Vol. 1380, pp 1–24. https://doi.org/10.1021/bk-2021-1380.ch001.
(36) Hepburn, C. *Polyurethane Elastomers*; Springer Netherlands: Dordrecht, 1992. https://doi.org/10.1007/978-94-011-2924-4.
(37) Somarathna, H. M. C. C.; Raman, S. N.; Mohotti, D.; Mutalib, A. A.; Badri, K. H. The Use of Polyurethane for Structural and Infrastructural Engineering Applications: A State-of-the-Art Review. *Constr. Build. Mater.* **2018**, *190*, 995–1014. https://doi.org/10.1016/j.conbuildmat.2018.09.166.

(38) Atiqah, A.; Mastura, M. T.; Ali, B. A. A.; Jawaid, M.; Sapuan, S. M. A Review on Polyurethane and Its Polymer Composites. *Curr. Org. Synth.* **2017**, *14* (2), 233–248. https://doi.org/10.2174/1570179413666160831124749.

(39) Chattopadhyay, D. K.; Webster, D. C. Thermal Stability and Flame Retardancy of Polyurethanes. *Prog. Polym. Sci.* **2009**, *34* (10), 1068–1133. https://doi.org/10.1016/j.progpolymsci.2009.06.002.

(40) Subramani, S.; Lee, J. M.; Lee, J.-Y.; Kim, J. H. Synthesis and Properties of Room Temperature Curable Trimethoxysilane-Terminated Polyurethane and Their Dispersions. *Polym. Adv. Technol.* **2007**, *18* (8), 601–609. https://doi.org/10.1002/pat.860.

(41) Coogan, R. G. Post-Crosslinking of Water-Borne Urethanes. *Prog. Org. Coat.* **1997**, *32* (1), 51–63. https://doi.org/10.1016/S0300-9440(97)00010-6.

(42) Wang, S.-C.; Chen, P.-C.; Hwang, J.-Z.; Yeh, J.-T.; Huang, C.-Y.; Chen, K.-N. Performance Properties of Self-Curing Aqueous-Based PU System with Tri-Glycidyl Phosphate Curing Agent. *J. Polym. Res.* **2012**, *19* (3), 9844. https://doi.org/10.1007/s10965-012-9844-2.

(43) Sardon, H.; Irusta, L.; Fernández-Berridi, M. J.; Luna, J.; Lansalot, M.; Bourgeat-Lami, E. Waterborne Polyurethane Dispersions Obtained by the Acetone Process: A Study of Colloidal Features. *J. Appl. Polym. Sci.* **2011**, *120* (4), 2054–2062. https://doi.org/10.1002/app.33308.

(44) Sardon, H.; Irusta, L.; Fernández-Berridi, M. J.; Lansalot, M.; Bourgeat-Lami, E. Synthesis of Room Temperature Self-Curable Waterborne Hybrid Polyurethanes Functionalized with (3-Aminopropyl)Triethoxysilane (APTES). *Polymer* **2010**, *51* (22), 5051–5057. https://doi.org/10.1016/j.polymer.2010.08.035.

(45) Saw, L. K.; Brooks, B. W.; Carpenter, K. J.; Keight, D. V. Different Dispersion Regions during the Phase Inversion of an Ionomeric Polymer–Water System. *J. Colloid Interface Sci.* **2003**, *257* (1), 163–172. https://doi.org/10.1016/S0021-9797(02)00030-9.

(46) Chen, S.-A.; Hsu, J.-S. Polyurethane Anionomers. II. Phase Inversion and Its Effect on Physical Properties. *Polymer* **1993**, *34* (13), 2776–2782. https://doi.org/10.1016/0032-3861(93)90120-Y.

(47) Pandya, H.; Mahanwar, P. Fundamental Insight into Anionic Aqueous Polyurethane Dispersions. *Adv. Ind. Eng. Polym. Res.* **2020**, *3* (3), 102–110. https://doi.org/10.1016/j.aiepr.2020.07.003.

(48) Bossion, A.; Olazabal, I.; Aguirresarobe, R. H.; Marina, S.; Martín, J.; Irusta, L.; Taton, D.; Sardon, H. Synthesis of Self-Healable Waterborne Isocyanate-Free Poly(Hydroxyurethane)-Based Supramolecular Networks by Ionic Interactions. *Polym. Chem.* **2019**, *10* (21), 2723–2733. https://doi.org/10.1039/C9PY00439D.

(49) Maisonneuve, L.; Lamarzelle, O.; Rix, E.; Grau, E.; Cramail, H. Isocyanate-Free Routes to Polyurethanes and Poly(Hydroxy Urethane)s. *Chem. Rev.* **2015**, *115* (22), 12407–12439. https://doi.org/10.1021/acs.chemrev.5b00355.

(50) Gomez-Lopez, A.; Panchireddy, S.; Grignard, B.; Calvo, I.; Jerome, C.; Detrembleur, C.; Sardon, H. Poly(Hydroxyurethane) Adhesives and Coatings: State-of-the-Art and Future Directions. *ACS Sustain. Chem. Eng.* **2021**, *9* (29), 9541–9562. https://doi.org/10.1021/acssuschemeng.1c02558.

(51) Tretbar, C. A.; Neal, J. A.; Guan, Z. Direct Silyl Ether Metathesis for Vitrimers with Exceptional Thermal Stability. *J. Am. Chem. Soc.* **2019**, *141* (42), 16595–16599. https://doi.org/10.1021/jacs.9b08876.

(52) Zhao, B.; Hang, G.; Li, L.; Zheng, S. Nanocomposites of Polyethylene with Polyhedral Oligomeric Silsesquioxane: From Thermoplastics to Vitrimers through Silyl Ether Metathesis. *Mater. Today Chem.* **2022**, *24*, 100759. https://doi.org/10.1016/j.mtchem.2021.100759.

(53) Osthoff, R. C.; Bueche, A. M.; Grubb, W. T. Chemical Stress-Relaxation of Polydimethylsiloxane Elastomers1. *J. Am. Chem. Soc.* **1954**, *76* (18), 4659–4663. https://doi.org/10.1021/ja01647a052.

(54) Nishimura, Y.; Chung, J.; Muradyan, H.; Guan, Z. Silyl Ether as a Robust and Thermally Stable Dynamic Covalent Motif for Malleable Polymer Design. *J. Am. Chem. Soc.* **2017**, *139* (42), 14881–14884. https://doi.org/10.1021/jacs.7b08826.

(55) Zheng, P.; McCarthy, T. J. A Surprise from 1954: Siloxane Equilibration Is a Simple, Robust, and Obvious Polymer Self-Healing Mechanism. *J. Am. Chem. Soc.* **2012**, *134* (4), 2024–2027. https://doi.org/10.1021/ja2113257.

(56) Tobolsky, A. V.; MacKnight, W. J.; Takahashi, M. Relaxation of Disulfide and Tetrasulfide Polymers. *J. Phys. Chem.* **1964**, *68* (4), 787–790. https://doi.org/10.1021/j100786a013.

(57) Canadell, J.; Goossens, H.; Klumperman, B. Self-Healing Materials Based on Disulfide Links. *Macromolecules* **2011**, *44* (8), 2536–2541. https://doi.org/10.1021/ma2001492.

(58) Amamoto, Y.; Otsuka, H.; Takahara, A.; Matyjaszewski, K. Self-Healing of Covalently Cross-Linked Polymers by Reshuffling Thiuram Disulfide Moieties in Air under Visible Light. *Adv. Mater.* **2012**, *24* (29), 3975–3980. https://doi.org/10.1002/adma.201201928.

(59) Rekondo, A.; Martin, R.; Luzuriaga, A. R. de; Cabañero, G.; Grande, H. J.; Odriozola, I. Catalyst-Free Room-Temperature Self-Healing Elastomers Based on Aromatic Disulfide Metathesis. *Mater. Horiz.* **2014**, *1* (2), 237–240. https://doi.org/10.1039/C3MH00061C.

(60) Wang, Y.; Gao, M.; Li, S.; Liu, J.; Feng, A.; Zhang, L. Recyclable, Self-Healable and Reshape Vitrified Poly-Dimethylsiloxane Composite Filled with Renewable Cellulose Nanocrystal. *Polymer* **2022**, *245*, 124648. https://doi.org/10.1016/j.polymer.2022.124648.

(61) *Silane Coupling Agents - Combination of Organic and Inorganic Materials*; Shin-Etsu Chemical Co.,Ltd. https://www.shinetsusilicone-global.com/catalog/pdf/SilaneCouplingAgents_e.pdf (accessed 2025-01-16).

(62) Aziz, T.; Ullah, A.; Fan, H.; Jamil, M. I.; Khan, F. U.; Ullah, R.; Iqbal, M.; Ali, A.; Ullah, B. Recent Progress in Silane Coupling Agent with Its Emerging Applications. *J. Polym. Environ.* **2021**, *29* (11), 3427–3443. https://doi.org/10.1007/s10924-021-02142-1.

(63) Pavia, D. L.; Lampman, G. M.; Kriz, G. S. *Introduction to Spectroscopy: A Guide for Students of Organic Chemistry*; Harcourt College Publishers, 2001.

(64) Schoustra, S. K.; Asadi, V.; Smulders, M. M. J. Probing the Solubility of Imine-Based Covalent Adaptable Networks. *ACS Appl. Polym. Mater.* **2023**, *6* (1), 79–89. https://doi.org/10.1021/acsapm.3c01472.

(65) Breuillac, A.; Kassalias, A.; Nicolaÿ, R. Polybutadiene Vitrimers Based on Dioxaborolane Chemistry and Dual Networks with Static and Dynamic Cross-Links. *Macromolecules* **2019**, *52* (18), 7102–7113. https://doi.org/10.1021/acs.macromol.9b01288.

(66) Snijkers, F.; Pasquino, R.; Maffezzoli, A. Curing and Viscoelasticity of Vitrimers. *Soft Matter* **2016**, *13* (1), 258–268. https://doi.org/10.1039/C6SM00707D.

(67) Ricarte, R. G.; Shanbhag, S. Unentangled Vitrimer Melts: Interplay between Chain Relaxation and Cross-Link Exchange Controls Linear Rheology. *Macromolecules* **2021**, *54* (7), 3304–3320. https://doi.org/10.1021/acs.macromol.0c02530.

(68) Stukenbroeker, T.; Wang, W.; Winne, J. M.; Du Prez, F. E.; Nicolaÿ, R.; Leibler, L. Polydimethylsiloxane Quenchable Vitrimers. *Polym. Chem.* **2017**, *8* (43), 6590–6593. https://doi.org/10.1039/C7PY01488K.

(69) Chen, X.; Hu, S.; Li, L.; Torkelson, J. M. Dynamic Covalent Polyurethane Networks with Excellent Property and Cross-Link Density Recovery after Recycling and Potential for Monomer Recovery. *ACS Appl. Polym. Mater.* **2020**, *2* (5), 2093–2101. https://doi.org/10.1021/acsapm.0c00378.

(70) Porath, L. E.; Evans, C. M. Importance of Broad Temperature Windows and Multiple Rheological Approaches for Probing Viscoelasticity and Entropic Elasticity in Vitrimers. *Macromolecules* **2021**, *54* (10), 4782–4791. https://doi.org/10.1021/acs.macromol.0c02800.

(71) Sehaqui, H.; Zhou, Q.; Berglund, L. A. Nanostructured Biocomposites of High Toughness—a Wood Cellulose Nanofiber Network in Ductile Hydroxyethylcellulose Matrix. *Soft Matter* **2011**, *7* (16), 7342–7350. https://doi.org/10.1039/C1SM05325F.

(72) Benítez, A. J.; Walther, A. Counterion Size and Nature Control Structural and Mechanical Response in Cellulose Nanofibril Nanopapers. *Biomacromolecules* **2017**, *18* (5), 1642–1653. https://doi.org/10.1021/acs.biomac.7b00263.

(73) Daicho, K.; Saito, T.; Fujisawa, S.; Isogai, A. The Crystallinity of Nanocellulose: Dispersion-Induced Disordering of the Grain Boundary in Biologically Structured Cellulose. *ACS Appl. Nano Mater.* **2018**, *1* (10), 5774–5785. https://doi.org/10.1021/acsanm.8b01438.

(74) Khakalo, A.; Filpponen, I.; Rojas, O. J. Protein-Mediated Interfacial Adhesion in Composites of Cellulose Nanofibrils and Polylactide: Enhanced Toughness towards Material Development. *Compos. Sci. Technol.* **2018**, *160*, 145–151. https://doi.org/10.1016/j.compscitech.2018.03.013.

(75) Haraguchi, K. Synthesis and Properties of Soft Nanocomposite Materials with Novel Organic/Inorganic Network Structures. *Polym. J.* **2011**, *43* (3), 223–241. https://doi.org/10.1038/pj.2010.141.

(76) Chen, Q.; Chen, H.; Zhu, L.; Zheng, J. Fundamentals of Double Network Hydrogels. *J. Mater. Chem. B* **2015**, *3* (18), 3654–3676. https://doi.org/10.1039/C5TB00123D.

(77) Bossion, A.; Aguirresarobe, R. H.; Irusta, L.; Taton, D.; Cramail, H.; Grau, E.; Mecerreyes, D.; Su, C.; Liu, G.; Müller, A. J.; Sardon, H. Unexpected Synthesis of Segmented Poly(Hydroxyurea–Urethane)s from

Dicyclic Carbonates and Diamines by Organocatalysis. *Macromolecules* **2018**, *51* (15), 5556–5566. https://doi.org/10.1021/acs.macromol.8b00731.

(78) Yuen, A.; Bossion, A.; Gómez-Bengoa, E.; Ruipérez, F.; Isik, M.; Hedrick, J. L.; Mecerreyes, D.; Yang, Y. Y.; Sardon, H. Room Temperature Synthesis of Non-Isocyanate Polyurethanes (NIPUs) Using Highly Reactive N-Substituted 8-Membered Cyclic Carbonates. *Polym. Chem.* **2016**, *7* (11), 2105–2111. https://doi.org/10.1039/C6PY00264A.

Chapter 5. Synopsis

Affiliation

[1]Life-Like Materials and Systems, Department of Chemistry, University of Mainz, Duesbergweg 10-14, 55128 Mainz, Germany.

5.1 Introduction

In the introduction of this thesis (**Chapter 1**), I outlined the overarching goal: to utilize the dynamic properties of covalent adaptable networks (CANs) for unique structural and thermoresponsive properties in bioinspired (nano)composites. Bioinspired composites are generally known for their complex hierarchical structures and a range of interesting properties, achieved through the synergistic interaction of their phases.[1] However, many of these systems face limitations in processability and recyclability, challenges that CANs are well-positioned to address.[2] CANs are moreover capable of other benefits, such as dynamic chemistries that enable improved interphase interactions or induce shape-memory actuation.

Crucially, the concept of incorporating dynamic CAN properties into composite materials is broadly applicable and does not depend on specific components, whether on the polymer side or on the reinforcement side of things. To demonstrate this versatility, the thesis discussed three distinct bioinspired (nano)composite designs, each employing a unique combination of composite type, polymer system, and preparation method. Finally, this synopsis chapter also explores future strategies for integrating and utilizing the dynamic properties of CANs in bioinspired composite materials.

5.2 Discussion and Future Research Directions

In **Chapter 2** I emphasized the design of a new tunable CAN system, based on an aspartic acid-derivative. Our bottom-up approach to designing these CANs allowed us to incorporate functions that are difficult to achieve in existing systems. For example, we introduced several features to promote and enhance internal catalysis of the transesterification bond exchange in this setup. Internal catalysis can offer several advantages, such as faster bond exchange rates and improved stability or integration of the catalyst within the network.[3,4] It also eliminates the need for heavy metal catalysts, addressing concerns about toxicity and sustainability.

The pre-CANs of our system are based on acrylamide-modified monomers polymerized into linear copolymers. The aspartic acid-based monomer can facilitate transesterification via an anhydride intermediate in a dissociative process. Additionally, we incorporated a covalently tethered sulfonic acid moiety to further catalyze the reaction, and an ethylene glycol-modified monomer to plasticize the final materials. By exploring various monomer ratios, we identified an optimal distribution of the three comonomers. The resulting linear copolymers constitute a system that can use different crosslinkers to produce a range of final materials with varied properties. Incorporating a tertiary amine into the crosslinkers is an additional way of achieving internal catalysis. Moreover, varying between crosslinkers with altered valencies or polar groups greatly impacts the mechanical

properties as well. Such tunability for the same copolymer is only reliant on a simple aqueous mixing step with small-molecule commercial crosslinkers, followed by curing. It represents a strategy for preparing a diverse range of CANs by varying crosslinkers in a single principal system.

This is the only CAN in this thesis, and one of few in literature, that is hydrophilic enough to be fully compatible with water. The components are completely soluble at high concentrations, while the formed network, though insoluble due to its crosslinked structure, is highly swellable. In contrast, the other CANs, despite being relatively hydrophilic, are less water-compatible. Although water-resistance is often desirable, water compatibility offers unique advantages for safety, environmental concerns, and various nanocomposite (NC) preparation methods, as discussed in this thesis.[1] While this chapter placed less emphasis on the NC aspect, we utilized this CAN system to prepare clay-based NCs, showing high stiffness, shapeability, and even weldability without the need for external additives.

Future work could refine this system by exploring the combination of different crosslinkers. For example, one crosslinker may contribute to increased bond exchange, while another could improve creep resistance. Together, they could provide a better balance of both dynamic behavior and stability. If effective, combining different monomers would allow for greater flexibility in fine-tuning properties, as they would not need to be mixed in equal proportions but could be varied in any ratio, thereby unlocking the full range of intermediate properties. Another avenue for future research involves designing custom crosslinkers tailored to specific applications and combining them with the existing copolymer, providing flexibility in the development of new systems without needing to redesign the entire material. Additionally, by attaching additional functional groups through alcohol-ester linkages, it might be possible to incorporate properties typically not found in polymers, such as antibacterial, flame-retardant, or conductive features. Alternatively, given the inherent water-compatibility of our CAN, designed for use in aqueous NC preparation, further exploration could involve combining it with various reinforcements. For instance, graphene oxide, a reinforcement with notable properties, could integrate well due to its hydroxy, epoxide, and acid groups interacting with the CAN, potentially leading to covalent bonding between phases.[5,6]

In contrast to the first project, **Chapter 3** revolved around the reinforcing phase. Continuous delignified wood scaffolds are likely the most intricate type of reinforcement to be used in polymer composites, based on their hierarchical structure, with a complex interplay of chemical and physical properties across multiple length scales.[7] For this purpose, we selected an established CAN system and further tailored it to ensure compatibility with the wood scaffold and the impregnation and curing methods.[8] We used a thioepoxy resin, as it cures efficiently into highly crosslinked networks and can be catalyzed by various acid and base catalysts. Additionally, epoxy resins have been used with delignified wood scaffolds to form composites, highlighting their suitability for the desired purpose.[9,10] We ensured all components were liquid and the monomer formulation had sufficiently low viscosity

to enable impregnation, which we achieved through acetone dilution of the already liquid monomer formulation.

On a chemical level, this CAN relies on the transesterification reaction, similar to the CANs of the first project. However, unlike the more uncommon anhydride-catalyzed dissociative mechanism of the previous system, this network follows the standard associative transesterification that relies on an excess of hydroxyl groups. The resulting material possesses slower dynamicity and a more glassy mechanical state. And although this resin is more hydrophilic than many other polymers due to its hydroxyl groups and esters, it is less hydrophilic than the previous system as well. The hydroxyl and ester groups can also provide interphase interactions and bonding between the cellulose and the CAN in the final composite materials. We achieved wood impregnation by performing solvent-exchange on the wood scaffolds, transferring them from a wet state to an acetone-soaked state. While a more environmentally friendly approach might involve using a system that would be compatible with the aqueous wet state, this present significant challenges. Specifically, incomplete pore filling due to using a solvent can cause gaps and poor interphase adhesion in the final material. Moreover, the presence of water can cause problems with curing and compression molding. On the other hand, using a less polar impregnating phase can result in more water-resistant composites, offering an advantage over native wood.[11]

In terms of the composites, the use of wood scaffolds offers distinct advantages, including environmental benefits and the cohesiveness of continuous reinforcements.[7] The hierarchical structure of wood provides exceptional reinforcement along the fiber direction. Additionally, these wood-based composites are transparent, offering potential for tailored optical properties due to the anisotropic nature of wood.

A key feature of our wood composite relies on the dynamicity of the CAN, which, while sacrificing some mechanical performance, allows for more extreme shaping than typically possible. This flexibility facilitates reuse, as samples initially prepared for one purpose can be easily adapted for others. Moreover, the potential for complex shaping enables entirely new applications. In contrast to the three-dimensional shapes we prepared, which were mainly used for demonstration purposes, future research could explore the creation of functional shapes that are not feasible with traditional wood-based materials. Such functional shapes could enable the use of renewable resources in applications currently dependent on machined metals or cast polymers. To further improve the shaping of these composite materials, a shift from manual to machine-based methods is essential. While more extreme and complex shapes are achievable, the shaping process must be gradual and performed at elevated temperatures to allow internal stresses to relax. Instead of sharp bends, more rounded shapes should be targeted. While shaping by hand under heat is challenging, a mold that slowly closes in an oven or hot press could effectively improve upon the shaping we performed by hand.

We also achieved a version of full recycling, which does not recover the same material but does constitute further usage of the original resources after the main material is used up or broken. We did not further test the dynamicity of this 2nd Life composite, although this is certain to display dynamic properties as well. It can likely also be recycled multiple times over, especially when moderate temperatures are used, which would further the sustainability of our approach. Finally, while shape memory is not a new concept, the shape memory of high-stiffness materials enables actuators capable of generating significant force, a feature that makes composite actuators distinct from soft actuators, such as hydrogels. A unique aspect of CANs with shape memory is that their "permanent" return shape is not fixed but can be programmed, offering greater versatility. Future research could explore the potential of shape memory for active actuation, as well as investigate improvements in shape recovery, particularly in the fiber direction.

A second important feature of our composites involves the cellulose dissolution effect caused by the catalyst we used, similar to ionic liquids. The organometallic catalyst significantly enhances interphase diffusion and interaction, improving processability and recyclability. This effect plays a key role in achieving superior impregnation, shapability, and shape memory behavior, but it also contributes to reduced mechanical properties. Future research could explore several avenues, including testing different organometallic catalysts, investigating their effects at various concentrations and on various wood types, and extending the approach to other polymer systems. An interesting direction could be deliberately using less formulation during impregnation to enable further compression of partially dissolved cellulose via compression molding and achieve dynamic composites with even higher cellulose contents. The question would then be if the dynamicity of the CAN could still be significantly expressed in the reinforced composites.

In **Chapter 4** we explored a previous research topic from the group in more detail: the combination of cellulose nanofibrils (CNFs) and polyurethanes (PUs) into bioinspired NCs with exceptional mechanical performance.[12] This project bridges the gap between those discussed in Chapter 2 and Chapter 3, combining aspects of both. The bioinspired NCs are prepared through aqueous mixing of CNF nanoparticles and polymer, which then assemble hierarchically via ambient evaporation, similar to the first project. However, the use of CNFs as nanoparticles aligns more with the wood scaffolds in the second project.

Our approach involved preparing a range of PU dispersions for two main reasons. First, we aimed to replicate the synergy between CNFs and PUs observed in a previous study, where the PU was a commercial formulation with unknown composition.[12] Second, by systematically varying PU properties, such as crosslinking, chain extenders, and crystallinity, we sought to understand their impact on NC properties. Interestingly, our results suggest that the dispersion characteristics, such as particle size and dispersity, may play a more significant role than the chemical nature of the PUs. This outcome is intriguing and warrants further investigation to fully understand the synergy between

what are essentially PU nanoparticles, despite not being initially conceptualized as such, and CNF nanofibers.

In this project, we demonstrated potential applications of the dynamic properties of the NCs, including shaping and laminate formation. Additionally, welding or annealing of samples can also be envisioned. However, we did not focus on these aspects as they have already been explored in detail with other CAN-based CNF NCs.[13] What is particularly unique about our approach is the potential to achieve dynamic NCs that also exhibit the superior properties mentioned earlier. In addition, the incorporation of two bond exchange chemistries enhances the dynamic properties of these NCs. Future research could explore how far laminate formation can be pushed. For example, what is the maximum sample thickness achievable? Could laminating NC films with offsets in the X and Y planes enable the creation of larger cohesive NCs? Taking this concept further, could properly designed molds allow for the formation of three-dimensional laminates using films? If successful, this would enable shapes beyond the capability of individual composites, as internal stress could potentially be alleviated using separate films. Additionally, it would be interesting to investigate whether these NCs can be milled and subsequently compression molded into new NCs, similar to the process explored in Chapter 3.

Overall, these results demonstrate the successful integration of dynamic properties from CANs into bioinspired composite materials. We highlighted the need for tailored approaches to ensure compatibility between the polymer phase and the different composite types, while showcasing that the CAN field enables us to design or adapt systems to meet these needs. This adaptability makes such strategies highly applicable to a broader range of composite materials. Additionally, we emphasized the advantages of dynamic properties in composites, particularly their potential to enhance recyclability, improve production methods, optimize interphase interactions, and enable more complex shapes. In conclusion, dynamic composite materials possess the potential to address both technical challenges and environmental concerns across multiple industries.

5.3 References

(1) Lossada, F.; Hoenders, D.; Guo, J.; Jiao, D.; Walther, A. Self-Assembled Bioinspired Nanocomposites. *Acc. Chem. Res.* **2020**, *53* (11), 2622–2635. https://doi.org/10.1021/acs.accounts.0c00448.

(2) Van Zee, N. J.; Nicolaÿ, R. Vitrimers: Permanently Crosslinked Polymers with Dynamic Network Topology. *Prog. Polym. Sci.* **2020**, *104*, 101233. https://doi.org/10.1016/j.progpolymsci.2020.101233.

(3) Lijsebetten, F. V.; Holloway, J. O.; Winne, J. M.; Du Prez, F. E. Internal Catalysis for Dynamic Covalent Chemistry Applications and Polymer Science. *Chem. Soc. Rev.* **2020**, *49* (23), 8425–8438. https://doi.org/10.1039/D0CS00452A.

(4) Cuminet, F.; Caillol, S.; Dantras, É.; Leclerc, É.; Ladmiral, V. Neighboring Group Participation and Internal Catalysis Effects on Exchangeable Covalent Bonds: Application to the Thriving Field of Vitrimer Chemistry. *Macromolecules* **2021**, *54* (9), 3927–3961. https://doi.org/10.1021/acs.macromol.0c02706.

(5) Dikin, D. A.; Stankovich, S.; Zimney, E. J.; Piner, R. D.; Dommett, G. H. B.; Evmenenko, G.; Nguyen, S. T.; Ruoff, R. S. Preparation and Characterization of Graphene Oxide Paper. *Nature* **2007**, *448* (7152), 457–460. https://doi.org/10.1038/nature06016.

(6) Putz, K. W.; Compton, O. C.; Segar, C.; An, Z.; Nguyen, S. T.; Brinson, L. C. Evolution of Order During Vacuum-Assisted Self-Assembly of Graphene Oxide Paper and Associated Polymer Nanocomposites. *ACS Nano* **2011**, *5* (8), 6601–6609. https://doi.org/10.1021/nn202040c.

(7) Kumar, A.; Jyske, T.; Petrič, M. Delignified Wood from Understanding the Hierarchically Aligned Cellulosic Structures to Creating Novel Functional Materials: A Review. *Adv. Sustain. Syst.* **2021**, *5* (5), 2000251. https://doi.org/10.1002/adsu.202000251.

(8) Hayashi, M.; Katayama, A. Preparation of Colorless, Highly Transparent, Epoxy-Based Vitrimers by the Thiol-Epoxy Click Reaction and Evaluation of Their Shape-Memory Properties. *ACS Appl. Polym. Mater.* **2020**, *2* (6), 2452–2457. https://doi.org/10.1021/acsapm.0c00397.

(9) Koch, S. M.; Pillon, M.; Keplinger, T.; Dreimol, C. H.; Weinkötz, S.; Burgert, I. Intercellular Matrix Infiltration Improves the Wet Strength of Delignified Wood Composites. *ACS Appl. Mater. Interfaces* **2022**, *14* (27), 31216–31224. https://doi.org/10.1021/acsami.2c04014.

(10) Frey, M.; Schneider, L.; Masania, K.; Keplinger, T.; Burgert, I. Delignified Wood–Polymer Interpenetrating Composites Exceeding the Rule of Mixtures. *ACS Appl. Mater. Interfaces* **2019**, *11* (38), 35305–35311. https://doi.org/10.1021/acsami.9b11105.

(11) Yang, Z.; Meng, X.; Zeng, G.; Wei, J.; Wang, C.; Yu, W. Effect of Resin Content on the Structure, Water Resistance and Mechanical Properties of High-Density Bamboo Scrimbers. *Polymers* **2024**, *16* (6), 797. https://doi.org/10.3390/polym16060797.

(12) Lossada, F.; Jiao, D.; Guo, J.; Hoenders, D.; Eckert, A.; Walther, A. Outstanding Synergies in Mechanical Properties of Bioinspired Cellulose Nanofibril Nanocomposites Using Self-Cross-Linking Polyurethanes. *ACS Appl. Polym. Mater.* **2019**, *1* (12), 3334–3342. https://doi.org/10.1021/acsapm.9b00774.

(13) Lossada, F.; Guo, J.; Jiao, D.; Groeer, S.; Bourgeat-Lami, E.; Montarnal, D.; Walther, A. Vitrimer Chemistry Meets Cellulose Nanofibrils: Bioinspired Nanopapers with High Water Resistance and Strong Adhesion. *Biomacromolecules* **2019**, *20* (2), 1045–1055. https://doi.org/10.1021/acs.biomac.8b01659.

Back Matter

Acknowledgements

This content has been redacted in accordance with data protection regulations.

Funding Acknowledgements

The work done in this thesis has received funding from the European Union's horizon research and innovation programme under the Marie Skłodowska-Curie Grant agreement no. 860911. AW acknowledges funding via a Gutenberg Research Professorship underpinning his Life-Like Materials Program.





This project has received funding from the European Union's Horizon 2020 research and innovation programme under the Marie Skłodowska-Curie grant agreement No 860911

Statement on AI Use

Large language models (ChatGPT-4) were used for purposes of text correction, never for text generation.

Curriculum Vitae